HIERARCHICALLY BUCKLED SURFACE ENGINEERING OF TEXTILE SUBSTRATES WITH STRETCHABLE POROUS MICROARCHITECTURES

HAN JING

PhD

The Hong Kong Polytechnic University

2025

The Hong Kong Polytechnic University

School of Fashion and Textiles

Hierarchically Buckled Surface Engineering of Textile Substrates with Stretchable Porous Microarchitectures

HAN JING

A thesis submitted in partial fulfilment of the requirements

for the degree of Doctor of Philosophy

December 2024

CERTIFICATE OF ORIGINALITY

I hereby declare that this thesis is my own work and that, to the best of my knowledge and belief, it reproduces no material previously published or written, nor material that has been accepted for the award of any other degree or diploma, except where due acknowledgement has been made in the text.

_____ (Signed)

_____HANJING_____ (Name of student)

Abstract

Textile wearables have been widely used in our daily lives and regarded as the second human skin. They have attracted significant attention in wearable technologies owing to their unique natures and remarkable properties such as excellent flexibility, good air permeability, lightweight, thermal-protective, versatile structure designs, and robust mechanical deformation capacities. In practical applications, fibers usually require further modifications with functional materials for the enhancement of their physicochemical properties or the incorporation of specific advanced functions by physical or chemical methods. However, there is still a considerably difficult challenge in endowing the textiles with desired functionalities or microstructures while keeping their unique fiber texture features and inherent properties. In this research, inspired by the surface buckling of finger joint skin, a new kind of hierarchically buckled porous microstructured textiles (HBPMTs) has been delicately designed and fabricated using stretchable elastic textiles and polymer brick materials, by a unique strategy involving a modified breath figure (BF) method. BF is a unique self-assembly strategy in which water droplet arrays are used as templates for the assembly of polymer brick materials to generate hierarchically porous microstructures on different substrates with tunable sizes in the range from hundreds of nanometers to dozens of micrometers.

The first study introduces a novel fabrication strategy for hierarchically buckled

porous microstructured fibers (HBPMFs), inspired by the surface buckling of finger joint skin. By using a combination of material system manipulation, interfacial self-assembly, stretching-releasing control, and thermal annealing, the research demonstrates the development of fibers with skin-like buckling and stretchable porous microarchitectures. These HBPMFs exhibit enhanced stretchability, increased specific surface area, and the ability to incorporate functional nanomaterials effectively. Application demonstrations, such as photocatalytic degradation of organic pollutants using TiO_2-integrated HBPMFs, highlight significantly improved performance compared to conventional fiber materials. This work provides an efficient approach for designing advanced functional fibers with customizable features for wearable and environmental applications.

The second study proposes an innovative development of hierarchically buckled porous microstructured fabrics (HBPMFs) tailored for energy harvesting and self-powered sensing applications. Utilizing a surface self-assembly approach, HBPMFs were fabricated from commercially available elastic fabrics, incorporating a combination of unique microarchitectural designs and functional nanoparticles such as TiO_2, $BaTiO_3$, and Ag. The research demonstrates the significant enhancement of triboelectric nanogenerators in terms of structural stability, stretchability, and electrical outputs, with Ag NPs-doped HBPMFs-TENGs exhibiting voltage, current, and charge

enhancements of 4, 3, and 6 times respectively over the HBPMFs-TENGs. Moreover, Ag NPs-doped HBPMFs-TENGs effectively powered wearable electronics and acted as self-powered sensors capable of detecting fine motions, such as breathing and joint movements, illustrating their potential for integration into smart wearables and healthcare monitoring systems.

The third study explores an advanced modification of carbon fibers through a core-spun yarn structure, where elastic fibers serve as the core wrapped by carbon fibers, creating a composite material with enhanced flexibility and mechanical properties. Utilizing the high-humidity breath figure (BF) fabrication method, the core-spun yarn carbon fibers are processed into hierarchically buckled porous structures (HBPFSs) and coated with nickel-cobalt layered double hydroxide (NiCo-LDH) nanostructures via hydrothermal treatment. This approach yields stretchable supercapacitors with excellent mechanical resilience and electrochemical performance. Even under significant tensile strain, the devices maintain robust energy storage capabilities, showcasing the potential of integrating core-spun yarn processing with hierarchical structural design for next-generation flexible and stretchable energy storage systems, particularly in wearable electronics and smart textiles.

The fourth study presents a new approach to develop highly flexible and efficient energy storage systems for wearable electronics. By employing a novel fabrication

method, carbon nanotube (CNT) and styrene-butadiene-styrene (SBS) composites are processed into hierarchically buckled porous structureson knitted carbon fabrics under high-humidity conditions. This structure enables uniform hydrothermal growth of nickel-cobalt layered double hydroxide (NiCo-LDH) nanostructures, achieving an optimized balance between mechanical flexibility and electrochemical performance. The device of stretchable supercapacitors retains 94% of their capacitance under 80% tensile strain and demonstrates excellent durability with only 8% degradation over 20,000 charge-discharge cycles, with a maximum specific capacitance of 4948 mF cm^{-2} at 2 mA cm^{-2} and an energy density of 801.6 μWh cm^{-2}. Its application potential is further demonstrated by powering wearable electronics under dynamic deformation conditions, making it a strong candidate for next-generation smart textiles and wearable technologies.

This comprehensive research highlights the remarkable versatility of hierarchically buckled porous microstructured textiles and their associated functionalized systems. The innovative methodologies and advanced designs outlined across these studies demonstrate significant improvements in mechanical resilience, energy harvesting, sensing, and energy storage capabilities. Thus, the findings provide promising pathways for the development of next-generation textile-based wearables, offering transformative potential for applications in healthcare, environmental monitoring, and

smart electronic systems.

Publications

Published Journal Papers:

[1] **Han, J.**, Xu, B., Fang, C., Wei, J., Li, Z., Liu, X.& Zhang, J. (2025). Hierarchically Porous Wearable Composites for High‐Performance Stretchable Supercapacitors. *Advanced Science*, 2500835.

[2] **Han, J.**, Li, Z., Fang, C., Liu, X., Yang, Y., Wang, Q., Zhang J. & Xu, B. (2024). Hierarchically porous architectured stretchable fibrous materials in energy harvesting and self-powered sensing. *Nano Energy*, *129*, 110080.

[3] **Han, J.**, Xu, B., Li, Z., Tang, Y., Huang, J., Liu, X., Yang, Y. & Chung, K. Y. (2023). Skin-inspired hierarchically buckled fibers with stretchable porous microarchitectures and customizable functionalities. *Chemical Engineering Journal*, *464*, 142606.

Conference Publication:

[1] **Han, J**., Xu, B., & Li, Z. (2023, September). Study on Hierarchically Buckled Surface Regulation for Stretchable Porous Microarchitectures Fibers. In *Journal of Physics: Conference Series* (Vol. 2587, No. 1, p. 012076). IOP Publishing.

Submitted Journal Paper:

Han, J., Xu, B., Fang, C., Wei J., Li Z., Liu X., Yang Y., Wang Q., Zhang J. (2024) Hierarchically Porous NiCo-LDH@CNT/SBS Composites for High-Performance Stretchable Supercapacitors in Wearable Electronics (Submitted)

Acknowledgements

First and foremost, I would like to express my deep gratitude to Prof. XU Bingang, my chief supervisor, for offering me a valuable opportunity to pursue my Ph.D. study and providing me a lot of advice during my study. His constant encouragement, patient guidance, incisive comments, and constructive criticism have been vital to my academic life, inspiring me to keep improving and giving me the courage to overcome difficulties.

I shall extend my thanks to all my research teammates and colleagues, especially Dr. LI Zihua, Dr. JING Titao, Dr. YIN Xin, Dr. GUAN Xiaoyang, Dr. TAN Di, Dr. LU Jian, Ms. GAO Yuanyuan, Ms. LI Meiqi, Ms. YANG Yujue, Ms. WANG Qian, Mr. LIU Xinlong, Mr. ZHANG Junze, Mr. HUANG Junxian, and Ms. King Yan Chung, Mr. HU Xin for their great assistance and encouragement in my work and life.

More thanks to the technicians of the laboratory for their help in offering me the resources and advice during my experiments.

Last but not least, I wish to thank my parents and my friends for their constant love, support, and encouragement throughout my study and my life these years.

Table of Contents

List of Figures

List of Tables

Abbreviations

HBPMTs	hierarchically buckled porous microstructured textiles
BF	breath figure
HBPMFs	hierarchically buckled porous microstructured fibers
NiCo-LDH	nickel-cobalt layered double hydroxide
CNT	carbon nanotube
SBS	styrene-butadiene-styrene
3CPM	3D conformal porous microstructural
SEM	scanning electron microscope
TEM	transmission electron microscope
TGA	thermogravimetric analyser
FTIR	fourier transform infrared spectroscopy
EDX	energy-dispersive X-ray spectroscopy
CVD	chemical vapor deposition
LbL	layer-by-layer
CC	cotton cloth
FP	filter paper
CF	chemical fabric
HBS	hierarchically buckled structures
TENG	triboelectric nanogenerators
CAFMFs	continuous advanced functional material fibers
PU	polyurethane
PMMA	poly(methyl methacrylate)
CS_2	carbon disulfide

SCFFs	solid coating functional fibers
PCFFs	porous coating functional fibers without buckling structures
MB	methylene blue
NR	neutral red
b-PU	braided PU fiber
AFFMs	advanced functional fibrous materials
SCFs	solid coating fabrics
PCFs	porous coating fabrics without buckling structures
PAAm	polyacrylamide
HBPMFs-TENG	HBPMFs fabric-based TENG
Ag@HBPMFs	Ag NPs doped HBPMFs
CNTs	carbon nanotubes
EDLC	electrochemical double-layer capacitance
MWCNTs	multi-walled carbon nanotubes
$CoSO_4 \cdot 6H_2O$	cobalt(II) sulfate hexahydrate
$NiSO_4 \cdot 6H_2O$	nickel(II) sulfate hexahydrate
KOH	potassium hydroxide
SDBS	odium dodecylbenzene sulfonate
BMAA	acrylamide, N,N′-methylene-bisacrylamide
KPS	potassium persulfate
TEMED	tetramethylethylenediamine
HBPS	buckled porous carbon fibers
NiCo@HBPS	NiCo-LDH coating applied to the porous carbon fibers
CV	cyclic voltammetry
GCD	galvanostatic charge-discharge

EIS	electrochemical impedance spectroscopy
HBPFSs	hierarchically buckled porous structure fabrics
CNT_aSBS_b@F	HBPFSs were coated with a mixture of different radio of SBS/$CHCl_3$ and CNT/$CHCl_3$ solutions
Ni_xCo_y LDH@CNT_aSBS_b@F	nickel-cobalt layered double hydroxide (NiCo-LDH) nanostructures was applied to CNT_aSBS_b@F
HR-TEM	high-resolution transmission electron microscopy
Rct	internal resistance Rs and charge transfer resistance
AI	artificial intelligence

Chapter 1 Introduction

1.1 Background

The body of human beings is a perfect marvelous organic machine. Taking human skin as an example, it is three-dimensional complex, soft, extensible (3-55% strain) and multifunctional (such as regulating temperature, moisture, pressure via perspiration)[1,2]. It is also the first barrier to infection from environment to guard the underlying muscles, bones, etc. When the dynamic framework of bones (i.e. skeleton) are in movement, the soft and flexible human skin can not only keep perfectly conformable with small deformation, but also can easily cope with the large deformation caused by the bending/stretching of joint parts through the generation of surface buckling.

In recent years, wearable electronics have been actively employed in sports, healthcare and entertainment, but they usually emerged as some special accessories using flexible and/or light supporters to integrate with rigid miniaturized electronics, such as watches, wrist bands and glasses. Development of truly wearable electronics with desired functional performance, uncompromised safety, and good wearing comfort is a common goal of scholars and professionals from a diverse background of fields[3–6]. One key challenge is to develop a kind of flexible materials that can integrate both advanced functions and common cloth advantages (i.e. conformable, breathable, stretchable, etc.). Existed materials for wearable electronics usually possess excellent

desired functions and/or some good mechanical properties. The reported approaches for such kinds of advanced functional materials involve complex fractal design of thin metal ribbons on elastomer substrates[7–9], intrinsically stretchable semiconducting polymer synthesis[10,11] and the wrapping of specific nanomaterials (e.g. carbon nanotube sheets) on elastomer filaments[12]. These creative works are highly valuable and inspired, and their mechanical performance is also getting closer to some requirements of truly wearable applications. In fact, the most successful and mature materials for truly wearable applications are textiles. They have been broadly used to fabricate garments and accessories for thousands of years, which can be regarded as the second skin for human beings. However, the main functions of conventional textile materials still remain in physical protection, passive thermal management and fashion, which can no longer satisfy the urgent and quick demands of smart wearable electronics. Benefiting from the breakthroughs in functional polymers and nanomaterials, textile materials can be directly used as substrates or supporters for a kind of advanced functional textile-based composites that can sense, actuate, regulate temperature, change color, convert and store energy by surface modification and conventional coating[13–16]. Unfortunately, the inherent advantages of textiles (such as air-permeability, stretchability, conformability and even flexibility) for truly wearable comfort are often sacrificed or totally lost, because such kind of textile-based composites usually has a

solid, rigid and/or thin layer of composites. In addition, the final functional performance is usually far below that of employed nanomaterials because most of them are fully embedded in the formed solid layer/matrix[17,18].

Inspired by human skin that is multifunctional, soft, breathable and highly stretchable via the generation of surface buckling, this research study aims to design and study a new kind of hierarchically buckled porous microstructured textiles (HBPMTs) by rational surface design and engineering of stretchable textile substrates (such as elastic fibers and fabrics) with hierarchically buckled and porous microarchitectures using desired brick materials (such as frequently-used polymers and functional nanomaterials). Owing to the special design and construction of brick materials as buckled porous architectures along the surface of textile substrates, the resultant HBPMTs are expected to introduce the advanced functions of functional materials and meanwhile maintain the inherent advantages of textile substrates such as flexibility, air-permeability and stretchability. Moreover, the porous structures hierarchically contouring to the textile surface at the microscale will also establish a micro-bridge connecting macroscopic fibers and functional nanomaterials, which possesses flexible and versatile designability for rational incorporation of nanocomponents with more exposed surface area for higher performance. Such kind of HBPMTs can achieve both advanced functions with high performance and

indispensable wearable comfort requirements for a kind of truly wearable systems with customized advanced functions.

1.2 Research Objectives

This research study aims at developing a new kind of multifunctional HBPMFs that are not only able to take better advantages of flexibility and stretchability of fiber materials and porosity of buckled microarchitectures, but also possess the customizable functionalities of the incorporated functional nanocomponents. The detailed research objectives are as follows:

1. to develop a new kind of hierarchically buckled porous microstructured textiles (HBPMTs) with flexible, stretchable characteristics by mimicking human skin;
2. to develop a general physicochemical strategy consisted of mechanical control, selective swelling, interfacial self-assembly and thermal annealing for hierarchically buckled surface engineering of textile material substrates;
3. to carry out a systematic study on various influential parameters on the formation and properties of hierarchically buckled porous microstructures;
4. to study, evaluate and characterize the performance of the developed HBPMTs, and to incorporate functional materials into the HBPMTs for further applications.

1.3 Research Methodology

In accordance with the research objectives mentioned above, this research study

focuses on design and study a new kind of hierarchically buckled porous microstructured textiles (HBPMTs) by rational surface design and engineering of stretchable textile substrates (such as elastic fibers and fabrics) with hierarchically buckled and porous microarchitectures using desired brick materials (such as frequently-used polymers and functional nanomaterials). The strategies being adopted in this research are listed below:

1.3.1 HBPMTs Design

Elastic 1D materials (such as rubber and polyurethane fibers) and fabric materials (such as rubber or polyurethane fibers-blended knitted fabrics) will be used as textile substrates. The thermoplastic elastomers such as PS-block-polybutadiene-block-PS (SBS) will be used as polymeric bricks to be dissolved in their good solvents with low boiling points such as chloroform ($CHCl_3$) and tetrahydrofuran (THF) for the preparation of polymer solutions. The textile substrate will be stretched and held at a certain level of tensile strain. The stretched textile substrate will then be immersed in the solution for swelling. And the swelling degree can be controlled by adjusting the soaking time. Through using solvent to open the cross-linked polymer network by swelling, some linear polymeric bricks are expected to penetrate the surface layer of textile substrate. Then stretched textile substrate coated with polymer solution will be quickly transferred to a high-humidity environment (RH >90%) for the BF process at

room temperature.

The BF technique[19] is the unique bottom-up strategy of using nontoxic water droplets as soft templates for interfacial self-assembly of brick materials. Taking the elastic fiber as example, after soaking in a kind of functional solution (e.g. polymer solution such as SBS/$CHCl_3$, or its hybrid suspension containing both polymer solution and functional components such as metal nanomaterials, carbon nanotubes, graphene) with required time, it will be taken out and quickly transferred into a high-humidity environment with RH>90% for BF process. Owing to the low boiling point of solvent, it will evaporate quickly and introduce the nuclei and growth of water droplets as spherical shapes (owing to high surface energy) on the solution surface by evaporative cooling. And the formed water droplets will tend to form hexagonal arrays driven by coupled effects of thermocapillary and Marangoni convection. Meanwhile water will act as nonsolvent to induce the self-assembly of brick materials at the interfaces between the isolated spherical water droplets and solvent. This dynamic BF process is one-step and can be regarded as terminated when the phenomenon of gelation or solidification occurs. After removal of residual solvents and waters by simple air drying, only brick materials (such as SBS, or SBS with functional components) will be left on the fiber surface to form a kind of 3D conformal porous microstructured fibers. With a similar mechanism, a kind of 3D conformal porous microstructured fabric can also be

obtained when using elastic fabrics as substrates. The formation and removal of water droplets as well as self-assembly of brick materials are both spontaneous. This BF process usually lasts from dozens of seconds to several minutes. Therefore, besides the formation of porous microstructures by templating spherical water droplets, the penetration of linear chains of polymeric bricks into the surface layer of fibers during the swelling process is also expected to be fixed/mapped at the cross-linked network of fiber substrates owing to the quick removal of solvent. This will contribute to the enhancement of interfacial strength between functional layers of brick materials and elastic textile substrates. Combined with the choice of thermoplastic elastomer (SBS), therefore, the formed 3D conformal porous microstructural (3CPM) layer is expected to be still well-maintained by thermal annealing and controllable releasing for generation of buckling/wrinkles owing to the recovery of elastic substrates. The thermal annealing temperature will be controlled with the glass transition temperature (Tg) of polymeric bricks as reference to increase the elasticity of 3CPM layer and maintain its porous microstructures. The releasing rate will be carefully controlled by observing the surface rupturing phenomenon. This will lead to form a new kind of hierarchically buckled porous microstructured textiles (HBPMTs) or hybrid HBPMTs (i.e. with incorporation of functional components) with flexible, porous and stretchable characteristics by mimicking human skin.

1.3.2 Fundamental Studies of HBPMTs

1.3.2.1 Material Matrix and Fabrication Parameters

HBPMT is mainly composed of two components of textile and brick materials. The former acts as stretchable substrates. Textile substrates with good elasticity such as elastic fibers (e.g. rubber and polyurethane fibers) and elastic fabrics (e.g. rubber or polyurethane fibers-blended fabrics) will be used. And the latter, such as SBS, and metal nanomaterials (e.g. Ag NWs, Cu NWs), carbon nanotubes, graphene and TiO_2, will be used as brick polymers and functional components, respectively. Low boiling point solvents such as THF and $CHCl_3$ will be used to disperse desired brick materials with adjustable concentration for the BF process. The used solvent shall not dissolve and can swell the fiber materials of textile substrates. The influential factors that may affect the architectures, properties and performance of HBPMTs will also be studied. The pre-stretched ratio plays a key role on the final stretchable degree of HBPMTs. The soaking time is expected to control the swelling degree of textile substrates for the penetration of polymeric bricks to adjust the interfacial bonding strength. The BF conditions will be fixed at room temperature with the relative humidity >90%, because based on our experience, this will contribute to nucleation, growth and self-assemble of water droplets for templating self-assembly of brick materials to form porous microstructures. Thermal annealing temperature and releasing rate are also two keys to

form surface buckling of HBPMTs with no ruptures. The annealing temperature should be close to the Tg of used polymeric bricks, which can endow the polymeric layer with some crinkly mobility, but meanwhile maintain the porous microstructures of polymeric layer. And the releasing rate shall be matched with the mobility of polymeric layers, which shall not be too quick otherwise would result in the interfacial debonding or rupture phenomena.

1.3.2.2 Experimental Design and Optimization of HBPMTs

This proposed study covers the choice of textile substrate, polymer material, functional component, preparation of solution, and fabrication parameters design of HBPMTs. There are various factors that may influence the performance of HBPMTs, including materials (i.e. textile substrates, polymer and functional materials), pre-stretched parameters (i.e. stretched ratio and stretched direction), BF condition (i.e. solvent type, solution concentration and soaking time), and post-treatment condition (i.e. thermal annealing temperature and releasing rate). Their relationships with the properties of HBPMTs will be carefully and systematically studied and analyzed. Considering the complexity of study caused by many kinds of materials and influential factors, a experimental design will be proposed for a more feasible and effective investigation. It will first focus on the influence of materials on the porous microstructure formations of stretched 3D conformal porous microstructured textiles

(3CPMTs). Then, the influence of various processing parameters, including pre-stretched parameters, BF and post-treatment conditions, will be investigated on the formation and properties of HBPMTs. Porosity and buckling size are two important structural parameters of HBPMTs that will be carefully measured and characterized. Besides, physical and mechanical properties involving stretchability, air permeability, and interfacial boding strength will also be measured and evaluated, as they are important to the performance and properties of HBPMTs.

1.3.3 Application Studies

Owing to rational structural design with buckled porous microarchitectures, HBPMTs are expected to have greatly improved functional and structural performance with well-maintained stretchable and air-permeable performance of textile substrates. And their properties and functions can be adjusted using different polymeric and functional bricks for different target applications.

1.3.3.1 Photocatalysis and Environmental Applications

HBPMTs are developed into functional fibers loaded with TiO_2 nanoparticles, showcasing enhanced photocatalytic degradation of organic pollutants. The hierarchically buckled and porous structure provided an increased surface area and efficient light absorption, significantly improving the degradation of methylene blue (MB) and neutral red (NR). This application highlights the potential of HBPMTs in

environmental remediation technologies, particularly in textile-based photocatalytic systems.

1.3.3.2 Energy Harvesting and Self-Powered Sensing

HBPMFs are integrated into triboelectric nanogenerators (TENGs) for wearable energy harvesting. Incorporating nanoparticles such as TiO_2, $BaTiO_3$, and Ag into the HBPMFs further enhanced their triboelectric performance. Demonstrative applications included wearable sensors for detecting human motions such as breathing, joint movements, and walking modes. These results underline the potential of HBPMFs in self-powered healthcare monitoring and wearable electronics.

1.3.3.3 Advanced Composite Supercapacitors

By combining hierarchically buckled porous structures with advanced nanomaterials like NiCo-LDH and CNT composites, HBPMTs will achieve both superior electrochemical performance and mechanical flexibility. These materials will be designed to maintain stability and functionality under dynamic mechanical deformation, paving the way for their integration into next-generation smart textiles and adaptive energy storage devices.

These studies will establish HBPMTs as versatile and transformative materials, addressing critical challenges in environmental sustainability, wearable technologies, and flexible energy systems, thus contributing to a more sustainable and connected

future.

1.3.4 Testing, Evaluation and Characterization of HBPMTs

The physicochemical properties of brick materials, chemicals and textile substrates, suchmechanical properties of substrates, will be determined (or tested). And the experimental conditions involving humidity and temperature for BF process will be measured and monitored by the hygrometer and thermometer, respectively. Structural characterization of textile substrates, 3CPMTs and HBPMTs such as pore size, pore regularity, and functional component distributions, porosity, buckling size and cross-section will be systematically conducted by the combination of optical microscopy and scanning electron microscope (SEM). Their mechanical properties like stretchability and elastic modulus will be tested by tensile testers. Their interfacial bonding strength will be evaluated, while their air permeabilities under different stretching states will be also measured by air-permeability tester. The component analysis for polymers, functional components and their 3CPMTs and HBPMTs will be based on the combined use of Fourier Transform Infrared Spectroscopy (FTIR), Energy-dispersive X-ray spectroscopy (EDX) and/or X-ray photoelectron spectroscopy. Moreover, the electrical performances of TENG under different applied forces, frequencies and different sample tensile ratios were evaluated by a button/key durability life test machineequipped with a high-speed self-configuring digital indicator. The open-circuit voltage, short-circuit

current, and short-circuit charge transfer were recorded by an electrometer. The electrochemical properties of HBPMTs with energy storage functions will be measured by using cyclic voltammetry, galvanostatic charge/discharge, and AC electric impedance techniques with an electrochemical workstation. These structural and functional performance of HBPMTs energy storage devices will also be analysed and evaluated comprehensively by comparing to those of control composite samples without buckled porous microarchitectures.

1.4 Research Significance and Values

The preparation of highly ordered pores using the BF method is an example of humans devising a technique inspired by nature. The seemingly simple process endows the resultant substrate with both an ordered surface structure and patterned distributions of functional groups on the surface, which provides more opportunities to further modify and functionalize the substrate, thus broadening their applications. This technique has now made a large impact in the area of materials and has created a general interest that has extended to a large scientific community at the frontiers of chemistry, physics, biology, and medicine.

Therefore, developing new manipulation methods is essential in future research. Inspired by human skin that is multifunctional, soft, breathable and highly stretchable via the generation of surface buckling, this project aims to design and study a new kind of hierarchically buckled porous microstructured textiles (HBPMTs) by rational surface design and engineering of stretchable textile substrates with hierarchically buckled and porous microarchitectures using common brick materials. In this research, we explored to fabricate novel fibers/textiles that maintain high interfacial activities of incorporated functional materials for a kind of stretchable smart wearables with high performance. The innovative methodologies and advanced designs outlined across these studies demonstrate significant improvements in mechanical resilience, energy harvesting, sensing, and energy storage capabilities. The findings provide promising pathways for the development of next-generation textile-based wearables, offering transformative potential for applications in healthcare, environmental monitoring, and smart electronic

systems.

1.5 Outline of the Report

1.5.1 Chapter 1: Introduction

This chapter introduces the background and significance of the research, which draws inspiration from the hierarchical buckling of human skin to design and develop innovative hierarchically buckled porous microstructured textiles (HBPMTs), outlining the objectives, methodology, and potential applications of the study in the context of wearable electronics and smart textiles.

1.5.2 Chapter 2: Literature Review

A comprehensive review of existing studies on surface engineering of textile substrates, hierarchically buckled structures, and porous microarchitectures is presented; the chapter emphasizes the advantages and limitations of current approaches, identifies critical research gaps, and establishes the rationale for the development of HBPMTs.

1.5.3 Chapter 3: Skin-inspired Hierarchically Buckled Fibers

This chapter describes the innovative design and fabrication methods for hierarchically buckled porous microstructured fibers (HBPMFs), focusing on the influence of material systems, pre-stretching conditions, and solution concentrations on structural and functional performance, with a particular emphasis on photocatalytic applications.

1.5.4 Chapter 4: HBPMFs in Energy Harvesting and Sensing

The design and development of HBPMFs integrated with functional nanoparticles for energy harvesting and self-powered sensing applications are discussed, highlighting their enhanced triboelectric performance and versatility in powering wearable devices and monitoring fine motions like breathing.

1.5.5 Chapter 5: HBPFSs for Supercapacitors

This chapter focuses on the development of hierarchically buckled porous structure fabrics (HBPFSs) with incorporation of NiCo-LDH nanostructures through hydrothermal treatment. These materials exhibit excellent stretchability, mechanical resilience, and energy storage performance, demonstrating their suitability for flexible and wearable supercapacitors.

1.5.6 Chapter 6: NiCo-LDH@CNTaSBSb@F for Supercapacitors

This chapter investigates the development of NiCo-LDH@CNTaSBSb@F composites, where hierarchically porous structures are achieved by combining carbon nanotubes (CNTs), styrene-butadiene-styrene (SBS), and nickel-cobalt layered double hydroxides (NiCo-LDH). The integration of NiCo-LDH nanostructures enhances the electrochemical performance, achieving high specific capacitance, excellent energy density, and remarkable durability. These composites exhibit exceptional mechanical flexibility and stability under tensile strain, making them highly suitable for wearable and adaptive energy storage devices in next-generation smart textiles.

1.5.7 Chapter 7: Conclusions and Recommendations

This final chapter summarizes the key findings of the research, emphasizing the transformative potential of HBPMTs in wearable and environmental applications, while recommending future work on scalability, multifunctionality, and sustainable manufacturing, alongside the use of AI for material design and optimization.

Chapter 2 Literature Review

2.1 Surface Engineering of Textile Substrates

Surface engineering of textile substrates is critical for enhancing their functionality, enabling their use in diverse applications such as wearable electronics, energy harvesting, and healthcare. Native textiles, while offering flexibility, breathability, and lightweight properties, often lack advanced functionalities such as conductivity, stretchability, or dynamic responsiveness. This gap is addressed through surface engineering, which tailors the material's surface properties without compromising its inherent mechanical and structural features.

2.1.1 Conventional Surface Engineering Approaches

Conventional surface engineering approaches have played a foundational role in enhancing material properties, enabling applications across various industries such as aerospace, healthcare, and flexible electronics. These methods, including coating, plasma treatment, and chemical functionalization, have been widely used, remain widely used due to their adaptability and proven effectiveness in specific contexts. This section explores these established techniques, highlighting their strengths, limitations, and relevance to modern material applications.

Surface coating technology

Surface coating technology plays a pivotal role in enhancing material performance and broadening its application scope. By introducing modified coatings, it improves material durability, functionality, and adaptability. Despite significant advancements,

this field still faces persistent challenges and debates. Chemical vapor deposition (CVD), recognized for its superior high-temperature and oxidation resistance, is often regarded as the preferred method for high-performance coatings. However, its industrial adoption is hindered by high equipment costs, complex processes, and significant energy consumption. Traditional methods, such as spraying and dip coating, are lauded for their simplicity and low cost but often suffer from issues of insufficient coating uniformity and adhesion, particularly in demanding applications. Meanwhile, high-precision techniques like thin film deposition and layer-by-layer (LbL) coatings demonstrate remarkable potential in flexible electronics and medical devices due to their versatility and precise control. However, these methods face challenges such as intricate workflows and environmental sensitivity. Furthermore, thermal expansion mismatches between different coating materials can lead to cracks and interface failures, while solvent-based traditional coatings pose environmental concerns. Addressing these issues is critical for furthering the adoption and impact of coating technologies.

A comparison of studies reveals significant variations in coating technologies regarding performance optimization and application domains. Nicholls et al.[20] highlighted the application of CVD in gas turbine coatings, demonstrating its exceptional high-temperature and oxidation resistance. However, they noted its limitations in terms of high costs and process complexity. Baruwa et al.[21] explored spraying and dip coating technologies, identifying their suitability for large-scale industrial applications while emphasizing the need for improved coating adhesion and uniformity. Voyer and Boulos et al. [22] emphasized the advantages of thermal spray

technology, particularly its high adhesion and wear resistance, though they acknowledged its limited scope of application. Butt et al. [23]and Rasool et al. [24] focused on thin film deposition and nanocoatings, respectively. Thin film deposition was praised for its multifunctionality in flexible electronics and medical applications, while nanocoatings demonstrated exceptional surface area and unique functionalities, showing promise in nanotechnology and electronic devices. Nevertheless, both techniques face challenges related to process complexity and thermal mismatch.

Collectively, these studies provide a solid theoretical and practical foundation for advancing coating technologies. However, significant breakthroughs are required in simplifying processes, reducing costs, and enhancing environmental sustainability. Future research should prioritize the development of coating methods that balance high performance with ecological considerations, addressing challenges such as versatility, adhesion, and thermal mismatch. These advancements will be crucial for expanding the adoption of coating technologies across industries, energy systems, and healthcare applications.

Plasma Treatments

Alters surface energy to enhance adhesion or introduce functional groups. While effective, it struggles with uniform treatment across complex textile geometries. Plasma is referred to as the fourth state of matter, primarily composed of a collection of atoms, molecules, electrons, free radicals, and various active groups. Plasma surface modification technology, also known as ion bombardment diffusion modification technology or impact diffusion modification technology, generally refers to the process

of obtaining plasma through glow discharge in a specific atmosphere below 0.1 MPa, and using the plasma to bombard and treat the surface of materials to achieve surface modification. Based on the particle temperature of the plasma, plasma modification technology is generally divided into high-temperature plasma modification technology and low-temperature plasma modification technology, with the latter commonly used for surface modification of materials. Low-temperature plasma can be generated at atmospheric or low pressure, with relatively low energy, only a few tens of electron volts. In contrast, the bond energy of the surface molecules of the polymer material to be modified is only a few to several tens of electron volts. Using isothermal plasma treatment can completely break the organic macromolecular chains on the surface of the polymer material (usually a few to several tens of nanometers) without affecting the performance of the material's matrix. Using isothermal plasma treatment, the surface of the modified material will undergo multiple chemical and physical changes, such as forming a dense cross-linked layer, becoming roughened due to etching, or introducing oxygen-containing polar groups, thereby improving adhesion, hydrophilicity, biocompatibility, dyeability, and optoelectronic properties. Moreover, the plasma treatment technology, with its advantages of simple operation, environmental friendliness, energy efficiency, and high efficiency, has been widely used in the field of material surface treatment.

As early as 1989 [25], continuous treatment with cold plasma significantly improved the interfacial shear strength of carbon fiber reinforced epoxy composites (from about 60 MPa to 100 MPa) by introducing functional groups such as hydroxyl groups,

increasing surface roughness and wettability, while maintaining the carbon fiber strength essentially unchanged, demonstrating advantages of simplicity, environmental friendliness, and potential for engineering applications. Cho et al. [26] explores the impact of plasma surface treatment on the mechanical properties of multi-scale hybrid composites (polycarbonate/carbon nanotubes/carbon fibers, PC/CNT/CF).The study shows that plasma treatment significantly improves the interfacial bonding performance between fibers and matrix by increasing the surface roughness of carbon fibers and introducing functional groups. After optimization, the storage modulus of the composite material increased to 39 GPa (a growth of 387%), and the energy absorption capacity reached 5.3 J (a growth of 194%). This indicates that the combination of plasma treatment and carbon nanotube hybrid reinforcement has a significant synergistic effect. Moreover, Lee et al. [27] studied the enhancement of interfacial affinity and mechanical properties of carbon fiber reinforced polymer composites (CFRP) through oxygen and nitrogen plasma-assisted mechanochemistry (PMC) treatment. By introducing functional groups (such as hydroxyl and amino groups) on the surface of carbon fibers and carbon nanotubes, the interfacial bonding was significantly enhanced, resulting in an increase in tensile strength (20%) and Young's modulus (31%). PMC technology is environmentally friendly and efficient, suitable for industrial-scale production of high-performance composite materials.

Chemical Functionalization

Surface modification of textile fibers plays a crucial role in advancing materials science and engineering, particularly in improving the physical, chemical, and

functional properties of fibers. Graft modification technology, which introduces specific functional groups onto fiber surfaces, has become a widely adopted method due to its versatility and efficiency. Functional groups such as carboxyl and amino groups can enhance hydrophilicity and adhesion, respectively, while acrylamide promotes surface reactivity. Despite its potential, graft modification technology still faces critical challenges in industrial application, including technical complexity, environmental sustainability, and achieving multifunctional optimization.

Graft modification introduces functional groups onto fiber surfaces through chemical or physical methods, altering their surface properties to meet specific performance requirements. Techniques such as free radical polymerization, ultraviolet irradiation, and plasma treatment are commonly employed to generate active sites for functional molecule attachment. Recent advancements in nanotechnology have further improved the accuracy and efficiency of grafting processes, paving the way for applications in smart textiles, medical materials, and high-performance composites.

Existing research demonstrates the diverse applications of graft modification technology. Chen et al. [28] developed graft copolymerized cotton fabrics with improved antibacterial properties, addressing hygiene and medical applications. Amin et al. [29] demonstrated the successful grafting of chitosan onto wool fibers, significantly enhancing flame retardancy, making it suitable for high-security textiles. He et al. [30] improved the hydrophilicity of polyester fibers through grafting, catering to the demands of functional textiles. Tian et al. [31] explored chemical grafting to improve the adhesion of polypropylene fibers to maleic anhydride, showing promising results for

composite materials. Nayak et al. [32] highlighted the importance of green chemistry in graft modification of flax fibers, emphasizing sustainability. Collectively, these studies underscore the versatility of graft modification across different fibers and application areas, showcasing its broad potential. However, significant challenges and controversies remain. First, the technical complexity of many grafting methods, requiring complex reaction conditions and expensive equipment, limits scalability. Second, the environmental impact of some grafting processes, particularly those involving solvents or toxic reagents, raises sustainability concerns, necessitating the development of greener alternatives. Third, optimizing multiple properties simultaneously remains difficult; for instance, enhancing hydrophilicity might compromise mechanical strength. Lastly, achieving material compatibility in composite applications is still a technical bottleneck, as the interfacial stability and durability of grafted fibers require further improvement.

Graft modification technology offers vast potential for enhancing textile fiber properties and broadening their applications. However, its industrial adoption requires overcoming challenges related to process complexity, environmental impact, and multifunctional balance. Future research should focus on simplifying and greening grafting processes, developing solvent-free methods, and leveraging artificial intelligence for material design. Such advancements will enable the broader application of graft modification technology in smart textiles, high-performance composites, and biomedicine, while also promoting sustainable development in textile materials.

While conventional surface engineering approaches have proven their value in

advancing material technologies, their limitations, such as high costs, environmental concerns, and process complexity, underscore the need for continuous innovation. Future developments should focus on improving the scalability, efficiency, and sustainability of these methods, ensuring their compatibility with emerging applications in smart textiles, high-performance composites, and beyond.

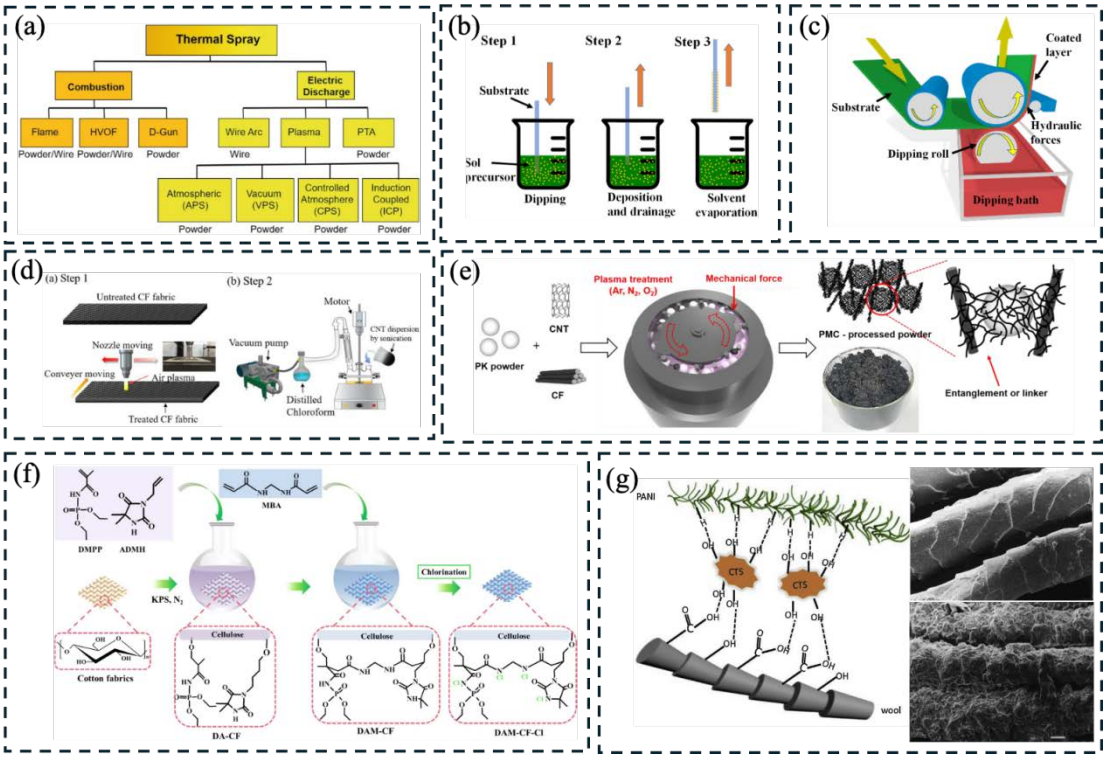

Figure 2.1 Conventional surface engineering approaches (a) Overview of thermal spray Technologies[21]. (b) Sequential stages of the sol–gel dip-coating method for thin film deposition (c) Roll-coating [23] (d) plasma treatment apparatus for CF surface treatment, and vacuum-assisted distillation set-up for CNT/PC/chloroform solution[26],(e) Schematic illustration of plasma-assisted mechanochemistry processing[27], (f) graft modification technology[28], (g) Schematic of wool fabric co-doped with polyaniline (PANI) and chitosan (CTS) through a one step in situ polymerization method using carboxylic and hydrochloric acid as the doping acids[29].

2.1.2. Emerging Strategies in Surface Engineering

Hierarchical Surface Engineering

Hierarchical surface engineering has emerged as a research hotspot in materials

science due to its ability to significantly enhance material performance and diversify functionalities. By integrating micro and nanoscale textures, this technology improves surface mechanical adaptability, roughness, and adhesion, finding applications in high-performance coatings, bionic designs, and thermal management systems. Despite notable progress, the industrial adoption of hierarchical surface engineering faces critical challenges, including preparation complexity, environmental sustainability, and achieving multifunctional optimization.

Hierarchical surface engineering achieves precise control over surface properties by combining multi-scale textures, such as micropillars and dome arrays with nanopores and nanowires. This integration improves surface area-to-volume ratios and interfacial properties, enhancing functionalities such as wettability, adhesion, and optical performance. For example, solvent-assisted laser technology was employed to construct self-similar micro-nano textures on silicon surfaces, significantly enhancing superhydrophilicity and light absorption[33]. Furthermore, bioinspired designs, mimicking natural structures, have expanded applications by enabling properties such as superhydrophobicity and efficient heat transfer[34]. In terms of preparation technology, He al et. proposed an efficient and versatile preparation method to achieve superhydrophobic properties on a variety of substrates by building hierarchical textures[35]. Stratakis al et. summarized the key role of laser technology in regulating wettability and optical properties[34]. Furthermore, in the field of functionalized applications, Zhang al et. demonstrated the possibility of constructing micro-nano textures on the aluminum surface to significantly improve heat transfer efficiency, while

Chung al et. achieved a higher surface through the combination of micro-domes and nanopores hydrophobicity [36,37].

Despite its potential, hierarchical surface engineering still faces significant hurdles. Preparation complexity remains a critical bottleneck, as advanced methods like two-photon polymerization and laser etching require sophisticated equipment and costly processes, limiting scalability. Multifunctional optimization presents another challenge; for example, achieving high hydrophobicity or light absorption often compromises mechanical strength or durability [38]. Additionally, environmental concerns arise from certain processes involving high energy consumption or toxic reagents, necessitating the development of greener and more sustainable manufacturing solutions [39]. Addressing these challenges is vital for the broader adoption of this technology.

Hierarchical surface engineering has demonstrated significant potential in optimizing material properties and diversifying functionalities through the integration of micron- and nanoscale structures. From efficient preparation methods to bioinspired designs and advanced functional applications, recent studies have provided strong theoretical and practical support for this field. However, future research should prioritize the greening and scalability of these technologies by developing eco-friendly and cost-effective preparation methods. Incorporating artificial intelligence for optimized design and leveraging emerging green technologies could further drive the industrialization of hierarchical surface engineering, enabling breakthroughs in smart materials, thermal management systems, and high-performance composites.

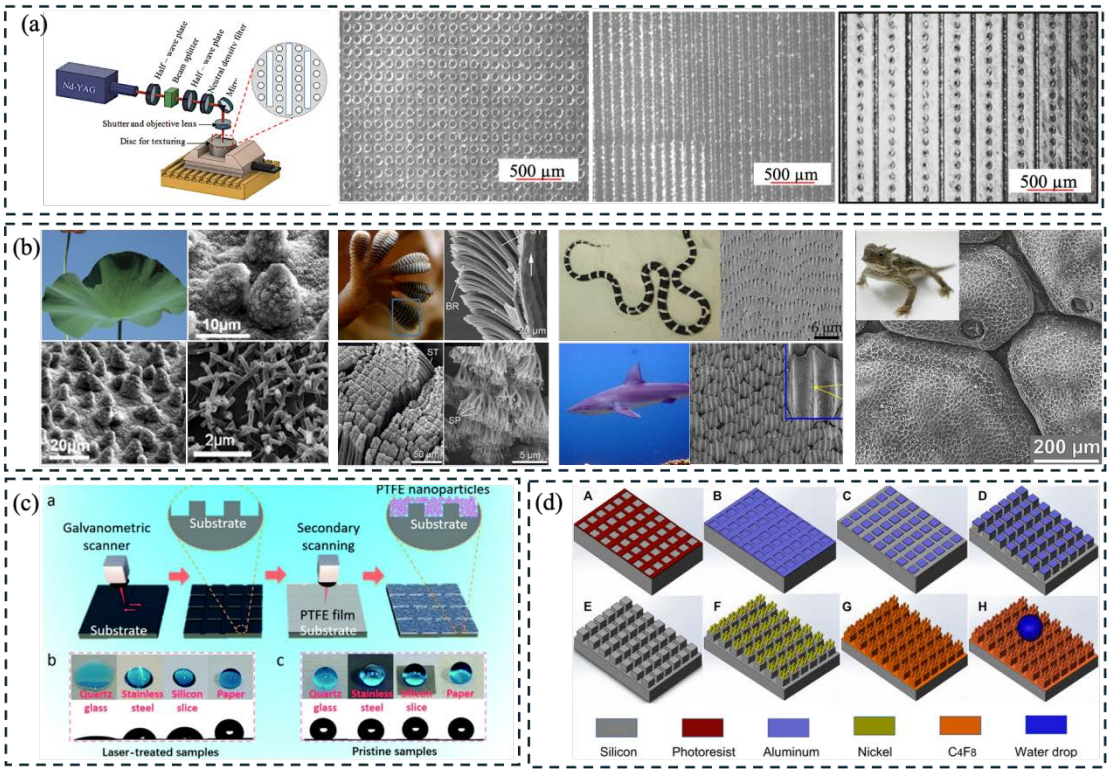

Figure 2.2 Hierarchical Surface Engineering. (a) Schematic sketch of laser micro texturing Micro dimple surface , Micro grooved surfaceHybrid surface[33], (b) Lotus surface and its surface in different magnifications. close-up photograph of the underside of a gecko‘s (Gecko gecko) foot as it walks on vertical glass, SEM micrographs of the hierarchical structures on the foot of the gecko. Picture of California King Snake and SEM-image of the ventral scales of its skin. Picture of Galapagos shark and scale patterns on various fast-swimming shark. lizard and its SEM image of dorsal scales[34]. (c) Schematic illustration of the fabrication procedure of the robust superhydrophobic surface; (b and c) water droplets are placed on the pristine and laser-treated samples of four substrates (quartz glass, stainless steel, silicon slice, and paper)[35], (d) Schematic illustration of the major fabrication processes of micro/nano hierarchical structure[38].

Dynamic and Stimuli-Responsive Modifications

Self-healing and stimulus-responsive surfaces have become important technological innovations in the field of smart textiles, enabling materials to dynamically adapt to changing mechanical and environmental conditions. These surfaces are capable of repairing damage or changing properties in response to external stimuli such as temperature, pH or mechanical stress, expanding the range of textile applications in wearable technology, medical fabrics and adaptive clothing. In recent

years, research into stimuli-responsive polymers, hydrogels, and nanostructured coatings has made significant progress, significantly enhancing the durability and versatility of materials. However, this area still faces key challenges such as large-scale production, environmental sustainability and long-term durability, and more in-depth research and technological innovation are urgently needed to realize its full potential.

These strategies represent a shift towards multifunctional and adaptive textile surfaces. However, integrating hierarchical and porous structures into textiles remains a significant opportunity for innovation[40,41].

The functionality of self-healing and stimuli-responsive surfaces relies on advanced materials, such as functional polymers, hydrogels, and nanocomposites, which are able to physically or chemically respond to external stimuli. For example, shape memory polymers and hydrogels can repair physical damage or adjust their structure to adapt to environmental changes. Shape memory polymer fibers have been used in biomedical scaffolds and sensors to enhance the adaptability of smart textiles[42]. Chen al et. have shown that solvent-assisted hydrogels have been integrated into textiles to create adaptive surfaces that can self-heal and enhance adhesion properties, especially under complex mechanical conditions. Hydrogels with antifreeze, self-healing and underwater adhesion capabilities have become an important component of wearable electronic devices, showing enhanced durability under extreme environmental conditions[43]. In addition, The integration of conductive polymers such as PEDOT:PSS has also made stretchable, flexible and self-healing materials possible in advanced applications such as electronic skin and adaptive clothing. Technological advances such

as luminescent coatings and ion-conducting organic hydrogels have further expanded the application of these materials in wearable electronic devices and adaptive clothing, providing robust solutions for durability and flexibility[44,45].

Despite these encouraging developments, the field of self-healing and stimulus-responsive textiles still faces significant challenges. First, large-scale production of these materials faces difficulties because many involve complex and expensive synthesis processes, limiting industrial applications[42]. In addition, there are still uncertainties about the long-term durability of these materials under real mechanical and environmental stresses, and many systems can only perform well under controlled conditions[43]. Environmental sustainability is also a pressing issue, as some self-healing materials involve non-degradable components or energy-intensive production methods, which requires the development of greener and more cost-effective alternatives[44].

Taken together, self-healing and stimulus-responsive surfaces offer great potential for the transformation of smart textiles, which can provide adaptable, durable and versatile solutions for wearable technology, medical fabrics and other fields. While recent research has provided the field with a solid theoretical and practical foundation, challenges related to scaled production, durability, and sustainability must be addressed to unlock its full industrial potential. Future research should focus on developing environmentally friendly, highly durable self-healing materials while incorporating AI-assisted material design and nanotechnology to further enhance the adaptability and performance of smart textiles.

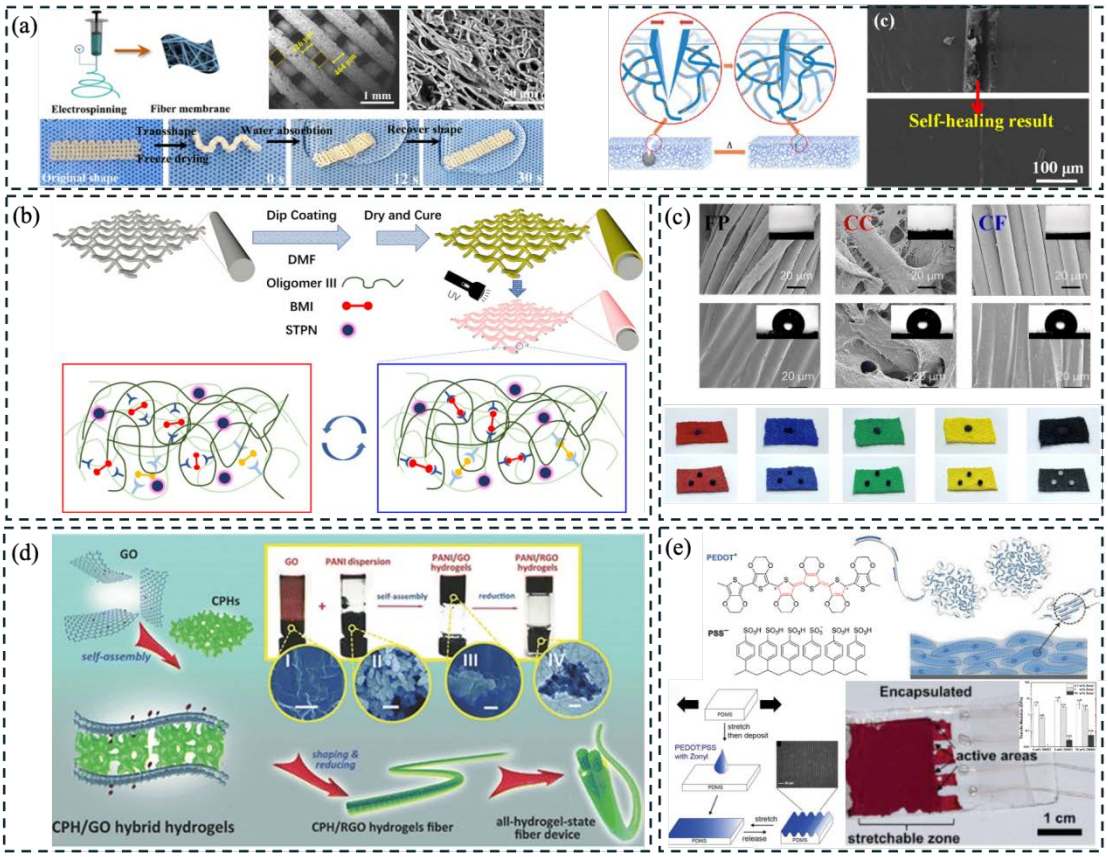

Figure 2.3 （a）Shape recovery process of shape memory polymer fibers exposed upon water stimuli conditions. schematic illustration of the coating morphology and the shape memory assisted self-healing concept[40].(b) preparation process of luminescent and hydrophobic textile coatings with reversible networks comprising of Diels-Alder reactions. (c) SEM images of cotton cloth (CC), filter paper (FP), and chemical fabric (CF) before and after coating. Photos of droplets of distilled water on pieces of colored CFs before and after coating[41]. (d) Schematic for the formation of PANI/GO hybrid hydrogels[42]. (e) Physical approaches toward stretchable PEDOT. Fabrication scheme for stretchable PEDOT:PSS on PDMS by buckling and optical microscopy image of buckled PEDOT:PSS on PDMS, and PUR-encapsulated solar cell with PEDOT:PSS electrodes[45].

2.2 Hierarchically Buckled Structures

2.2.1. Definition and Formation Mechanisms

Hierarchically buckled structures (HBS) have become a research hotspot in the field of materials science in recent years due to their important role in multifunctional surface design, flexible electronic devices and adaptive systems. Such structures exhibit dynamic mechanical properties such as reversible deformation and high ductility by

forming multiscale patterns through mechanical instabilities such as prestraining, compression, or interlayer modulus mismatch. These properties make it have important application potential in smart materials, soft robotics and bionics. However, although the research on HBS has made significant progress, its formation mechanism and industrial application still face many challenges, including complex preparation processes and difficulties in functional optimization.

The formation of HBS relies on mechanical instability, and common mechanisms include pre-strain method and modulus mismatch system. In the pre-strain method, a controllable wrinkle pattern is formed by applying tensile or compressive stress on the substrate and releasing it[46,47]. The modulus mismatch system naturally produces hierarchical wrinkles by introducing differences in mechanical properties in the layered material[48]. These mechanisms can achieve the adjustability of the pattern at the micron to nanometer scale, and synergize with external stimuli (such as heat or mechanical force) to further enhance its dynamic response performance[49,50]. At the same time, the bionic design method introduces the hierarchical structure in nature into the material system, providing new ideas for the design of adjustable adhesion, flexible electronics and smart coatings[51].

In recent years, research on HBS has made significant progress in terms of formation mechanisms, design methods, and functional applications. Regarding the formation mechanism, researchers have analyzed the mechanical basis of material hierarchical shrinkage behavior through multi-scale modeling, providing theoretical support for the design of high-performance composite materials[51,52]. For example, a

study shown a method to achieve complex wrinkle patterns in films with gradient mechanical properties. By controlling the gradient distribution, efficient performance optimization of flexible electronic devices was achieved[53]. In terms of design methods, the combination of Kirigami technology and pre-strained planar preparation methods makes programmable hierarchical shrinkage structures possible, laying the foundation for the development of soft robots and wearable devices[46,47]. In terms of functional applications, research has demonstrated the potential of HBS in flexible electronics[54], thermally responsive polymer films[49] and surface adhesion regulation[46], providing diversified solutions for the design of smart material systems.

Despite the significant advantages of HBS, several challenges and controversies remain in its preparation and application. The first is the complexity of preparation. Many methods rely on precision equipment and complex processes, which restricts the feasibility of industrial application. Secondly, function optimization is still a technical bottleneck. For example, achieving high ductility may result in the loss of adhesion properties, and the realization of multifunctional balance needs further exploration. In addition, the formation of some HBS relies on irreversible chemical or mechanical processing, making it difficult to adapt to multiple uses in dynamic environments. Future research needs to focus on how to improve the environmental adaptability and recyclability of materials while simplifying the preparation process.

The potential of hierarchical buckled structures in smart material systems has been widely studied and verified. From the formation mechanism to practical applications, various studies have provided theoretical and technical support for high-performance

flexible electronic devices, adaptive coatings and soft robots. However, future research needs to solve the problem of simplifying complex processes in the industrialization process, while exploring the path to achieve green manufacturing and multifunctional performance balance. By combining nanotechnology, bionic design and artificial intelligence-assisted material design, hierarchical shrinkage structures are expected to achieve greater breakthroughs in the fields of smart materials and advanced manufacturing.

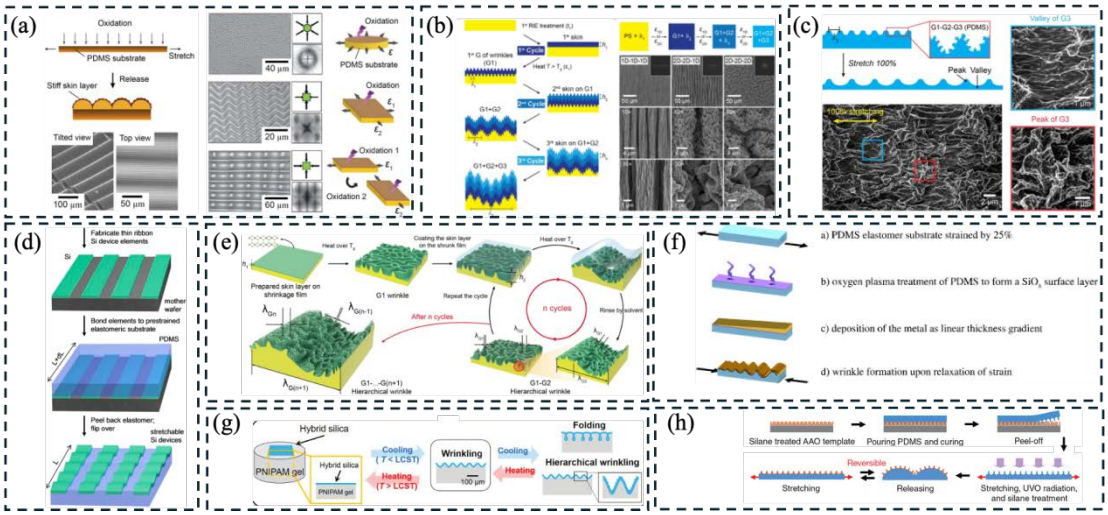

Figure 2.4 (a)Hierarchical micro- and nanostructures by self-similar wrinkling at high strain regimes, sequential strain relief. And sequential nanowrinkling to form out-of-plane hierarchical structures. (b) Scheme for fabrication processes and resulting structural hierarchies with controlled wrinkle orientations. (c) Dynamically stable, superhydrophobic substrates after mechanical deformation, partial preservation of structural hierarchy after 100% stretching G1–G2–G3 PDMS wrinkles[46]. (d) Schematic illustration of the process for fabricating stretchable single-crystal Si devices on elastomeric substrates[54]. (e)Sequential nanowrinkling of low-dimensional nanomaterials, with MoS2 6as a representative example of using sequential wrinkling with sacrificial skin layers[46]. (f) Preparation scheme for gradient wrinkle patterns based on wrinkled gradient metal films[48]. （g）Strategy for thermoresponsive wrinkles and soft linear actuators[49]. (h) Scheme of the fabricating hierarchical surface structure from various pre-patterned PDMS films[53].

2.2.2 Functional Advantages of HBS

HBS is a multi-scale pattern formed by mechanical instability and has attracted

extensive attention in the field of materials science and engineering in recent years. HBS exhibits unique mechanical adaptability, dynamic responsiveness and enhanced surface area performance, making it of great application value in flexible electronic devices, wearable technologies and energy conversion systems. These structures are formed through mechanisms such as pre-strain, modulus mismatch and shell shrinkage. Their controllability and multifunctionality provide new possibilities for the development of smart materials and advanced manufacturing. However, the practical application of HBS still faces challenges such as preparation complexity, multifunctional optimization and environmental stability. Therefore, it is of great significance to sort out the current research progress and the technical bottlenecks it faces to promote the further development of HBS.

HBS research has made significant progress in functional realization, material design and practical applications. In terms of mechanical adaptability, research shows that HBS can maintain functional integrity under high strain conditions, which is crucial for the development of flexible electronic devices[55]. Dynamic responsiveness is another major feature of HBS. Through precise design, HBS can quickly respond and recover under the action of external forces, providing new technical support for flexible sensors and adaptive systems[54]. In addition, the enhanced surface area characteristics of HBS have brought new breakthroughs to energy conversion systems. For example, by optimizing surface roughness design, the output efficiency of triboelectric nanogenerators (TENG) has been significantly improved[56]. These studies indicate that the multifunctional properties of HBS have broad application prospects in the field of

smart materials.

Hierarchical shrinkage structures have shown great potential in flexible electronics, smart sensors, and energy conversion systems through their excellent mechanical adaptability, dynamic responsiveness, and enhanced surface area characteristics. From pre-strain design to shell shrinkage mechanism, the formation theory and functional optimization research of HBS lays the foundation for the future development of high-performance materials. However, in order to achieve its wide industrial application, future research needs to make more efforts in simplifying the preparation process, balancing functional performance, and improving environmental stability. In addition, combined with bionic design, artificial intelligence-assisted material design, and green manufacturing technology, HBS is expected to play a greater role in the fields of smart materials and advanced manufacturing.

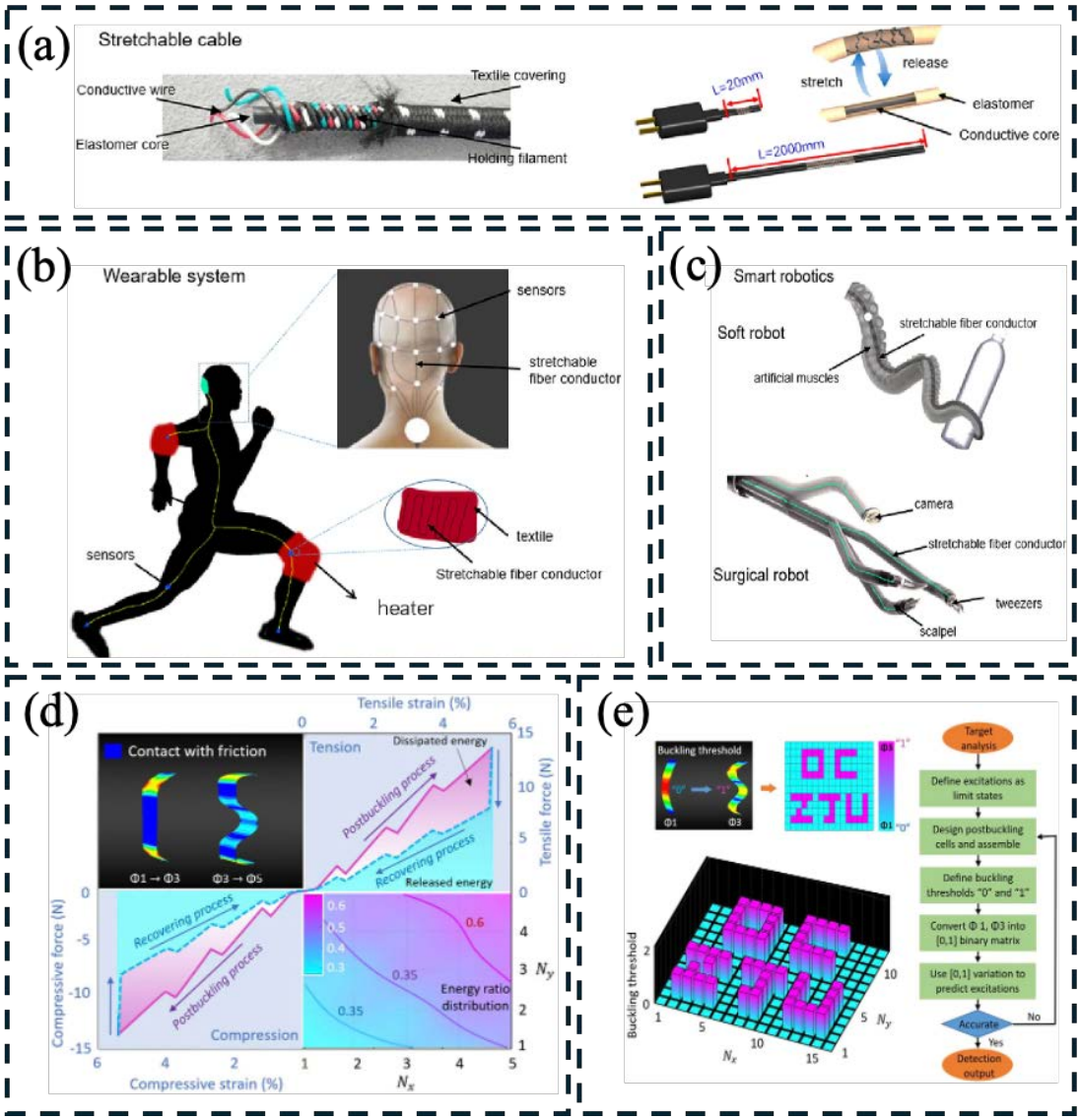

Figure 2.5 (a) Applications of stretchable fiber conductors. Stretchable cables for mobile devices (charging cables, earphone cables). (b) application of stretchable fiber as a communication cable and heating component in wearable systems. (c) Application of stretchable fiber as a communication cable in the smart robots[55]. (d) Vision for the potential applications of the hierarchical metastructures. Energy dissipation through the postbuckling and recovering processes due to the friction between the contacted elasticas and constraints, and the numerically obtained distribution of the energy dissipation ratio between the dissipated and released energies. (e) Illustration of the application of the metastructures in damage detection as mechanical sensors that use postbuckling response as a buckling threshold[56].

2.2.3 Applications of HBS in Textiles

The application of HBS in textile materials has become a hot research topic in recent years. Its unique strain adaptability, multifunctionality and bionic properties provide

new designs for flexible electronic devices, smart textiles and energy harvesting systems. plan. HBS's design inspiration comes mainly from nature, such as the wrinkled structure of knuckle skin and the high strength and flexibility of spider silk[57,58]. Through the design of hierarchical microstructure, HBS can maintain the stability of mechanical properties under stress environments while significantly improving the functional efficiency of electronic and mechanical devices[55,59].

The research and application of HBS in the textile field mainly focuses on the following three aspects. First, wearable devices require materials with high flexibility, strain adaptability, and long-term durability. Meng[55] et al. significantly improved the resistance stability of the conductor under extreme strain conditions by optimizing the design of HBS. This research not only expands the application scenarios of HBS in wearable sensors, but also provides technical support for the development of smart medical devices. Li[57] et al. developed highly flexible fibers through bionic design and successfully achieved a combination of mechanical adaptability and high-performance sensing capabilities. The second is the research on smart textiles and multifunctional soft robots, which benefit from the versatility of HBS. Hu[60] et al. used thermodynamic coupling to achieve the morphological regulation of HBS in flexible materials, thus providing a theoretical basis for the performance optimization of smart textiles. At the same time, Li[61] et al. developed a hydrogel-based humidity-driven actuator, which not only has excellent flexibility, but also can adapt to complex usage scenarios, providing an important reference for the field of smart actuators and bionic soft robots. The third is in the field of energy harvesting. The introduction of HBS significantly optimizes the

charge transfer efficiency. Wang[59] et al. developed a strain sensor based on MXene/carbon nanotubes, whose hierarchical structure effectively improves the sensitivity and durability of the device. In addition, in subsequent research, the team used dynamic chemical bonding and liquid metal technology to further improve the self-healing ability of the sensor and expand its application scope in complex environments[62]. The application of HBS in smart actuators has also made important progress. Leng[63]et al. explored twisted fiber artificial muscles based on HBS, which provides new ideas for the development of energy conversion and flexible actuators.

Although the research on HBS has made significant progress, its practical application still faces many challenges. First, the structural stability of HBS in long-term complex environments needs to be further optimized, especially in textile usage scenarios, where the fatigue resistance and durability of the material are the keys to restricting its application. Secondly, the preparation process of HBS is complex and costly, which limits its large-scale production and commercial application. In addition, how to realize the functional integration of HBS without sacrificing the softness and durability of traditional textile substrates is also an urgent problem to be solved.

In summary, HBS provides an important opportunity for the intelligentization and functionalization of textile materials due to its excellent mechanical flexibility and functional diversity. Future research needs to focus on the optimization of the preparation process to achieve low-cost, large-scale production. In addition, the exploration of HBS in multifunctional integration should be strengthened, combining dynamic chemical bonds with nanocomposite technology to improve its performance

stability and adaptability in complex environments. Through interdisciplinary collaboration, HBS is expected to be widely used in wearable devices, energy harvesting systems and smart textiles, and become the core technology of the next generation of smart materials.

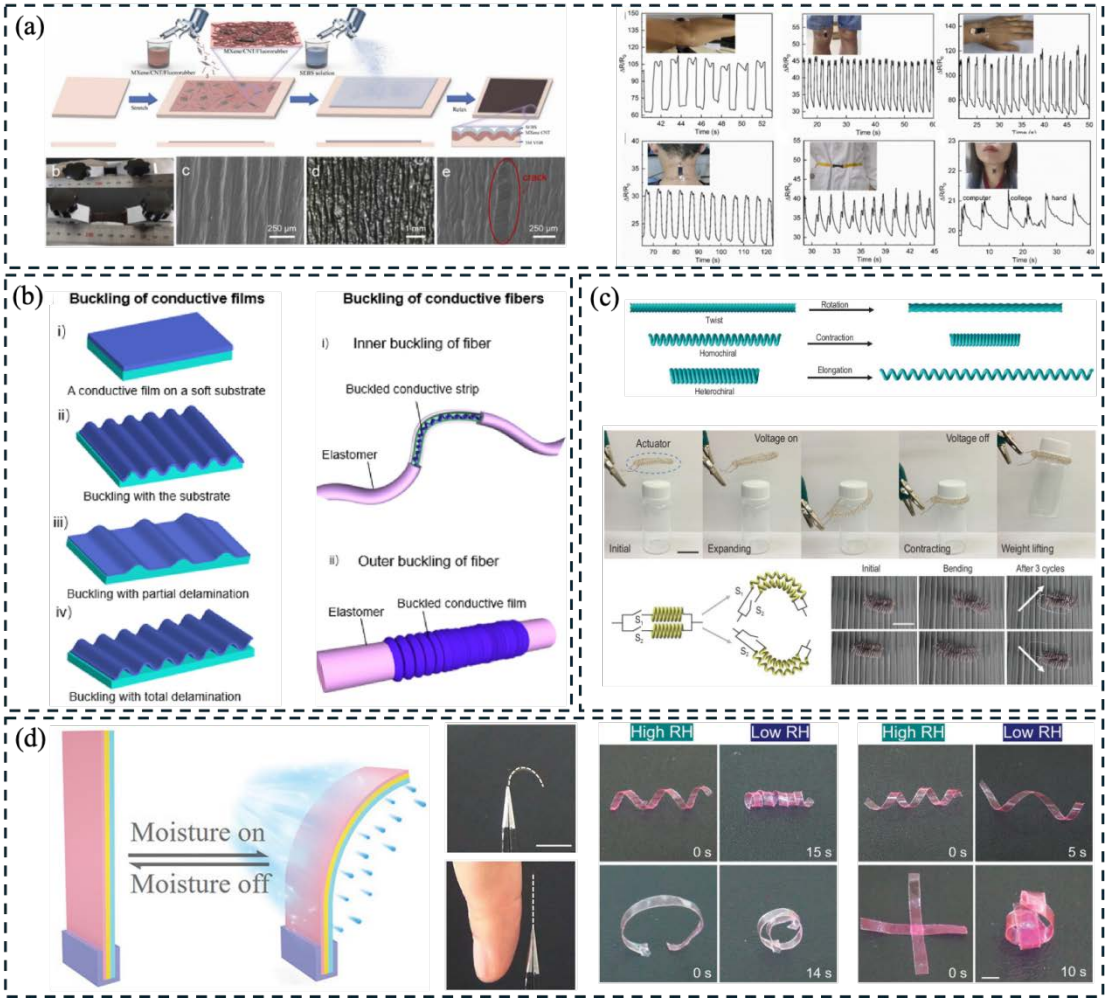

Figure 2.6 (a)Schematic illustration and characterization of flexible strain sensors and Sensing performance of the MXene/CNTs/fluoro-rubber strain sensor in terms of the real-time detection of muscle movement and human movement[40]. (b) Schematic illustration of the buckling structure for a thin film on a flexible substrate[55]. (c) Schematic illustration of torsional, contractile and elongational deformations realized by twisted, homochiral coil and heterochiral coil fibre muscles. And an electrically driven gripper used to pick up an object. Locomotive soft robot made of two independently controlled coiled heterochiral muscles aligned in parallel, which can control the direction of locomotion[60].(d) Schematic illustration of actuation mechanism driven by moisture. Snapshots of the actuation response when a moist finger was close to the actuator. Programmable morphing of the Yin–Yang-interface actuator under high and low humidity[61].

2.3 Porous Microarchitectures

2.3.1. Importance and Role of Porosity

The application of porous structures in textiles has gradually become a research hotspot in recent years. These structures can not only significantly improve the basic physical properties of textiles, such as breathability, softness and comfort, but also give the materials more functionalities, such as energy harvesting, moisture management and intelligent response. As smart textiles and wearable devices continue to develop, it is particularly important to understand and optimize the properties of porous structures. Porous structures increase the surface area of a material by creating tiny pores, or voids, in the material, thereby enhancing its physical and chemical functionality. First, these voids help improve the material's breathability and moisture management capabilities, making it more comfortable in wearable devices, which is especially important in sports and health monitoring applications. In addition, the porous structure can greatly improve the energy collection efficiency of textiles or promote chemical reactions, giving them the functions of energy storage, sensing and environmental response (for example, energy collection through triboelectric effect). Therefore, the application of

porous structures in smart textiles has broad prospects.

In the past few years, significant progress has been made in the research and application of porous structures in textiles. For example, Piyali et al.[64] explored the application of porous polymer materials in energy storage and conversion, and pointed out that porous structures can significantly improve energy conversion efficiency, especially in wearable devices. Ding et al.[65] further studied the potential of porous textile materials in energy harvesting, especially their application in triboelectric nanogenerators (TENGs), and proposed that porous structures can effectively improve energy harvesting capabilities. Islam et al.[66] discussed the application of porous textiles in wearable electronic sensors, emphasizing the role of porous structures in improving sensor sensitivity and comfort. Zhao et al.[67] discussed porous polymer nanocomposites with shape memory functions, and proposed that these materials can dynamically adjust their structures according to changes in the external environment, thereby improving comfort and adaptability. In addition, Ju et al.[68] studied the design of porous composite materials, emphasizing their advantages in breathability and comfort, especially for sports and medical textiles. Lin et al.[69] discussed the application of porous nanostructures in health monitoring sensors, demonstrating their potential in improving sensor performance.

Although the advantages of porous structures in textiles are gradually emerging, they still face some challenges in practical applications. First, the production process of porous structures is complex, and the control requirements for porosity, structural accuracy and distribution are high, which makes large-scale production difficult and

costly. Zhang et al.[70] pointed out that how to control production costs while ensuring the functionality of porous structures is still an urgent problem to be solved. Secondly, although porous structures can improve the comfort and functionality of materials, how to improve their long-term stability and mechanical properties is still a difficult point in research. Porous textiles may experience problems such as pore blockage, structural deformation or performance degradation after long-term use. Therefore, how to ensure the durability of these materials and maintain their functionality in practical applications is one of the core challenges of current research.

The importance of porous structure in textiles is reflected in its significant improvement in physical properties such as breathability, softness and comfort, as well as its wide range of applications in functions such as energy harvesting, moisture management and intelligent response. Despite challenges such as production cost and long-term stability, future research will focus on how to optimize the performance of porous structures, reduce manufacturing costs, and improve the durability of the material to promote its practical applications in smart textiles and wearable devices.

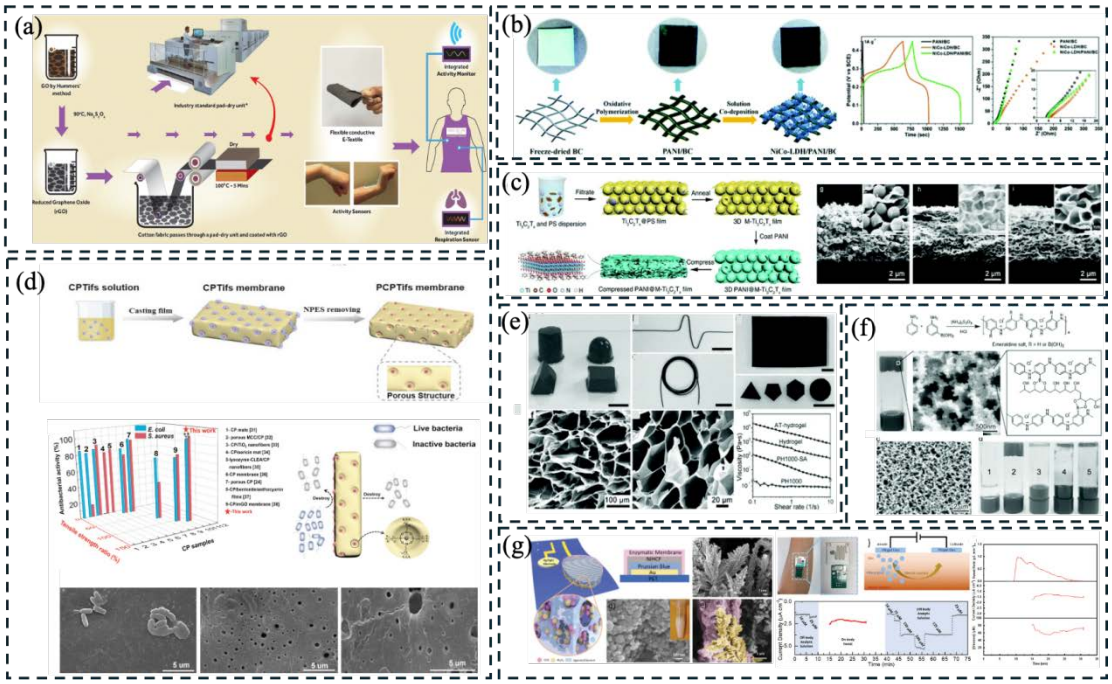

Figure 2.7 (a) Schematic illustration of the fabrication process of graphene-based wearable e-textiles[66]. (b) Preparation of the bacterial cellulose fabrics @polyaniline@Ni-Co layered double hydroxide (BC@PANI@NiCo-LDH) electrode, and their GCD and EIS curves. (c) Preparation and SEM images of the PANI@3D MXene film electrode[67]. (d) Schematic showing the fabrication process of PCPTifs membrane. The antibacterial mechanism of the PCPTifs membrane and SEM images[68]. (e) Arbitrary structures of the PEDOT:PSS hydrogels and their SEM images. (f) Optical and SEM images and the synthesis mechanism of the PANI/PVA hydrogel electrode which used boronic acid as the crosslinker[67]. (g) Schematic illustration of nanotextured glucose sensors with porous enzymatic membrane and demonstration of on-body sweat glucose monitoring[69].

2.3.2. Techniques for Porous Structure Fabrication

With the increasing demand for material functionality, controlling the porosity and pore structure of materials has become the key. In recent years, electrospinning technology, template-assisted methods (including breathing pattern technology) and 3D printing technology have been widely used in the manufacture of porous structures. These methods achieve precise control of pore structures by combining physical, chemical and mechanical processing methods. For these three main porous structure preparation technologies, their principles, implementation steps and latest applications are

introduced in detail, and the advantages, limitations and future research directions of each method are discussed.

Electrospinning is a preparation method that uses a high-voltage electrostatic field to generate nanoscale fibers. By applying an electric field, the solution or molten material is stretched into ultrafine fibers under the action of the electric field, and finally deposited on the collector to form a porous structure. The advantage of electrospinning technology is that it can accurately control the diameter and porosity of the fiber, and can control the characteristics of the pore structure by adjusting the concentration of the solution, the injection voltage and the type of collector. The electrospinning process is usually divided into several steps: First, a polymer solution of a certain concentration and viscosity is prepared. Then, a high-voltage electrostatic field is used to drive the solution to form fibers. As the electric field increases, the solution forms a Taylor cone at the nozzle, and the fiber is stretched and gradually becomes thinner under the action of the electric field, and finally solidified on the collector to form a nanofiber structure. By adjusting the concentration, voltage and other parameters of the solution, the diameter and porosity of the fiber can be controlled. Chen et al.[71] demonstrated a cartilage regeneration scaffold fabricated by combining 3D printing and electrospinning technology, and the fiber network fabricated by electrospinning technology provided the scaffold with high porosity and biocompatibility. This study shows that electrospinning technology has great application potential in the field of tissue engineering, especially in customizing porous scaffolds and promoting cell growth.

Template-assisted methods control the size and morphology of porous structures by

using templates during the manufacturing process. These templates are removed after fabrication, leaving behind porous materials with a specific pore size. The templates can be hard templates (such as polymers, ceramics, or metals) or soft templates (such as self-assembled materials). The shape of the template allows precise control of the pore size and porosity of the final product. The advantages of this method are that it can be mass-produced and can produce materials with highly regular pore structures. Breath figure technology is a typical method in the template-assisted method. The breath figure method is a method for making a regular pore structure based on the water vapor condensation phenomenon. Under specific conditions, the solution is dripped onto the surface and exposed to a humid environment, and the water vapor condenses to form a porous structure with uniform pore size. The honeycomb-shaped ordered porous membrane is prepared by using the breath figure method, which can make the polymer film material form a micro-nano scale structure, and at the same time make it have the functional characteristics of the microstructure. Cui et al.[72] applied the breath figure technique to develop sensors with ordered dimple structures, demonstrating the potential of the template-assisted method in the field of flexible sensors.

3D printing technology is a technology that manufactures complex three-dimensional structures by stacking materials layer by layer. Compared with traditional processing methods, 3D printing has design flexibility and a high degree of pore structure control, and can achieve high-precision porous material manufacturing. Through computer-aided design (CAD) software, researchers can accurately control the pore distribution in the design stage to ensure that the printed porous structure meets specific application

requirements. The 3D printing process includes steps such as designing models, selecting printing materials, layer-by-layer printing, and post-processing. In the model design stage, CAD software is used to define the geometry and spatial distribution of the pores. In the printing stage, printing technologies such as fused deposition modeling (FDM) and stereolithography (SLA) are used to deposit materials layer by layer to finally form the target structure. After printing is completed, post-processing steps such as support removal and surface modification are usually required to further optimize the pore structure. Tetik et al.[73] explored the application of 3D printing in the manufacture of aerogels and stents. The study showed that 3D printing can achieve complex shapes and precisely control pore structures while maintaining the functionality of the material. Zarei et al.[74] combined electrospinning and 3D printing technology to manufacture multi-layered vascular stents, demonstrating the advantages of synergistic optimization of the two technologies.

Although electrospinning technology, template-assisted methods, and 3D printing technology have made significant progress, each method still faces some challenges that restrict its widespread promotion in practical applications. Electrospinning technology still has difficulties in precisely controlling fiber arrangement and porosity consistency, Dilamian et al.[75] discussed template-assisted methods can achieve highly precise pore control, the template removal process may involve complex chemical or thermal treatments. Ni et al.[76] pointed out that although 3D printing technology has design flexibility, it needs further optimization in terms of material diversity, printing speed and production cost. Noroozi et al.[77] mentioned that 3D printing technology

Improvements in material selection and production efficiency still need to be made.

Future research should aim to combine these techniques to leverage their respective strengths while compensating for the limitations of a single approach. By developing hybrid technologies (such as combining electrospinning and 3D printing technologies), multifunctional materials with complex pore structures can be more effectively manufactured, promoting their applications in biomedicine, energy storage and other fields.

Porous structure preparation technology has made great progress, and electrospinning technology, template-assisted method and 3D printing technology each have unique advantages. Electrospinning technology is suitable for the manufacture of high surface area, porous fiber materials; template-assisted methods, especially breath figure technology, can accurately control the orderly arrangement of pores; and 3D printing technology has significant advantages in design flexibility and large-scale production Advantages. By organically combining these technologies, porous materials with superior properties can be developed in the future, promoting their wide application in medical, energy and other fields.

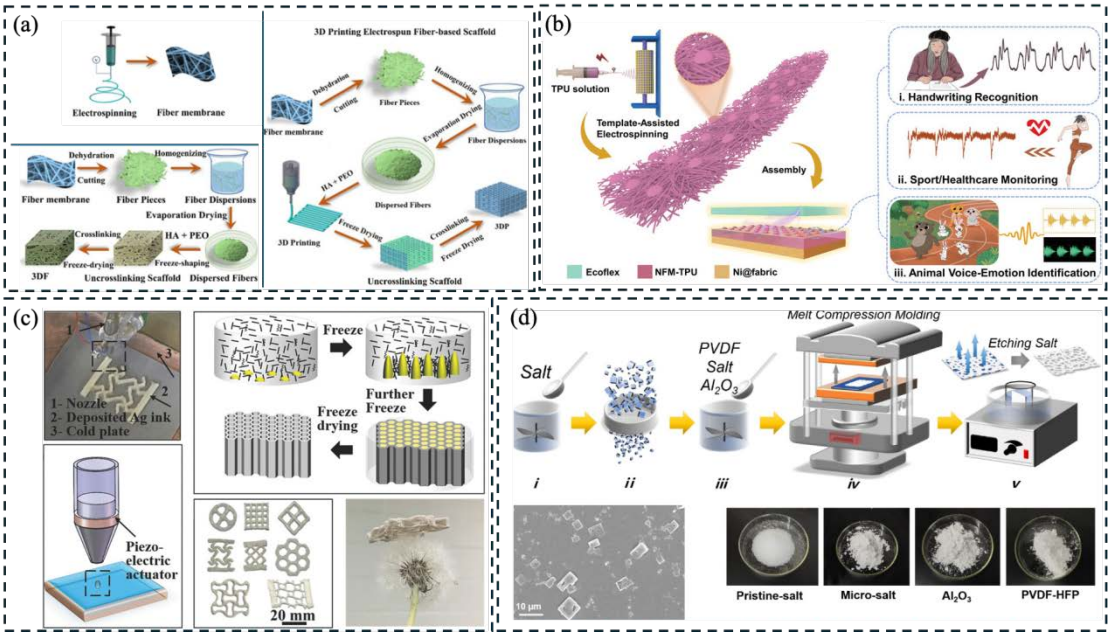

Figure 2.8 (a) Schematic of various electrospun fiber scaffolds[71]. (b) The preparation process of NFM-TENG. Prospective applications of NFM-TENG in handwriting recognition, sport/healthcare monitoring, and animal voice-emotion identification[72].(c) Inkjet-based 3D printing process of rGO AgNW aerogels[73]. (d) Schematic of preparation process of PPCS, and PVDF-HFP, SEM image of micron-level salt particles, Digital images of pristine-salt, micro-salt, Al_2O_3[76].

2.3.3. Applications of Porous Textiles

Porous materials have received extensive research attention in recent years, especially in applications such as energy harvesting, wearable electronic devices, sensors, and filtration systems. These materials have become an important component of many advanced functional materials due to their excellent air permeability, light weight, flexibility, and adjustable pore structure. In these applications, the optimization of pore structure can effectively improve the performance of materials and meet the needs of smart textiles and smart devices in changing environments. Porous textile materials can provide complex structural gaps, which give them unique advantages in many fields. In the field of energy collection, optimized pore structures can improve the efficiency of triboelectric nanogenerators (TENGs) and piezoelectric devices, thereby collecting

mechanical energy in the environment; in the field of wearable devices, porous materials can combine comfort and functionality to provide lightweight, breathable textiles with energy harvesting and sensing capabilities; and in terms of filtration and sensors, by designing appropriate pore structures, efficient filtration or sensing of specific substances can be achieved.

The application of porous materials in energy harvesting has attracted widespread attention. Triboelectric nanogenerators (TENGs) and piezoelectric devices can harvest energy from mechanical vibration or motion, and the introduction of porous materials can help improve the energy conversion efficiency of these devices. For example, by embedding nanomaterials in porous textiles, the performance of TENGs can be significantly enhanced, thereby improving energy harvesting efficiency [78]. Designing porous materials with appropriate pore distribution can also effectively improve the mechanical strength and durability of the material, making it suitable for a wider range of practical applications[79].

The application of porous textile materials in wearable electronic devices has demonstrated its excellent performance, especially in the balance between comfort and functionality. Due to its excellent breathability and softness, porous materials can effectively reduce discomfort when worn, and can also be combined with electronic components to achieve multiple functions such as energy harvesting and health monitoring[80]. For example, some studies use nanofiber materials containing pores to make smart clothing with self-powered functions. These clothes can not only collect energy generated by human movement, but also monitor physiological changes in the

body[81]. In addition, the optimization of the pore structure can also improve the mechanical properties of these materials and ensure their durability under high-intensity use[79].

Another major application area of porous textile materials is sensors, especially in environmental monitoring and health testing. Since porous materials have good selective permeability, their pore structure can be adjusted to detect and filter specific substances[82]. For example, studies have shown that introducing metal nanoparticles or conductive polymers into porous textiles can enhance the material's responsiveness to gases and liquids, thereby achieving real-time monitoring of environmental changes[83]. In addition, porous materials also play a vital role in human health monitoring, detecting harmful substances in sweat or monitoring air quality through gas sensors[84]. Porous textile materials are also widely used in air and water filtration systems. In these applications, the size and distribution of pores are crucial to the filtration effect. By adjusting the pore structure, efficient filtration of specific particles, gases or liquids can be achieved, thus playing an important role in environmental protection and health monitoring[85]. In addition, some studies have proposed intelligent filtration systems based on porous textiles, which can automatically adjust their air permeability and filtration effect according to environmental changes, thereby improving overall performance and efficiency[86,87].

Although porous textile materials have shown great potential in many application fields, they still face some challenges in practical applications. First, how to balance the pore structure and mechanical properties of porous materials is still an urgent problem to be

solved. Although the porous structure improves the functionality of the material, it usually leads to a decrease in its strength and stability, especially in applications that need to withstand external forces or work in extreme environments[88]. Therefore, how to design porous materials with good porosity and high strength and stability is one of the current research hotspots. Secondly, although existing manufacturing technologies can control the pore structure of porous materials, how to ensure the uniformity and accuracy of the pore structure during large-scale production is still a technical challenge. With the diversification of needs, researchers need to continuously optimize the preparation process to ensure the consistency of the material's performance in mass production[89]. In addition, with the increase in environmental protection requirements, how to improve the sustainability of porous textile materials has also become an important issue. Some studies have shown that while improving the performance of porous materials, how to ensure their environmental friendliness and degradability is a key direction for future development[90,91]. Therefore, how to achieve green production and recycling of materials without sacrificing functionality is another challenge that needs to be solved in the future.

The application fields of porous textile materials are wide and diverse, especially showing great potential in energy harvesting, wearable devices, sensors and filtration systems. As technology continues to develop, researchers have made significant progress in optimizing the properties of porous materials. However, how to solve problems such as mechanical properties, pore structure control, and environmental sustainability are still important challenges in current research. In the future, as these

problems are solved, porous textile materials will play an important role in more fields and provide support for green technology and smart life.

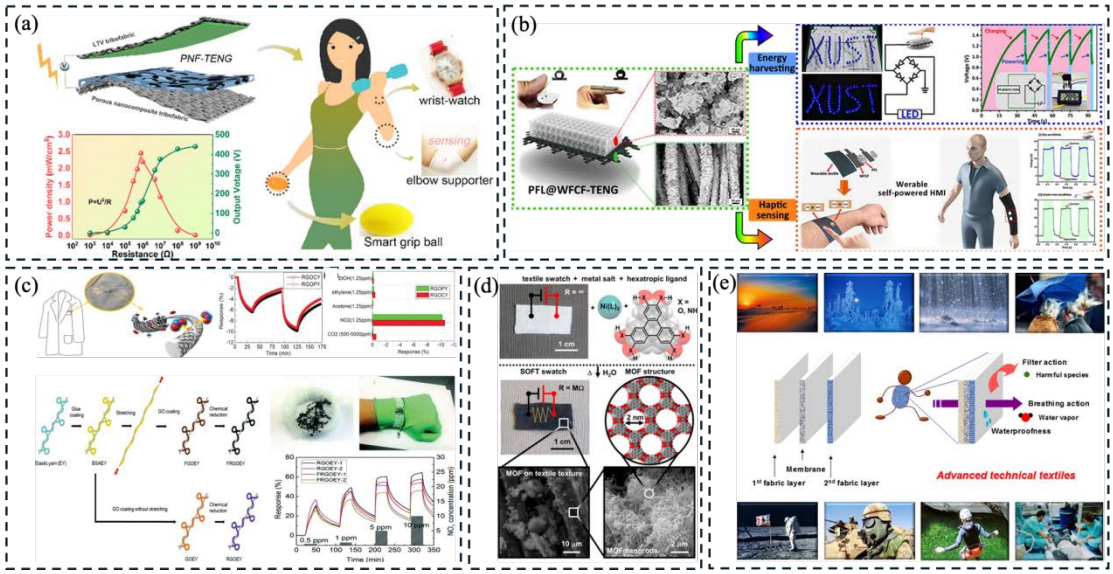

Figure 2.9 (a) Preparation, characterization and applications of the porous nanocomposite fabric, and structure of the PNF-TENG[78]. (b) Fabrication process and applications of PFL@WFCF-TENG[79]. (c) Chemiresistive type e-textile based sensors for NO2 detection[82]. (d) Fabrication of MOF devices and sheet resistance of SOFT-sensor devices[83]. (e) Membrane engineering for innovation in wearable fabrics and protective textiles[88].

2.4 Synergy Between Hierarchically Buckled and Porous Structures

2.4.1 Advantages of combining hierarchical bending and porous structure

The combination of hierarchical buckled structures and porous structures (HBPS) brings performance improvements to the design of textile materials, especially in the applications of wearable devices, energy harvesting, sensors and other smart textiles. This combination not only enhances the versatility of the material, but also optimizes its overall performance in many aspects.

First, enhanced dynamic stretchability and adaptability are a prominent advantage of the combination of hierarchical bending and porous structures. The hierarchical buckled structure, through its reversible deformation characteristics, enables the material to

undergo large deformations under the action of external forces without losing functionality. The introduction of the porous structure further optimizes the breathability and comfort of the material, which is especially important in the application of wearable devices. For example, materials with porous structures can effectively disperse external forces and avoid local stress concentration, thereby making the material have higher stretchability and adaptability. In addition, the combination of hierarchical buckled and porous structures not only improves breathability, but also improves stability during stretching, compression or other mechanical deformations, which is particularly suitable for dynamic use environments, such as wearable devices and smart textiles[92–94].

Secondly, the significant increase in functional surface area is another key advantage of combining these two structures. The hierarchical buckled structure increases the effective surface area of the material by introducing microscopic surface roughness, and the porous structure further amplifies this effect. With increased surface area, such structures can provide more surfaces for functional applications such as coatings, catalytic reactions, or energy conversion. Specifically, in applications such as triboelectric nanogenerators (TENGs), the combination of hierarchical buckled and porous structures can significantly improve energy harvesting efficiency because they can effectively improve the accumulation and transfer efficiency of electrons. This efficient energy conversion and integration enables materials to exhibit higher performance in areas such as energy harvesting, sensors, and self-powered systems .

Finally, improved mechanical toughness and durability are significant advantages of

combining these two structures. The porous structure itself is lightweight and tough, while the hierarchical buckled structure further enhances the material's compression and tensile resistance. The hierarchical buckled structure allows the material to maintain better morphological stability in high-stress environments by dispersing external forces and reducing stress concentration. At the same time, the existence of pores can disperse the load and avoid local rupture, which allows the material to exhibit high strength and durability under complex dynamic conditions. For example, in the application of wearable devices, this combination can effectively improve the durability and performance stability of the device over long periods of use. These advantages make the material have great application potential in smart textiles and other functional products[98,99].

Thus, the combination of hierarchical buckled structure and porous structure provides an innovative way to design textile materials and significantly improves the overall performance of the material. By enhancing dynamic stretchability, increasing functional surface area and improving mechanical toughness, the synergistic effect of the two shows great application potential in wearable devices, energy harvesting, sensors and other fields. This combination not only provides a new direction for the design of future smart textiles and multi-functional devices, but also lays the foundation for efficient and durable material solutions in more fields.

2.4.2 Challenges in Integration

In terms of the combination of porous structures and hierarchically buckled structures, how to optimize these structures to improve the mechanical properties, conductivity

and energy storage capacity of textiles has become a key challenge. A porous structure refers to a structure with a large number of tiny pores, which can effectively provide a large specific surface area, excellent ion accessibility and good mechanical flexibility. In energy storage systems (such as supercapacitors and lithium-ion batteries), porous structures can promote the diffusion of electrolytes and improve ion transport during charging and discharging, thereby increasing energy storage density and power density. On the other hand, hierarchically buckled structures are a method of enhancing the flexibility and stretchability of materials by designing microstructures. Through this structural design, it is possible to achieve excellent mechanical properties and deformation capabilities of the material under high stretching. In addition, the hierarchically buckled structure can also enhance the self-healing and durability of the material, so it is crucial for the stability of electrochemical performance during long-term use.

Although some progress has been made in the combination of porous structures and hierarchical curved structures, there are still many challenges and controversies. First, the porous structure provides a large specific surface area, which is suitable for ion storage and diffusion. However, too many pores may lead to reduced mechanical strength of the material, especially under high tensile stress. How to maintain a balance between porosity and mechanical strength in the design is a key issue in current research[100]. For example, researcher points out that when using MOF templates to synthesize hierarchical carbon fibers, although a large specific surface area can be obtained, the mechanical stability of this structure is still challenged. In addition,

excessive pores may also affect the conductivity of the material, especially under higher stress[101].

Second, although the existing research has achieved remarkable results in small-scale experiments, it is still a challenge to ensure the uniformity and stability of the material in large-scale production. For example, the removal process of the MOF template usually requires the use of highly corrosive chemicals, which not only increases the cost but may also affect the quality and environmental friendliness of the final material[101]. For this reason, the development of a greener and more efficient production method has become one of the current research focuses.

Third, the combination of hierarchical buckled structures and porous structures often involves a trade-off between mechanical and electrochemical properties[100]. Although the layered bending structure can significantly improve the stretchability of the material, how to further improve its mechanical strength and electrochemical stability without sacrificing electrical conductivity is still a key issue that needs to be solved[102].

Although some progress has been made in combining hierarchical curved structures with porous structures to achieve high-performance energy storage materials, there are still many technical challenges. These challenges mainly focus on the balance between mechanical and electrochemical properties and the development of scalable manufacturing processes. Solving these problems requires starting from multiple aspects such as new material design, green manufacturing processes, and performance testing methods to achieve the widespread application of porous textiles in wearable electronics, energy storage and other fields.

2.4.3 Early Progress and Applications

HBPS have become a research hotspot in the fields of materials science and engineering in recent years due to their potential in multiple high-tech applications. These structures can significantly improve the mechanical properties, elastic response and energy absorption properties of materials through precise control of porosity and buckled morphology. Especially in the fields of energy storage, flexible electronics, sensors, and environmental remediation, hierarchical porous materials have demonstrated excellent performance and broad application prospects.

In the field of wearable electronics, composite materials of HBPS demonstrate their superior stretchability and breathability, making them ideal materials for high-performance wearable sensors. By integrating these structures into textiles, biological signals (such as heart rate, electromyography, respiration, etc.) can be effectively monitored while maintaining comfort. For example, a study demonstrated that biosensors based on HBPS composites maintained good signal stability under high stretch conditions, making them suitable for long-term wear and dynamic use[103]. In addition, the HBPS structure improves the sensing accuracy by improving the bending and extensibility of the fiber and forming a uniform electric field distribution on the sensor surface. The performance of these sensors can not only adapt to the ever-changing mechanical environment, but also work stably under extreme conditions (such as high temperature and high humidity), especially in the fields of health monitoring and sports tracking[104].

In the field of energy harvesting devices, the combination of HBPS have significantly

improved the performance of TENGs. TENGs generate charges through friction and contact, which is an effective way to harvest energy and is widely used in portable and self-powered devices. However, the performance of TENGs is limited by charge transfer rate and interface adaptability. The introduction of HBPS improves the electrical performance, allowing the device to maintain high electrical energy conversion efficiency under deformation conditions such as stretching and bending. HBPS-based textile materials exhibit higher surface area and enhanced charge storage capability in TENGs, which in turn promotes fast charge transfer and higher output power. These structures not only improve the mechanical stability and ductility of TENGs, but also improve the reliability of the equipment in complex environments. By optimizing the HBPS, the efficiency of energy collection can be effectively improved, providing support for the long-term stable operation of smart textiles and self-powered devices[51,100,102].

HBPS also shows good application prospects in self-powered sensors. These sensors are able to harvest energy through external mechanical stress without an external power source. HBPS greatly improves the efficiency of self-powered sensors by optimizing the charge generation and storage mechanism. After absorbing mechanical energy, the composite material can quickly convert it into electrical energy and effectively drive the sensor system, which has a wide range of applications in smart textiles, health monitoring, environmental monitoring and other fields. The main advantage of these self-powered sensors is that they can provide long-term energy support for wireless devices, eliminating the dependence on external batteries or charging. With the

continuous optimization of HBPS in material design, these sensors are expected to become the core components of smart textiles and other wearable electronic devices in the future[105,106].

HBPS has demonstrated significant performance improvements in wearable electronics, energy harvesting devices, and self-powered sensors. These materials not only provide higher flexibility and adaptability, but also enhance energy conversion efficiency and charge storage capabilities, showing a wide range of application potential. However, achieving large-scale applications of these materials still requires solving the balance between porosity and mechanical strength, as well as long-term stability and manufacturing process challenges. As research continues to deepen, HBPS composite materials are expected to promote the development of smart textiles and wearable devices and open up more application areas.

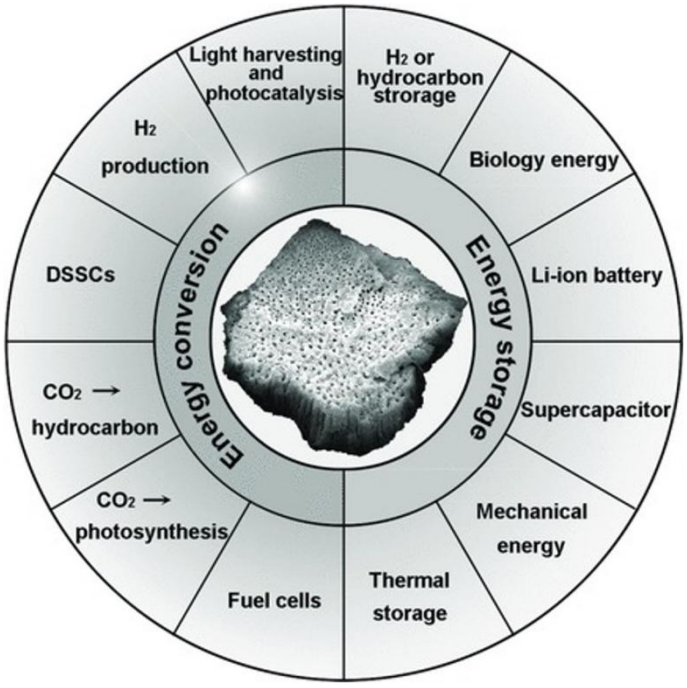

Figure 2.10 Illustration of the potential application on energy convertion and storage of the hierarchically porous materials.

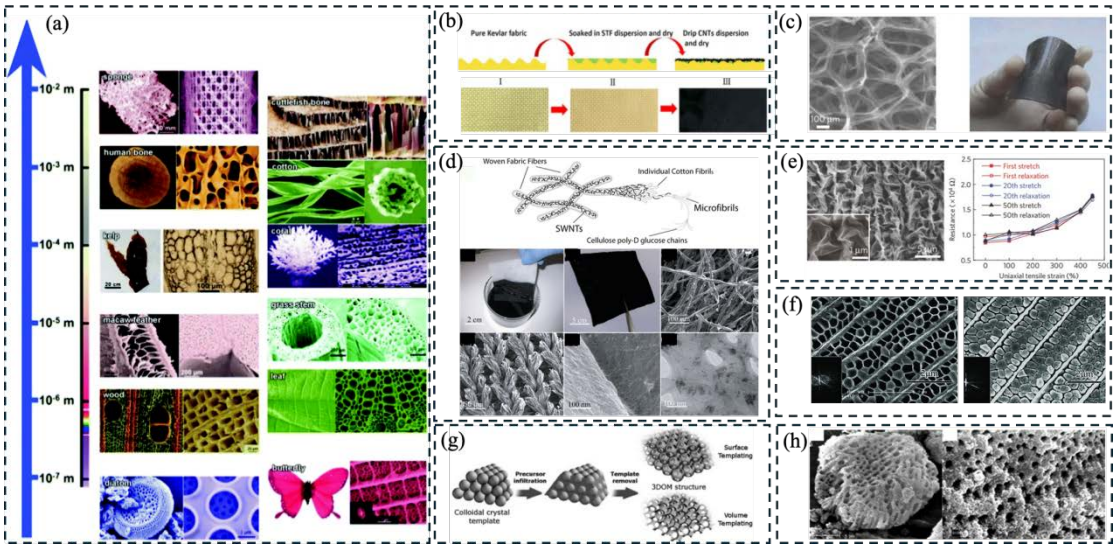

Figure 2.11 (a) Schematic that shows the basic steps in colloidal crystal templating[102]. (b) Illustration of the procedure of the CNT/STF/Kevlar composite , neat Kevlar (I); STF/Kevlar (II); CNT/STF/Kevlar composite (III)[93].(c) Graphene-based stretchable materials: graphene foam and crumpling of graphene sheet[94]. (d) Porous textile conductor fabrication[100]. (f) Graphene-based stretchable materials: crumpling of graphene sheet[94]. (g) Schematic that shows the basic steps in colloidal crystal templating. (h)SEM images of the synthesised zirconia particles showing uniform microporosity[107].

2.5 Research Gaps and Future Directions

Although HBPS have shown broad application potential in wearable electronic devices, energy harvesting devices, and self-powered sensors, there are still many technical challenges and research gaps in the practical application and industrialization process. To address these issues, further exploration and innovation are needed to achieve more efficient and sustainable material solutions.

2.5.1 Balance of mechanical properties and functional properties

Current research has proven that HBPS can significantly improve the surface area and mechanical properties of materials. However, how to achieve a balance between

large porosity and high mechanical strength is still a difficult problem that needs to be solved. Excessive pores may lead to a decrease in material strength, and the pursuit of enhanced mechanical properties may sacrifice the flexibility and functionality of the material. Future research needs to resolve this contradiction by optimizing structural design and developing new composite materials. Using dynamic chemical bonds combined with nanocomposite technology, it is possible to enhance mechanical properties while maintaining high porosity and functionality.

2.5.2 Scalability and cost optimization

Although HBPS have shown promising performance in laboratory-scale studies, these materials still face significant challenges in large-scale manufacturing. Existing methods such as template removal, high-precision laser etching, and complex multi-step manufacturing processes are often costly and inefficient. Additionally, the chemical reagents and energy-intensive operations in these processes can be taxing on the environment. Future research should focus on developing green manufacturing technologies, such as using degradable templates, low-energy self-assembly processes, or a combination of 3D printing and electrospinning technology to improve production efficiency and reduce manufacturing costs.

2.5.3 Long-term stability and environmental adaptability

The long-term stability of HBPS in dynamic environments still requires further study. Especially in the fields of wearable devices and environmental monitoring, materials need to maintain their functionality under extreme conditions such as

moisture and high temperatures. However, many current materials will suffer from pore clogging, structural deformation or performance degradation after long-term use. To this end, further research is needed on how to improve the environmental adaptability and service life of materials through dynamic self-healing mechanisms or the introduction of weather resistance enhancement technology.

2.5.4 Function integration and multiple performance optimization

In terms of functional integration, how to achieve synergistic optimization among flexibility, conductivity, mechanical strength and multifunctionality within a material system is still an important technical bottleneck. For example, improving the electrical conductivity of materials often leads to a decrease in mechanical flexibility or durability. Future research should focus on the design of multifunctional materials with the help of artificial intelligence (AI)-assisted material optimization and multi-scale modeling to achieve a dynamic balance between different properties. In addition, combining bionic design and new nanomaterials (such as graphene, MXene) may provide new technological paths for functional integration.

2.5.5 Environmental sustainability and recycling

Under the current global requirements for sustainable development, the environmental impact of HBS-porous composite materials has become a focus of attention. Some non-degradable ingredients or production processes with high energy consumption used in the existing technology are contrary to the goal of sustainable development. Future research needs to focus on developing recyclable, degradable or

recyclable materials and designing lower carbon manufacturing processes. For example, the introduction of bio-based materials or renewable resources as raw materials, combined with green chemistry methods, will help improve the environmental protection properties of these materials.

2.5.6 Application diversity and new field expansion

While existing research focuses on wearable devices, sensors and energy harvesting, the potential of HBS and porous structures goes far beyond that. For example, its applications in medical implants, soft robotics, energy storage devices, and environmental remediation remain underexplored. Future research can further expand its application in multidisciplinary fields, such as applying it to intelligent drug release systems, bionic interfaces, and autonomous repair materials in complex environments.

2.6 Summary

This review underscores the complementary roles of hierarchically buckled structures and porous microarchitectures in functional textile engineering. By integrating these features, it is possible to achieve unprecedented levels of adaptability, functionality, and mechanical robustness. These hybrid designs represent a frontier in textile research, unlocking new opportunities for advanced applications in wearable technology, energy devices, and beyond.

Chapter 3 Skin-inspired Hierarchically Buckled Fibers with Stretchable Porous Microarchitectures and Customizable Functionalities

3.1 Introduction

Textile wearables have been widely used in our daily lives and regarded as the second human skin[108,109]. They have attracted significant attentions in wearable technologies owing to their unique natures and remarkable properties such as excellent flexibility, good air permeability, light-weight, thermal-protective, versatile structure designs, and robust mechanical deformation capacities[110–112]. Fibers (or yarns), as the basic constituent unit of textiles, can be acquired through different spinning methods, such as dry spinning[113,114], melt spinning[115,116], wet spinning[117,118], and electrospinning[119,120]. In practical applications, fibers usually require further modifications with functional materials[121] for the enhancement of their physicochemical properties or the incorporation of specific advanced functions by physical or chemical methods such as surface treatment[122], direct coating[123] and their hybrid techniques[124]. These valuable techniques have been well used for advanced functional fibers to enhance or introduce some desired functionalities based on different practical applications. However, there is still a considerably difficult challenge in endowing the modified fibers with desired functionalities or microstructures while keeping their unique fiber texture features and inherent properties. Therefore, incorporating functional nanomaterials into the modified fibers with continuous conformal and porous microstructures will be an efficient and attractive strategy for

developing continuous advanced functional material fibers (CAFMFs).

The breath figure (BF) was a unique self-assembly strategy in which water droplet arrays were used as templates for the assembly of polymer brick materials to generate hierarchically porous microstructures on different substrates with tunable sizes in the range from hundreds of nanometers to dozens of micrometers[19,125]. This method not only has facile scalability and nondestructive features, but also possesses rapid, cost-effective, and energy-saving advantages. Recently, we reported an BF-based approach for fabricating functional textile wearables with a flat porous microstructure[126–128]. The obtained wearables demonstrated improved physicochemical properties with inherent textures. Nevertheless, the developed functional wearables are not stretchable at all because of their simple flat porous microstructures that will collapse under stretching, and therefore cannot meet the stretchability requirement which is one of the most important properties of functional wearables. Moreover, the specific surface area of the developed functional wearables is constrained by flat microstructures, which should be further increased with a new design of non-flat porous microstructures for higher functional performance when loading functional nanomaterials.

The body of human beings is a perfectly marvellous organic machine. Taking human skin[129–131] as an example, it is three-dimensional complex, soft, extensible (3-55% strain) and multifunctional device that can regulate human temperature, moisture and pressure. It is also the first barrier to infection from environment to guard the underlying muscles, bones, etc. When the dynamic framework of bones (i.e., skeleton) is in movement, the soft and flexible human skin can not only keep perfectly

conformable with small deformation, but also can easily cope with the large deformation caused by the bending/stretching of joint parts through the generation of surface buckling. If the human joint (e.g. finger joint) skin-like buckling[12,132] can be introduced into the conformal porous microstructures of fibers, the CAFMFs will not only obtain good stretchability of porosity but also possess large specific surface area, which would be greatly helpful for the design and development of customized functional wearables with better performance.

Herein, inspired by the surface buckling of finger joint skin, a new kind of hierarchically buckled porous microstructured fibers (HBPMFs) has been delicately designed and fabricated using stretchable elastic fibers (e.g. polyurethane (PU) or rubber) and polymer brick materials (e.g. polystyreneblock-polybutadiene-block-polystyrene triblock copolymer (SBS), poly(methyl methacrylate) (PMMA)) by a special physicochemical strategy consisted of material systems manipulation, interfacial self-assembly, stretching-releasing control and thermal annealing. Through the rational surface design and engineering, the obtained HBPMFs have been constructed with hierarchically skin-like buckling and conformal porous microarchitectures, possessing superior advantages of stretchable porous microarchitectures and more exposed porous surface area for higher performance. In this study, the main influential factors including polymer bricks, solutes, solvents, concentrations, fiber substrates and pre-stretching strain on surface buckling and porous microarchitectures were systematically studied. Moreover, the HBPMFs strategy can also be used for directly fabricating a new kind of hybrid CAFMFs that integrate desired

functional nanomaterials in the stretchable porous microstructures. Thanks to the skin-inspired buckling and hierarchically porous microstructures, the resultant HBPMFs demonstrates a larger specific porous surface area, superior loading capacity of functional nanomaterials, and unique stretchable microarchitectures of porosity. As a demonstration of application, the CAFMFs based on TiO_2/HBPMFs that integrated photocatalytic TiO_2 nanoparticles were assembled for the photodegradation of organic pollutants. Compared with control samples, the TiO_2/HBPMFs showed significantly improved properties on photocatalytic degradation of pollutants. These high-performed CAFMFs are not only able to take better advantages of flexibility and stretchability of fiber materials and porosity of buckled microarchitectures, but also possess the customizable multifunctionalities of the incorporated functional nanocomponents, which is expected to widely extend the application fields of fiber materials with enhanced and customized performance

3.2 Experimental Section

3.2.1 Materials

Polystyrene-block-polybutadiene-block-polystyrene triblock copolymer (SBS, MW~133,800, ≥99.5%), Poly(methyl methacrylate) (PMMA, MW ~120,000, ≥99.5%) and chloroform ($CHCl_3$, anhydrous, ≥99.9%), carbon disulfide (CS_2, anhydrous, ≥99.9%) and tetrahydrofuran(THF, ≥99.9%) were purchased from Sigma-Aldrich Co. Titanium dioxide nanoparticles (TiO_2 NPs, 17-30 nm), copper nanoparticles (Cu NPs, 40-60nm), zinc oxide nanoparticles (ZnO NPs, 50-100nm), and

silver nanoparticles (Ag NPs， 25-50nm) were purchased from XFNANO, Inc. Methylene blue (MB) and neutral red (NR) were purchased from Sinopharm Chemical Reagent Co. Ltd. Polyurethane (PU) fibers and rubber fibers were provide by a local textile company. All materials were used directly without further processing.

3.2.2 Preparation of HBPMFs

For the fabrication of HBPMFs, four different polymer brick solutions including SBS/$CHCl_3$, SBS/CS_2, SBS/THF, and PMMA/$CHCl_3$ were first prepared with different solutes (SBS and PMMA) and solvents ($CHCl_3$, CS_2 and THF), respectively. Then different elastic 1D materials such as rubber and PU fibers with a smooth surface and braided structures were selected as substrates and ultrasonically cleaned by immersion in alcohol and then dried in an oven at 60°C for one hour. The concentrations of their polymer brick solutions were also set to 50 to 250 mg/ml to systematically study the formation conditions of buckling and porous microstructures. The elastic fiber substrate was pre-stretched to 20%, 40%, 60%, 80%, 100%, 120% and 140% respectively with a homemade stepper machine. And then the fixed elastic fibers with a given pre-stretching ratio was immersed into a variety of polymer brick solutions for 30s and selective swelling to achieve the dip-coating process. Subsequently, the fiber substrates coated with polymer bricks were drawn vertically out of bricks solutions and then rapidly transferred into a high-humidity (RH>90%) environment for internal self-assembly between the brick polymer and the water droplet. After waiting one minute, the modified fibers were removed out from high humidity environment, and the surface water droplets of the fibers were quickly evaporated to form porous

honeycomb microstructures on the polymer surface of elastic fibers. The pre-stretched elastic fiber was then released at a controlled rate of 1 mm/s using a homemade stepper. The as-prepared buckled elastic fiber was put into a thermal annealing environment at the glass transition temperature of the respective brick material to remove the stress effect and avoid interfacial peeling failure. For comparison, solid coating functional fibers (SCFFs) and porous coating functional fibers without buckling structures (PCFFs) were also prepared at a humidity of about 10% and 90%, respectively.

3.2.3 Design and fabrication of CAFMFs

To investigate the feasibility and versatility of HBPMFs for incorporating functional nanomaterials for the fabrication of CAFMFs, various nanoparticles (e.g., TiO_2 NPs, Cu NPs, ZnO NPs, and Ag NPs) were introduced into the SBS/$CHCl_3$ solution respectively with a concentration of 150 mg/ml to form the hybrid suspension. The mass ratio of additives/polymer was set at 1:20 wt% for TiO_2 NPs, 1:40 wt% for Ag NPs, 1:60 wt% for Cu NPs and 1:80 wt% for ZnO NPs, respectively. Then, the well-dispersed hybrid suspension was obtained after ultrasonication and magnetic stirring for 30 min at room temperature. The HBPMFs were directly prepared with the hybrid solution by the same process of HBPMFs with a pre-stretching strain. For the photocatalytic control experiments, TiO_2 loaded porous microstructured fibers (TiO_2/PCFFs) but without buckled structures and TiO_2 loaded solid coating fibers (TiO_2/SCFFs) were also prepared. It was worth noting that the TiO_2/SCFFs were carried out at a humidity environment of about 10%.

3.2.4 Photocatalytic degradation of organic pollutant

Ten TiO_2/HBPMFs with a length of 3 cm and a weight of 0.5 g were prepared as the experimental sample, and ten TiO_2/PCFFs and TiO_2/SCFFs with the same weight were also prepared as the control samples. Then, they were placed in a 5 ml transparent vial containing a 1.65×10^{-5} M solution of MB or NR, respectively. To eliminate the influence of fiber adsorption on the photocatalytic action, three fibers were soaked in MB/NR solution overnight, and the absorbance at the beginning of photocatalysis was measured. During the photocatalytic process, the three fibers should be positioned close to the lamp's side, and an 18 W UV lamp was employed as the light source for the catalysis. The entire catalytic duration was 6 h, and the catalytic efficiency was measured by collecting MB /NR solution every hour, which was calculated by:

$$D = \frac{n_0 - n}{n_0}\%$$

where n_0 represents the initial absorption intensity of MB at 664 nm or NR at 460 nm, n represents the absorption intensity of MB at 664 nm or NR at 460 nm at different degradation times, and D represents the degradation efficiency of MB % or NR%.

3.2.5 Characterization

Scanning electron microscopy (SEM) (TESCAN) at 5 kV was used to examine the morphologies of pristine elastic fibers and HBPMFs prepared with different parameters. After being coated with a thin layer of sprayed gold and subject to SEM(VEGA3) at 15.0 kV accelerating voltage, CAFMTs images with different experimental parameters were obtained. The elemental composition of CAFMFs were analyzed by using a SEM equipped with an Energy-dispersive X-ray spectroscopy (EDX). N_2 adsorption-

desorption isotherms and the specific surface area were tested by Micromeriticis ASAP 2460. The photocatalytic activity of the prepared CAFMFs was investigated using a digital camera and a UV–Visible absorption spectrometer (UV–Vis, Lambda 18) to monitor the photocatalytic degradation efficiency of organic pollutants. The mechanical property tests were carried using a universal tensile testing machine (Instron Co., Ltd.) at a loading rate of 10 mm/min.

3.3 Results and Discussion

3.3.1 Design and fabrication of skin-inspired HBPMFs

Inspired by the skin of finger joints, herein we proposed a novel surface engineering strategy to fabricate a new kind of advanced functional fibers with skin-inspired buckling features and conformal porous surface microstructures on the PU fiber with smooth surface, namely hierarchically buckled porous microstructured fibers (HBPMFs), in which the fibers can achieve both high stretchability and porosity. The skin of finger joints can be bent and straightened with comfort *via* the generation of surface buckling structure, where the folds of the joint skin play an essential role in stretching and matching with the internal muscles nicely, achieving synchronization and harmony between the surface structure and the interior muscle (**Figure 3.1(a)**). Inspired by the skin of finger joints, herein we proposed a novel strategy to fabricate a new kind of advanced functional fibers with skin-inspired buckling features and conformal porous microstructures, namely hierarchically buckled porous microstructured fibers (HBPMFs), in which the fibers can achieve both high stretchability and porosity (**Figure 3.1(b)**). Based on the prepared HBPMFs, functional

nanomaterials can be further incorporated to develop continuous advanced functional material fibers (CAFMFs) for desired applications such as the photocatalytic degradation of organic pollutants (**Figure 3.1(c)**).

The fabrication techniques of HBPMFs involving material systems adjustion, interfical self-assembly process, stretching-releasing control, and thermal annealing are shown in **Figure 3.1(d)**. The pre-stretching strain was initially applied to the pristine elastic fibers (**Figure 3.1(d) I** and **II**), which is one of key parameters for the fabrication of HBPMFs with desired finger joint skin-like buckling features. **Figure 3.1(d**) **III** showed that the elastic fibers with a given pre-stretching ratio was immersed into a kind of polymer brick solutions or their mixtures with nanocomponents for selective swelling to achieve the dip-coating process. Owing to the solvent volatile property of polymer brick solutions, the conformal porous microstructures of HBPMFs can be readily obtained, and the surface morphologies of porous microstructures will also be affected by the volatilization of solvents. The formation mechanism of BF process can be explained as **Figure 3.2**: (1) the rapid evaporation of low boiling point of solvent facilitates the nucleation of the moisture and small water droplets on the polymer solution surface; (2) with the growth and self-assembly of water droplets, an ordered and closely packed water droplet array is formed and covers the whole surface of the polymer solution; and (3) the evaporation of water droplets and solvent will result in dry polymer layers with hexagonal pore arrays on the fibers. The detailed interfical self-assembly procedures of porous microstructures are illustrated in **Figure 3.1(d) VII-IX** and **Figure 3.2**. In brief, the obtained polymer bricks coated fiber (**Figure 3.1(d) III**) was quickly transported to

a high humidity environment, in which water droplets will precipitate on the surface of the fiber because of the evaporation of the solvent with low boiling point and high volatility in polymer brick solutions (**Figure 3.1(d) VII-VIII**). Condensed water droplets remained on the surface of the fiber after nucleation, expanding and eventually self-assembling into ordered arrays of water droplets that were embedded on the polymer's surface ((**Figure 3.1(d) IX**). After being transferred to a typical indoor environment (e.g. ~25℃), the elastic fiber's surface temperature was allowed to rise to room temperature, where the water droplets evaporated[133], leaving porous honeycomb microstructures on the polymer surface of elastic fibers (**Figure 3.1(d) IV**). To obtain finger joint skin-inspired buckling surface, the pre-stretched elastic fiber was gradually released at a controlled rate using a homemade stepper under a thermal annealing environment (**Figure 3.1(d) X-XI**) at the glass transition temperature of the respective brick material to remove the stress effect and interfacial peeling failure, and finally the HBPMFs with both skin-inspired buckling and porous microstructures were obtained (**Fig 3.1(d) V and VI**). In this proposed strategy, the thermal annealing would endow the buckling layer with desired crinkly mobility and maintain the porous microstructures, eliminate the stress mismatch between fiber substrate and polymer layer, and also promote the reinforcement of mechanical properties because of the improved crystallinity and removed internal stress of polymer chains under thermal annealing[134,135].

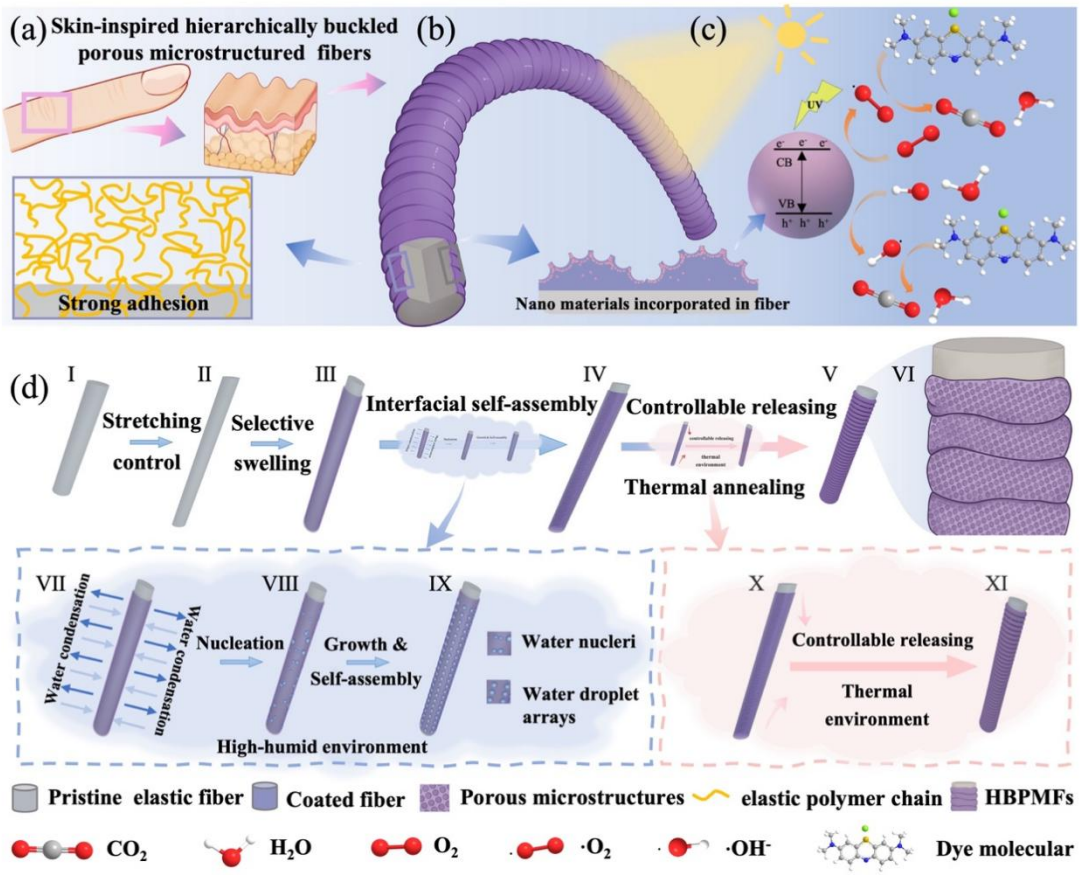

Figure 3.1 Design and fabrication of HBPMFs. (a) Schematic of the skin structure of finger joints. (b) Design of HBPMFs inspired by skin buckling features. (c) Potential application of HBPMFs. (d) The fabrication process of HBPMFs.

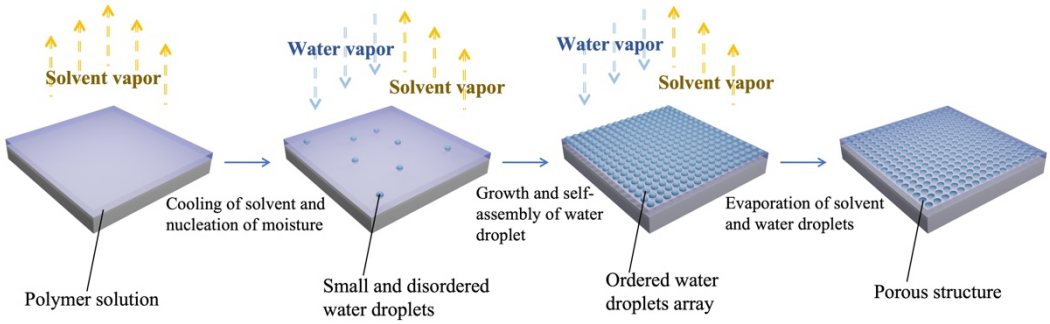

Figure 3.2 The mechanism of the self-assembly process.

3.3.2 Influence of material systems for HBPMFs

The preparation of HBPMFs is a complex kinetic and thermodynamic procedure that is affected by various factors such as ambient conditions, material systems, and substrate properties[136,137]. For the interfacial self-assembly process to progress in an

orderly way, it is preferred to keep the conditions of room temperature and high humidity. This is because the interfacial self-assembly can be performed facilely, and water droplets can condense on the fiber's surface more easily in a high-humidity and room temperature environment. In order to obtain uniform and ordered porous microstructure arrays, HBPMFs were prepared in an enclosed container at ambient temperature (~25°C) and relative humidity (~90%).

Material systems consisting of various solutes (polymer bricks), solvents, and solution concentrations were then systematically studied to fabricate the optimized HBPMFs. **Figure 3.3** shows that the typical surface morphologies of the prepared HBPMFs with different polymer brick solutions and fiber substrates, and the detailed fabrication procedures are provided in the experimental section. In the fabrication process, the polymer brick material plays a decisive role in the morphology and function of HBPMFs. As shown in **Figure 3.3 (a)-(c)**, the pristine PU fiber demonstrated a smooth and continuous surface. When 150 mg/ml of SBS/$CHCl_3$ was employed as the polymer brick solution, ordered porous honeycomb microstructures and hierarchically skin-like buckling were formed on the surface of PU fiber (**Figure 3.3 (d)-(f)**), indicating that SBS/$CHCl_3$ is an ideal polymer brick solution. To investigate the effect of solutes on the porous microstructures, other polymers such as PMMA was also chosen as the brick material of PU fiber to prepare HBPMFs. As shown in **Figure 3.3 (g)-(i)**, porous microstructures with small pore sizes and low porosity were obtained when PMMA was used as the brick material, and the buckling effect of HBPMFs prepared with PMMA/$CHCl_3$ was also lower than that of HBPMFs

prepared with SBS/$CHCl_3$ because the hydrophobic branch of PMMA cannot stabilize water droplets effectively. Moreover, PMMA was not soft enough due to its rigidity, which also restricted its development as a brick material. As the most important features, the buckled and porous microstructural morphologies are conducive to enlarge the specific surface area of HBPMFs, thereby enhancing their functionalities. Thus, SBS is regarded as an ideal polymer brick material for the fabrication of optimal HBPMFs.

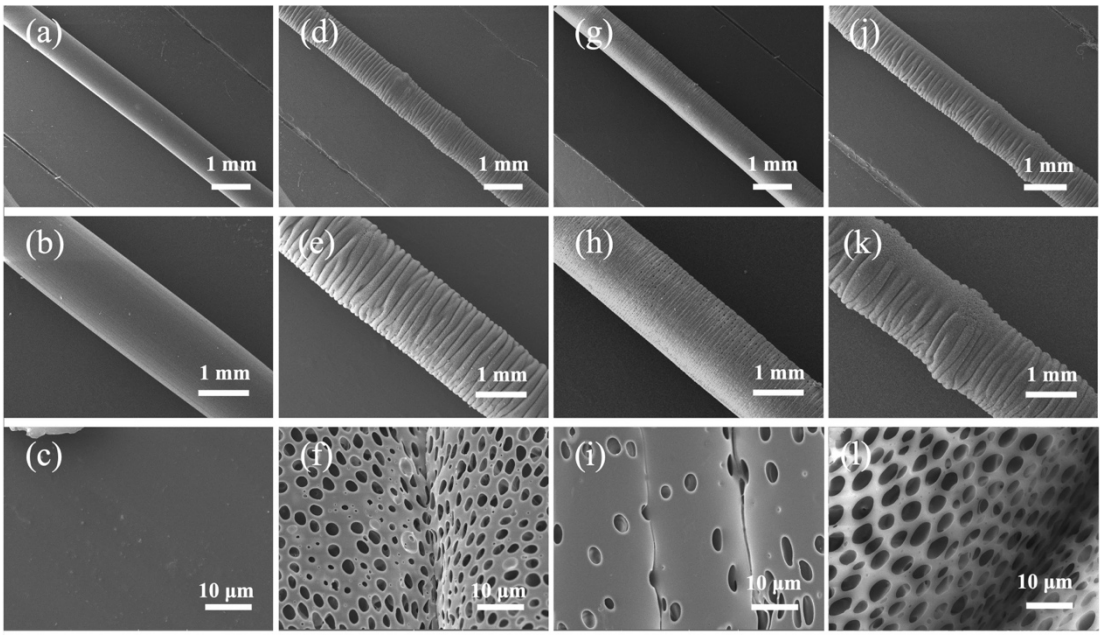

Figure 3.3 Typical surface features and various magnification SEM images of HBPMFs prepared with different solutes and fiber substrates. (a-c) pristine PU fibers, (d-f) HBPMFs with PU fibers and SBS/$CHCl_3$, (g-i) HBPMFs with PU fibers and PMMA/$CHCl_3$, and (j-l) HBPMFs with single-strand rubber fibers and SBS/$CHCl_3$. The concertation of all polymer brick solutions was set at 150 mg/ml.

In addition to polymer bricks, solvent is also one of key parameters for the formation of porous microstructures. When CS_2 was selected as the solvent for SBS polymer brick solution, the porous structures with large pore sizes and uneven morphologies were formed on the surface of PU fibers due to its lower boiling point and faster evaporation rate, as shown in **Figure 3.4 (a-c)**. When THF was chosen as the

solvent for SBS polymer brick solution, fibers could not obtain an ordered honeycomb structure due to the mutual solubility of THF with water (**Figure 3.5**). The above results indicated that the selection of nonpolar and highly evaporative solvents is one of the key factors in the formation of HBPMFs. Firstly, the relative density of THF[138] is smaller than that of water, and the water vapor could not nucleate uniformly during solvent evaporation. Then the polymer film formation process provided limited support to wrap the water droplets, resulting in the formation of an interwoven and disordered network structure on the surface of fibers after the solvent and water evaporated completely[139]. The relative densities of all solvents were higher and insoluble with water, except for THF which had better solubility with water and lower relative density than water. The volatility of organic solvents has been reported to reduce the surface temperature of solutions to -6 to 0 °C[140]. The volatility of $CHCl_3$ can reduce the surface temperature to 0 to 6 °C, and the volatility of CS_2 can reduce the temperature to -6 °C. Solvents with strong volatility can reduce the surface temperature of solutions rapidly but may destabilize the arrangement of water droplets on the surface of solutions. The boiling points of CS_2, $CHCl_3$ and THF were 46.7, 61.7 and 66.1℃, respectively. Therefore, $CHCl_3$ may be a preferred solvent for the fabrication of HBPMFs with obviously skin-like buckling features and hierarchically porous microstructures.

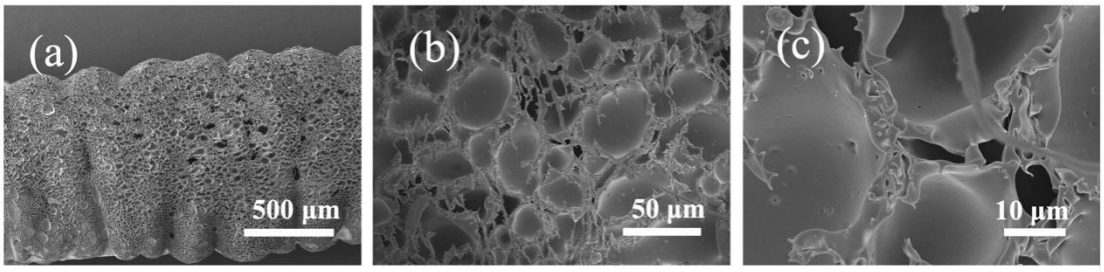

Figure 3.4 (a-c) SEM images of HBPMFs prepared with PU fibers and SBS/CS_2.

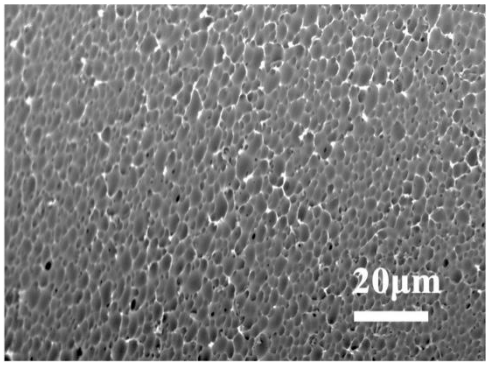

Figure 3.5 SEM image of HBPMFs prepared with PU fibers and SBS/THF.

The fiber substrate and its surface structure also played a very important role in the formation of orderly porous microstructures and hierarchically buckling features. Based on our preliminary studies, porous microstructures can be conformally formed on various hydrophilic and hydrophobic surfaces of substrates. In this study, three kinds of elastic fibers including smooth PU fiber, braided PU fiber (*b*-PU), and smooth rubber fiber were selected as substrates to prepare HBPMFs. As shown in **Figure 3.3** (d)-(f), hierarchical skin-like buckling and ordered porous microstructures were well formed onto the surface of the smooth PU fiber. **Figure 3.6** and **Figure 3.3** (j)-(l) show the surface morphologies of HBPMFs made from *b*-PU fiber and rubber fiber, respectively. The results shown that they all appear to have a buckled porous structure, indicating that the proposed method is capable of producing a hierarchically buckled structure on different fibers. However, HBPMFs made from *b*-PU fiber and rubber fiber demonstrated poor surface morphologies of buckling and porous structures as compared to HBPMFs made from smooth PU fiber. In **Figure 3.3** (j)-(l), the uneven buckling and interconnected porous structures were formed on the rubber fiber substrate. **Figure 3.6** depicts that nonuniform pore size distribution can be observed on the surface of the *b*-PU fiber substrate probably because water droplets did not self-assemble

uniformly on the fiber surface. Hence, smooth PU fiber will be selected as the main substrate material for the investigation of HBPMFs in the following studies.

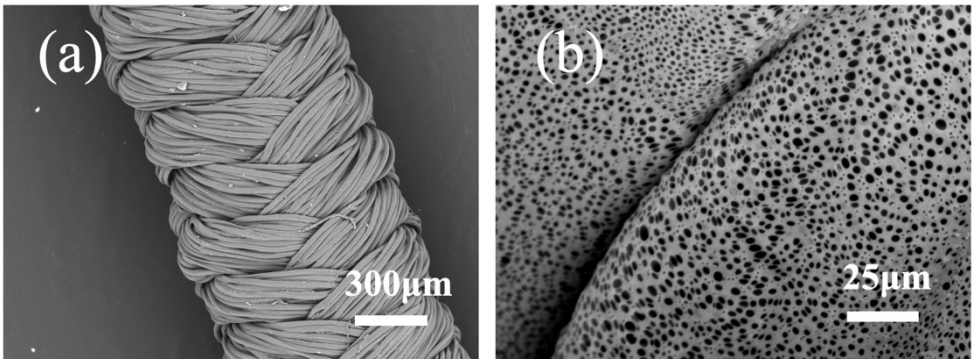

Figure 3.6 (a) and (b) Typical surface features and SEM images of HBPMFs prepared with *b*-PU fiber and SBS/$CHCl_3$.

3.3.3 Influence of solution concentrations for HBPMFs

To investigate the influence of solution concentration on the formation of HBPMFs, SBS/$CHCl_3$ solutions with different concentrations of 50, 100, 150, 200, and 250 mg/ml were employed to prepare HBPMFs with the smooth PU fiber substrate. To acquire hierarchically porous microstructures formed by solutions of varying concentrations, the process was carried out under a relative humidity of about 90%. For forming skin-inspired buckling, the pre-stretching ratio of PU fiber was set to 100%. **Figure 3.7** demonstrates that different concentrations of SBS/$CHCl_3$ solutions could generate different buckled surfaces on PU fibers. In general, when the concentration was gradually increased from 50 to 250 mg/ml, the surface of HBPMFs at various magnifications showed both hierarchically skin-like buckling features and regular porous structures that were uniformly distributed and densely arranged. **Figure 3.7 (a)** demonstrated that a dense buckled structure emerged at a brick solution concentration of 50 mg/ml, with an arrangement direction parallel to the fiber cross-section. **Figure**

3.7 (b) shows a hierarchically buckled width (i.e. the width of one full buckle) of about 90 μm. The structure of pores was regular and circular with considerable gaps among them (**Figure 3.7 (c)**), and the average pore size was about 1.40 μm (**Figure 3.7 (d)**). **Figure 3.7 (e)-(h)** shows that the buckled width (~100 μm) and pore size (~1.22 μm) were slightly increased when the concentration of the brick solution was increased from 50 to 100 mg/ml. From **Figure 3.7 (i)**, it is noted that the buckling morphology looks more similar to the buckled of human finger joints when the concentration of the brick solution was increased to 150 mg/ml, with a thicker buckled width of about 140 μm (**Figure 3.7 (j)**) and uniform and densely distributed pores (**Figure 3.7 (k)**). From **Figure 3.7 (l)**, it is also noted that the pore sizes approximately followed a normal distribution, with average pore size of 1.51 μm. Since the solution viscosity increases gradually with concentration, the support strength of water droplets was enhanced, and the system stability was improved from 50 mg/ml to 150 mg/ml. It was conducive to the growth of water droplets and the gradual formation of a HBPMFs with larger pore size[141]. In this stage, the primarily influence was attributed to the concentration of SBS/$CHCl_3$ solution, so the increase in evaporation time helps the formation of pores of a bigger size. As shown in **Figure 3.7 (m-p)**, the average pore size was reduced to 1.28 μm and the buckled width tended to decrease (~110 μm) with the further increase of brick solution concentration because the solvent evaporation process cools the fiber surface[142]. The time needed for evaporation increased as the concentration of the polymer solution was increased because of the solution's increased viscosity, decreased evaporation rate, and reduced temperature differential due to heat absorption during

evaporation. However, as demonstrated in **Figure 3.7 (q-t)**, the buckled width and pore size were both largest at a concentration of 250mg/ml as compared to other concentrations. The biggest pore size (1.96 μm) was achieved by increasing the concentration of the brick solution, which substantially decreased its fluidity and allowed for a greater number of water droplets to self-assemble on the surface[143,144]. When the temperature difference between the surface of PU fiber and ambience was decreased, water droplets that have self-assembled on them evaporated more slowly, and the resulted interaction between the two caused the development of larger pore diameters. Comparing the pore size distributions and buckling effects of HBPMFs at various concentrations showed that the 150 mg/ml concentration of SBS/$CHCl_3$ solution exhibited the most regular pore size distribution and the most preferred buckling morphology with respect to the buckled of human finger joints. Therefore, the SBS/$CHCl_3$ solution was set at an optimal concentration of 150 mg/ml for HBPMFs.

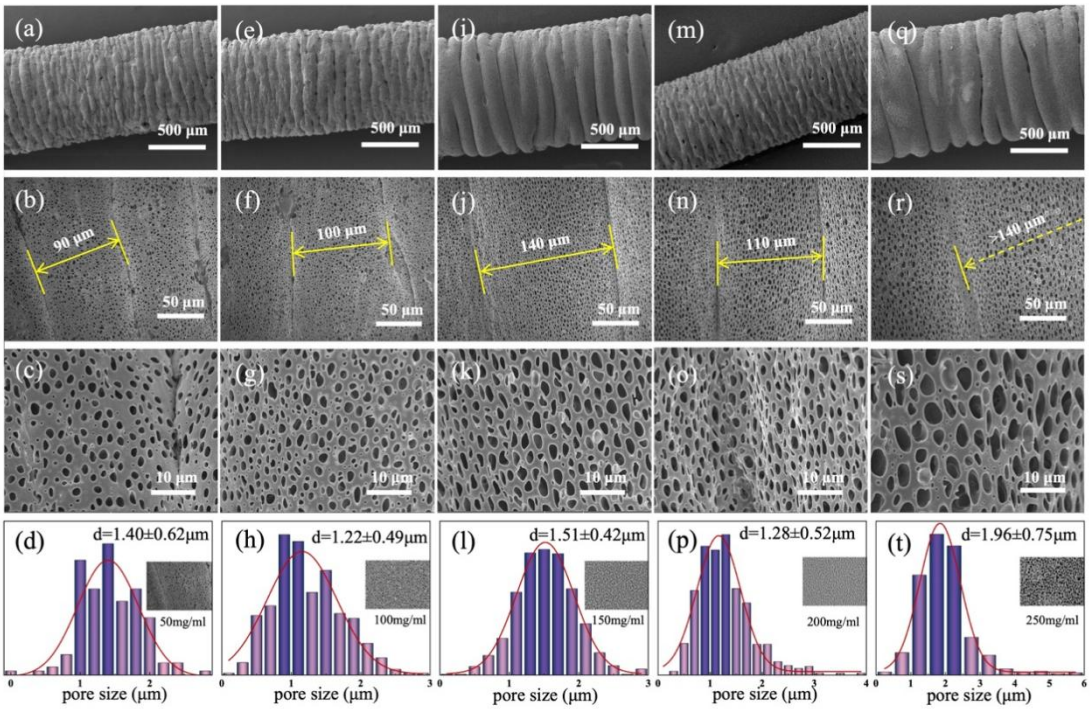

Figure 3.7 Typical SEM images and pore size distributions of HBPMFs prepared with different concentrations of SBS/$CHCl_3$ solutions and PU fibers. (a-d) 50 mg/ml, (e-h) 100 mg/ml, (i-l) 150 mg/ml, (m-p) 200 mg/ml, (q-t) 250 mg/ml.

3.3.4 Influence of pre-stretching strain for HBPMFs

In addition to ambient conditions, material systems and solution concentrations, the pre-stretching strain of elastic fibers will also have a significant effect on hierarchically buckled porous microstructures of HBPMFs. To investigate the influence of pre-stretching, various HBPMFs with different pre-stretching ratios were prepared and evaluated, where PU fiber was mechanically controlled and held at a tensile strain of 20-140%. In brief, the stretched PU fiber was immersed in 150 mg/ml SBS/$CHCl_3$ solution for swelling and quickly transferred to a high-humidity environment (RH >90%) for the self-assembly process. The stretching-releasing rate was set at 1 mm/s by a home-made stepper. When the pre-stretching ratio is <40%, the buckling structure of the HBPMFs can be not observed (**Figure 3.8**). As the pre-stretching ratio of the PU fibers was increased, the buckling effect became more apparent. In **Figure 3.10 (a-c)**, when the pre-stretching ratio reached 60%, the polmer brick layer of HBPMFs (i.e. SBS layer) exhibited some planar folding rather than the knuckle skin-like buckling, and the pore size is an average of 1.98 μm (**Figure 3.9**). As the pre-stretching ratio was increased to 80%, the SBS layer looked closer to the finger joint skin-like buckling, and the average pore size reached about 2.38 μm (**Figure 3.10 (d-f)** and **3.9**). When the pre-stretching ratio was further increased to 100%, the surface of PU fiber presented optimal finger joint skin-like buckling features (**Figure 3.10 (g-i)**), and the average pore size (2.37 μm) was similar to that of the PU fiber with a pre-

streching strain of 80%, but the pore size range was the most uniform. At a stretching ratio of 120%, the buckled structure became irregular, and the pores attained their maximum average size of 2.89 μm (**Figure 3.10 (j-l)** and **3.9**), which may be ascribed to the increased tensile pore size caused by the folding intensification. When the pre-streching strain exceeds 120%, some cracks emerged in the buckling portion because the interaction force between polymer brick materials and fiber substrates decreases slightly (**Figure 3.10 (m-o)**), and the average pore size was decreased to the minimum value of 1.54 μm (**Figure 3.9**). The results showed that pre-stretching strains not only affect the formation of skin-like buckling but also determine the average pore size of microstructures. And the ratio of pre-stretching grows from 20% to 100%, the buckled structure becomes more obvious, and the buckled structure increases the diameter of the fiber, which gradually increases from the diameter 0.89 mm corresponding to the pre-stretching ratio of 40% to 0.91 mm when the pre-stretching ratio is 100%. And further, when the pre-stretch ratio is increased from 100% to 140%, the irregularity of the buckled structure results in erratic variations in the diameter of the same fiber, which is maintained at roughly 0.91 mm. Considering the structural integrity, the optimal pre-stretching ratio was set at 100%. The successful fabrication of HBPMFs provided optimal circumstances for subsequent loading and application of functional materials.

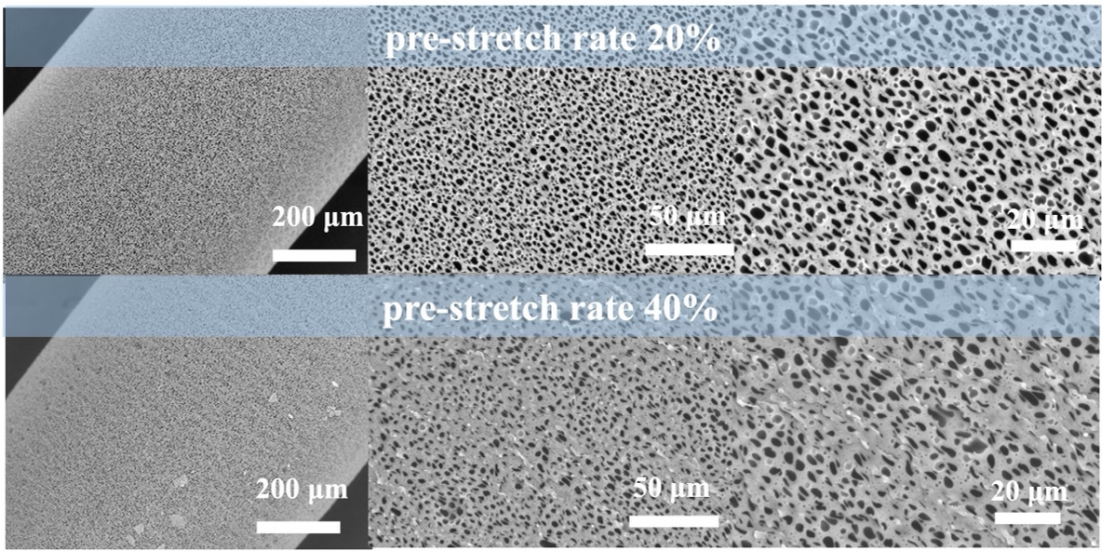

Figure 3.8 Results on the HBPMFs with pre-stretching ratio of 20% and 40%, respectively. PU fiber and SBS/$CHCl_3$ served as fiber substrate and polymer brick solution, respectively.

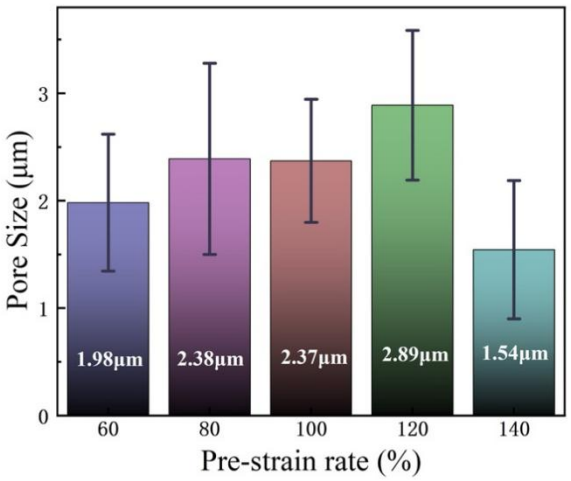

Figure 3.9 The average pore size of HBPMFs under different pre-stretching ratios. PU fiber and SBS/$CHCl_3$ served as fiber substrate and polymer brick solution, respectively.

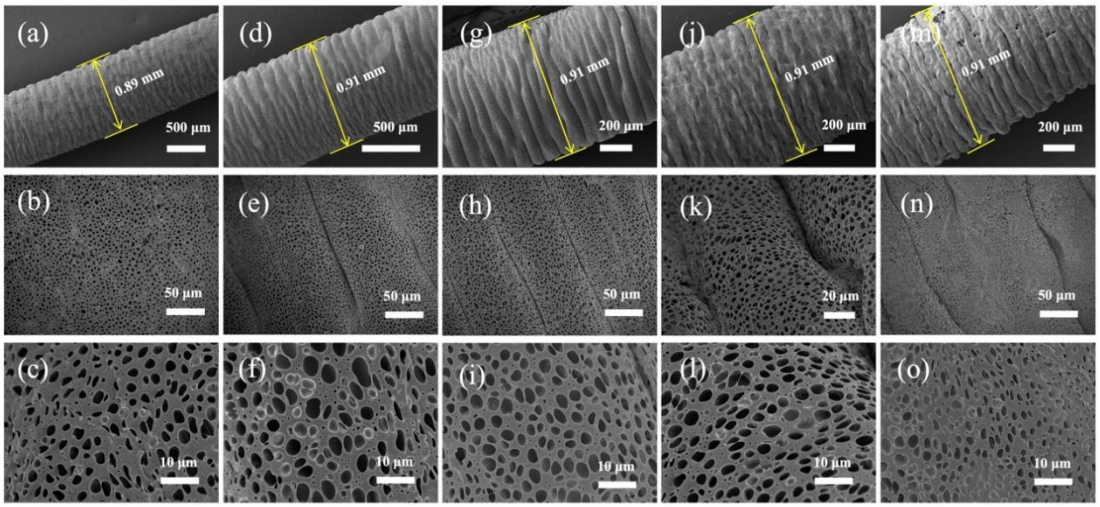

Figure 3.10 SEM images and surface morphologies of HBPMFs prepared with SBS/$CHCl_3$ (150 mg/ml) and PU fibers under various pre-stretching strains. (a-c) pre-stretching of 60%, (d-f) pre-stretching of 80%, (g-i) pre-stretching of 100%, (j-l) pre-stretching of 120%, (m-o) pre-stretching of 140%.

Moreover, morphology changes of HBPMFs were also recorded and studied by SEM to investigate their mechanical properties and durability. At the initial state (i.e., a tensile strain of 0%), the HBPMFs made from PU fiber and SBS/$CHCl_3$ exhibited an obvious finger joint skin-like buckling feature and conformal porous microstructures (**Figure 3.11 (a-b)**). When the HBPMFs was stretched to 100% of the initial length, the hierarchical buckling structure was extended to a smooth surface accompanied by porous microstructures (**Figure 3.11 (c-d)**). This phenomenon is similar to that the skin of finger joints fold and expansion as the joints move. However, the HBPMFs made from PU fiber and PMMA/$CHCl_3$ showed a poor performance as compared to that of SBS/$CHCl_3$ and a mechanical failure occurred at PMMA layers, when it was stretched to 100% of the initial length (**Figure 3.11 (e-f)**). This is because PMMA lacks sufficient elasticity as compared to SBS. Moreover, on the base of PU and rubber fiber, the HBPMFs made from SBS/$CHCl_3$ and PMMA/$CHCl_3$ were also performed with the

stretching-releasing process of 100 cycles respectively to investigate their durability. As shown in **Figure 3.12 (a)-(b)**, the HBPMFs made from PU and rubber fiber showed excellent durability and stable surface morphologies after 100 cycles of stretching-releasing, when SBS/$CHCl_3$ was selected as the polymer brick solution. The robust mechanical stability is attributed to the synergistic effect of highly elastic materials (PU fiber and SBS polymer) and thermal annealing. As a contrast, the HBPMFs based on PU fiber and PMMA/$CHCl_3$ presented weak mechanical strength and rupture of polymer layers after 100 tensile cycles due to the poor stretchability of PMMA (**Figure 3.12 (c)**).

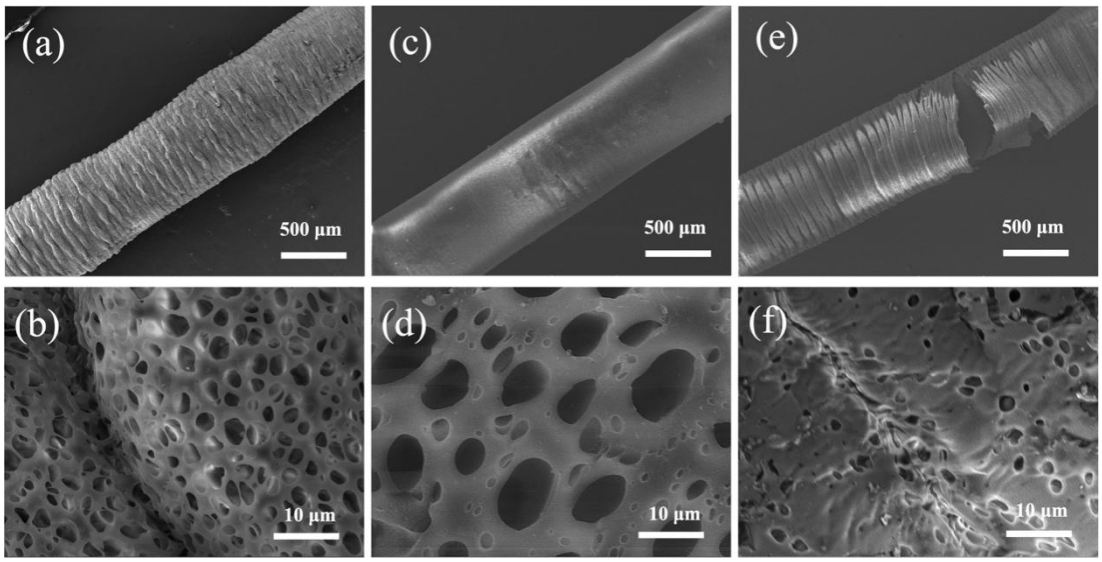

Figure 3.11 The morphology of the HBPMFs fixed at different tensile strains. Different magnification SEM images: (a, b) HBPMFs prepared with PU fibers and SBS/$CHCl_3$ at 0% tensile strain. (c, d) HBPMFs prepared with PU fibers and SBS/$CHCl_3$ at 100% tensile strain (e, f) HBPMFs prepared with PU fibers and PMMA/$CHCl_3$ at 100% tensile strain.

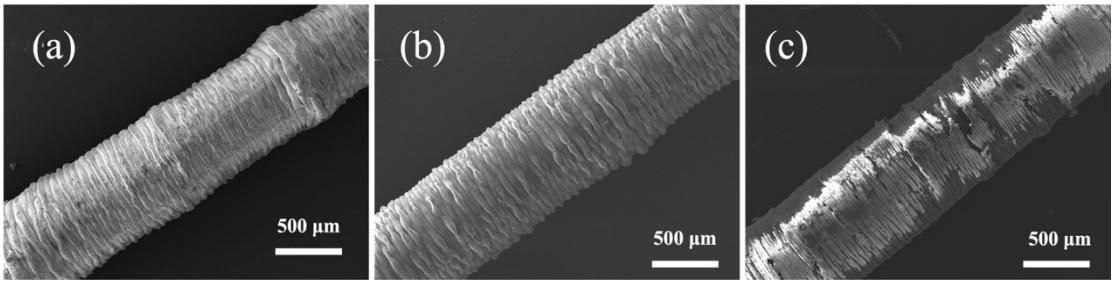

Figure 3.12 Morphologies of the HBPMFs after 100 times of stretching-releasing at 100%. (a) HBPMFs prepared with PU fibers and SBS/$CHCl_3$. (b) HBPMFs prepared with rubber fibers and SBS/$CHCl_3$. (c) HBPMFs prepared with PU fibers and PMMA/$CHCl_3$.

3.3.5 Development of CAFMFs based on the prepared HBPMFs

Nanoparticles such as TiO_2 NPs, Ag NPs, Cu NPs and ZnO NPs were proved to be efficient functional materials. The in-situ integration of these nanoparticles on the surface or framework of carriers with porous structures can largely prevent from the aggregation of nanoparticles during fabrication and enlarge exposed surface area for high performance. By adding functionality to HBPMFs, we can develop a series of CAFMFs with improved properties and increased possible applications. In this study, TiO_2 NPs, Ag NPs, Cu NPs and ZnO NPs were used to investigate the viability and adaptability of the HBPMFs technique for directly fabricating CAFMFs with incorporation of different functional nano-additives with elastic fibers. Different NPs were mixed with the SBS/$CHCl_3$ polymer solution to form mixed suspension for fabricating CAFMFs (**Figure 3.15**). Moreover, two other kinds of functional fibers were also prepared for the comparison, namely solid coating functional fibers (SCFFs) and porous coating functional fibers without buckling structures (PCFFs), as shown in **Figure 3.13** and **S14**.

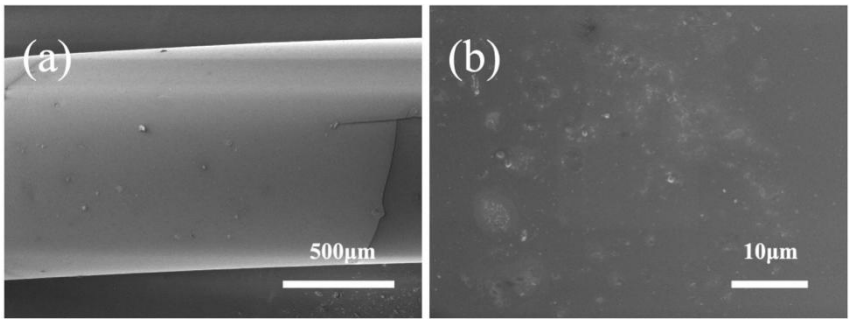

Figure 3.13 SEM images and surface morphologies of SCFFs based on PU fiber and SBS/$CHCl_3$. The concertation of polymer brick solution was 150 mg/ml.

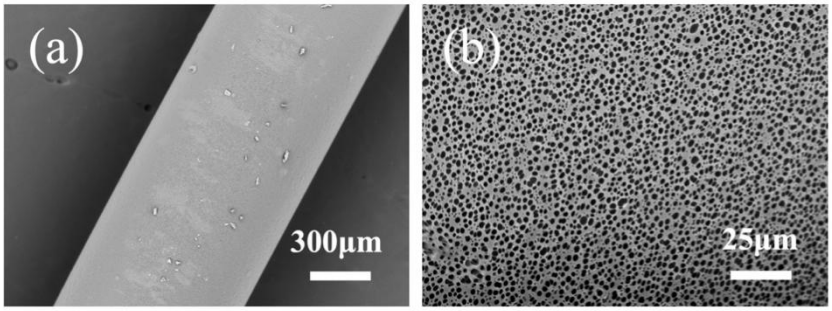

Figure 3.14 SEM images and surface morphologies of PCFFs based on PU fiber and SBS/$CHCl_3$. The concertation of polymer brick solution was 150 mg/ml.

In **Figure 3.15**, the synergistic effect and pickering emulsion effect[145,146] facilitate the nanocomponents to self-assemble at the droplet-solution interface during the buckled formation process of HBPMFs. Larger specific surface area would be achieved by preserving the porous structure and introducing the skin-like buckling of fibers prepared by the proposed fabrication strategy. The enlarged specific surface area is beneficial to the loading of functional nanocomponents. When the nanocomponents are incorporated into the surface of the fiber using the conventional solid coating method (**Figure 3.15 (b)**), the surface of SCFFs will not create a porous structure, and the nanocomponents will tend to aggregate among themselves (**Figure 3.13**). When the solvent was evaporated, the nano-additives were permanently a portion of the coating. In **Figure 3.15 (c)**, the nanocomponents can also be evenly distributed in porous surfaces of PCFFs by exploiting the created porous microstructures. Although PCFFs can utilize the porous surfaces to integrate nanocomponents, their functionalities would be greatly reduced due to the lack of buckling structures as compared to HBPMFs. Meanwhile, the performance of PCFFs and its application fields will also be greatly affected under the large strain conditions. As seen in **Figure 3.15**, HBPMFs owns the

largest exposed surface area than that of SCFFs and PCFFs under the same length condition, allowing more and effective loading of functional nanoparticles for enhanced performance. BET tests on HBPMFs and PCFFs were conducted to investigate the impact of bucked porous microstructure on the specific surface area of fibers. HBPMFs have a specific surface area that is roughly twice more than that of PCFFs. For porous structure fibers without pre-stretching treatment, the specific surface area is only 846.676 m^2/g, but the specific surface area of HBPMFs is significantly increased, reaching 1,235.47 m^2/g (**Figure 3.16**).

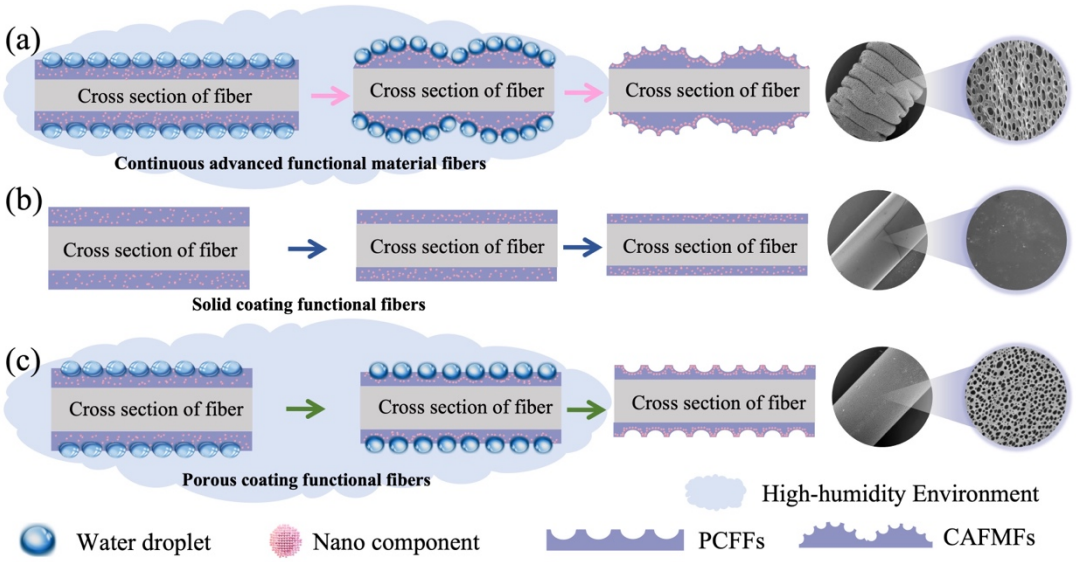

Figure 3.15 Schematic cross-sectional diagrams of nanocomponents loaded on HBPMFs (a), SCFFs (b), and PCFFs (c).

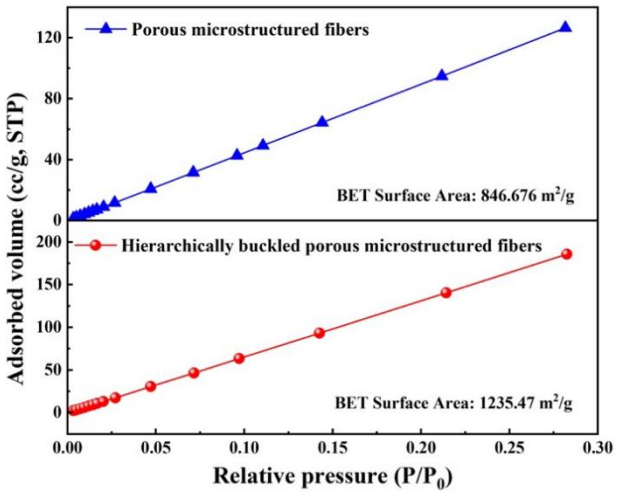

Figure 3.16 The BET surface curves of porous microstructured fibers and hierarchically buckled porous microstructured fibers.

To further investigate the formation of CAFMFs from HBPMFs, different nanoparticles filled SBS/$CHCl_3$ solutions with various doping mass ratios were prepared, including TiO_2 NPs (1:20 wt%), Ag NPs (1:40 wt%), Cu NPs (1:60 wt%) and ZnO NPs (1:80 wt%), respectively. **Figure 3.17 (a)**, **(d)**, **(g)**, and **(j)** showed that all CAFMF samples have a hierarchically skin-like buckled structure, indicating that different nanoparticles do not impede the formation of the buckled porous microstructures. As seen in **Figure 3.17 (b)-(l)**, all functional nanoparticles were successfully incorporated to HBPMFs with a slight variation of pore sizes due to the influence of different doping nanoparticles. In addition, it was found that the doped nanoparticles slightly increased the pore sizes of prepared CAFMFs as compared to HBPMFs, which is probably due to that the hydrophilic properties of those nanoparticles can promote the attaching capacity of water droplets on the polymer surface of HBPMFs.

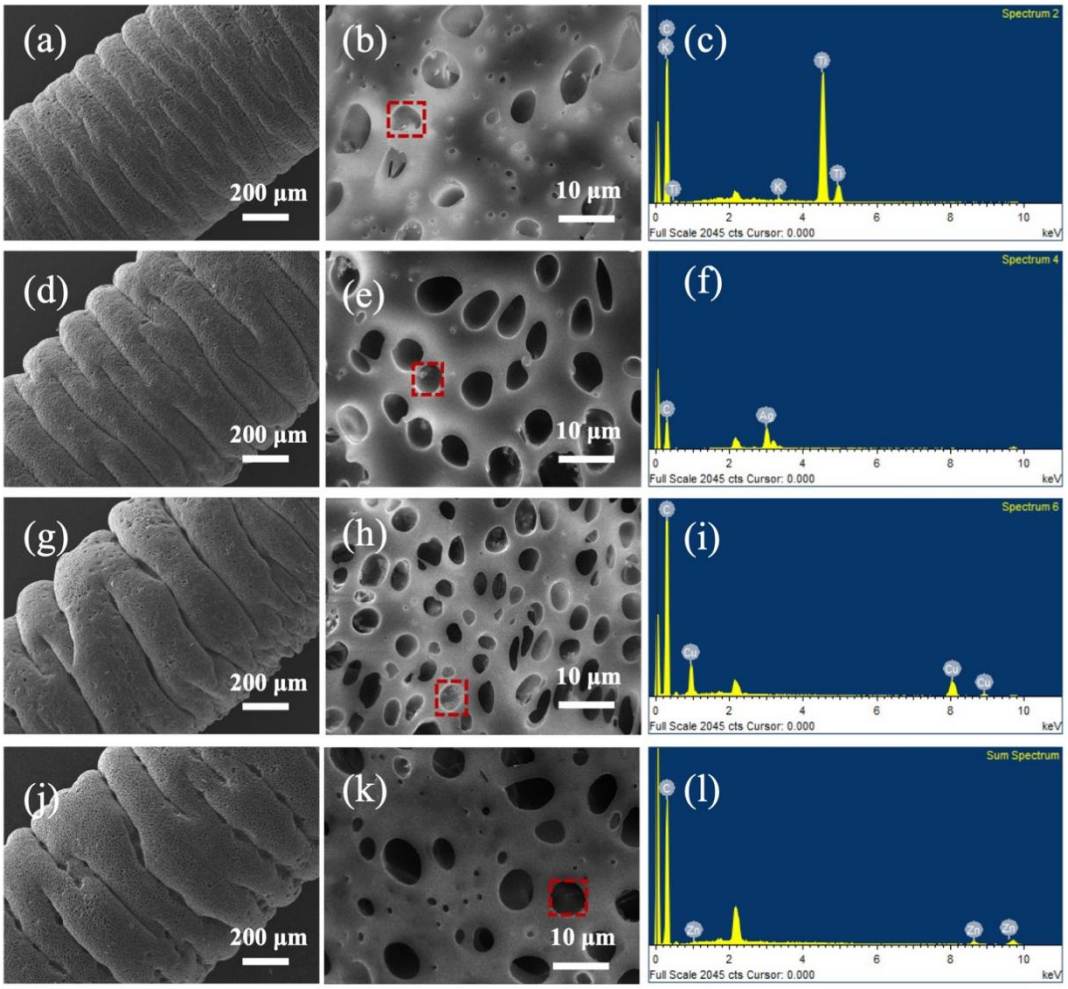

Figure 3.17 SEM images and EDS spectra of different CAFMFs. Different magnification SEM images of TiO_2/HBPMFs (a) and (b), Ag/HBPMFs (d) and (e), Cu/HBPMFs (g) and (h), and ZnO/HBPMFs (j) and (k), respectively. Corresponding EDS spectra for TiO_2/HBPMFs (c), Ag/HBPMFs (f), Cu/HBPMFs (i), and ZnO/HBPMFs (l), respectively.

3.3.6 Photocatalytic application of CAFMFs

As demonstration of application, CAFMFs were employed for photocatalytic degradation of organic pollutants in this this study. The TiO_2 photocatalyst possesses the advantages of non-toxicity, broad application, low cost, reusability, and no secondary pollution in the reaction at room temperature, and it exhibits outstanding results in the treatment of biodegradable industrial effluent[147]. Nevertheless, the powdered TiO_2 photocatalyst is susceptible to agglomeration and loss, which raises the

cost of TiO_2 photocatalysis. Fixing, reusing, and exposing the catalytic surface of powdered TiO_2 have therefore become the subject of research[148]. As shown in **Figure 3.18**, CAFMFs, that were, TiO_2 incorporated HBPMFs (TiO_2/HBPMFs), were utilized as catalysts for the efficient removal of organic pollutants. Considering its skin-inspired buckling features and porous microstructures of CAFMFs, the contact area between the catalyst and the pollutant was significantly enhanced, which not only increases the photocatalytic efficacy but also enables the reuse of the immobilized TiO_2 particles and the efficient and cost-effective degradation of organic pollutants. As control groups, TiO_2 incorporated SCFFs (TiO_2/SCFFs) and PCFFs (TiO_2/PCFFs) were also employed to perform photocatalytic degradation of organic pollutants. Methylene blue (MB) and neutral red (NR) were degraded by these three kinds of functional fiber to evaluate their photocatalytic degradation capacities. **Figure 3.18 (a)** shows their different degradation efficiencies. The degrading efficiency of TiO_2/HBPMFs reached 99%, which was significantly higher than TiO_2/PCFFs of 80% and TiO_2/SCFFs of 60%. Cyclic studies of MB degradation were further carried out by using TiO_2/HBPMFs under UV light. The reacting TiO_2/HBPMFs was collected, cleaned for several times with ethanol and distilled water, and then put to the initial MB solution for 6 hours of degrading under UV light irradiation. **Figure 3.18 (b)** showed the cycling properties of the TiO_2/HBPMFs for the degradation of MB. After five cycles, the absorbance was increased from 0.07 abs. to 0.16 abs. (**Figure 3.18 (c)**), and the degradation efficiency was reduced from 99% to 89.0% (**Figure 3.18 (b)**). As shown in **Figure 3.18 (d-f)**, TiO_2/HBPMFs have the best performance of photocatalytic degradation than that of

TiO_2/PCFFs and TiO_2/SCFFs, where the concentration of MB was reduced from the initial 1.508 abs. to 0.09 abs. after 6 hours (**Figure 3.18 (d)**). The color of samples (inset in **Figure 3.18 (d)** were changed from an initially deep blue to a nearly transparent solution. Both TiO_2/PCFFs and TiO_2/SCFFs contributed to the decolorization of MB from an initial absorbances of 1.508 abs. to 0.3 abs. and 0.5 abs., respectively, as shown in **Figure 3.18 (e)** and **(f)**.

Similar results were also obtained when NR was employed as target pollutant. **Figure 3.18 (g)** illustrates the degrading efficiency of the three functional fibers. TiO_2/HBPMFs still exhibited the highest rate of degrading efficiency of 97% after six hours of UV light exposure as compared to that of TiO_2/PCFFs and TiO_2/SCFFs (80% and 65% respectively). After re-washing the TiO_2/HBPMFs, the photocatalytic adsorption of NR solution was repeated for five times under the same conditions, and the rate of decolorization remained above 89% (**Figure 3.18 (h)**). This indicates that the photocatalytic degradation performance of TiO_2/HBPMFs was relatively stable, and the absorbance was increased from 0.07 abs. to 0.156 abs. (**Figure 3.18 (i)**). **Figure 3.18 (j)** demonstrates that the absorbance spectra of NR at the concentration of 1.65×10^{-5} M in the presence of TiO_2/HBPMFs. The inserted photo in **Figure 3.18 (j)** showed the NR solution was nearly transparent after 6h of degradation, indicating TiO_2/HBPMFs has good photocatalytic degradation capacity for NR. As a contrast, TiO_2/PCFFs and TiO_2/SCFFs exhibited relatively poor photocatalytic degradation properties, and the inset of **Figure 3.18 (k)** and **(l)** demonstrates that NR solution was not well degraded after 6 h with its red color still discernible. The photocatalytic degradation of the as-

prepared CAFMFs is merely one of many potential applications, HBPMFs can be integrated with different advanced functional materials (e.g. triboelectric, electroactive, and conductive materials) to develop other CAFMFs with various functionalities for energy harvesting, energy storage and flexible circuits in the future.

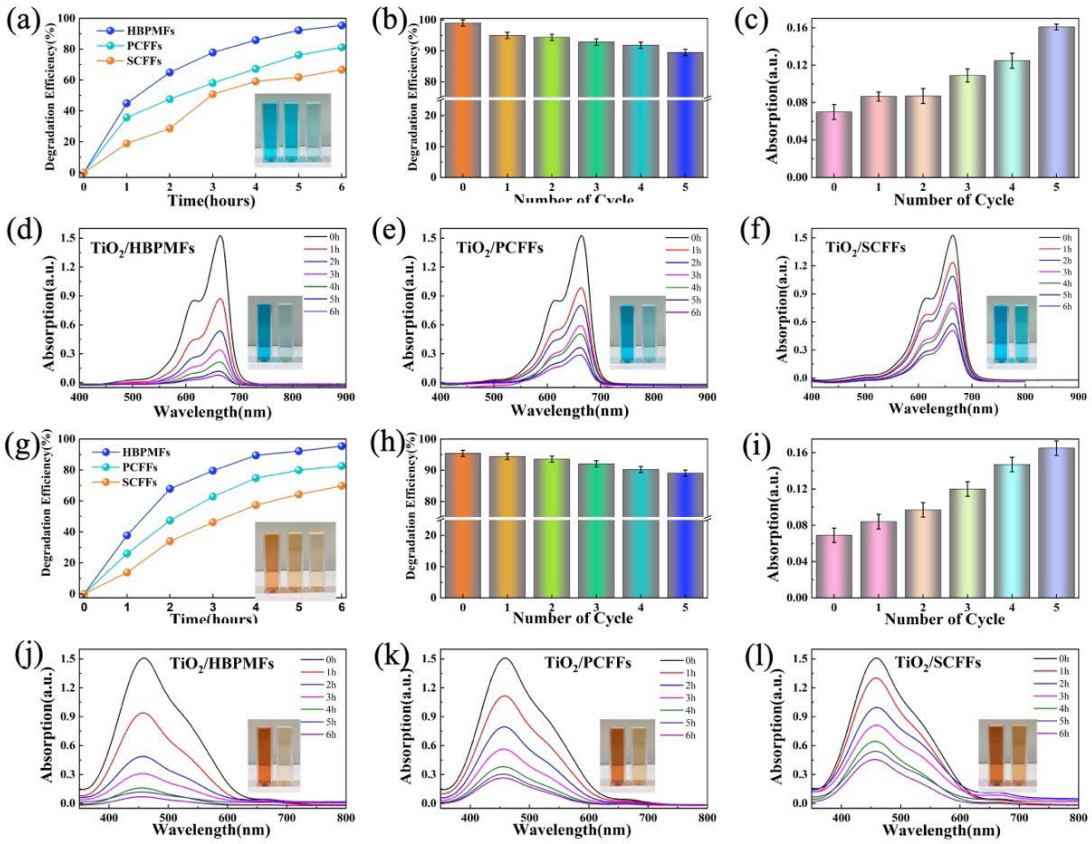

Figure 3.18 Photocatalytic degradation capacities and comparison of different functional fibers for organic pollutants. (a) and (g) The degradation efficiency profiles of MB and NR of different samples. (b) and (h) The photocatalytic degradation efficiency of MB and NR using by TiO_2/HBPMFs in five cycles of testing. (c) and (i) UV-vis absorption values of MB and NR using by TiO_2/HBPMFs in five cycles of testing. UV-vis absorption spectra of MB and NR at different durations of degradation in the presence of: (d) and (j) TiO_2/HBPMFs, (e) and (k) TiO_2/PCFFs, (f) and (l) TiO_2/SCFFs, where insets were digital photographs of MB and NR aqueous solution before and after 6 h of UV irradiation.

3.4 Conclusion

In summary, inspired by the surface buckling of finger joint skin, we designed and fabricated a novel kind of hierarchically buckled stretchable porous microstructured

fibers (HBPMFs) based on a general physicochemical strategy consisted of material systems manipulation, interfacial self-assembly, stretching-releasing control, and thermal annealing. By elaborately investigating the experimental parameters consisting of polymer bricks, solution concentration, solvent types, and fiber substrates, the obtained HBPMFs retained hierarchically skin-like buckled and conformal porous microarchitectures simultaneously, possessing superior advantages of stretchable porous microarchitectures and more exposed porous surface area, which contribute to enhanced electrical output performance of the triboelectric nanogenerator. It was also found that the pre-stretching ratio of elastic fibers plays an important role in the formation of surface buckling. Furthermore, different functional nanomaterials can also be directly incorporated into hierarchically buckled porous microstructures of HBPMFs for forming a new type of hybrid CAFMFs with customized functionalities. Meanwhile, benefiting from the enlarged specific porous surface area introduced by skin-like buckling, the HBPMFs become more effective in incorporating functional nanomaterials. As a demonstration of application, CAFMFs with incorporation of TiO_2 nanoparticles exhibited significantly enhanced photocatalytic performance of organic pollutants than the control samples. This proposed strategy of HBPMFs was expected to extend the application fields of advanced functional fibers with enhanced and customized performance.

Chapter 4 Hierarchically Porous Architectured Stretchable Fibrous Materials in Energy Harvesting and Self-powered Sensing

4.1 Introduction

Advanced functional fibrous materials that combine intrinsic properties of textiles and customized functionalities have attracted more and more attentions in next-generation intelligent wearables, such as personal healthcare, human–machine interfaces, soft robotics, and so forth[149–153]. Elastic fabrics with their unique stretchability and flexibility have become the ideal platform for wearable electronic devices[153–159]. However, with the continuous expansion of application scenarios, the great challenge of AFFMs is to effectively integrate fibrous materials and functional component to fulfill both stretchability and functionality. To address these issues, effort has been devoted to developing stretchable AFFMs by different strategies. For instance, Liu et al. fabricated stretchable sheath-core fibers with carbon nanotube sheets as the sheath and rubber fiber as the elastic core[160]. Meng et al. reported multi-functional fibres with a coil-structure by inserting a giant twist into spandex-core fibres wrapped in a carbon nanotube sheath[55]. Though these fibers have achieved good stretchability and functionality, the complex preparation process limits their further application. Moreover, the simple surface structure of these fibers lacks an effective conjunction channel with the additive functional nanomaterials.

Porous materials that possess a number of intrinsic properties including high specific surface area, large pore volume, tunable pore size and shape, have great

application potential in many fields, especially with surface or interface-related processes [161–166]. Breath figure (BF) technique[126,127,167], a surface self-assembly method with simplicity, low cost, and high tunability that forms ordered honeycomb-like porous structures on the surface of materials using environmental water droplets as dynamic templates, has shown great application prospects in smart textiles. The porous structures[132,168,169] prepared through the BF technique not only significantly increase the specific surface area of the textiles but also enhance the active sites of reactive nanomaterials, thereby greatly enhancing their functionality[170]. Therefore, the effective combination of buckled features and porous structure will make them more widespread and influential in wearable devices in virtue of their high surface area and excellent mechanical adaptability. Recently, research showed that flexible and stretchable TENGs have broad prospects in energy harvesting and self-powered sensors. For example, through innovative manufacturing methods, such as laser etching and crumpling method, have shown significant potential in preparing high-precision structures and achieving multi-functional integration [171]. At the same time, independent stretch sensing platforms, such as systems based on human motion, biofuels, and radio frequency drive, are constantly expanding the application boundaries of smart wearable devices. In the aspect of multi-modal sensors, it achieves high-precision independent detection of multiple physical quantities by optimizing material and structural design. They are widely used in fields such as flexible electronics, wearable devices, and smart medical care, significantly improving the versatility and reliability of devices [172].

Herein, we have designed and developed a novel stretchable hierarchically buckled porous microstructure fabric (HBPMFs) using elastic commercial textile and polystyreneblock-polybutadiene-block-polystyrene triblock copolymer (SBS) by a surface self-assembly method. The influential factors on the architecture, characteristics, and performance of HBPMFs are investigated to optimize the surface buckled porous microstructures, including pre-stretching ratio, swelling time, self-assembly condition, annealing temperature and tensile-release rate. The buckled porous microstructures endow HBPMFs with high capacity for loading various nanoparticles containing TiO_2, $BaTiO_3$ and Ag. Based on the optimized HBPMFs, fabric-based TENGs (HBPMFs-TENGs) are designed and assembled with nanoparticles loaded HBPMFs as a tribo-positive layer, silicon rubber as a tribo-negative layer and polyacrylamide hydrogel as an elastic electrode. Results showed that the charge of the triboelectric performance of Ag@HBPMFs-TENG is 6 times higher than that of the original elastic fabric. As a sustainable power source, Ag@HBPMFs-TENG can efficiently drive electronic watches, digital calculators, and light-emitting diodes (LEDs) by efficiently harvesting biomechanical energy. As a wearable self-powered sensor, Ag@HBPMFs-TENG can also detect subtle expressions, breathing, and human movements. The obtained HBPMFs are expected to have great potential in wearable electronic textiles.

4.2. Experimental Section

4.2.1 Materials

Polystyrene-block-polybutadiene-block-polystyrene triblock copolymer (SBS, MW~133,800, ≥99.5%), Poly(methyl methacrylate) (PMMA, MW ~120,000,

≥99.5%) and chloroform ($CHCl_3$, anhydrous, ≥99.9%), carbon disulfide (CS_2, anhydrous, ≥99.9%), tetrahydrofuran (THF, ≥99.9%), acrylamide (AAm), 2-Hydroxy-40(2-hydroxyethoxy)-2-methylpropiophenone (Irgacure 2959), 20 kDa PEGDA, N, N-methylenebisacrylamide (MBAA), methanol, benzophenone(BP) and Lithium chloride (LiCl) were purchased from Sigma-Aldrich Co. Ecoflex 00-30 was purchased from SMOOTH ON, Inc.. Titanium dioxide nanoparticles (TiO_2 NPs, 17-30 nm), Barium titanate nanoparticles ($BaTiO_3$ NPs, 50nm), and silver nanoparticles (Ag NPs，3μm) were purchased from XFNANO, Inc.. 180gsm knitted 90 polyester 10 spandex stretch fabric were provided by a local textile company. All materials were used directly without further processing.

4.2.2 Formation of different HBPMFs

For the fabrication of HBPMFs, the concentration of different brick solutions (SBS/$CHCl_3$, SBS/CS_2, SBS/THF, and PMMA/$CHCl_3$) were fixed at 50 to 250 mg/. Then the cleaned elastic textiles were pre-stretched to 40% to 140%. In the following format hierarchical buckled microstructure process, to guarantee the complete recovery of the elastic textiles and the formation of a well-organized single-sided buckled structure, the ecoflex material performed an insufficient curd process and adhered to a single surface of the textiles. The operations were conducted in a high relative humidity environment. The fixed pre-stretching ratio elastic fabrics were immersed into various polymer brick solutions for 30s and selective swelling to achieve the dip-coating process. Then the fabric substrates coated with polymer bricks were drawn vertically out of brick solutions for internal self-assembly between the brick polymer and the

water droplet. After waiting one minute, the pre-stretched elastic fabrics were then released at a stable rate of 1 mm/s. The modified fabrics were removed from a high humidity environment, and the surface water droplets of the fabrics were quickly evaporated to form porous honeycomb microstructures on the polymer surface of elastic fabrics. Finally, the as-prepared buckled elastic textiles were put into a thermal annealing environment at the glass transition temperature of the respective brick material to remove the stress effect and avoid interfacial peeling failure. Advanced functional material fabrics, solid coating fabrics (SCFs), and porous coating fabrics without buckling structures (PCFs) were also prepared for comparison. For the fabrication of advanced functional material fabrics, various nanoparticles (e.g., TiO_2 NPs, $BaTiO_3$ NPs, and Ag NPs) were introduced into the SBS/$CHCl_3$ solution, respectively, with a concentration of 200 mg/ml to form the hybrid suspension. The mass ratio of additives/polymer was set at 1 wt% for TiO_2 NPs, 10 wt% for $BaTiO_3$ NPs, and 0.4 wt% for Ag NPs, respectively. Advanced functional material fabrics were also prepared in the same process of HBPMFs with a pre-stretching strain. SCFs and PCFs were also designed to not pre-stretch at 10% and 90% humidity, respectively.

4.2.3 Fabrication of TENGs

Making flexible Polyacrylamide (PAAm) hydrogel electrodes in conjunction with HBPMFs is a component of TENG manufacturing. Then spraying the ecoflex material, the HBPMTs were spraying again a solution containing benzophenone (10 wt.% in ethanol). The fabrics underwent a triple methanol washing process followed by thorough drying. Eventually, UV light was employed to crosslinker the assembly of the

PAAm hydrogel onto a specific surface of the peeling ecoflex textiles. PAAm typical hydrogel was prepared by directly curing the degassed pre-gel solution (23 wt.% AAm, 0.051 wt.% MBAA, 0.2 wt.% Irgacure 2959 and 8M LiCl).

4.2.4 Characterization and evaluation

The surface morphologies of samples were characterized by SEM (VEGA3**)** under 5 kV after being coated with a thin layer of gold. The elemental composition of advanced functional material fabrics was analyzed by using SEM equipped with an Energy-dispersive X-ray spectroscopy (EDX). The XRD pattern was performed on a Bruker X-ray diffractometer (D8 Advance) with Cu Kα radiation. FTIR absorption spectra were carried out on a Perkin Elmer spectrometer (Spectrum 100). Tensile/compression measurements were performed on a universal tensile testing machine (Instron 4411). Electrical performances of TENG under different applied forces, frequencies and different sample tensile ratios were evaluated by a button/key durability life test machine (ZX-A03, Zhongxingda, Shenzhen) equipped with a high-speed self-configuring digital indicator (Interface 9860). The open-circuit voltage, short-circuit current, and short-circuit charge transfer were recorded by an electrometer (Keithley 6514, Tektronix). The instantaneous power density of the TENG was calculated by $P = I^2R/A$, where P was the power density, I was the output current, R was the corresponding external load resistance, and A is the size of TENG, which was 10 cm^2, respectively. The size of the sensor was sated as 1cm × 1cm. Motion monitoring was carried out with the assistance of a volunteer (one of the authors of this article). The study was approved by the Human Subjects Ethics Sub-committee of Hong

Kong Polytechnic University and informed written consent was also obtained from the volunteer.

4.3 Results and Discussion

4.3.1 Design and fabrication of HBPMFs

In this work, we have developed a novel strategy for fabricating hierarchically buckled porous microstructure fabrics (HBPMFs). These fabrics exhibit a unique surface morphology with buckling, porosity, and hierarchical microarchitecture. A notable feature of HBPMFs is their fusion of good stretchability and buckled porosity, enabling the embedding of functional nanoparticles to enhance textile functionalities (**Figure 4.1 (a) I**). The pre-stretching ratio of elastic fabrics is a crucial component in creating buckled characteristics for HBPMFs. The porous microstructure formation is significantly influenced by the polymer solution's evaporation dynamics and the rough texture of the underlying fabric. The polymer brick solution's propensity for rapid evaporation, coupled with the environmental humidity, leads to the formation of water droplets on the fabric's surface. In a high humidity environment, water droplets will form on the surface of the polymer brick-coated fabrics with the evaporation of the solvent at a low boiling point and high volatility in the polymer brick solutions. The construction of porous structures is shown in Figure S1(b) I to IV, where (1) the rapid evaporation of a solvent with a low boiling point promotes the formation of moisture and small water droplets on the surface of the polymer solution through nucleation; (2) as the water droplets grow and self-assemble, they arrange themselves in an ordered and densely packed array, covering the entire surface of the polymer solution; and (3)

the evaporation of both the water droplets and the solvent leads to the formation of dry polymer layers on the fabrics, characterized by hexagonal pore arrays. The as-made fabric was further annealed at the glass transition temperature of the respective brick material to eliminate the stress effect and interfacial peeling failure. The optimized details on HBPMFs will be discussed in the following sections.

In brief, a commercially elastic fabric is pre-stretched to a specific rate and cast with brick polymer solution in a highly humid environment (**Figure 4.1 (a) II** and **Figure 4.2 (a-b)**). Then, the pre-processed elastic fabric is released at a controlled rate at an annealing temperature (i.e. glass phase transition temperature, Tg) of brick polymer to obtain HBPMFs. The resultant HBPMFs surface keeps inherent textile features and can be deformed randomly, such as distorting, stretching, and folding (**Figure 4.1 (b)**). Thanks to the unique surface microstructure, HBPMFs can be an ideal candidate for integrating with functional materials to achieve promising applications, such as HBPMFs-based conductive smart textiles. As a demonstration, **Figure 4.2 (c)** shows the integration process of HBPMFs and hydrogel. In brief, silicon layer (Ecoflex) and photo-crosslinking agent (BP) are sprayed on one side of HBPMFs in turn to improve its adhesive capability with hydrogel, and then acrylamide (AAm) monomer is photopolymerized to form PAAm hydrogel layer on the surface of HBPMFs. A certain amount of LiCl is used as a conductive agent to improve the ionic conductivity of hydrogel. The molecular structure of the hydrogel and the magnified diagram of HBPMFs integrated with PAAm hydrogel are depicted in **Figure 4.1 (a) III** and **IV**, respectively. **Figure 4.1 (c)** shows that the hydrogel surface can tolerate different

deformations, indicating a strong interfacial interaction is established between HBPMFs and PAAm hydrogel. Moreover, the high water retention of PAAm/LiCl hydrogel is conducive to maintaining conductivity for a long time, keeping stable electric performance.

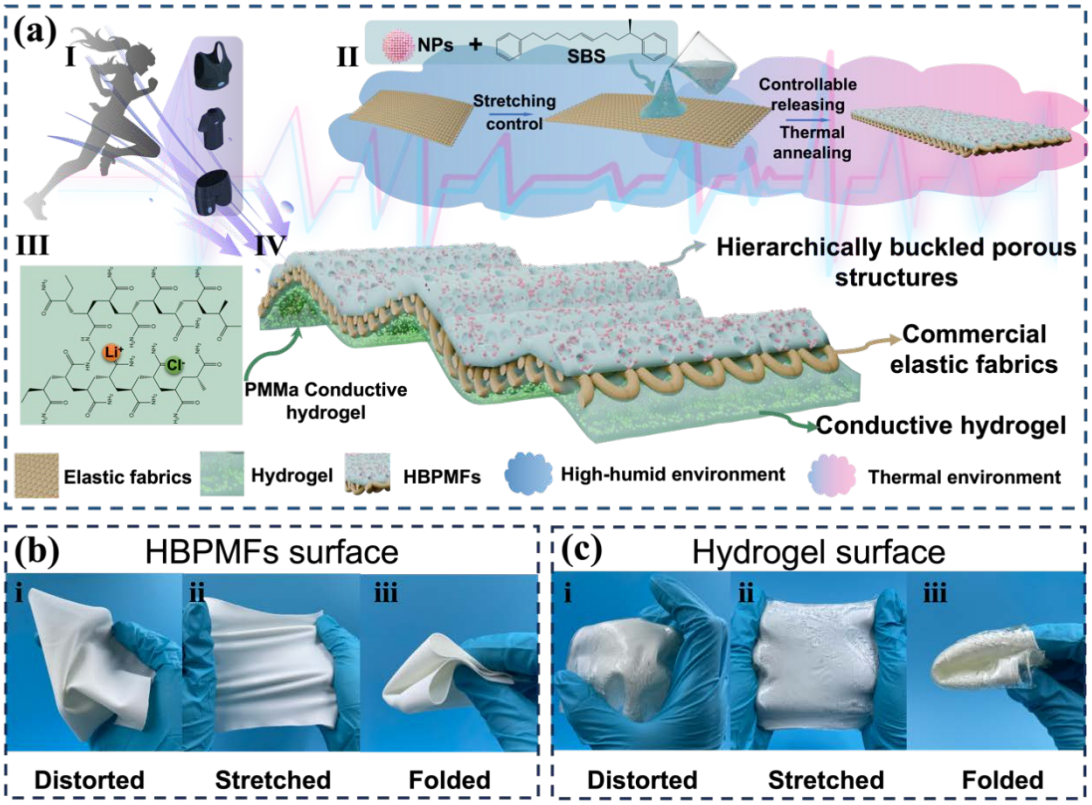

Figure 4.1 Design and fabrication of HBPMFs. (a) Design, fabrication and potential application of HBPMFs. Photographs of (b) HBPMFs surface and (c) hydrogel surface under different deformations, including distorted (i), stretched (ii), folded (iii) status.

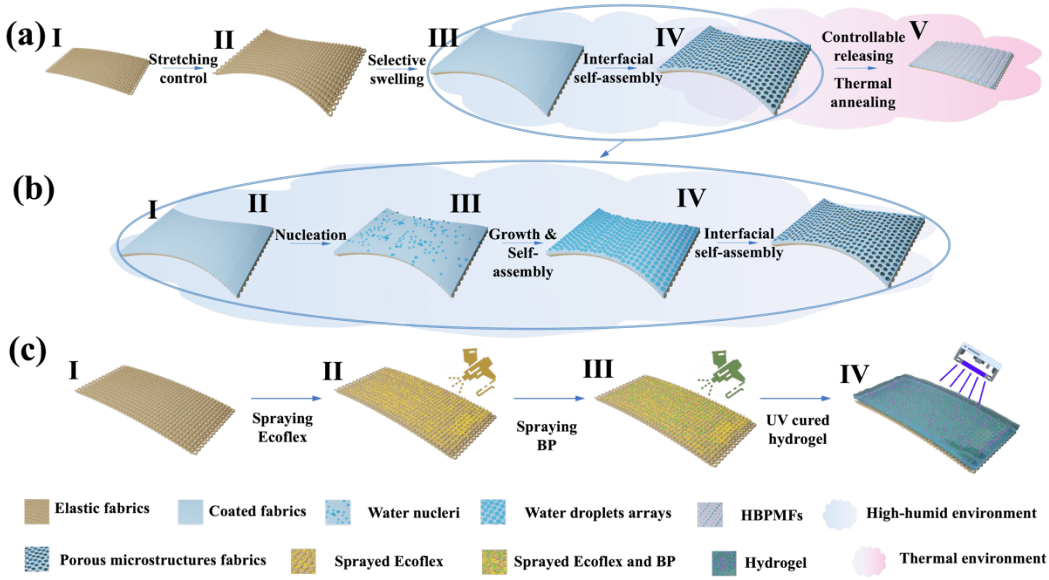

Figure 4.2 Fabrication of HBPMFs. (a) and (b) the fabrication process of HBPMFs. (c) the fabrication process of the conductive hydrogel.

4.3.2 Influence of material systems and durability test for HBPMFs

The buckled porous microstructures strongly rely on various influence factors, such as material systems, self-assembly process, pre-stretching ratio and thermal annealing. To clarify the factors affecting the surface morphology of HBPMFs, we investigated their self-assembling buckled and porous microstructures across different solute and solvent conditions (materials systems), with a constant pre-stretching ratio of 120% and thermal annealing temperature. Considering the formation condition[136,137], organic solvents used to dissolve the elastic brick polymers are nonaqueous and highly volatile. Therefore, SBS and PMMA solutes, and $CHCl_3$, CS_2 and THF solvents are used to prepare buckled and porous microstructures. **Figure 4.3 (a)** and **(b)** show the surface morphologies of HBPMFs prepared with 200 mg/ml SBS/$CHCl_3$. Thanks to the pre-stretching process of the elastic fabric substrate, the uniform buckled structure of

HBPMFs is observed (**Figure 4.3 (a)**), and the surface of HBPMFs maintains a uniform and closely arranged porous structure (**Figure 4.3 (b)**). The cross section of HBPMFs (**Figure 4.3 (c)**) shows a clear sandwich-like structure, comprising an upper SBS casting layer, a middle elastic fabric interlayer, and a lower hydrogel layer, indicating the capability of elastic fabrics to act as structural 'bridges' for enhanced stability. The hydrogel is seamlessly integrated with HBPMFs, which makes the sandwich-like structure particularly suitable for flexible stretchability and arbitaray tailoring (**Figure 4.4**).

To study the influence of the solvent on the surface structure, different solvents such as CS_2 and THF are also employed to dissolve SBS and further prepare HBPMFs. Although the buckled structure of HBPMFs can be obtained in 200mg/ml SBS/CS_2 brick solution (**Figure 4.5 (a)** and **(b)**), it results in large pores and less uniformity compared to those produced using SBS/$CHCl_3$ of HBPMFs. This is because CS_2, having a lower boiling point and greater volatility than $CHCl_3$, reduces the temperature of the polymer surface, leading to the aggregation of large water droplets on the polymer surface[140,173]. When CS_2 was used to dissolve SBS, the porous templates formed by water droplets were larger than those using $CHCl_3$, resulting in a relatively larger pore size of HBPMFs. During the self-assembling preparation process of formation ordered and disordered porous structure (**Figure 4.6**), solvent volatilization speed impacted the final porous structure. In **Figure 4.6 (b)**, the water droplets adsorbed in the solution are in a state of rapid nucleation and growth, which is not conducive to uniform droplet size. The droplets remain in a thermodynamically unstable state, with

varying fusion speeds of the droplets, which results in an inconsistent final porous structure. The higher boiling point of $CHCl_3$ relative to CS_2 leads to a more stable thermodynamic state and enhanced stabilization of water droplets in a 200mg/ml SBS/$CHCl_3$ solution, compared to a similar concentration of SBS/CS_2. Consequently, the SBS/$CHCl_3$ solution forms more uniformly porous structures than the SBS/CS_2 solution at equivalent concentrations.

In addition to the volatility of organic solvents, the polarity of organic solvents can also affect the pore regularity of HBPMFs. When 200mg/ml SBS/THF is selected as the brick solution, the buckled structure is obvious (**Figure 4.5 (c)**), but the SBS layer with an ordered porous structure cannot be obtained (**Figure 4.5 (d)**). This is because THF has a specific mutual solubility with water, and the relative density of THF is smaller than that of water[138,174]. In the evaporating process, the SBS film surfaces fuse THF solvent with water droplets to form an intertwined and disordered network structure. Therefore, $CHCl_3$ is identified as the preferred solvent for fabricating porous and buckled HBPMFs via the self-assembling SBS copolymers on elastic fabrics.

The solutes (i.e. brick polymer materials) will also play a vital role in the surface structure of HBPMFs. The surface morphology of HBPMFs with 200 mg/ml PMMA/$CHCl_3$ was also investigated. A regular buckled surface with small pore size and low porosity is obtained under a pre-stretching of 120% (**Figure 4.5 (e)** and **(f)**). Considering the requirement of high stretchability and complex deformation, PMMA with limited flexibility may not be the preferred material for building HBPMFs. Therefore, the formation condition of the porous structure of HBPMFs can be attributed

to the following (**Figure 4.6 (a)**): (i) the solvent is immiscible with water; (ii) the volatilization of solvent, an endothermic process, when coupled with the optimal concentration of brick polymer, can produce a suitable temperature difference at the fabric surface; and (iii) in a high-humidity environment, the surface of fabric effectively condenses water vapor, facilitating orderly nucleation and growth of water droplets, leading to a porous structure with the uniform arrangement and size.

To demonstrate the structure stability, the durability tests of HBPMFs with different brick solutions were conducted through cyclic stretching-releasing procedures, extending the HBPMFs from 0 to 125%. After 100 stretching-releasing cycles, the buckled and porous microstructures of HBPMFs with SBS/$CHCl_3$ brick solution remain intact (**Figure 4.3 (d)** and **(e)**), and its cross-section SEM (**Figure 4.3 (f)**) indicates that functional layers also maintain a tight connection. We further carried out tensile-release cycles of HBPMFs at a stretching ratio of 125%. The test demonstrates HBPMFs can still maintain their mechanical properties even at a higher cycle number of 1,000, demonstrating stable durability and reliability (**Figure 4.7**). When HBPMF was casted with 200mg/ml SBS/CS_2, its buckled and porous structures remained as initial (**Figure 4.5 (g)** and **(h)**). The HBPMFs cast with 200mg/ml SBS/THF brick solution maintained their original structure (**Figure 4.5 (i)** and **(j)**). While using PMMA/$CHCl_3$ as the brick solution, the HBPMFs has poor cycling stretchability due to its intrinsic low elasticity. **Figure 4.5 (k)** and **(l)** show that the buckled structure cracked when the HBPMF was stretched to 30%, and the elastic fabric substrate was exposed. The stress-strain tests of SBS/$CHCl_3$ HBPMFs were recorded to investigate their high elasticity, rebound

resilience, and structural stability. As shown in **Figure 4.3 (g)**, tensile strain-modulus curves maintain an upward trend across various strain ratios from 25% to 125%. The photographs of strained HBPMFs with different stretching ratio are shown in the insets of **Figure 4.3 (g)**. The results indicate that HBPMFs has good rebound resilience and structural stability, which are significant for the performances of corresponding TENGs. To further investigate the tensile properties and stability, the cycling stress-strain tests of HBPMFs were measured at different stretching ratios. As shown in **Figure 4.3 (h)**, the tensile-strain curves of HBPMFs exhibit excellent cycling stability at different strain ratios from 25% to 125%. The good mechanical properties of HBPMFs are attributed to the formation of strong interfacial binding force among buckled porous structure SBS layer, elastic fabric substrate and hydrogel.

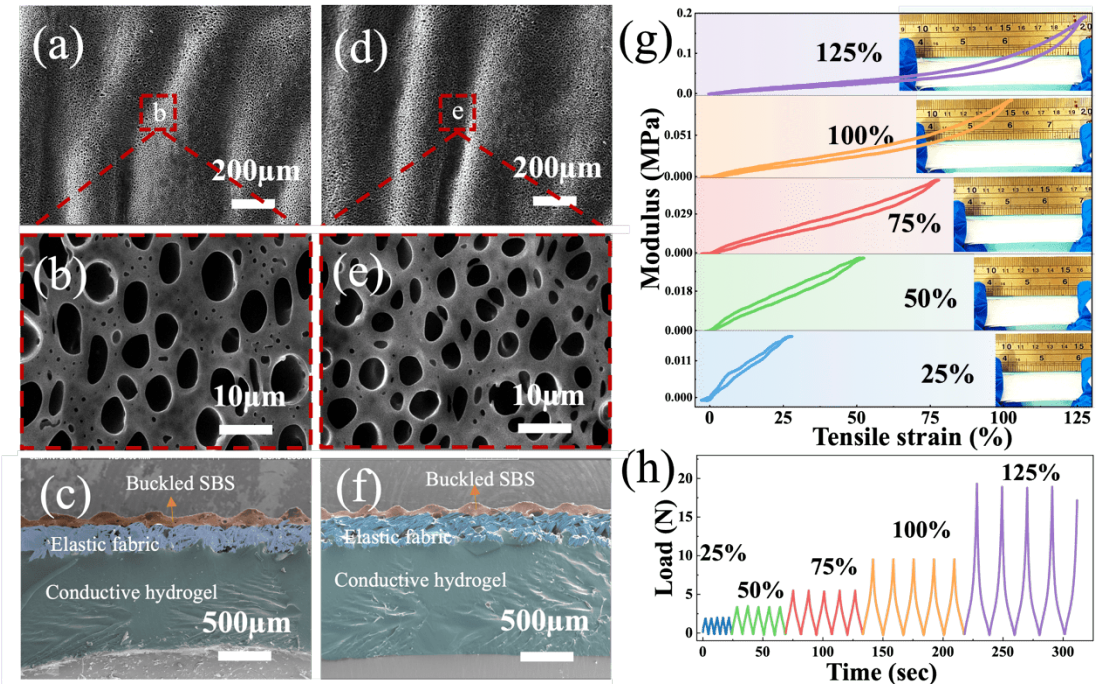

Figure 4.3 Typical surface and cross section features and various magnification SEM images prepared with 200mg/ml SBS/$CHCl_3$. Before (a-c) and after (d-f) 100 times of stretching-releasing at 100%. (g) Stress–strain curve of HBPMFs casted SBS/$CHCl_3$. The inset shows photos of different ratio strained HBPMFs. (h) HBPMFs under 5 cyclic stretch/release from 0 to 125% strain radio.

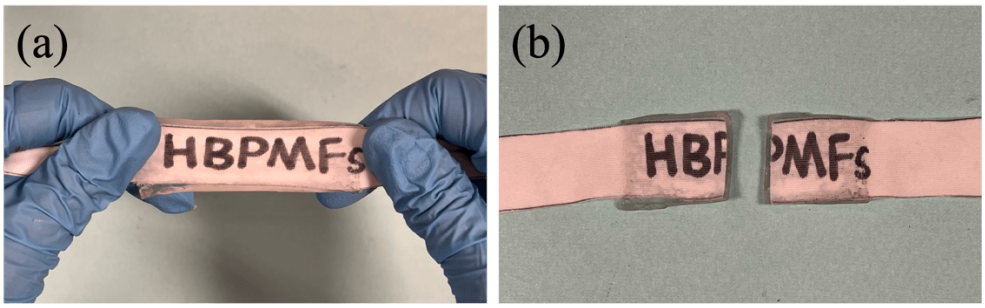

Figure 4.4 The arbitrary tailoring photo of HBPMFs. Before (a) and after (b) tailor.

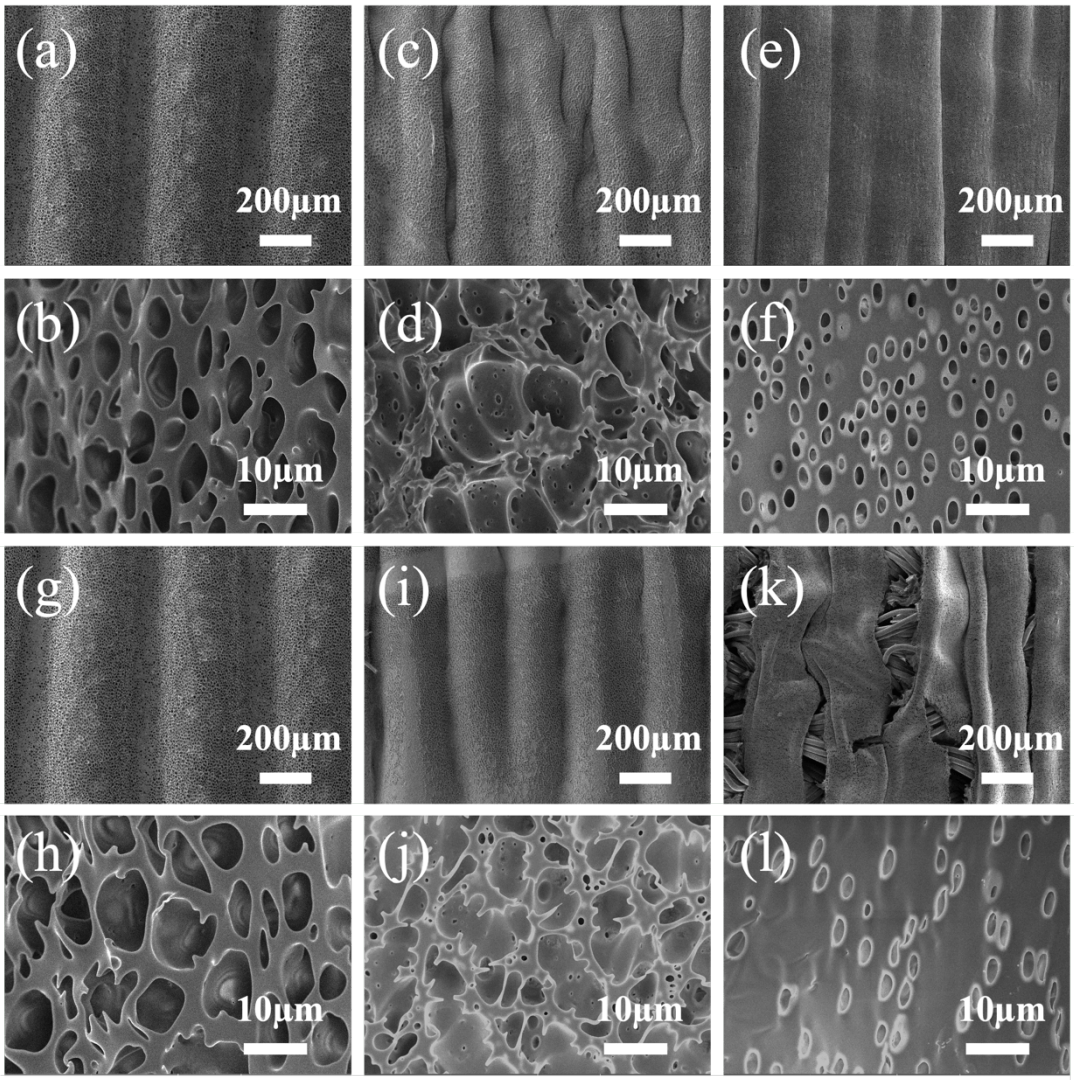

Figure 4.5 Typical surface features and various magnification SEM images prepared with different solutes and solvents. And after 100 times of stretching-releasing at 120%. (a, b) 200mg/ml SBS/CS_2 and (g, h) after 100 times of stretching-releasing at 100%, (c, d) 200mg/ml SBS/THF and (i, j) after 100 times of stretching-releasing at 100%. (e, f) PMMA/$CHCl_3$ and (k, l) after 100 times of stretching-releasing at 100%.

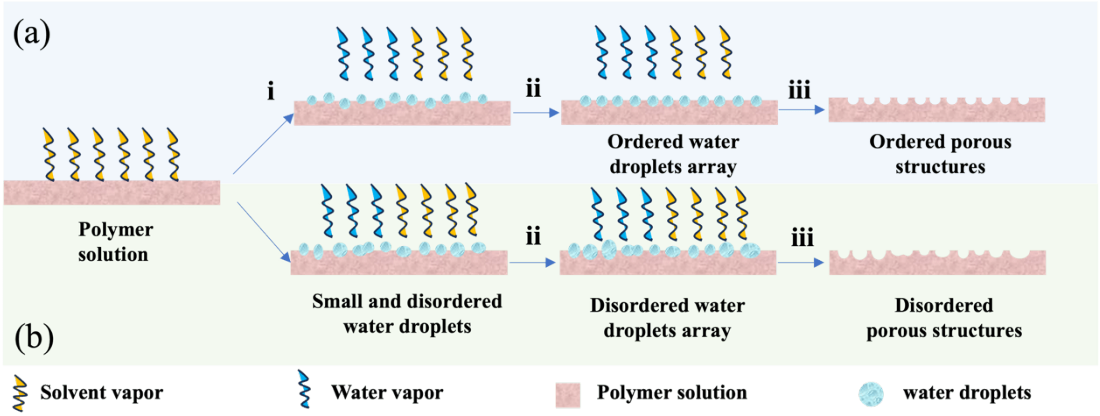

Figure 4.6 Formation mechanism for ordered and disordered structures.

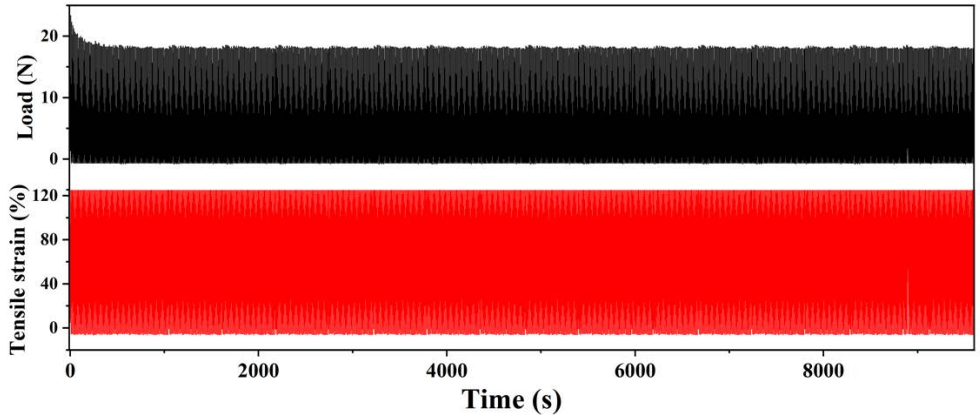

Figure 4.7 Tensile cycling 1,000 tests of HBPMFs.

4.3.3 Influence of solution concentrations and pre-stretching strain for HBPMFs

The morphology of HBPMFs is significantly influenced by the concentration of SBS/$CHCl_3$ solutions and the pre-stretching strain applied during fabrication. **Figure 4.8 (a-h)** and **Figure 4.9** and **4.10** show the surface morphologies of HBPMFs made from different SBS/$CHCl_3$ solution concentrations under a pre-stretching of 120%. When 50 mg/ml SBS/$CHCl_3$ is used to prepare the HBPMFs, the fabric's original surface texture remains partially obscured. This results in a non-uniform distribution of

buckled structures and a heterogeneous pore size (**Figure 4.9**). This discrepancy can be attributed to the high proportion of the solute, which prolongs the duration of the condensation process. A low solute concentration is insufficient to stabilize water droplets on the fabrics. An effective and simple way to solve this problem is to gradually increase the concentration of the casting solution. Increasing the solution concentration to 100 mg/ml facilitates the development of continuous porous structures on the textile surface. However, the process results in a somewhat disordered arrangement of buckled microstructures, attributable to the solution's limited covering capability (**Figure 4.8 (a)** and **(b)**, and **4.10 (a)**). The elevation in solute concentration aids in supporting the condensation of water droplets on the fabric surface, facilitating the formation of the observed structures. When the solution concentration increased to 150 mg/ml (**Figure 4.8 (c)**, **(d)**), the fabric surface was wrapped by SBS layer, and the morphology was changed from the intrinsic fabric texture to a buckled microstructure. As shown in **Figure 4.8 (c)**, combined with the characteristics of the buckled formation, the coating ridges appear to have continuous gradients and regular distribution. The overall coating surface showed a dense and regular morphology. Raising the concentration makes it easier for water droplets to form and stay on the fabric surface, developing buckled and porous structures. With the increase in solution concentration, the porous microstructure on the fabric surface appears uniform, orderly and densely arranged (**Figure 4.10 (b)**). The rounded porous structure shown in **Figure 4.8 (d)** results from the pre-stretching of the fabrics, which exerts minimal mechanical stress on forming the shape of the porous structure, compared to other modification processes using

solutions at less than 150 mg/ml concentrations. When the solution concentration is 200 mg/ml (**Figure 4.8 (e)**, **(f)** and **4.10 (c)**), it is found that a more regular porous structure is formed conformally and continuously over the textile substrate's irregular surface contours, regardless of the areas with large height differences and severe bending. The topography of buckled structures is more prominent, the porous size is more consistent, and the distribution is more even. By selecting an optimal solution concentration, water droplets are induced to condense on the fabric surface, and release heat to compensate for the heat absorbed by volatilization to achieve a balance. At 250 mg/ml, however, the buckled structure becomes irregular. This irregularity arises from uniform pores during solvent evaporation at higher solution concentrations (**Figure 4.8 (g)**, **(h)** and **4.10 (d)**). These results indicate that identifying the optimal concentration of the casting solution is essential for developing brick materials characterized by continuously buckled microstructures on textile substrates. By adjusting the solution concentration and self-assembly technology, buckled porous microstructures can be well introduced on textile substrates.

In addition, the pre-stretch ratio of the elastic fabric substrate also greatly influences the form of the buckled and porous microstructure. Therefore, the morphologies of HBPMFs made from 200 mg/ml SBS/$CHCl_3$ under different pre-stretching ratios are studied (**Figure 4.8 (i-p)** and **4.11**). The pre-stretch ratio is set from 0% to 140%. **Figure 4.8(i, j)** shows the surface morphology of fabric coated by SBS without pre-stretching. The surface porous structure of fabric has slight unevenness, which is caused by the complex texture structure of the elastic fabric. It can be found that the stretching ratio

of 40% (**Figure 4.11 (a**, **b)**) has a buckled microstructure similar to that of HBPMFs without stretching. When the pre-stretch ratio is increased to 60% (**Figure 4.8 (k**, **l)**), the buckled structure begins to appear, but it cannot completely get rid of the influence of the original fabric structure. As the pre-stretching ratio increases (80%, 100% and 120%), the buckled structure becomes increasingly obvious, as shown in **Figure 4.11 (c-f)** and **4.8 (m, n)**. HBPMFs with a pre-stretching ratio of ⩽120% have a complete and ordered porous structure. When the pre-stretching ratio increases to 140% (**Figure 4.8 (o**, **p)**), the porous structure exhibits deformation under compression, resulting in noticeable pore distortion. **Figure 4.8 (q)** illustrates how the buckled and porous microstructures form. In brief, when the SBS brick solution is cast into a stretched elastic fabric base, the swelling process between them makes the two closely bonded. When the elastic fabric is released, the bonding force between the two interfaces induces the formation of a buckled structure. As the pre-stretching rate increases, the shape of the porous structure of the fabricated geometric pattern gradually changes from a circle to an ellipse. This detailed observation emphasizes the crucial role of solution concentration, solvent characteristics, and pre-stretching degrees in shaping the microstructural attributes of HBPMFs. Optimizing these parameters enables control over the fabric's morphology, which is crucial for developing advanced fabrics with specific functional properties. The ideal conditions identified in this study involve a 200 mg/ml SBS/$CHCl_3$ solution concentration and a 120% pre-stretching ratio, balancing the morphological integrity and functional performance of HBPMFs.

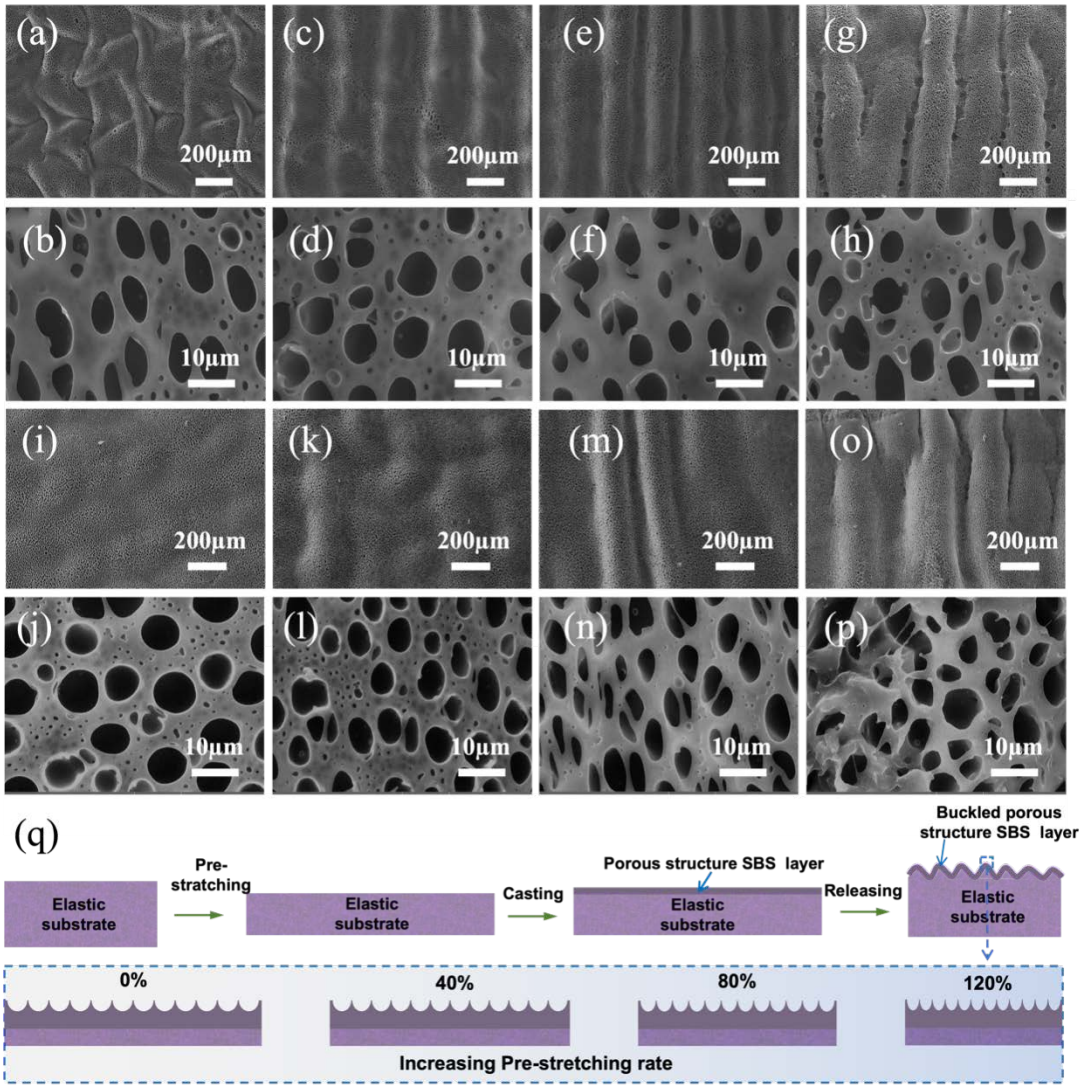

Figure 4.8 Typical SEM images of elastic fabrics prepared with different concentrations. (a, b) 100 mg/ml, (c, d) 150 mg/ml, (e, f) 200 mg/ml, (g, h) 250 mg/ml. Typical SEM images and schematic of elastic fabrics with various pre-stretching strains of 200 mg/ml SBS/$CHCl_3$ solutions and elastic fabric (i, j) not pre-stretching, (k, l) pre-stretching of 60%, (m, n) pre-stretching of 100%, (o, p) pre-stretching of 140%. (q) Schematic of the fabrication process of the buckled porous structure.

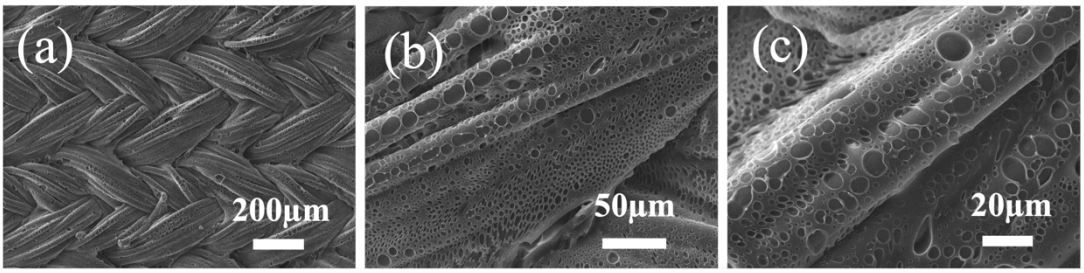

Figure 4.9 Typical SEM images of elastic textiles prepared with different concentrations of SBS/$CHCl_3$ solutions and PU fibers. (a-c) 50 mg/ml.

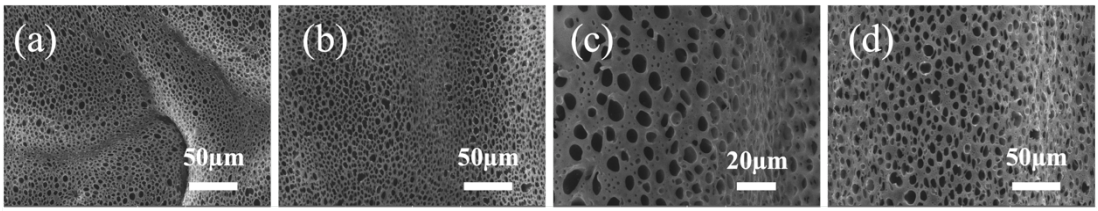

Figure 4.10 Typical SEM images of elastic textiles prepared with different concentrations of SBS/$CHCl_3$ solutions and PU fibers. (a) 100 mg/ml, (b) 150 mg/ml, (c) 200 mg/ml, (d) 250 mg/ml.

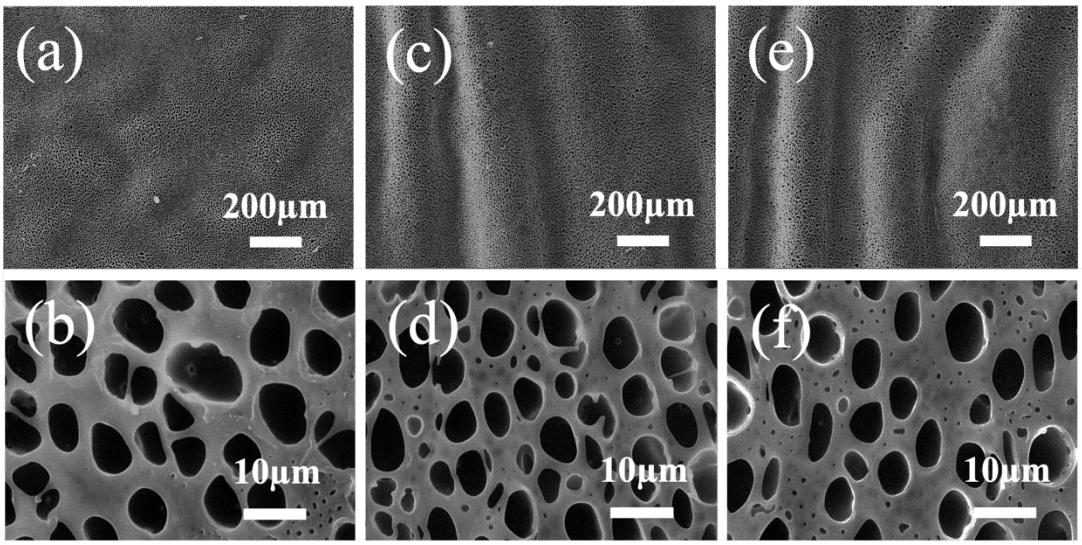

Figure 4.11 SEM images and surface morphologies of elastic textiles prepared with SBS/$CHCl_3$ (200 mg/ml) and fabrics under various pre-stretching strains. (a,b) pre-stretching of 40%, (c, d) pre-stretching of 80%, (e, f) pre-stretching of 120%.

4.3.4 Development of hybrid HBPMFs with nanoparticles

By capitalizing on the hierarchically buckled porous microstructures, HBPMFs are expected to incorporate functional materials, enabling the acquisition of specialized functionalities. In this study, TiO_2 NPs, Ag NPs, and $BaTiO_3$ NPs are employed as typical functional nanomaterials to introduce into the microstructure of HBPMFs. The HBPMFs containing functional nanoparticles can be easily prepared by blending these nanoparticles with SBS/$CHCl_3$ without other changes in the self-assembly process. Owing to the Pickering effect, nanoparticles can be uniformly dispersed into the porous

microstructure of HBPMFs without aggregation[175]. The introduced nanoparticles can help stabilize the water droplet and expand the exposed surface area of porous microstructures (**Figure 4.12**). As shown in **Figure 4.13**, the hierarchically buckled porous features of HBPMFs have no obvious interference after incorporating nanomaterials. **Figure 4.14 (a)**, **(b)** show that $BaTiO_3$ NPs can be seen in the porous structure and pore size of HBPMFs. The average pore size of $BaTiO_3$@HBPMFs is 18 μm (**Figure 4.14 (b)**). TiO_2 and Ag NPs are also evenly distributed in the pores of HBPMFs, and their average pore size is 5 and 6.8 μm (**Figure 4.14 (c-f)**), respectively.

The chemical components of HBPMFs loaded with nanoparticles were confirmed by X-ray diffraction (XRD) (**Figure 4.14 (g)**). XRD patterns show pristine HBPMFs have a broad peak at $2\theta = 18°$, assigned to SBS. In contrast, three types of nanoparticles doped HBPMFs exhibit typical diffraction peaks in respective XRD patterns, indicating nanoparticles are successfully incorporated in HBPMFs. In addition, Fourier transform infrared (FTIR) was also performed to investigate the components of nanoparticles doped HBPMFs. Three types of nanoparticles doped HBPMFs and pristine HBPMFs show similar FTIR spectra. The trans double bond hydrocarbon out-of-plane bending vibration peak in the polystyrene segment at 966 cm^{-1}, methyl scissor vibration absorption peak at 1,380cm^{-1}, skeleton vibration absorption peaks of benzene ring at 1,490 cm^{-1} and 1,450 cm^{-1}. The two side-by-side double peaks at 1,600 cm^{-1} and 1,640 cm^{-1} are also characteristic peaks of the butadiene C=C double bond. These characteristic peaks prove the existence of SBS in HBPMFs (**Figure 4.14 (h)**). The absorption peaks of three nanoparticles cannot be observed, which may be attributed to

the smaller doping amount.

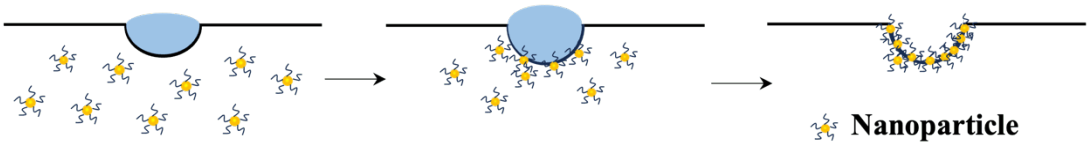

Figure 4.12 Formation of hybrid nanoparticles HBPMFs.

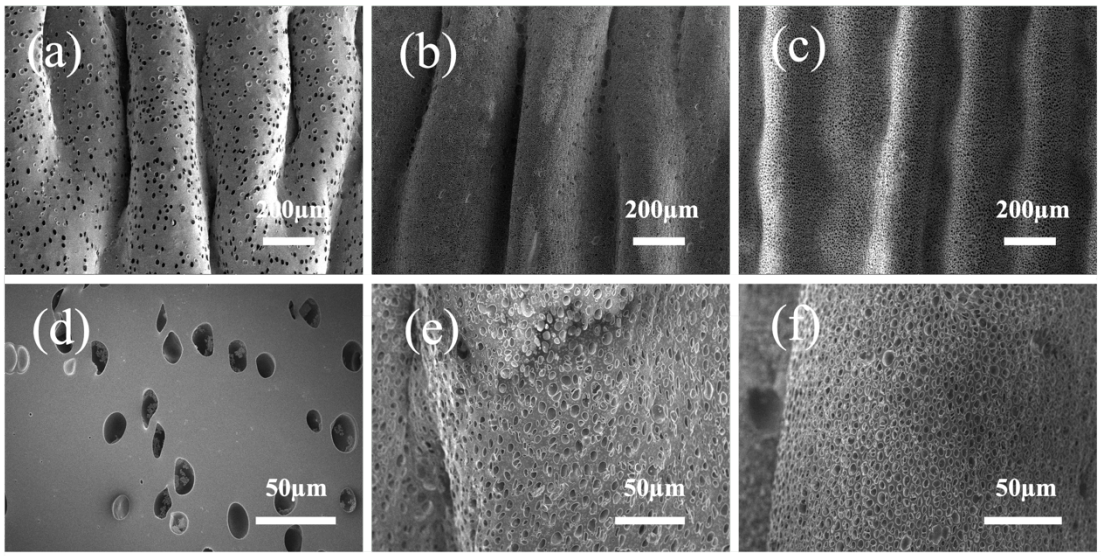

Figure 4.13 Typical SEM images of elastic textiles prepared with SBS/$CHCl_3$ solutions doping different ratio nanoparticles. (a) and (d)10 wt% $BaTiO_3$ NPs, (b) and (e)1 wt% TiO_2 NPs, (c) and (f) 0.4 wt% Ag NPs

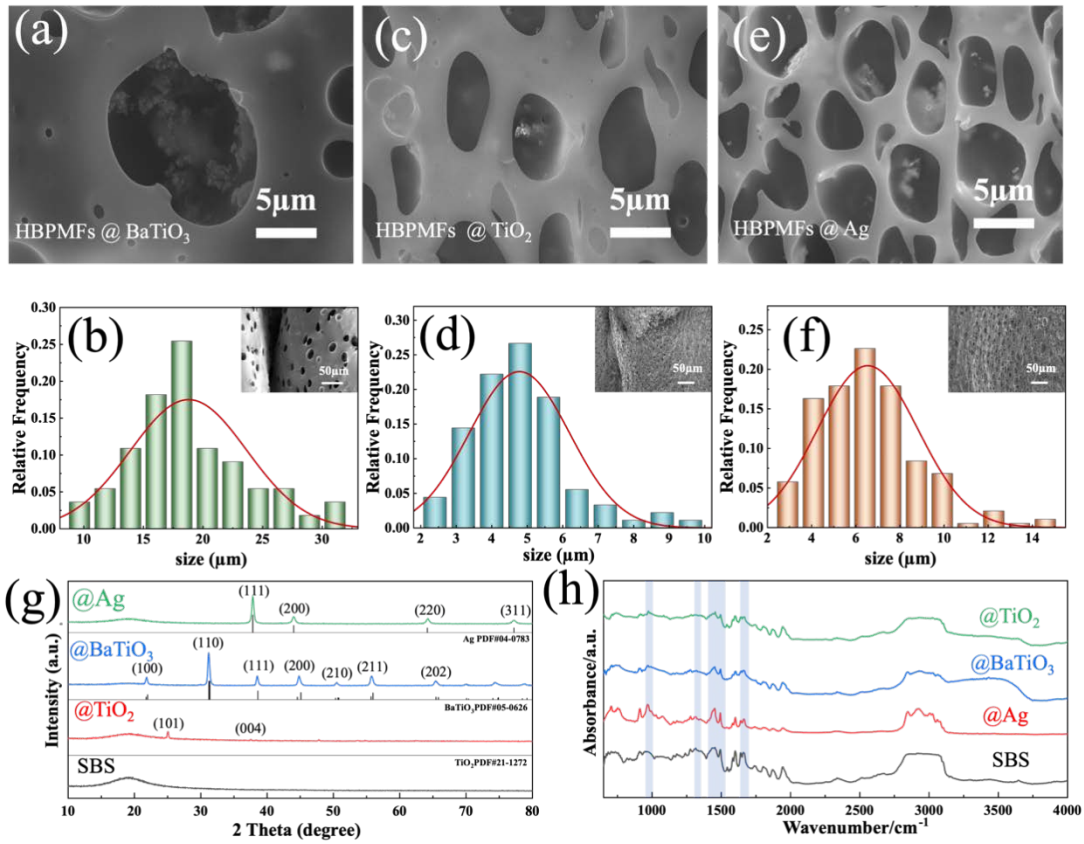

Figure 4.14 SEM images, pore size distributions, XRD and FTIR spectra of different HBPMFs. SEM images of $BaTiO_3$@HBPMFs (a), TiO_2@HBPMFs (c), Ag @HBPMFs (e), respectively. Corresponding pore size distributions for $BaTiO_3$@HBPMFs (b), TiO_2@HBPMFs (d), Ag@HBPMFs (f), respectively. (g) XRD of different nanoparticles@HPBMTs, (h) FTIR spectra of different nanoparticles@HPBMTs.

4.3.5 Demonstrative Application of HBPMFs

Based on the unique microstructure of HBPMFs, a novel fabric-based TENG (HBPMFs-TENG) was designed and developed. HBPMFs-TENG working on the contact-separation mode (**Figure 4.15**) utilizes HBPMFs and Ecoflex film as the triboelectric layers, and PAAm hydrogels serve as stretchable electrodes. The working mechanism of HBPMFs-TENG is shown in **Figure 4.15**. Initially, it can be assumed that the surfaces of the two friction layers exhibit no charge accumulation (**Figure 4.15 I**). When external pressure is applied, the friction layers come into contact, facilitating electron transfer from HBPMFs to the Ecoflex film, resulting in no potential

difference at complete contact (**Figure 4.15 II**). As the layers separate, a potential difference generates and drives electrons from the upper electrode to the lower electrode to balance the potential, thus producing an external current (**Figure 4.15 III-IV**). This cycle of contact and separation produces an alternating current signal (**Figure 4.15 II-V**), demonstrating the device's ability to convert mechanical energy into electrical energy efficiently.

In a comparative study, several fabrics featuring varied surface architectures were fabricated and employed as triboelectric components in corresponding TENGs, for different triboelectric fabrics of surface structure, including pristine elastic fabrics, solid SBS coating fabrics (SCFs), porous SBS coating fabrics (PCFs), and Ag NPs doped HBPMFs (Ag@HBPMFs). The SEM images of pristine elastic fabrics, SCFs, PCFs and HBPMFs are shown in **Figure 4.16**. The size of these TENGs is set to 2.5cm × 4cm. Their electrical performance was evaluated under an applied normal stress of approximately 100 kPa, derived from an impact force of 10 N acting on the defined contact area. (**Figure 4.17 (a)**, **(b)**). Compared to other structural fabrics-TENG, Ag@HBPMFs-TENG shows the best voltage, current, and charge of 420 V, 16 μA, and 110 nC, which are approximately 4, 3, and 6 times higher than those of the HBPMFs-TENGs, respectively. The excellent electric performance of Ag@HBPMFs-TENG can be attributed to its unique microstructure and Ag NPs dopant. The hierarchically buckled porous microstructure of Ag@HBPMFs affords a high specific surface area, facilitating the accumulation of a greater quantity of surface charges on the friction layers during the contact separation process [176–178]. The strategic self-assembly of Ag

NPs within the triboelectric layer enhances electric charge storage capability because Ag NPs possess high electrical conductivity and act as localized electron traps, thereby facilitating more efficient charge transfer and retention at the dielectric interface. Moreover, their nanoscale size and uniform dispersion increase the interfacial area between the filler and polymer matrix, which enhances dielectric polarization. This synergistic effect results in a higher surface charge density and improved energy output of the TENG. [179].

To systematically investigate mechanical energy harvesting properties, the electric performance of Ag@HBPMFs-TENG was further measured under varying conditions. The effect of frequency on the output performance of Ag@HBPMFs-TENG is first evaluated at a constant impact force of 10N (**Figure 4.18 (a-c)**). Ag@HBPMFs-TENG has an obvious increase in the voltage and charge with the increase of frequency from 1 to 3 Hz. It may be attributed to external electrons flowing to reach equilibrium in a shorter time [180]. Then, the voltage and charge of Ag@HBPMFs-TENG maintain almost unchanged in the frequency range from 3 to 5 Hz. This interesting phenomenon is consistent with previous reports [181,182]. While the current of Ag@HBPMFs-TENG exhibits a gradually increasing trend in the range of 1-5 Hz. In addition, the voltage, current, and charge of Ag@HPBPMFs-TENG were evaluated under different working conditions of stretching ratios (25%-125%) and compression forces (1-30N), as shown in **Figure 4.19**. When the stretching ratio increases from 25% to 75%, the electrical properties of Ag@HPBPMFs-TENG are significantly enhanced, with voltage from 289V to 476V, current from 7.48 μA to 16.32 μA, and charge from 75 nC to 118 nC,

respectively, which exhibits good performance with respect to other stretchable and porous structure-based TENGs (**Table 4.1**) [126, 127, 149, 169, 176, 177, 183, 184]. It is because the partly closed porous structure and buckling structure can be extended as the stretching ratio increases, enlarging the effective contact area of the friction layer during the contact-separation process. While the voltage, current and charge dropped to 357V, 9μA and 90 nC, respectively, at the stretching ratio increases from 75% to 125%. It may be attributed to that the unfolded buckled structures are easier to flatten during the contact-separation process. The surface morphologic change of HBPMFs as the stretching ratio can be observed in **Figure 4.20**. Furthermore, the electrical performance of Ag@HBPMFs-TENG also depends on compression force, optimal electrical properties are observed at approximately 15N of compression force. As shown in **Figure 4.17**, the HBPMFs-TENG achieved a constant voltage of 210 V during 10,000 times of cyclic testing at 10 N and 3 Hz one, demonstrating good stability of our HBPMFs-TENG. From the morphology of HBPMFs before and after 10,000 compressions (**Figure 4.17 (d-g)**), the buckled structure remains well preserved, though the porous structure is slightly extruded, contributable to the inherent flexibility of SBS.

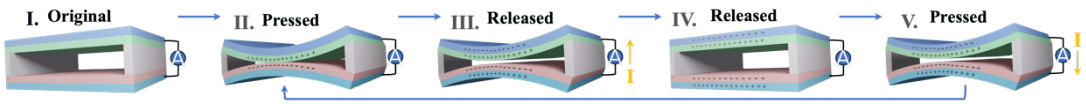

Figure 4.15 The working principle of double electrode mode TENG

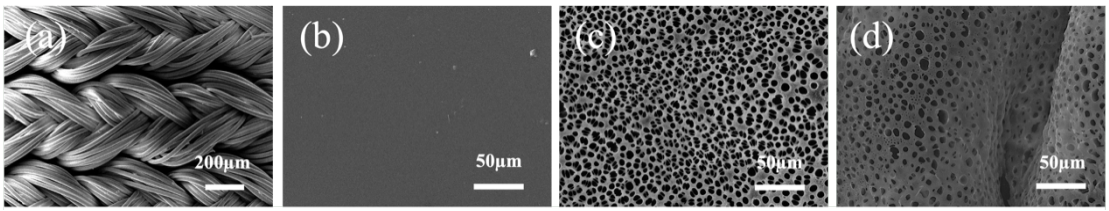

Figure 4.16 SEM images of (a) pristine elastic fabrics, (b) SCFs, (c) PCFs, and (d) HBPMFs, respectively.

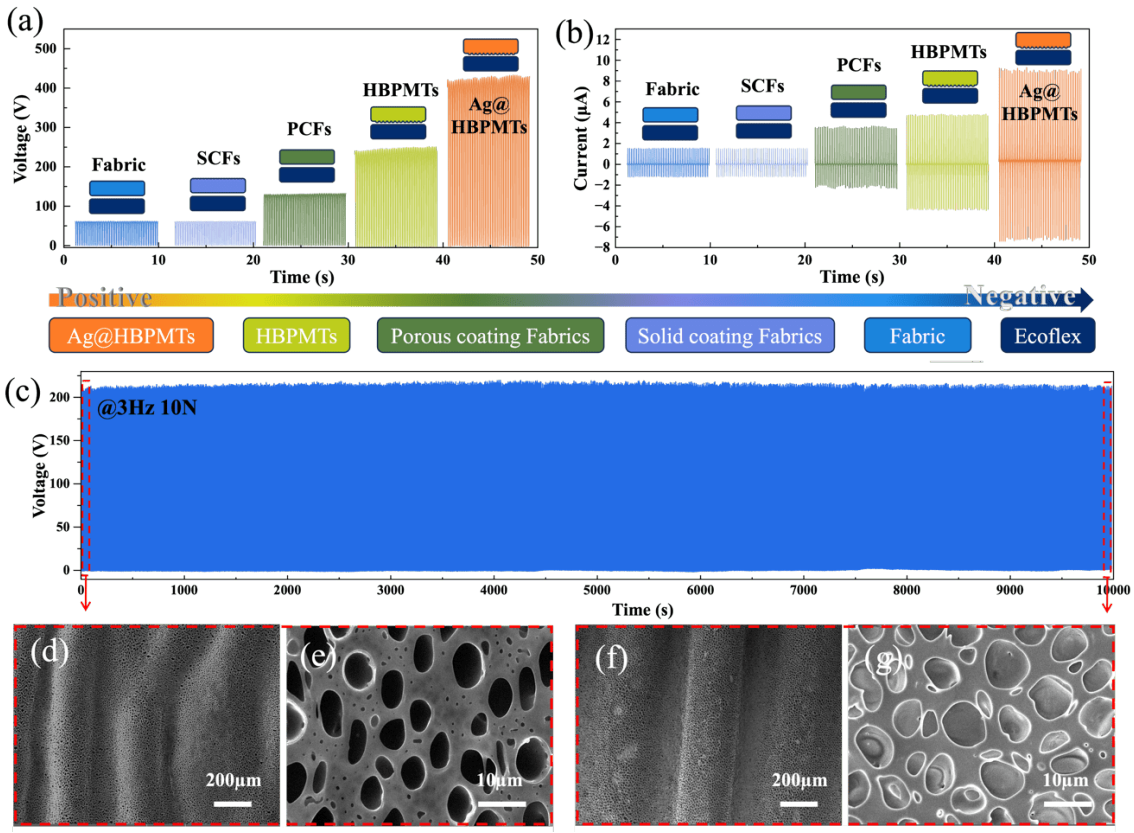

Figure 4.17 The electrical performance of double electrode mode TENG and various magnification SEM images before the test and after 10000 cycles. (a) voltage and (b) current of TENG with different fabrics. All fabrics were coupled with Ecoflex film. (c) Durability testing of HPBPMFs- TENG for continuous 10,000 cycles under 3Hz 10N. (d, e) different magnification HBPMFs of before 10,000 times compressions, (f, g) different magnification HBPMFs of after 10,000 times compressions.

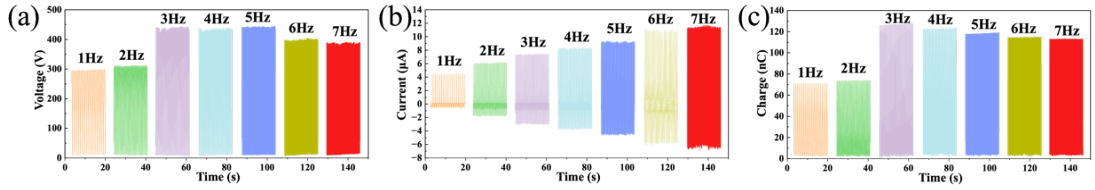

Figure 4.18 electrical performance of double electrode mode TENG. (a) voltage, (b) current, and (c) charge of HBPMFs-TENG with different frequencies.

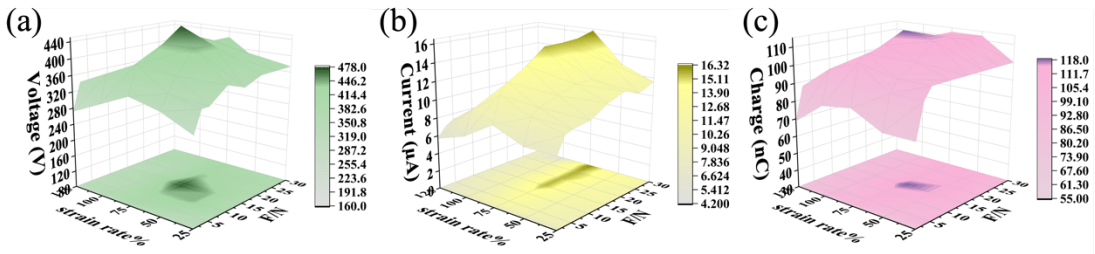

Figure 4.19 The electrical performance. (a) voltage, (b) current and (c) charge of Ag@HPBPMFs-TENG under the stretching operation (strain: 25–125%) and the different press (force: 1-30N).

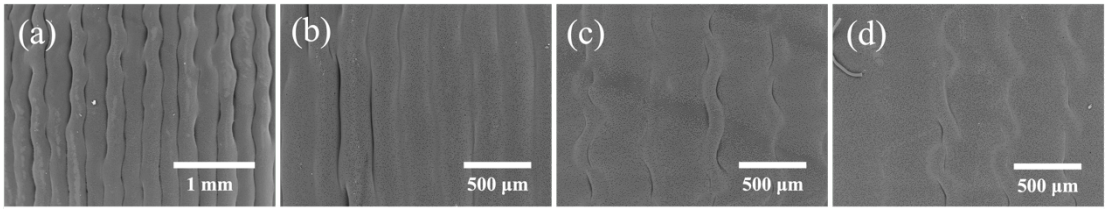

Figure 4.20 HBPMFs under different stretching ratios, (a) 0% stretching ratio, (b) 50% stretching ratio, (c) 75% stretching ratio and (d) 100% stretching ratio.

Table 4.1 Comparison of our TENG with other reported stretchable and porous structure-based TENG.

Triboelectric materials	**Maximum output voltage**	**Maximum output current**	**stretchability**	**Surface structure**	**Ref.**
SBS-Ecoflex	476V	16.32μA	125%	Hierarchically buckled porous structure	This work
PDMS	40V	2.24μA	25%	high-aspect-ratio nanotextured surface	[149]
SBS	97.3V	3μA	/	Honeycomb porous microstructure	[127]
SBS	7V	/	/	3D porous structure	[126]
PDMS	92V	/	50%	Anti-nickel foam structure	[169]
Nylon6-PVDF-HFP	80V	1.67μA	/	Crumpled nanofibrous	[176]
CNF/PEI aerogel-PVDF	106.2V	9.2μA	1%	Porous aerogels	[177]

PDMS	180.1V	/	100%	Wrinkled structure	[183]
Ecoflex	20.5V	1.25μA	100%	Micro-crack assisted wrinkled films	[184]

The power density of Ag@HBPMFs-TENG was measured with connected to a series of external resistances at 10 N and 3 Hz. As shown in **Figure 4.21 (a)**, as the load resistance increases from 1 kΩ to 1 GΩ, the output voltage of Ag@HBPMFs-TENG gradually increases while the output current of Ag@HBPMFs-TENG decreases. The instantaneous peak power density of Ag@HBPMFs-TENG can be determined by $P=I^2R/A$, where P, I, R and A represent power density, output current, external resistance and effective contact area, respectively. The Ag@HBPMFs-TENG reaches a peak power density of 0.54 W m^{-2} at a load resistance of 30 MΩ. The equivalent circuit of this self-powered system consists of the Ag@HBPMFs-TENG, a rectifier, a capacitor and various electronic components, as shown in **Figure 4.21 (b)**. This circuit is engineered to provide energy to small electronic devices, including capacitors, calculators, electronic watches and LEDs. Owing to its good power output, Ag@HBPMFs-TENG can be a sustainable power source to charge a series of commercial capacitors (1.5, 10, 22, 47, 100 and 680uF). **Figure 4.21 (c)** shows the rapid charging of 1.5, 10, 22, 33, 47, 100 and 680uF capacitors within 60 s, with charging rates of 3.2, 0.48, 0.18, 0.15, 0.12, 0.06 and 0.01 V/s, respectively. Ag@HBPMFs-TENG can also be used as a power source to drive small electrical appliances by continuously tapping with a hand. It charges a 22uF capacitor to 3V in 140 seconds.

Connecting the charged capacitor with a calculator and an electronic watch (**Figure 4.21 (d)** and **(e)**), the stored electricity can drive the calculator and electronic watch to work for about 20 seconds and 35 seconds. In addition, this device can also stably light up 128 LEDs (**Figure 4.21 (f)**).

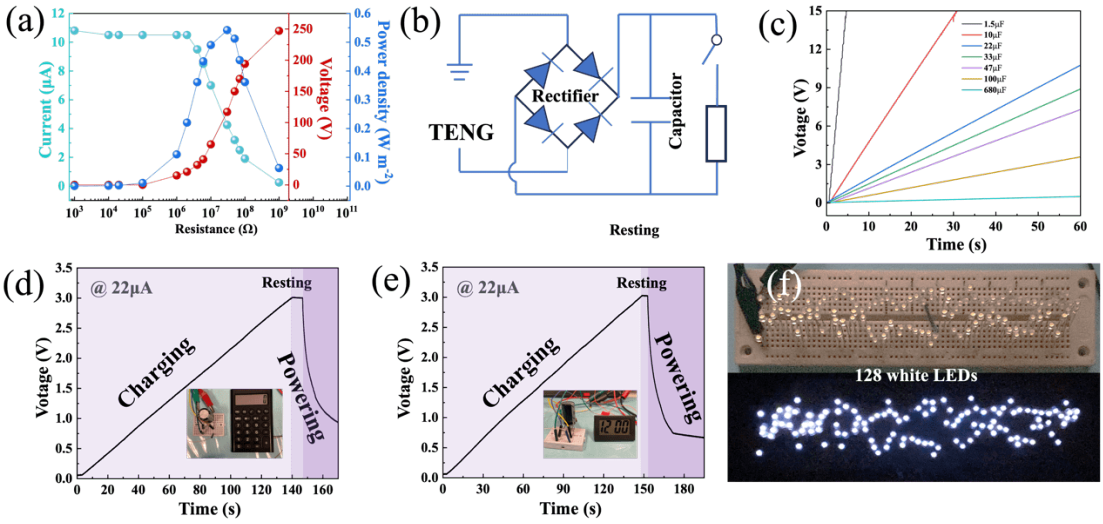

Figure 4.21 Energy harvesting demonstrations of TENG. (a) Output voltage, current and instantaneous peak power density of TENG at a series of external loadings. (b) Equivalent circuit. (c) Charging rates of different capacitors through TENG. Charging/discharging curves of a commercial capacitor connected with TENG for driving (d) a calculator and (e) an electrical watch. (f) Light up 128 LEDs.

Owing to the suitable electrical output performance, Ag@HBPMFs-TENG can be further developed as a wearable self-powered sensor. **Figure 4.22 (d)** shows the applications of Ag@HBPMFs-TENG affixed to various parts of the human body as a sensor in this study. When integrated into a medical surgical mask, Ag@HBPMFs-TENG serves as a sensor to monitor human respiration (**Figure 4.22 (a)**). During inhalation, breathing causes the mask to press the TENG closer to the skin, decreasing the gap between its triboelectric layers and thus generating a measurable electrical signal. Conversely, exhalation expands the mask, driving the TENG back to its initial state, causing the triboelectric layers to separate and re-generate electrical signals. This

cyclical breathing motion enables the generation of continuous electrical signals. Notably, the amplitude of these signals varies with the depth of breathing, ranging from 1.8 to 2V for normal breathing to 3 to 3.8V for deeper breaths, thereby indicating the sensor's capability to distinguish between different breathing intensities. Blinking activity conveys human emotions and serves as a means of communicating behavior. By pasting the Ag@HBPMFs-TENG onto the eyelids, the alternating blinking motion can be detected through regular and repeatable voltage signals (**Figure 4.22 (b)**) with an electric output of -0.1 to 0.2V. By fixing Ag@HBPMFs-TENG at the index finger joint, the bending angles of the finger will generate different voltage signals, which can be used to detect gestures, such as OK and curl up (**Figure 4.22 (c)**). Attaching Ag@HBPMFs-TENG to insoles (**Figure 4.22 (e)**) or knee (**Figure 4.22 (f)**) generates synchronized voltage signals under walking and running conditions, showing good stability and clear motion differentiation. This capability stems from bending angles and contact frequency changes, affecting signal amplitude and shape. Additionally, the device uses joint movements to produce varied electrical signals, enabling monitoring of body motions, such as the elbow's flexion from 30° to 90° with electric output from 25 V to 55 V, indicating distinct signal profiles for different bends (**Figure 4.22 (g)**). To further investigate the application potential of our Ag@HBPMFs-TENG, we developed a sensing array by integrating nine Ag@HBPMFs-TENGs in the warp and weft direction (**Figure 4.23 (a)**). When pressing on the surface of the array sensor, the Ag@HBPMFs-TENG at the corresponding position will produce an obvious voltage output signal. Through the multi-channel data acquisition system, the real-time voltage

signals of sensing units can be detected simultaneously or respectively. After signal processing, the real-time statistical results can be displayed in a display terminal. **Figure 4.23 (b)** shows the self-powered falling point distribution statistics system generated by the array sensor, which includes the distribution map of each pixel, the statistical results and the real-time voltage signals of all channels. As expected, a real-time signal update can be observed in the distribution map as the different position of the array sensor is pressed, and the corresponding statistical result is generated in each pixel, demonstrating the detecting performance of the system in the falling point position and statistical distribution. These results showed that Ag@HBPMFs-TENG has stable and reliable output signals as a wearable self-powered sensor for motion detection. Given its proven stability and repeatability, Ag@HBPMFs-TENG stands out as a promising tool for personal healthcare monitoring and human-computer interaction. These results indicate our Ag@HBPMFs-TENG as a wearable sensor can cope with most mechanical stress generated by human body and maintain a stable electrical output signal.

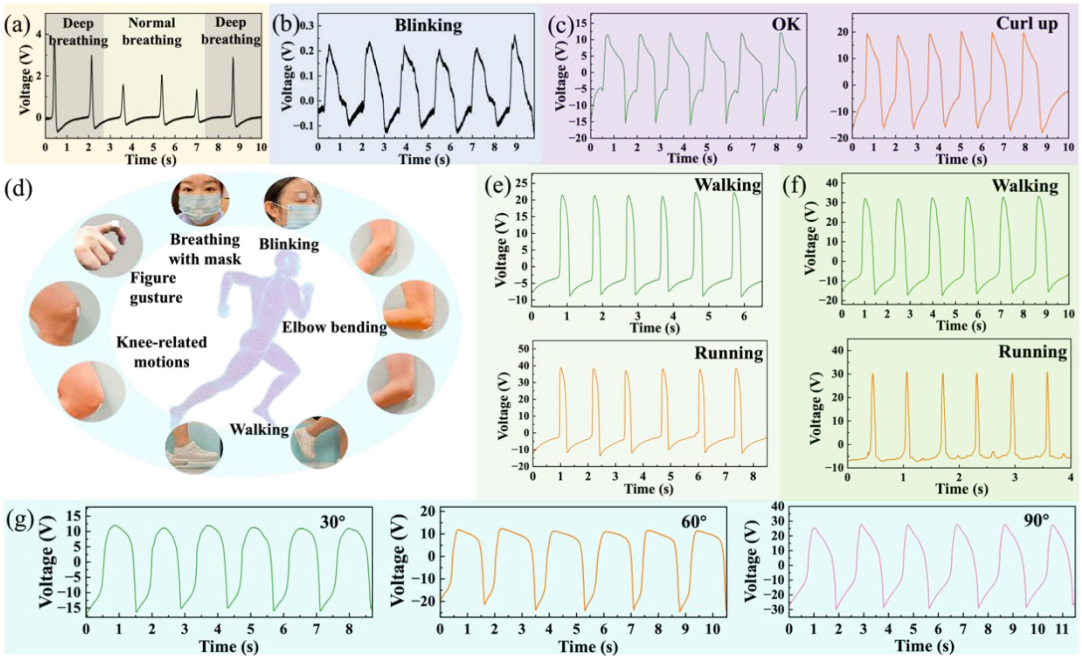

Figure 4.22 Application demonstrations of Ag@HBPMFs-TENG as a wearable self-powered sensor. (a) Nasal breathing monitoring by pasting TENG to a surgical mask. (b) Blinking activities sensing by sticking TENG on the eyelid. (c) Monitoring finger detect gestures (OK and curl up) by fixing TENG on the index finger. (d) Applications of Ag@HBPMFs -TENG fixed on different parts of the body. (e) Monitoring of different walking modes by pasting TENG on an insole. (f) Monitoring of knee-related motions by installing TENG on the knee joint. (g) Detection of elbow bending angles by attaching TENG to the elbow.

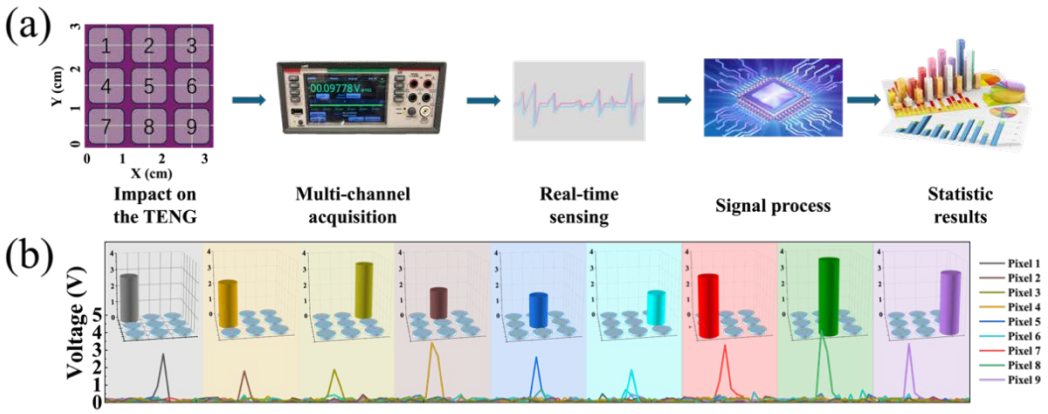

Figure 4.23 Application of the TENG in a self-powered falling point distribution statistical system. (a) Scheme diagram of the TENG based self-powered falling point distribution statistical system. (b) Real-time output voltage signals and statistic result.

4.4 Conclusion

In summary, we proposed a novel hierarchically buckled porous microstructure

fabric (HBPMFs) using a self-assembly strategy. Key factors influencing the design, properties, and functionality of HBPMFs were systematically explored, including pre-stretching ratios, swelling durations, fabrication conditions, and release mechanisms. By incorporating various nanoparticles into the HBPMFs, we successfully developed fabric-based TENG, among which the integration with 0.4 wt% Ag NPs showcased the best triboelectric performance. The optimized Ag@HBPMFs -TENG is 4, 3 and 6 times higher than the pristine elastic fabric in terms of voltage, current, and charge, respectively. Moreover, the Ag@HBPMFs-TENG can power electronic watches, digital calculator devices and LEDs, and it can also serve as a wearable self-powered sensor for detecting human body motions. The unique structural and functional attributes of HBPMFs underscore their significant potential for application in wearable electronics.

Chapter 5 Hierarchically Buckled Porous Microarchitectures of NiCo-LDH@carbon Fibers for High-Performance Stretchable Supercapacitors in Wearable Electronics

5.1 Introduction

The development of wearable electronic devices, such as health monitors, smart textiles, and fitness trackers, has generated a strong demand for energy storage systems that combine flexibility, stretchability, and mechanical resilience[185–187]. Fiber-based supercapacitors have attracted significant attention owing to their fast charge-discharge capabilities, high power densities, and long cycle lives[188,189]. However, conventional supercapacitors often face significant challenges in maintaining energy storage performance under mechanical deformations such as bending, twisting, or stretching[190]. This limitation underscores the importance of creating stretchable fiber-based supercapacitors[188,191,192] capable of enduring mechanical strains while retaining robust electrochemical properties, particularly for next-generation wearable technologies.

To address these challenges, significant research has been directed toward designing advanced fiber structures and integrating versatile materials. Carbon-based fibers[193], including carbon nanotubes (CNTs) and carbon fibers, are key materials because of their remarkable mechanical properties, excellent electrical conductivity, and electrochemical double-layer capacitance (EDLC). However, these materials exhibit limited energy storage capacity because of the inherent ion adsorption and desorption limitations of EDLC mechanisms[194–196]. Hybrid systems incorporating

pseudocapacitive materials, such as transition metal oxides (e.g., MnO_2)[197,198] and conductive polymers (e.g., polypyrrole)[199], have shown enhanced energy storage performance. For instance, recent studies demonstrated that CNT-based hybrid supercapacitors loaded with metal-organic framework-derived porous nanostructures significantly improved energy density and cycling stability[200]. Despite these advancements, many hybrid systems still experience performance degradation under high strain or repeated deformation cycles.

Nickel-cobalt layered double hydroxides (NiCo-LDH) have emerged as promising pseudocapacitive materials owing to their high faradaic activity, layered structure, and abundance of active sites[201,202]. These features enable efficient ion transport and redox reactions, making NiCo-LDH a suitable candidate for fiber-based supercapacitors. Recent research highlights the advantages of integrating NiCo-LDH with porous carbon materials to achieve high electrochemical performance while preserving flexibility[203,204]. For instance, hierarchical porous structures derived from Al-doped NiCo-LDH precursors exhibited excellent ion transport and mechanical stability under dynamic conditions, offering enhanced energy density and long-term cycling durability[205]. However, challenges such as reduced capacitance retention under deformation and the cycling fatigue of pseudocapacitive materials persist, limiting their practical application.

In this study, we report a novel approach to enhance the performance of fiber-based supercapacitors by utilizing a core-spun yarn structure, where elastic fibers form the core and are wrapped by carbon fibers to create a mechanically robust composite. These

core-spun yarn carbon fibers are further processed using the high-humidity breath figure (BF) method to form hierarchically buckled porous structures (HBPSs). The HBPFSs are subsequently coated with NiCo-LDH nanostructures via hydrothermal treatment. The stretched device is almost the same as the original device, indicating that the device can still maintain its structural integrity and excellent electrochemical performance after mechanical deformation. Additionally, the specific capacitance reaches 334.1 mF cm^{-1} at 0.5 mA cm^{-2}, surpassing conventional flexible energy storage systems. These findings underscore the potential of integrating core-spun yarn processing with hierarchical structural design for advanced wearable energy storage solutions.

5.2 Experimental Section

5.2.1 Materials

The following materials were purchased and used for the experiments: polystyrene-block-polybutadiene-block-polystyrene (SBS), multi-walled carbon nanotubes (MWCNTs), chloroform ($CHCl_3$), cobalt sulfate hexahydrate ($CoSO_4 \cdot 6H_2O$), nickelsulfate hexahydrate ($NiSO_4 \cdot 6H_2O$), potassium hydroxide (KOH), sodium dodecylbenzene sulfonate (SDBS), acrylamide, N,N′-methylene-bisacrylamide (BMAA), potassium persulfate (KPS), tetramethylethylenediamine (TEMED), and 3K carbon fibers. All reagents were of analytical grade and used without further purification.

5.2.2 Fabrication of conductive buckled porous carbon fibers

Elastic carbon fibers were fabricated using a core-spun yarn methodology, wherein elastic fibers served as the core material, encased by carbon fibers to form a mechanically robust composite structure. The resulting core-spun carbon fibers were subjected to a solution casting process utilizing a polymer solution comprising styrene–butadiene–styrene (SBS) dissolved in chloroform ($CHCl_3$) at a concentration of 200 mg/mL and carbon nanotubes (CNTs) dispersed in chloroform at a concentration of 40 mg/mL. These solutions were mixed in predetermined ratios of SBS/$CHCl_3$ to CNT/$CHCl_3$, specifically 1:0, 1:1, 1:2, and 1:3. During the casting process, the pre-stretched fibers were immersed in the prepared casting solution for 30 seconds to selective swelling and ensure uniform coating. Following this, the fibers were transferred to a high-humidity environment (relative humidity >90%) and maintained there for 1 minute to promote the formation of a buckled porous structure through the breath figure interfacial self-assembly. After this high-humidity exposure, the pre-stretch tension was gradually released, then the fibers were removed and subjected to annealing and drying at 90°C, ensuring complete solvent evaporation and stabilization of the porous morphology. The final samples were designated as $HBPS_0$, $HBPS_1$, $HBPS_2$, and $HBPS_3$, based on the respective ratios of SBS/$CHCl_3$ to CNT/$CHCl_3$ in the casting solution.

5.2.3 Preparation of NiCo-LDH-Coated HBPS Fibers

The pre-dried buckled porous carbon fibers ($HBPS_1$, $HBPS_2$ and $HBPS_3$) were subject to hydrothermal treatment to grow NiCo-LDH nanostructures on their surfaces. The

hydrothermal process was conducted at 120°C for 12 hours using solutions with varying concentrations of cobalt sulfate hexahydrate, nickel sulfate hexahydrate, urea, and SDBS. The solutions were prepared as 20 mM $CoSO_4 \cdot 6H_2O$, 40 mM $NiSO_4 \cdot 6H_2O$, excess urea, and 0.1 wt% SDBS, respectively. After hydrothermal treatment, the fibers were dried under standard environmental conditions, and the samples were labeled based on the NiCo-LDH coating applied to the original porous carbon fibers ($NiCo@HBPS_1$, $NiCo@HBPS_2$ and $NiCo@HBPS_3$).

5.2.4 Fabrication of All-Solid-State Symmetric Supercapacitors

The gel electrolyte was prepared by dissolving 2.5 g of acrylamide and 2.5 mg of BMAA in 10 mL of deionized water under constant stirring at room temperature. With this solution, 0.06 g of KPS and 5 μL of TEMED were added, ensuring thorough mixing. Once the solution became homogeneous, 10 mL of 6 M KOH was rapidly introduced to create a pre-gel electrolyte solution. The $NiCo@HBPS_1$ fibers were immersed in the pre-gel electrolyte for 30 seconds to ensure uniform absorption of the solution. Following immersion, the fibers were solidified at 50°C for 30 minutes. This process was repeated 2-3 times to achieve a consistent and uniform gel electrolyte coating on the fibers. After the final coating step, two identically treated $NiCo@HBPS_1$ fibers were assembled to form a symmetric supercapacitor. The assembled devices were stored at room temperature to allow full solidification of the gel electrolyte before further use.

5.2.5 Characterization

To comprehensively analyze the samples of NiCo@HBPS, HBPS and pure carbon

fibers, several characterization techniques were employed. Scanning electron microscopy (SEM) was performed using a Tescan MIRA field emission SEM to examine surface morphology, coupled with energy-dispersive X-ray spectroscopy (EDX) to map the elemental distribution. High-resolution transmission electron microscopy (HRTEM) was conducted on a JEOL JEM-2010 to observe nanostructures and lattice fringes. X-ray photoelectron spectroscopy (XPS) was carried out with a Thermo Scientific Nexsa G2 system to analyze elemental composition and oxidation states. The electrochemical performance of the fabricated supercapacitors (NiCo@HBPS$_1$, size 1cm) and the all-solid-state symmetric supercapacitor were tested via an electrochemical workstation instrument (CHI 660E, shanghai chenhua instrument Co., Ltd.) The NiCo@HBPS, HBPS and pure carbon samples as a working electrode were evaluated using a three-electrode system in a 3 M KOH aqueous electrolyte. A graphite plate and a saturated calomel electrode served as the counter and reference electrodes, respectively. Cyclic voltammetry (CV), galvanostatic charge-discharge (GCD), and electrochemical impedance spectroscopy (EIS) were employed to characterize the capacitive behavior, rate performance, and impedance characteristics of the supercapacitor. Specific capacitances were calculated from the GCD profiles using the following equation:

$$C = \frac{I*\Delta t}{\Delta V}$$

where I is the discharge current (mA cm^{-2}), Δt is the discharge time (s), and ΔV is the potential window(V).

5.3 Results and Discussion

To enhance the stretchability and flexibility of carbon fibers in the preparation of supercapacitors, elastic fibers were used as the core which was wrapped with carbon fibers to form core-spun yarns (**Figure 5.1 (a)**). The core-spun yarns were arranged into a flexible twining structure, significantly improving the material's ability to deform under external stresses, allowing it to endure greater levels of stretching and bending. To achieve a high specific surface area and hierarchically buckled porous structure (HBPS) fibers, the pre-stretched carbon fibers were coated with various ratios of SBS/$CHCl_3$ and CNT/$CHCl_3$ solutions and treated under high humidity using the BF method **Figure 5.1 (b)**. This method utilizes evaporative cooling to induce water droplet condensation on the fiber's surface. These condensed droplets self-assemble into a structured micro-template, facilitating the formation of an ordered porous SBS/CNT network on the fiber surface (**Figure 5.1 (d)**). The elasticity of SBS imparts good durability and mechanical resilience to the composite material, while CNTs establish a continuous conductive network. Following this, hydrothermal treatment was applied to grow nickel-cobalt layered double hydroxide (NiCo-LDH) nanostructures (**Figure 5.1 (c)**). NiCo-LDH is recognized for its outstanding electrochemical activity and ion exchange properties. During hydrothermal synthesis, NiCo-LDH nanosheets are uniformly deposited onto both the surface and inner pores of the SBS/CNT porous composite **(Figure 5.1 (e)**, resulting in a hierarchical structure that increases the specific surface area and enhances the number of active sites. At the molecular and structural levels, the integration of CNTs and NiCo-LDH (**Figure 5.1 (f)** and **(g)**) promotes

efficient charge transfer and accelerates ion diffusion, thereby enhancing the capacitor's rapid charge-discharge performance. Additionally, the porous network provides strong mechanical interlocking, enhancing the adhesion between NiCo-LDH nanosheets and the substrate, ensuring stability and minimizing detachment during repeated charge-discharge cycles.

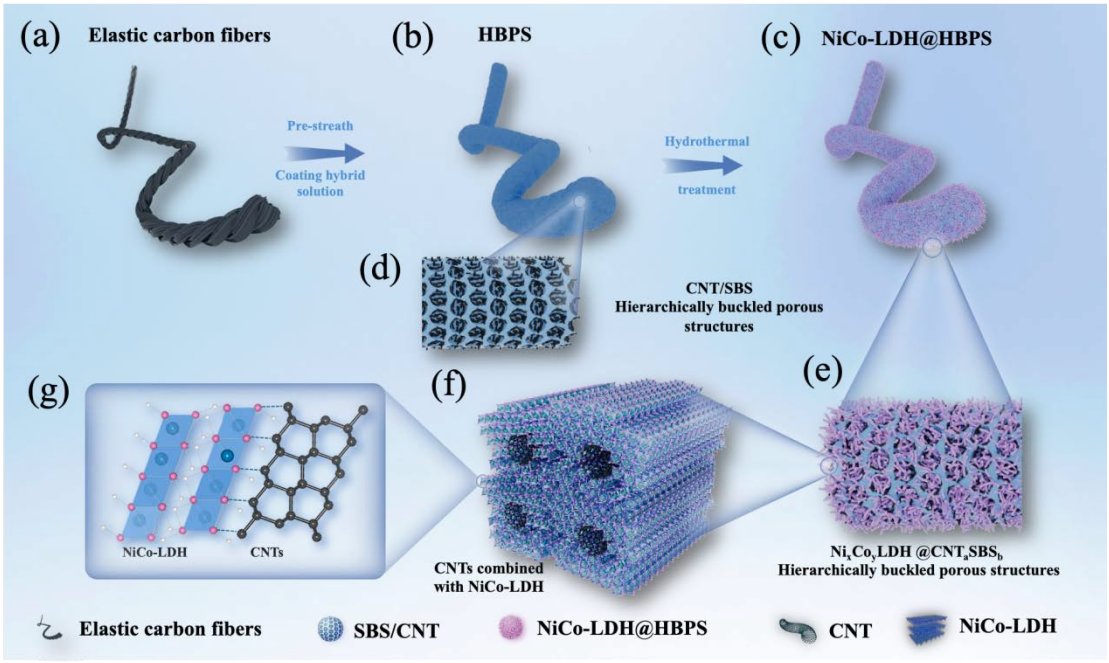

Figure 5.1 Schematic and mechanism illustration of the formation process of NiCo@HBPS. (a) Elastic carbon fibers were fabricated using a core-spun yarn structure. (b) Hierarchically buckled porous structure formation of HBPS on the Elastic carbon fibers. (c) NiCo-LDH growth on the HBPS. (d) HBPS magnified image. (e) NiCo-LDH@ HBPS magnified image. The schematic molecular model (f) and chemical structure (g) of CNTs combined with NiCo-LDH.

Figure 5.2 is the SEM image formed by coating different ratios of SBS and CNT solutions on elastic carbon fiber substrates. **Figure 5.2 (a, b)** are the morphologies of elastic carbon fibers. **Figure 5.2 (a)** is a low-magnification image, showing the overall appearance of elastic carbon fibers formed by using elastic fibers as the core and carbon fiber coating. The fibers are tightly arranged and have uniform surface features, providing a stable support platform for subsequent solution coating. **Figure 5.2 (b)** is a

high-magnification image, where it can be observed that the carbon fiber surface is smooth and has no pores, indicating that the fiber material itself does not have any porous structure before the BF coating. The design of the elastic fiber provides a sufficient mechanical elastic basis for subsequent morphology modification. **Figure 5.2 (c, d)** are the morphologies of $HBPS_1$ (1:1 ratio SBS/$CHCl_3$ and CNT/$CHCl_3$ coating). **Figure 5.2 (c)** is a low-magnification image showing the regular porous network formed on the carbon fiber surface after coating with a 1:1 ratio solution. The pores are evenly distributed, of uniform size, and have a wide coverage, indicating that the SBS matrix dominates the formation and stabilization of the water droplet template through the breath figure effect under high humidity conditions. **Figure 5.2 (d)** is a high-magnification image, which further reveals the detailed structure of the pores. The pore walls are smooth and regular in shape, reflecting the key role of SBS in maintaining the pore morphology and structural stability. This structure is of great significance to the subsequent deposition and functionalization of materials. **Figure 5.2 (e, f)** are the morphology of $HBPS_2$ (1:2 ratio SBS/$CHCl_3$ and CNT/$CHCl_3$ coating), **Figure 5.2 (e)** is a low-magnification image, showing the surface structure formed by the coating solution with a higher CNT ratio. The pores are significantly smaller and the network structure is denser, but the distribution of the pores is slightly irregular compared to the 1:1 ratio, reflecting the weakening of the pore network stability due to the reduction of the SBS matrix. **Figure 5.2 (f)** further shows the enlarged microscopic morphology of the pores. It can be observed that CNT begins to play a more significant role and gradually forms a porous structure with carbon nanotubes as the skeleton, but due to

the reduction of SBS content, the orderliness of the overall pore network is reduced. **Figure 5.2 (g, h)** are the morphologies of HBPS3 (coated with 1:3 ratio of SBS/$CHCl_3$ and CNT/$CHCl_3$): **Figure 5.2 (g)** shows the surface morphology after coating with 1:3 ratio solution. The SBS matrix is not sufficient to stabilize the breath figure effect, and the water drop template is unstable, resulting in the destruction of the pore structure and a highly irregular morphology on the overall surface. **Figure 5.2 (h)** reveals that the surface of the carbon fiber is mainly composed of rough areas composed of CNT accumulation, and there is almost no ordered pore structure. Although the high CNT content may improve the conductivity, the lack of pores may significantly limit the ion diffusion path, thereby affecting the electrochemical performance. It can be clearly seen from the SEM images that the ratio of SBS to CNT plays a decisive role in the formation of the porous structure on the surface of the carbon fiber. When the ratio of SBS to CNT is 1:1, the breath figure effect is most significant, the pore structure is stable and regular, and it is suitable for electrochemical material deposition and ion diffusion. When the SBS to CNT ratio increases to 1:2, the pore structure is more compact, but the regularity decreases. When the ratio is further increased to 1:3, excessive CNT content destroys the formation of the pore structure and significantly affects the orderliness and flatness of the surface morphology. This shows that during the BF process, the balance between SBS and CNT is crucial in optimizing the porous network structure, and too high or too low CNT content may have an adverse effect on the final performance.

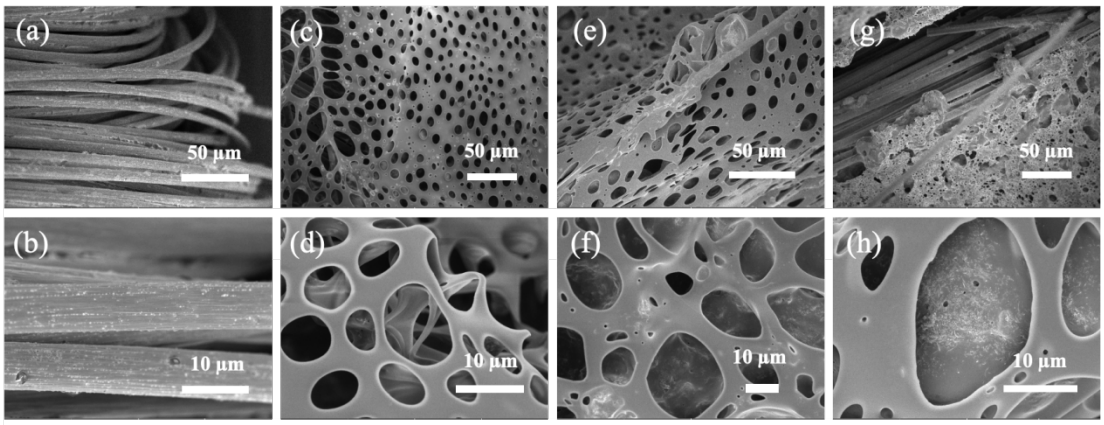

Figure 5.2 SEM images of different SBS and CNT ratios solution coatings on carbon fabric substrates at varying magnifications. (a, b) the morphology of Elastic carbon fibers, (c, d) the morphology of $HBPS_1$, (e, f) the morphology of $HBPS_2$, (g, h) the morphology of $HBPS_3$.

Figure 5.3 shows the NiCo-LDH structure formed on carbon fibers coated with different SBS to CNT ratios after hydrothermal treatment. **Figure 5.3 (a)** shows the low-magnification surface morphology of pure carbon fiber. The fiber surface is smooth and has no obvious pore structure, reflecting the initial state of the fiber before coating. **Figure 5.3 (b)** is a magnified image to observe the microscopic details of the fiber. There is no porous network on the surface, and only the characteristic of partial nanowire deposition is identified. **Figure 5.3 (c)** is a further magnified image for the surface structure of the fiber, and the active site or nanowire structure is weak. This provides a comparative basis for subsequent modification under different SBS and CNT ratios. **Figure 5.3 (d-f)** shows the growth morphology of NiCo-LDH on the surface of $HBPS_1$. Compared with $HBPS_0$, the increase in CNT content significantly increases the number of active sites, forming a denser and evenly distributed nanowire network, almost covering the entire pore structure. The enlarged view of **Figure 5.3 (e)** further reveals that the nanowires are evenly distributed around the pores, which not only increases the specific surface area, but also provides a good channel for electrochemical

reactions. **Figure 5.3 (f)** shows the network structure of NiCo-LDH nanowires at a higher magnification. This dense and uniform distribution makes full use of the highly active sites provided by CNTs and lays the foundation for the electrochemical performance of the material. The $HBPS_1$ sample exhibits an optimized pore and nanowire network structure, suggesting promising capabilities in facilitating ion transport and enhancing charge storage behavior. **Figure 5.3 (g-i)** shows the pore morphology of the NiCo@$HBPS_2$ surface. As the CNT content further increases, the breath figure template loses its stability, resulting in partial collapse of the pore structure and non-uniform deposition of NiCo-LDH. The enlarged image of **Figure 5.3 (h)** shows that NiCo-LDH aggregates into blocks on the surface, forming an irregular distribution, which may affect the uniform transport of ions. **Figure 5.3 (i)** further enlarges to show a more chaotic distribution of nanowires. The random distribution of pores and active sites may reduce the overall electrochemical performance of the material. **Figure 5.3 (j-l)** shows the surface morphology of the NiCo@$HBPS_3$. Due to the excessive CNT content, the pore structure almost completely collapsed, causing NiCo-LDH to form an extremely irregular structure on the surface. The enlarged images of **Figure 5.3 (k)** and **(l)** show that NiCo-LDH mainly exists in the form of clusters and is difficult to form a uniform nanowire network. This irregular structure may significantly reduce the ion transport efficiency of the material while reducing the accessibility of electrochemically active sites. **Figure 5.3** reveals the significant impact of different CNT to SBS ratios on the growth morphology of NiCo-LDH. NiCo@$HBPS_1$ successfully achieved a uniform and dense nanowire network at a moderate CNT content, which combined with a

regular pore structure, significantly increased the specific surface area and the number of active sites, providing ideal conditions for electrochemical reactions.

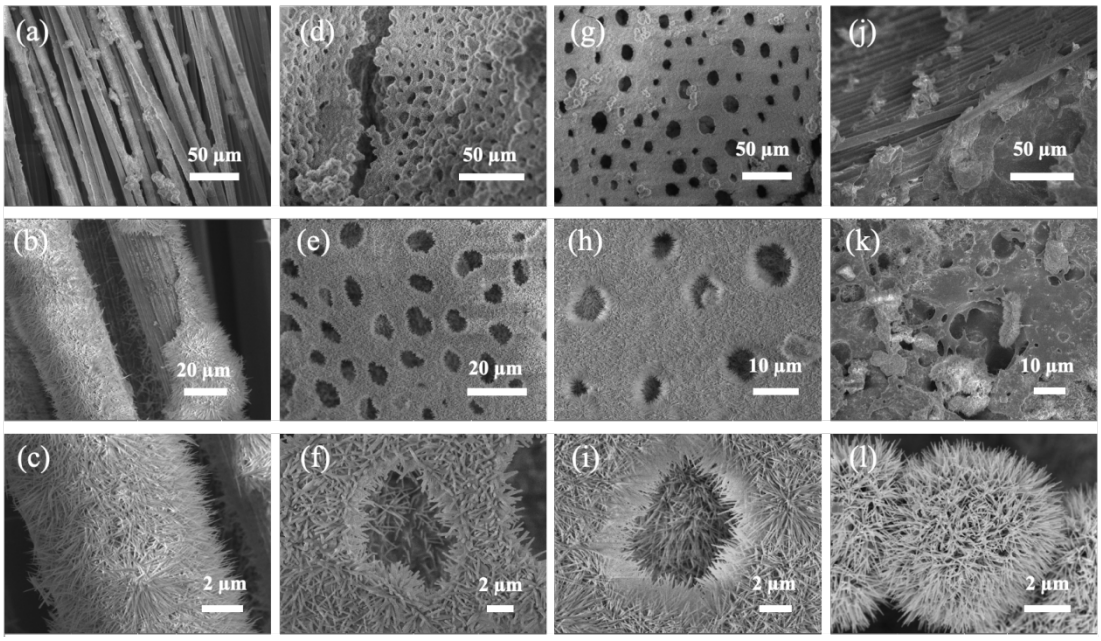

Figure 5.3 SEM images of NiCo-LDH on the Elastic carbon fibers cast with different SBS and CNT ratio solutions at different magnifications. (a-c) pure carbon fiber, (d-f) NiCo-LDH@ $HBPS_1$, and (g-i) NiCo-LDH@ $HBPS_2$, (j-l) NiCo-LDH@ $HBPS_3$.

Figure 5.4 shows a detailed analysis of the elemental composition, chemical state, and nanostructure characteristics of the NiCo-LDH sample. In the full-range XPS spectrum (**Figure 5.4 (a)**), the characteristic peaks of Ni 2p, Co 2p, O 1s, and C 1s were clearly detected, indicating that nickel and cobalt elements were successfully introduced into the sample, verifying the successful synthesis of NiCo-LDH. **Figure 5.4 (b)** shows the high-resolution spectrum of Ni 2p, which shows two main peaks at 873.5 eV and 855.3 eV, corresponding to Ni 2p1/2 and Ni 2p3/2, respectively. The deconvolution results of these peaks show the coexistence of Ni^{2+} and Ni^{3+} oxidation states in the sample, indicating that the sample has a multivalent nickel structure, which plays an important role in the redox reaction that enhances the electrochemical performance. **Figure 5.4 (c)** shows the high-resolution spectrum of Co 2p, where the main peaks at 796.4 eV and

781.4 eV correspond to Co 2p1/2 and Co 2p3/2, respectively. By deconvolution, the presence of Co^{2+} and Co^{3+} oxidation states in the sample was further confirmed, and this multivalent cobalt also contributes to the improvement of electrochemical reactions. **Figure 5.4 (d)** shows a transmission electron microscopy (TEM) image, showing the nanowire structure of NiCo-LDH, with a diameter of about 30 nm, indicating that the nanowires have uniform morphology and size distribution. **Figure 5.4 (e)** shows the HR-TEM image, in which clear lattice fringes were observed in the high-resolution transmission electron microscopy (HR-TEM) image, which further verifies the crystal structure of NiCo-LDH. The element distribution map clearly shows the uniform distribution of Ni, Co and O in the nanowire structure (**Figure 5.4 (f-i)**). This uniform element distribution is essential to ensure the consistency of the electrochemical performance of the material and enhance its reactivity. Figure 5.4 comprehensively shows the chemical composition and nanostructure characteristics of the NiCo-LDH sample, verifying its uniform element distribution, multivalent characteristics and regular crystal structure.

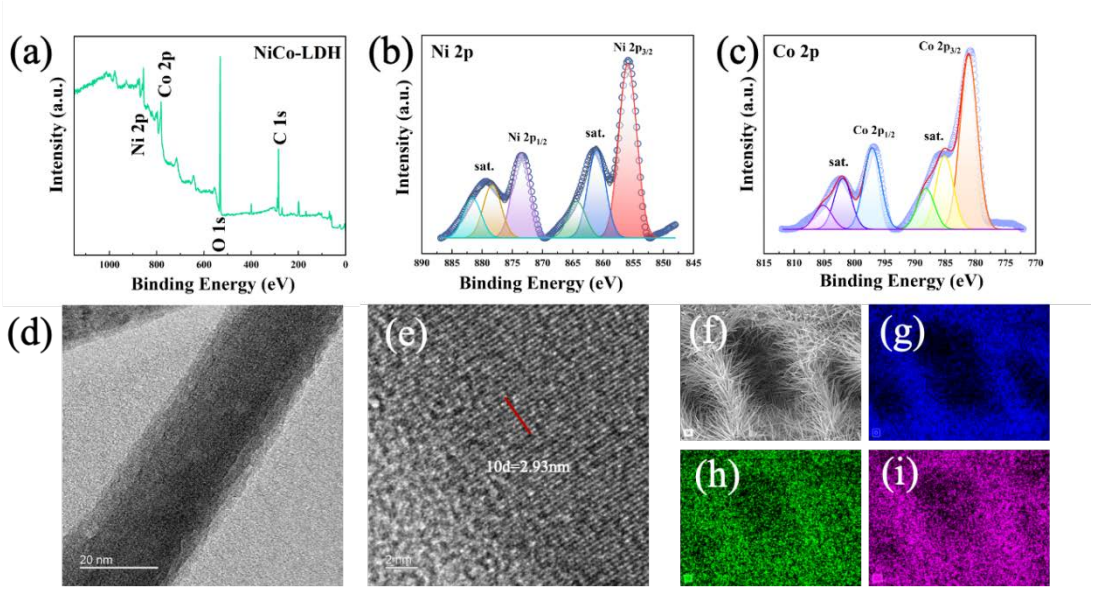

Figure 5.4 (a) XPS survey spectrum of the NiCo-LDH sample. (b) High-resolution XPS spectrum of Ni 2p. (c) High-resolution XPS spectrum of Co 2p. (d) TEM image of NiCo-LDH. (e) HR-TEM image of the NiCo-LDH structure. (f-i) Elemental mapping displays the Ni, Co, and O distribution in the nanostructure.

Figure 5.5 shows the electrochemical performance analysis of different samples. **Figure 5.5(a)** displays the cyclic voltammetry (CV) curves of HBPS, NiCo@HBPS, and pure carbon fiber samples at a scan rate of 20 mV/s, highlighting the electrochemical performance of each sample. Among all samples, NiCo@$HBPS_1$ exhibits the largest CV area, indicating its exceptional electrochemical performance. The improved electrochemical performance can be attributed to the uniform porous architecture and optimized distribution of NiCo-LDH nanowires, which facilitate more efficient charge storage and redox reactions. The curve area of NiCo@$HBPS_1$ is the largest, indicating its best electrochemical performance, while the CV area of NiCo@$HBPS_2$ and NiCo@$HBPS_3$ is reduced due to the uneven distribution of NiCo-LDH nanowires or the collapse of the pore structure. The CV curve area of NiCo@$HBPS_2$, NiCo@$HBPS_3$ and pure carbon fiber show a same area. For HBPS, especially $HBPS_1$, the CV curve area gradually increases with the optimization of the porous structure and CNT content. The CV areas of $HBPS_2$ and $HBPS_3$ are smaller, indicating that the electrochemical performance is reduced, which may be due to the destruction or inhomogeneity of the pore structure. **Figure 5.6** presents the cyclic voltammetry (CV) curves of NiCo@HBPS and HBPS samples at scan rates ranging from 2 mV/s to 50 mV/s, illustrating their electrochemical behavior. For NiCo@$HBPS_2$ (**Figure 5.6(a)**), the CV curves exhibit moderate redox activity, with distinct peaks that become less prominent at higher scan rates, reflecting limited charge transfer kinetics

likely caused by uneven NiCo-LDH distribution or partial pore collapse. NiCo@$HBPS_3$ (**Figure 5.6(b)**) displays further reduced CV areas and weaker redox peaks, indicative of structural degradation and lower accessibility of active sites. The HBPS samples exhibit overall poor electrochemical performance. $HBPS_0$ (**Figure 5.6(c)**) shows typical EDLC behavior with minimal redox activity and a small CV area, reflecting low charge storage capability. Similarly, $HBPS_1$ (**Figure 5.6(d)**), $HBPS_2$ (**Figure 5.6(e)**), and $HBPS_3$ (**Figure 5.6(f)**) all demonstrate limited electrochemical activity, attributed to structural inhomogeneities and pore collapse that hinder efficient charge transfer and storage. **Figure 5.7** illustrates the cyclic voltammetry (CV) curves of pure carbon fiber at scan rates ranging from 2 mV/s to 50 mV/s. The CV curves show weak but discernible redox peaks, reflecting a combination of electrochemical double-layer capacitance (EDLC) behavior and minor pseudocapacitive contributions.

Figure 5.5 (b) shows the constant current charge-discharge (GCD) curves of pure carbon fiber, HBPS, and NiCo@HBPS at a current density of 0.5 mA cm^{-2}. Compared with NiCo@$HBPS_1$, the discharge time of NiCo@$HBPS_2$ and NiCo@$HBPS_3$ is significantly shorter and close to that of pure carbon fiber. This may be due to the uneven distribution of NiCo-LDH, resulting in insufficient active sites, or the collapse of the pore structure, which limits the ion transport and charge storage capacity. For the HBPS samples, the charge and discharge times of $HBPS_1$, $HBPS_2$, and $HBPS_3$ are close, indicating that although their CNT contents are different, the destruction of the pore structure limits the further improvement of their electrochemical performance. Interestingly, the discharge time of $HBPS_0$ is better than that of $HBPS_1$, $HBPS_2$, and

$HBPS_3$, which may be due to the more regular pore structure of $HBPS_0$, and its uniform pore distribution still provides an effective path for ion transport and charge storage, thus showing better electrochemical performance. **Figure 5.8 (a-d)** shows the galvanostatic charge-discharge (GCD) curves of pure carbon fiber and different sample of NiCo@HBPS at different current densities (0.5, 1, 2, 5, 10 mA cm^{-2}). As the current density increases, the discharge time of each sample gradually shortens, but $NiCo@HBPS_1$ exhibits the longest discharge time at all current densities, indicating its highest energy storage capacity and favorable rate performance under varying current densities. In comparison, the discharge time of pure carbon fiber is significantly shorter, reflecting its limited energy storage capacity. The discharge time of $NiCo@HBPS_2$ and $HBPS_3$ is shorter than that of $NiCo@HBPS_1$, which further verifies the importance of the integrity of the pore structure and the uniformity of NiCo-LDH distribution to the energy storage performance. The Nyquist plots of pure carbon fiber, HBPS, and NiCo@HBPS show the characteristics of electrochemical impedance spectroscopy (**Figure 5.5 (c)**). $NiCo@HBPS_1$ shows a smaller semicircle in the high-frequency region, indicating its lower charge transfer resistance (Rct) and higher conductivity. In the low-frequency region, $NiCo@HBPS_1$ shows a steeper slope, indicating that its ion diffusion capacity is enhanced, which helps to improve the overall electrochemical performance. **Figure 5.5 (d)** shows the CV curves of $NiCo@HBPS_1$ at different scan rates (2 mV/s to 50 mV/s). As the scan rate increases, the redox peaks move symmetrically in the positive and negative directions, suggesting that the electrode maintains favorable redox reversibility with increasing scan rate. At lower scan rates

(such as 2 mV/s), the peaks are more obvious, reflecting that the pseudocapacitive behavior is mainly controlled by diffusion. **Figure 5.5 (e)** shows the logarithmic fitting curve of the peak current density and scan rate of NiCo@HBPS$_1$. The slopes corresponding to the two peaks are 0.6951 and 0.5762, respectively, indicating that the electrochemical behavior is dominated by the diffusion-controlled process. As the current density increases, the GCD curves of NiCo@HBPS1 at different current densities (0.5–10 mA cm^{-2}) show that the discharge time gradually decreases, but its overall charge and discharge curve remains symmetrical, indicating a high Coulombic efficiency (**Figure 5.5 (f)**). This performance is owing to the synergistic effect of NiCo-LDH and CNT, where the porous network structure provides an efficient ion diffusion path, while the uniformly distributed NiCo-LDH nanowires increase the contribution of pseudocapacitive behavior. In the CV curve of NiCo@HBPS$_1$ at 10 mV/s (**Figure 5.5 (g)**), the shaded part indicates that the diffusion control process accounts for about 53%. This indicates that at a lower scan rate, ions can penetrate into the porous structure and participate in the redox reaction. **Figure 5.5 (h)** is a comparison of the specific capacitance of different samples at a current density of 0.5 mA/cm^2. The NiCo@HBPS$_1$ exhibits the highest specific capacitance, reaching 334.1 mF/cm, which is mainly owing to its uniform pore structure and optimized distribution of NiCo-LDH nanowire network, which provides sufficient active sites and ion transport channels. In contrast, the specific capacitance of NiCo@HBPS$_2$ and NiCo@HBPS$_3$ is lower than that of NiCo@HBPS$_1$, and is similar to that of pure carbon fiber. The specific capacitance of the HBPS samples are much lower than that of the NiCo@HBPS samples, indicating

that the introduction of NiCo-LDH nanowires is crucial to improving the electrochemical performance. **Figure 5.5 (i)** shows the contribution ratio of diffusion-controlled and surface-controlled capacitance of NiCo@$HBPS_1$ at different scan rates. At a lower scan rate (2 mV s^{-1}), the diffusion control ratio is about 68%, indicating that ions can fully penetrate the porous structure to participate in the electrochemical reaction; at a higher scan rate (50 mV s^{-1}), the surface control ratio increases to 91%, indicating that charge storage is mainly concentrated on the electrode surface.

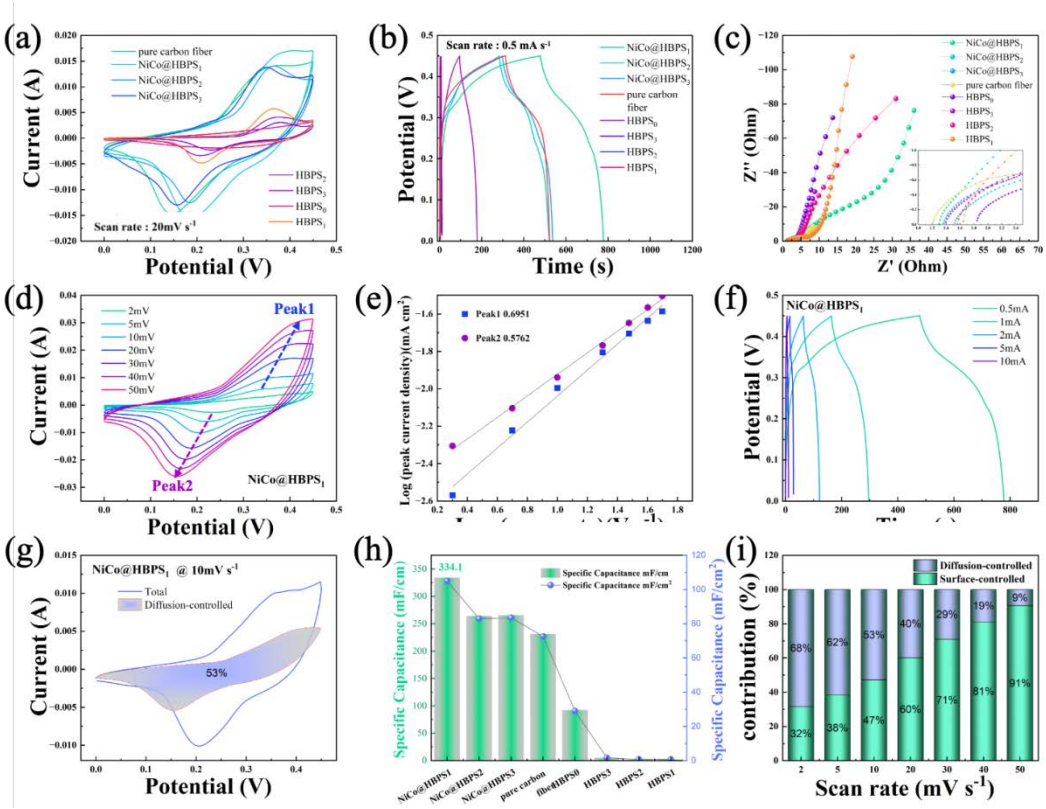

Figure 5.5 Electrochemical performance of different sample. (a) CV curves of pure carbon fiber, HBPS and NiCo@HBPS. (b) GCD curves of pure carbon fiber, HBPS and NiCo@HBPS at 0.5 mA cm^{-2}. (c) Nyquist plots of pure carbon fiber, HBPS and NiCo@HBPS, the inset shows the magnified high-frequency region. (d) CV curves of NiCo@$HBPS_1$ at varying scan rates. (e) Log-log plot of peak current density vs. scan rate for NiCo@$HBPS_1$. (f) GCD curves of NiCo@$HBPS_1$ at different current densities. (g) CV curves of NiCo@$HBPS_1$ at 10 mV s^{-1}, shaded area of diffusion-controlled contribution. (h) Specific capacitance of NiCo@$HBPS_1$ as a function of discharge current density. (i) Contribution of diffusion-controlled and surface-controlled capacitance for NiCo@$HBPS_1$ at different scan rates.

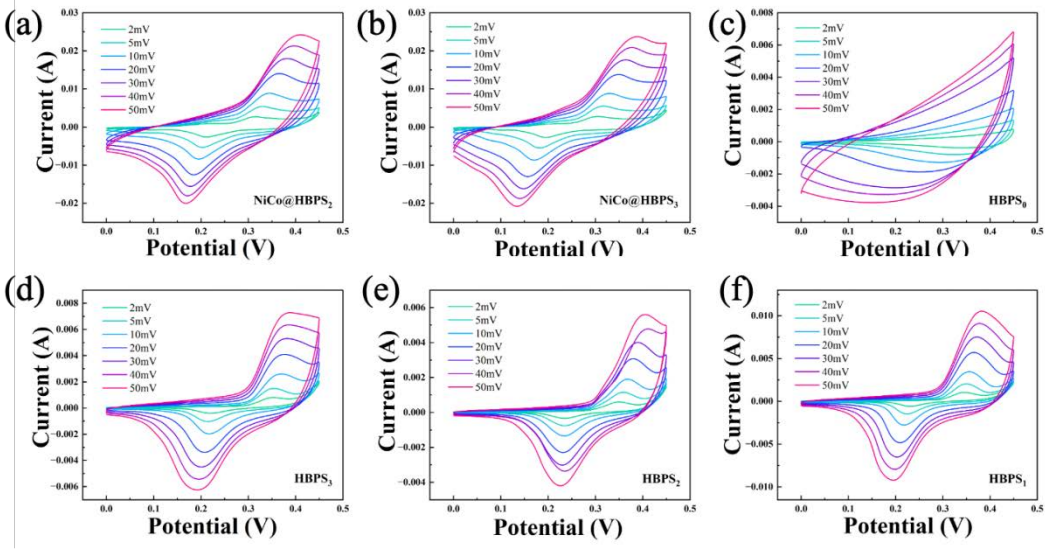

Figure 5.6 Cyclic voltammetry (CV) curves of HBPS and NiCo@HBPS at various scan rates (2 mV/s to 50 mV/s). (a) NiCo@$HBPS_2$, (b) NiCo@$HBPS_3$, (c) $HBPS_0$, (d) $HBPS_1$, (e) $HBPS_2$, and (f) $HBPS_3$.

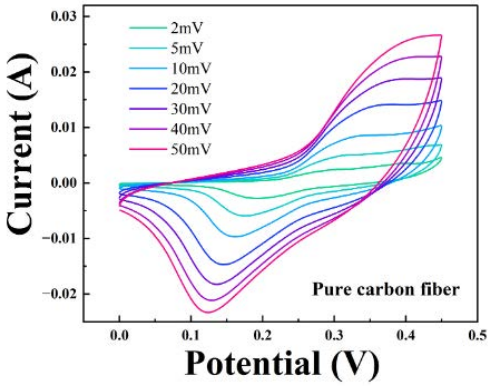

Figure 5.7 Cyclic voltammetry (CV) curves of pure carbon fiber.

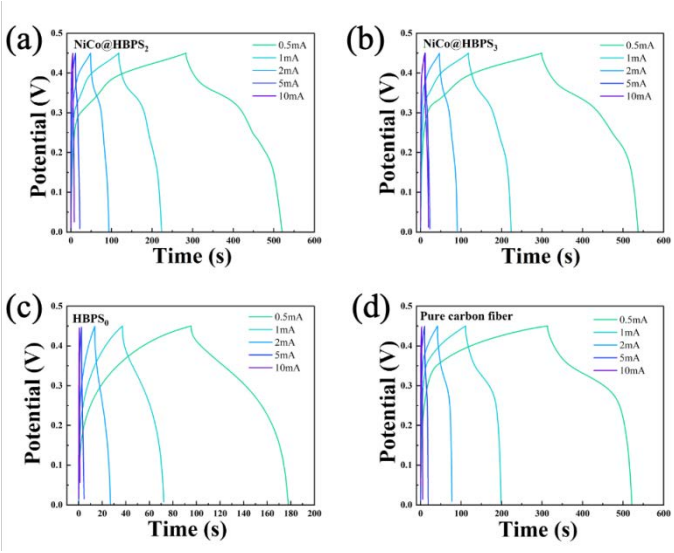

Figure 5.8 Galvanostatic charge-discharge (GCD) curves of pure carbon fiber and NiCO@HBPS at different current densities (0.5, 1, 2, 5, and 10 mA cm^{-2}).(a) $NiCo@HBPS_2$, (b) $NiCo@HBPS_3$, (c) $HBPS_0$, (d) pure carbon fiber.

Figure 5.9 shows the electrochemical performance of symmetric supercapacitors based on NiCo@HBPS1 electrodes. **Figure 5.9 (a)** shows the cyclic voltammetry (CV) curves of $NiCo@HBPS_1$ electrodes as the negative electrode (0 ~ 0.5 V) and the positive electrode (-0.9 ~ 0 V). The presence of distinct redox peaks in the curves suggests that the supercapacitor combines double-layer capacitance (EDLC) and pseudocapacitance characteristics, demonstrating the effective electrochemical activity of the NiCo-LDH and CNT composites. **Figure 5.9 (b)** shows the CV curves of the symmetric supercapacitor at different voltage windows (0.6 V to 1.35 V) under a scan rate of 20 mV/s. The curve maintains a quasi-rectangular shape, accompanied by the appearance of redox peaks, reflecting the enhancement of pseudocapacitive behavior. As the voltage window increases, the current response also increases accordingly, indicating that the supercapacitor has good energy storage capacity at higher voltages. At a constant current density (0.2 mA/cm^2), **Figure 5.9 (c)** shows the constant current

charge-discharge (GCD) curves at different voltage windows. The curves are quasi-triangular with an IR-drop and slight deviations from perfect symmetry, reflecting mixed capacitive/pseudocapacitive behavior and some polarization resistance; nevertheless, the charge–discharge process remains largely reversible, confirming acceptable coulombic efficiency. As the voltage window increases, the discharge time gradually increases, further demonstrating its energy storage capacity at high voltage. **Figure 5.9 (d)** shows the GCD curves at a fixed voltage (1.35 V) under different current densities. As the current density increases from 0.2 mA/cm² to 5 mA/cm², the discharge time gradually decreases, but the charge-discharge curves remain symmetrical, indicating that the device has high rate performance. **Figure 5.9 (e)** shows the relationship between specific capacitance and discharge current density. When the current density increases from 0.2 mA/cm² to 5 mA/cm², the specific capacitance gradually decreases from 18.37 mF/cm² to 7.4 mF/cm². This trend shows that the supercapacitor can still maintain good rate performance at high current density. Compared with recently reported fiber/yarn-based supercapacitors and other all-solid-state supercapacitors in terms of areal energy density, our device showed a prominent performance in energy storage, The NiCo-LDH device delivered a high energy density of 14.8 μWh cm^{-2} at a power density of 4.1 mW cm^{-1}, which was higher than its counterparts[206–213] (**Table 5.1**). **Figure 5.9 (f)** shows the GCD curves at 0.2 mA/cm² comparing the original device and the stretched state (30% and 80%). The charge and discharge curves of the stretched device are almost the same as the original device, indicating that the device can retain its structural integrity and favorable

electrochemical behavior under mechanical deformation. This performance is attributed to the elastic fiber support of the porous layered structure, which can provide effective ion transport channels under stretching.

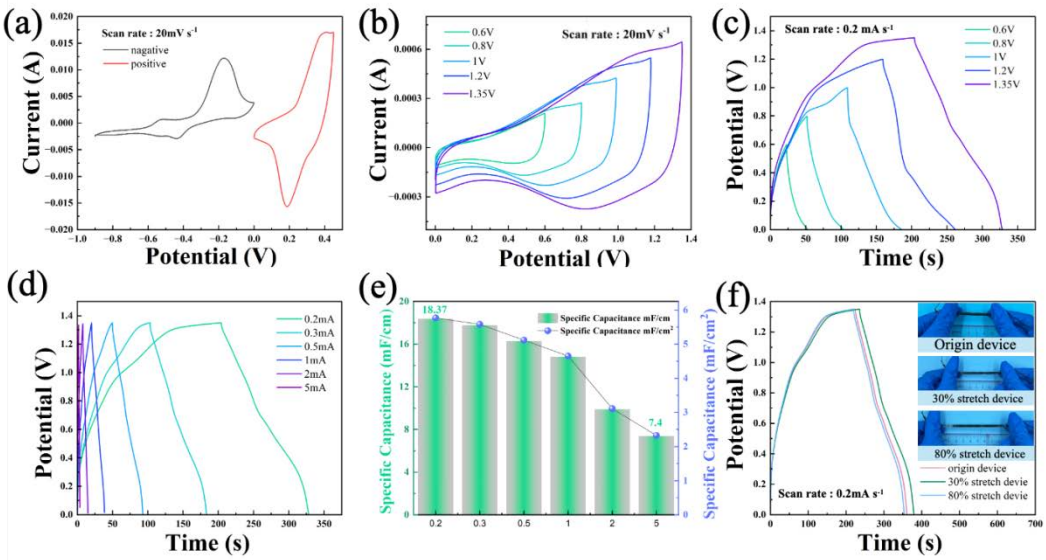

Figure 5.9 Electrochemical performance of the symmetric supercapacitor based on NiCo@HBPS$_1$ electrodes. (a) CV curves of sample I as negative and positive. (b) CV curves at different voltages and a scan rate of 20 mV s^{-1}. (c) Galvanostatic charge-discharge (GCD) curves at different voltages with a constant current density of 0.2 mA cm^{-2}. (d) GCD curves at varying current densities at 1.35V. (e) Specific capacitance as a function of discharge current density. (f) GCD curves at 0.2 mA cm^{-2}, comparing the performance of the original device and the device under stretch (30% and 80%).

Table 5.1 Comparison of electrode materials for fiber supercapacitors.

Electrode materials	Energy Density (E)	Power Density (P)	Ref.
reduced graphene oxide/polypyrrole composite	11 μWh cm^{-2}	0.03 mW cm^{-2}	206
reduced graphene oxide/CNT	3.84 μWh cm^{-2}	0.02 mW cm^{-2}	207
PET/Au/ conductive metal-organic framework	5.41 μWh cm^{-2}	0.034 mW cm^{-2}	208

reduced graphene oxide	6.8 μWh cm^{-2}	0.17 mW cm^{-2}	209
PPy/PEDOT:PSS	22.7 μWh cm^{-2}	2 mW cm^{-2}	210
PEDOT:PSS	15.73 μWh cm^{-2}	0.4 mW cm^{-2}	211
MXene ink	0.32 μWh cm^{-2}	0.11 mW cm^{-2}	212
PEDOT:PSS/Ag nanofibers	0.09 μWh cm^{-2}	0.93 mW cm^{-2}	213
NiCo-LDH nanowires	**14.8 μWh cm^{-2}**	**4.1 mW cm^{-2}**	**This work**

5.4 Conclusion

This study developed a new type of symmetrical all-solid-state supercapacitor based on NiCo-LDH@HBPS fiber. Through the core yarn structure and the breathing pattern method under high humidity conditions, a high-performance flexible electrode material with a hierarchical wrinkled porous structure was successfully constructed. The study showed that at a voltage of 1.35 V, the supercapacitor had a specific capacitance of up to 18.37 mF/cm^2 at a current density of 0.2 mA cm^{-1}, and could maintain its electrochemical performance almost unchanged under a tensile strain of up to 80%, indicating good flexibility and structural stability. The results of this study not only verified the key role of the synergistic effect of NiCo-LDH and hierarchical porous

structure in improving the electrochemical performance of supercapacitors, but also demonstrated its practical application potential in wearable electronic devices and smart textiles. This study provides new design ideas and technical references for the future development of high-performance, flexible and stretchable energy storage systems.

Chapter 6 Hierarchically Porous NiCo-LDH@CNT/SBS Composites for High-Performance Stretchable Supercapacitors in Wearable Electronics

6.1 Introduction

The rapid adoption of wearable electronic devices, including health monitors, e-textiles, and fitness trackers, has significantly increased the demand for flexible, stretchable, and durable energy storage systems[214,215]. Supercapacitors have garnered considerable attention among various energy storage technologies owing to their high-power density, fast charge-discharge capability, and long cycle life[216,217]. However, integrating traditional supercapacitors with wearable devices is challenging because these devices tend to lose energy storage capacity when subject to mechanical deformations such as bending, twisting, or stretching[111,218,219]. Therefore, stretchable supercapacitors that can maintain their electrochemical performance under deformation have become a focal point of research.

To meet the stringent mechanical and electrochemical requirements of wearable electronics, advanced material matchings and innovative structures have been designed to provide flexibility and energy storage. Carbon-based materials[220], particularly carbon nanotubes (CNTs)[221] and carbon fibers[222], have become indispensable in this field owing to their superior electrochemical double-layer (EDLC) energy storage nature, mechanical strength, and structural versatility. However, the energy storage capacity of carbon-based materials still needs to be improved due to the ion adsorption and desorption characteristics of EDLC. When combined with pseudocapacitive materials

like transition metal oxides (e.g., MnO_2) or conductive polymers (e.g., polyaniline), these hybrid systems can achieve higher energy storage capacity while maintaining the mechanical flexibility of carbon-based substrates[223,224]. For instance, fabric-shaped supercapacitors made from a rubber-like stretchable hybrid CNT film exhibited remarkable stretchability, retaining their capacitance under strains as high as 134%[225]. Flexible fiber-shaped CNT supercapacitors have improved the performance of elastomeric supercapacitors with a coiled MnO_2-biscrolled CNT yarn[226]. Despite these hybrid materials providing good flexibility, they still suffer from decreased capacitance under repeated or extreme stretching[227]. Additionally, although pseudocapacitive materials effectively enhance energy storage, the properties tend to degrade over time due to cycling fatigue, especially in highly stretchable systems. Therefore, achieving high electrochemical performance while maintaining mechanical durability under high continuity and extreme strain remains unresolved.

Nickel-cobalt layered double hydroxide (NiCo-LDH) has emerged as a superior pseudocapacitive material to conventional transition metal oxides or conductive polymers[228–230]. Owing to highly efficient faradaic activity, NiCo-LDH offers some active sites for redox reactions to boost energy storage capacity. Additionally, the layered structure of NiCo-LDH facilitates ion transport, improving charge storage efficiency. Compared with other transition metal oxides, NiCo-LDH also exhibits better mechanical flexibility, making it an ideal pseudocapacitive material candidate for stretchable supercapacitors. For example, a represented stretchable supercapacitor composed of MnO_2-deposited nylon/CNT fibers exhibited poor cycling stability,

reduced conductivity, and a 15% decrease in capacitance when stretched to 150% strain[231].

In contrast, the combination of NiCo-LDH with $Ti_3C_2T_x$ enhances the electrochemical performance and significantly improves mechanical stability, particularly under dynamic deformation conditions[232,233]. Recently, hierarchical porous structures have been proven to effectively increase the electrode surface area[234–236], thereby improving both charge storage capacity and ion diffusion, while maintaining excellent mechanical flexibility of the electrode system. Additionally, stretchable supercapacitors may be able to regain their electrochemical properties after being stretched thanks to elastic materials. This would extend their useful life under high continuity and extreme strain [237,238].

Herein, styrene-butadiene-styrene (SBS) was combined with CNTs for casting onto pre-stretched carbon fabric using the breath figure (BF) method under high-humidity conditions. This BF technique utilizes evaporative cooling to induce the condensation of water droplets on the material's surface, which then self-assemble into an ordered microstructure that acts as a dynamic template. The unique process resulted in a hierarchically, buckled, porous structure on the surface of the carbon fabric, which is crucial for the hydrothermal growth of NiCo-LDH. A novel stretchable electrode with hierarchical porous architecture was formed by using CNT/SBS as the stretchable skeleton for NiCo-LDH loading, achieving a synergistic improvement in the electrochemical performance and stretchability of the stretchable supercapacitor. Under an 80% tensile strain, the supercapacitor retains 94% of its initial capacitance,

showcasing excellent mechanical resilience and energy storage stability. In cyclic stability tests, the device demonstrated less than 8% degradation in capacitance over 20,000 charge-discharge cycles, further highlighting its long-term durability. Additionally, the specific capacitance of the device reaches up to 4948 mF cm^{-2} at 2 mA cm^{-2}, illustrating superior energy storage capability compared to conventional flexible energy storage systems. The combination of high flexibility, stable electrochemical properties, and strong cycling stability under dynamic conditions makes this stretchable supercapacitor a competitive candidate for next-generation wearable technology applications such as health monitoring and smart textiles.

6.2 Experimental Section

6.2.1 Materials

The following materials were used for the experiments: polystyrene-block-polybutadiene-block-polystyrene (SBS), multi-walled carbon nanotubes (MWCNTs), chloroform ($CHCl_3$), cobalt(II) sulfate hexahydrate ($CoSO_4 \cdot 6H_2O$), nickel(II) sulfate hexahydrate ($NiSO_4 \cdot 6H_2O$), potassium hydroxide (KOH), sodium dodecylbenzene sulfonate (SDBS), acrylamide, N,N′-methylene-bisacrylamide (BMAA), potassium persulfate (KPS), tetramethylethylenediamine (TEMED), and 3K carbon fibers were purchased from Sigma-Aldrich. All reagents were of analytical grade and used without further purification.

6.2.2 Fabrication of conductive buckled porous carbon fabrics

A 2×2 twill knitted of 3K carbon fibers was prepared to ensure sufficient elasticity

of the fabric. The knitted carbon fabrics were then subject to solution casting. The casting solution was a mixture of SBS/$CHCl_3$ (200 mg/mL) and CNT/$CHCl_3$ (40 mg/mL) in varying ratios. The three ratios used for solution casting were 200 mg/mL SBS/$CHCl_3$: 40 mg/mL CNT/$CHCl_3$ = 1:1, 1:2, and 1:3. Before casting, the carbon fabrics were pre-stretched to induce a buckled structure. The solutions were then cast onto the stretched carbon fabrics, allowing interfacial self-assembly the formation of a buckled porous structure through the breath figure method under high-humidity conditions (humidity >90%). After casting, the samples were dried completely at room temperature, then the fibers were removed and subjected to annealing and drying at 90°C. The resulting samples were labeled based on the casting solution used: CNT_1SBS_1@F, CNT_2SBS_1@F, and CNT_3SBS_1@F.

6.2.3 Preparation of NiCo-LDH coated the different CNT_aSBS_b@F

The buckled porous carbon fabrics samples (CNT_1SBS_1@F, CNT_2SBS_1@F, and CNT_3SBS_1@F) were fully dried, and they were subject to hydrothermal treatment to grow NiCo-LDH nanostructures on the surface. The hydrothermal process was carried out at 120°C for 12 hours. The hydrothermal solution consisted of varying concentrations of cobalt (II) sulfate hexahydrate, nickel (II) sulfate hexahydrate, urea, and SDBS. Three different solutions were prepared: 20 mM $CoSO_4 \cdot 6H_2O$, 20 mM $NiSO_4 \cdot 6H_2O$, excess urea, and 0.1 wt% SDBS; 20 mM $CoSO_4 \cdot 6H_2O$, 40 mM $NiSO_4 \cdot 6H_2O$, excess urea, and 0.1 wt% SDBS; 40 mM $CoSO_4 \cdot 6H_2O$, 20 mM $NiSO_4 \cdot 6H_2O$, excess urea, and 0.1 wt% SDBS, respectively. After the hydrothermal treatment, the resulting samples were labeled according to the NiCo-LDH coating

applied to the original porous carbon fabrics. The samples prepared with solution (20 mM $CoSO_4 \cdot 6H_2O$, 40 mM $NiSO_4 \cdot 6H_2O$) on the CNT_2SBS_1@F scaffold were named $Ni_{20}Co_{40}$ LDH@CNT_2SBS_1@F, where the total mass loading of NiCo-LDH nanoflakes was approximately 2 mg cm^{-2}. The other samples were labeled as $Ni_{20}Co_{20}$ LDH@CNT_1SBS_1@F and $Ni_{40}Co_{20}$ LDH@CNT_3SBS_1@F, respectively.

6.2.4 Fabrication of the all-solid-state symmetric supercapacitor

The gel electrolyte was prepared by dissolving 2.5 g of acrylamide and 2.5 mg of BMAA in 10 mL of deionized water. This solution added 0.06 g of KPS and 5 μL of TEMED under constant stirring at room temperature. Once homogeneous, 10 mL of 6 M KOH solution was rapidly added to form a pre-gel electrolyte solution. The prepared $Ni_{20}Co_{40}$-LDH@CNT_2SBS_1@F electrodes were immersed in the gel electrolyte for 30 seconds to ensure uniform absorption. The samples were then allowed to solidify at 50°C for 30 minutes. This process was repeated 2-3 times to ensure a uniform coating of the gel electrolyte on the fibers. After the final coating, the samples of two same-coated gel $Ni_{20}Co_{40}$-LDH@CNT_2SBS_1@F were assembled into symmetric supercapacitors and stored at room temperature for full solidification.

6.2.5 Characterization

To comprehensively analyze the samples of NiCo@CNTSBS@F, CNTSBS@F and fabrics, several characterization techniques were employed. Their air permeabilities under different stretching states will be also measured by air-permeability tester. Scanning electron microscopy (SEM) was performed using a Tescan MIRA field

emission SEM to examine surface morphology, coupled with energy-dispersive X-ray spectroscopy (EDX) to map the elemental distribution. High-resolution transmission electron microscopy (HRTEM) was conducted on a JEOL JEM-2010 to observe nanostructures and lattice fringes. X-ray photoelectron spectroscopy (XPS) was carried out with a Thermo Scientific Nexsa G2 system to analyze elemental composition and oxidation states. The XRD pattern was performed on a Bruker X-ray diffractometer (D8 Advance) with Cu Kα radiation. The electrochemical performance of the fabricated supercapacitors (NiCo @CNTSBS@F, size 1*1cm) and the all-solid-state symmetric supercapacitor were tested via an electrochemical workstation instrument (CHI 660E, shanghai chenhua instrument Co., Ltd.) The NiCo @CNTSBS@F samples as a working electrode were evaluated using a three-electrode system in a 3 M KOH aqueous electrolyte. A graphite plate and a saturated calomel electrode served as the counter and reference electrodes, respectively. Cyclic voltammetry (CV), galvanostatic charge-discharge (GCD), and electrochemical impedance spectroscopy (EIS) were employed to characterize the capacitive behavior, rate performance, and impedance characteristics of the supercapacitor. The cycling stability of the supercapacitors was evaluated through continuous GCD cycling at 20 mA cm^{-2} for 5000 cycles and 20,000 cycles, in the gel and solution electrolytes. Specific capacitances were calculated from the GCD profiles using the following equation:

$$C = \frac{I*\Delta t}{\Delta V}$$

where I is the discharge current (mA cm^{-2}), Δt is the discharge time (s), and ΔV is the potential window(V).

The energy density (E) and power density (P) were calculated using the following equations:

$$E = \frac{1}{2} * C * \frac{U^2}{3600}$$

$$P = \frac{E * 3600}{\Delta t}$$

where U and Δt are the voltage window (V) and the discharging duration (s), respectively.

6.3 Results and Discussion

In the preparation process of supercapacitor, to enhance the stretchability and flexibility of the carbon fabrics, the carbon fiber was initially knitted into the carbon fabrics (**Figure 6.1 (a)**). This knitted fabrics involved forming a flexible 2×2 twill structure through a knitted carbon fiber arrangement, which enhanced the material's ability to deform under external forces and allowed it to endure more significant levels of stretching and bending. To obtain a large specific surface area and hierarchically buckled porous structure fabrics (HBPFSs), the pre-stretched carbon fabrics were coated with a mixture of different radio of SBS/$CHCl_3$ and CNT/$CHCl_3$ solutions (named CNT_aSBS_b@F) and processed under a high-humidity environment using the BF Method[167,239] (**Figure 6.1 (b)**). This technique utilizes evaporative cooling to induce the condensation of water droplets on the material's surface. These water droplets self-assemble into an ordered microstructure, acting as a dynamic template that facilitates the formation of an ordered porous network of SBS/CNT on the fabric surface (**Figure 6.1 (d)**). The elasticity of SBS provides the composite material with excellent durability

and mechanical stability[240], while CNT establishes a continuous conductive pathway[241]. Following the formation of the porous conductive fabric, hydrothermal treatment was applied to induce the growth of different contents ratios of nickel-cobalt layered double hydroxide (NiCo-LDH) nanostructures (named Ni_xCo_y LDH@CNT_aSBS_b@F) (**Figure 6.1 (c)**). NiCo-LDH is recognized for its considerable electrochemical activity and ion exchange properties. Through hydrothermal synthesis, NiCo-LDH nanosheets are uniformly deposited across both the surface and inner pores of the SBS/CNT porous composite (**Figure 6.1 (e)**), resulting in a hierarchical structure that further enhances the material's specific surface area and active sites[242,243]. In the molecular and chemical structure of CNTs combined with NiCo-LDH (**Figure 6.1 (f) and (g)**), the distinctive configuration of NiCo-LDH nanowires effectively facilitates charge transfer and accelerates ion diffusion[244,245], which improves the capacitor's fast charge-discharge performance. Additionally, the mechanical interlocking provided by the porous network substantially strengthens the adhesion between NiCo-LDH nanosheets and the substrate, ensuring stability and minimizing detachment throughout repeated charge-discharge cycles[246,247].

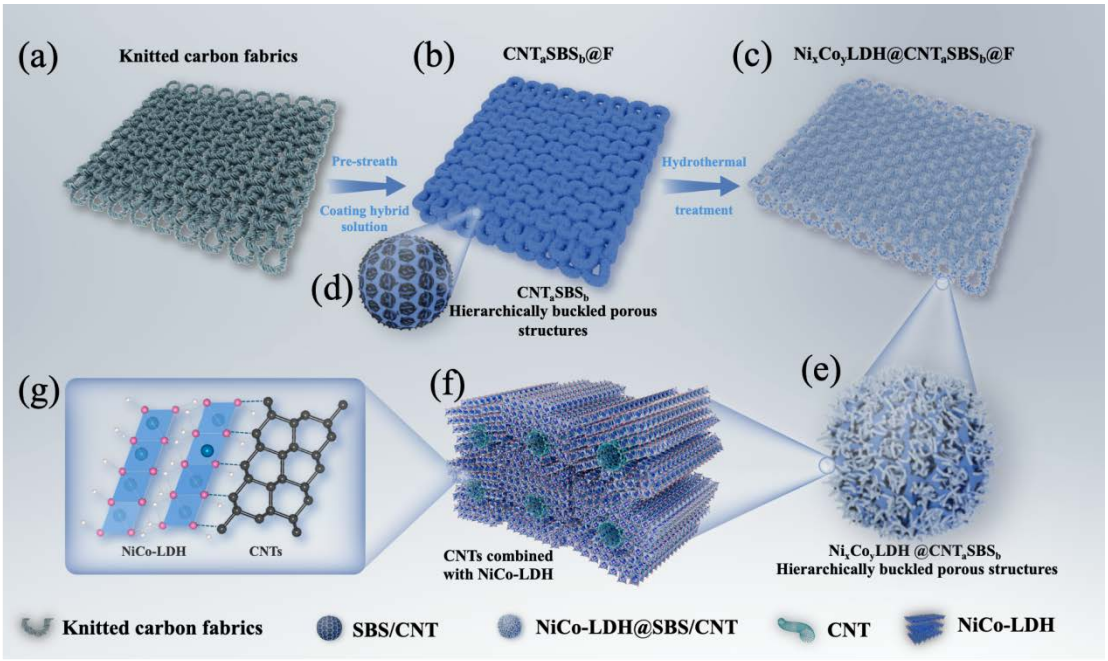

Figure 6.1 Schematic and mechanism illustration of the formation process of Ni_xCo_y LDH@CNT_aSBS_b@F. (a) Modified knitting fabrics. (b) Hierarchically buckled porous structure formation of CNT_aSBS_b on the knitted fabric. (c) Ni_xCo_y LDH growth on the CNT_aSBS_b@F. (d) CNT_aSBS_b@F magnified image. (e) Ni_xCo_y LDH@CNT_aSBS_b@F magnified image. The schematic molecular model (f) and chemical structure (g) of CNTs combined with NiCo-LDH.

SEM images are used to track the hierarchical porous structures of carbon fabrics with varying ratios of SBS/$CHCl_3$ and CNT/$CHCl_3$ solutions. At a 1:1 ratio of SBS/$CHCl_3$ to CNT/$CHCl_3$ solutions to form CNT_1SBS_1 @ F (**Figure 6.2 (a), (b)**), the SBS matrix dominates the formation of the porous structure through the breath figure template, resulting in a relatively regular and uniform porous network with large and evenly distributed pores across the carbon fabric surface. The low CNT content at this ratio does not significantly impact the pore formation, as SBS remains the primary factor in stabilizing the structure. The SBS matrix provides sufficient support to maintain a smooth and consistent porous structure, critically for subsequent material deposition. When the ratio of SBS/$CHCl_3$ to CNT/$CHCl_3$ increases to 1:2, the pore size decreases, and the structure of CNT_1SBS_1 @ F becomes more densely packed (**Figure**

6.2 (c), (d)). While the breath figure method is still effective at this ratio, the reduced SBS content leads to less stabilization of the pore network, making the structure slightly less orderly than the 1:1 ratio. The CNTs begin to play a more prominent role in forming the backbone of the porous structure, but the reduction of the SBS matrix compromises the regularity of the pores. When the ratio of SBS/$CHCl_3$ to CNT/$CHCl_3$ increases further to 1:3 (**Figure 6.2 (e), (f)**), the SBS matrix on the carbon fabrics is no longer sufficient to stabilize the breath figure process. The excess CNT content destabilizes the solution, disrupting the water droplet template and resulting in irregular or absent pores. These results suggest that a proper balance between SBS/$CHCl_3$ and CNT/$CHCl_3$ solutions is crucial for achieving a stable and regular porous network. Excessive CNT content, while potentially increasing electrical conductivity, can negatively impact pore formation, which may affect ion diffusion and charge transport.

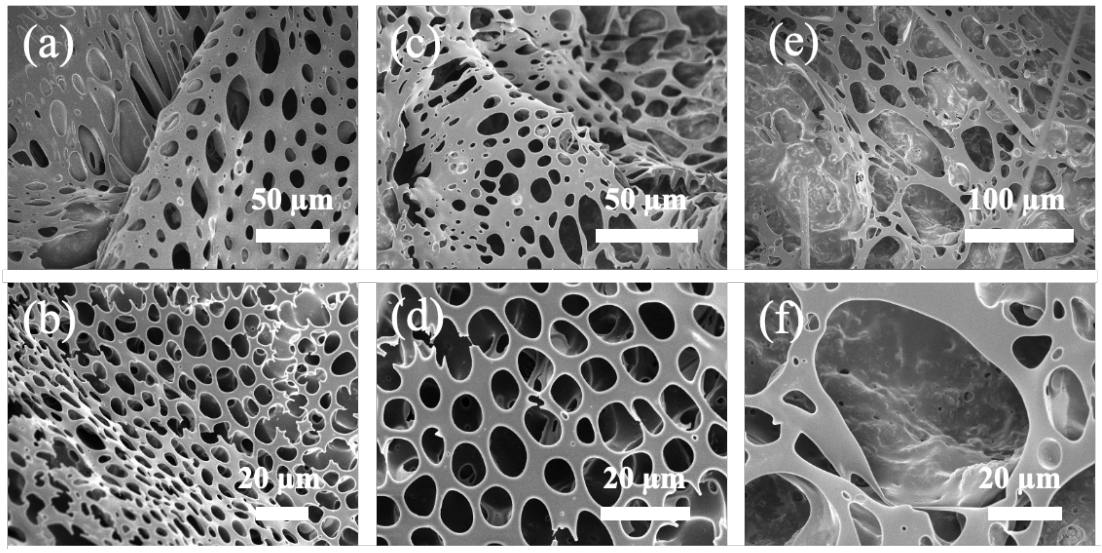

Figure 6.2 SEM images of different SBS and CNT ratios solution coatings on carbon fabric substrates at varying magnifications. (a, b) the morphology of CNT_1SBS_1 @ F, (c, d) the morphology of CNT_2SBS_1 @ F, (e, f) the morphology of CNT_3SBS_1 @ F.

The NiCo-LDH growth on carbon fabrics with different ratios of SBS/$CHCl_3$ and CNT/$CHCl_3$ solutions after hydrothermal treatment is also studied

with SEM images (**Figure 6.3**). **Figure 6.3 (a-c)** represent the SEM images of $Ni_{20}Co_{40}$ LDH@CNT_1SBS_1@F, where large and evenly distributed pores are observed on the carbon fabric surface, but NiCo-LDH growth is relatively sparse, indicating that the available CNT nucleation sites are limited at this ratio. The lower CNT content does not provide sufficient active sites for extensive NiCo-LDH deposition. The $Ni_{20}Co_{40}$-LDH @ CNT_2SBS_1@ F shows denser and more uniformly distributed NiCo-LDH growth. In **Figure 6.3 (d)**, the increased CNT content provides more nucleation sites for NiCo-LDH growth, resulting in a denser network of nanowires across the porous structure. The enhanced distribution of NiCo-LDH nanowires in **Figure 6.3 (e)** further demonstrates that a higher CNT content can improve the material's surface area, making it more favorable for electrochemical reactions. **Figure 6.3 (f)** illustrates that the NiCo-LDH layer covers a significant portion of the carbon fabric with a well-developed nanowire structure, suggesting more electrochemically active sites than the lower CNT content samples. However, at the highest CNT/$CHCl_3$ to SBS/$CHCl_3$ ratio of 3:1, the $Ni_{20}Co_{40}$ LDH @ CNT_3SBS_1 @ F exhibits an irregular porous structure. As seen in **Figure 6.3 (g)**, the excess CNT content disrupts the breath figure template, leading to the collapse of the pore structure and uneven growth of NiCo-LDH. **Figure 6.3 (h), (i)** show that NiCo-LDH aggregates on the surface, forming clumps that may hinder uniform ion transport. The destabilized pore structure and irregular nanowire growth can potentially reduce the material's electrochemical performance, as the distribution of active sites becomes less optimal. In conclusion, the $Ni_{20}Co_{40}$ LDH@CNT_2SBS_1@F exhibits the best porous structure and the most uniform NiCo-

LDH growth. The higher CNT content provides more growth sites, resulting in a denser nanosheet structure, which is expected to enhance electrochemical performance.

The influence of Ni and Co concentrations on the morphology of NiCo-LDH growth on the CNT_2SBS_1 @ F substrate is further investigated. At equal concentrations of Ni^{2+} and Co^{2+} (20 mM each, **Figure 6.4 (a), (b)**), the $Ni_{20}Co_{20}$ LDH @ CNT_2SBS_1 @ F shows well-ordered NiCo-LDH nanowires forming across the porous structure. The uniform distribution of these nanowires creates heavy active sites for electrochemical reactions, and the porous network remains intact, which is crucial for effective ion transport[243]. As the Co concentration increases to 40 mM (**Figure 6.4 (c), (d)**), the sample $Ni_{20}Co_{40}$ LDH @ CNT_2SBS_1 @ F exhibits denser nanowire growth, with smaller pore sizes, enhancing the surface area available for electrochemical activity. The compact arrangement of these nanowires provides an ideal balance between maintaining the porous structure and maximizing the number of active sites. In contrast, when the Ni^{2+} concentration is increased to 40 mM (**Figure 6.4 (e), (f)**), t the excessive NiCo-LDH $Ni_{40}Co_{20}$ LDH on the CNT_2SBS_1 @ F shows a nanosheet architecture instead of a nanowire structure, almost completely covering the original porous substrate. This dense layer of nanosheets obscures the underlying pore network, potentially reducing the accessibility of the electrochemically active sites and hindering ion diffusion. Fortunately, the air permeability of all samples without stretching reached 100mL/s, and the air permeability became larger after stretching. These results highlight the importance of controlling the Ni^{2+} and Co^{2+} concentrations to preserve the porous architecture while optimizing the nanostructure morphology for electrochemical

applications. EDX elemental mappings confirm the uniform distribution of Ni, Co, and O throughout the CNT_2SBS_1@ F substrate. **Figure 6.5 (a-c)** correspond to the samples $Ni_{20}Co_{20}$ LDH @ CNT_2SBS_1 @ F, $Ni_{20}Co_{40}$ LDH @ CNT_2SBS_1@F, and $Ni_{40}Co_{20}$ LDH@CNT_2SBS_1@F, respectively. The elemental mappings demonstrate that Ni and Co are evenly distributed across the surface of the porous structure, ensuring that the NiCo-LDH nanowires/nanosheets are uniformly integrated throughout the substrate.

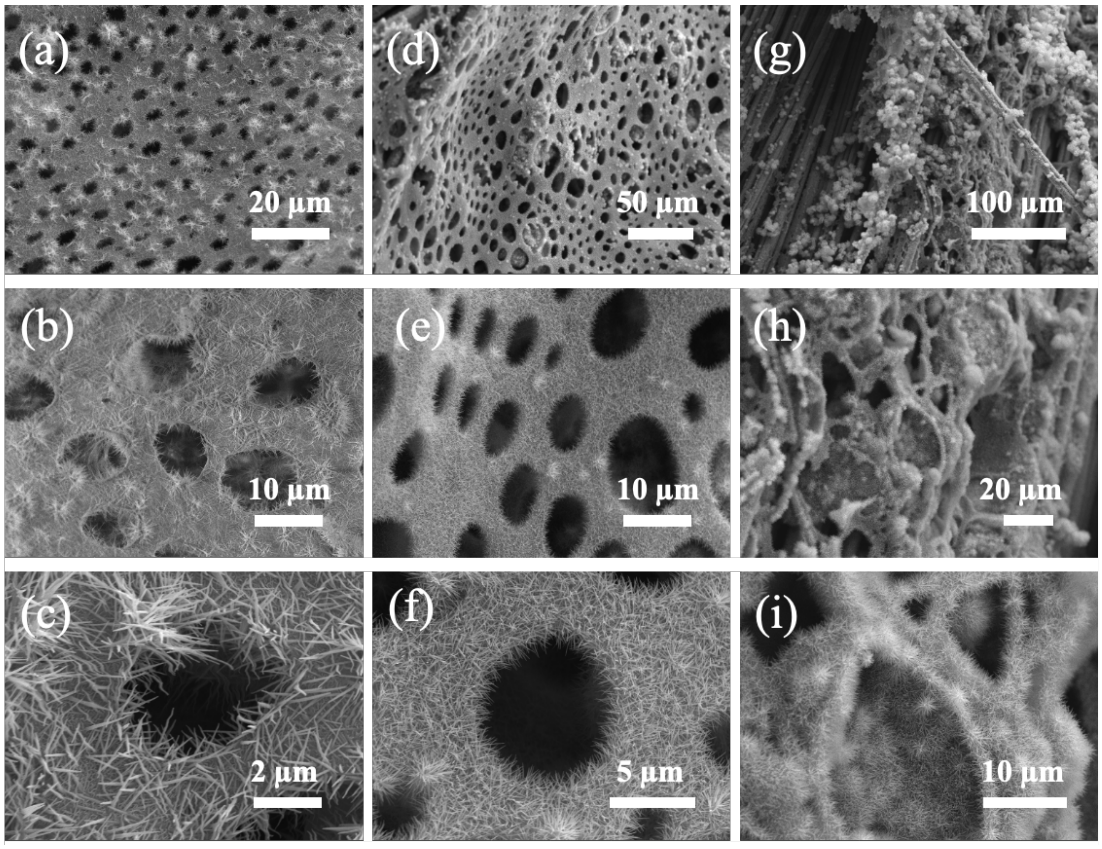

Figure 6.3 SEM images of NiCo-LDH on the carbon fabric cast with different SBS and CNT ratio solutions at different magnifications. (a-c) $Ni_{20}Co_{40}$ LDH @ CNT_1SBS_1 @ F, (d-f) $Ni_{20}Co_{40}$ LDH@CNT_2SBS_1@F, and (g-i) $Ni_{20}Co_{40}$ LDH@CNT_2SBS_1@F.

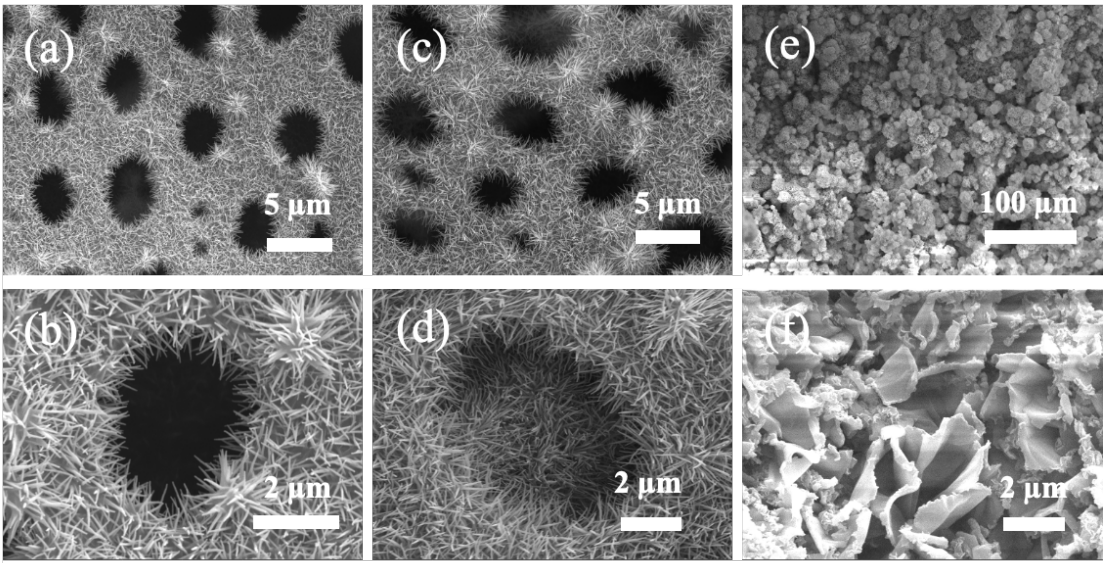

Figure 6.4 Micromorphology characterization of the growth and distribution of NiCo-LDH under the CNT_2SBS_1@F hydrothermal different Ni_2SO_4 and Co_2SO_4 mixed solutions. (a, b) different magnified typical SEM image of $Ni_{20}Co_{20}$ LDH @ CNT_2SBS_1 @ F, (c, d) different magnified typical SEM image of $Ni_{20}Co_{40}$ LDH@CNT_2SBS_1@F, and (e, f) different magnified typical SEM image of $Ni_{40}Co_{20}$ LDH@CNT_2SBS_1@F.

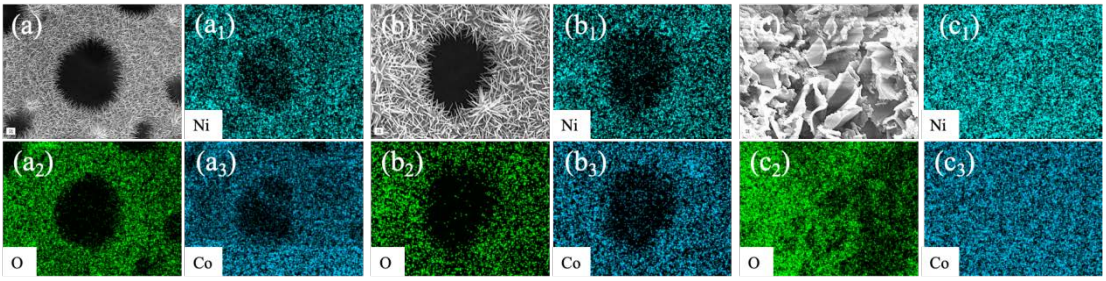

Figure 6.5 EDX elemental mappings for the three samples: (a-a3) $Ni_{20}Co_{20}$ LDH@CNT_2SBS_1@F, (b-b3) $Ni_{20}Co_{40}$ LDH@CNT_2SBS_1@F, and (c-c3) $Ni_{40}Co_{20}$ LDH@CNT_2SBS_1@F.

X-ray photoelectron spectroscopy (XPS) is used to analyze the elemental composition and chemical states of the as-prepared NiCo-LDH of $Ni_{20}Co_{40}$ LDH@CNT_2SBS_1@F. In the overall survey spectrum (**Figure 6.6 (a)**), distinct peaks corresponding to Ni 2p, Co 2p, O 1s, and C 1s confirm the presence of Ni and Co, verifying the successful formation of NiCo-LDH. High-resolution XPS spectra further reveal detailed information about the oxidation states of Ni and Co. The Ni 2p spectrum

(**Figure 6.6 (b)**) displays two main peaks at binding energies of 873.5 eV and 855.3 eV, corresponding to Ni $2p_{1/2}$ and Ni $2p_{3/2}$, respectively. The satellite peaks and deconvoluted components also indicate the coexistence of Ni^{2+} and Ni^{3+} oxidation states. The Co 2p spectrum (**Figure 6.6 (c)**) shows characteristic peaks at 796.4 eV (Co $2p_{1/2}$) and 781.4 eV (Co $2p_{3/2}$), with deconvolution revealing the presence of Co^{2+} and Co^{3+}. The NiCo-LDH structure is composed of a mixed valence of Ni and Co, which is crucial for enhancing the redox reactions in energy storage applications. The high-resolution transmission electron microscopy (HR-TEM) images provide further insights into the nano-structural features of the NiCo-LDH. **Figure 6.6 (d)** shows a well-defined nanowire structure, and the diameter is approximately 40 nm. The lattice fringes observed in **Figure 6.6 (e)** correspond to an interplanar spacing of 0.467 nm, indexed to the (003) plane of LDH. **Figure 6.7** presents the X-ray diffraction (XRD) pattern of $Ni_{20}Co_{40}$ LDH. The characteristic peaks at 11.3°, 33.5°, 34,4° and 61.3° are detected, which are attributed to the crystal planes of (003), (101), (012), and (113), respectively. Elemental mapping (**Figure 6.6 (f)**) further confirms the homogeneous distribution of Ni, Co, and O throughout the nanowire.

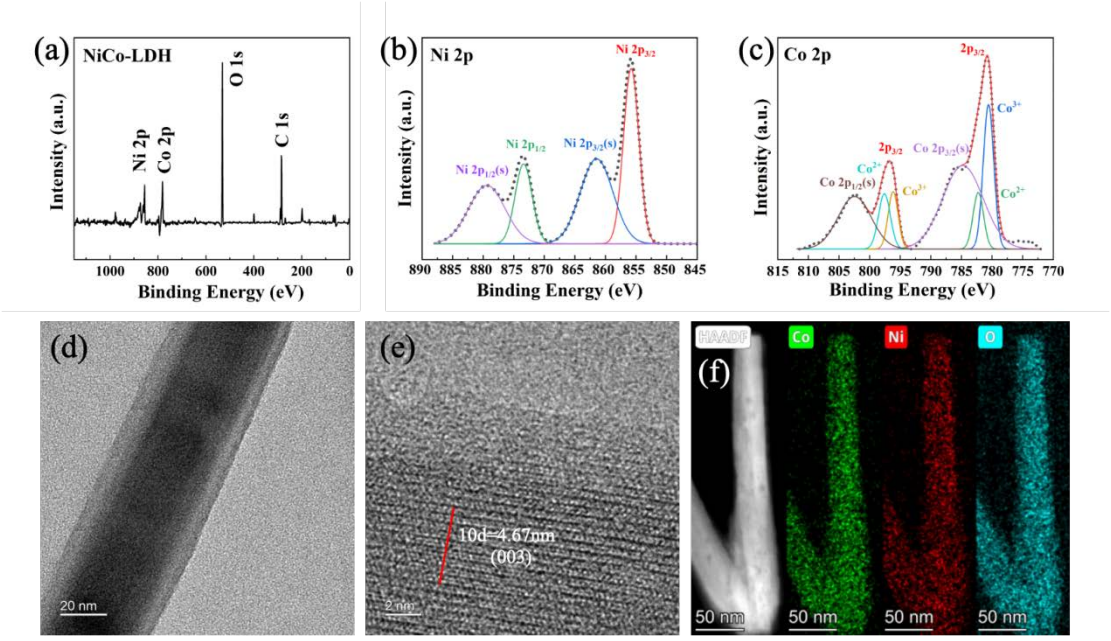

Figure 6.6 (a) XPS survey spectrum of the NiCo-LDH sample. (b) High-resolution XPS spectrum of Ni 2p. (c) High-resolution XPS spectrum of Co 2p. (d) TEM image of NiCo-LDH. (e) HR-TEM image of the NiCo-LDH structure. (f) Elemental mapping displays the Ni, Co, and O distribution in the nanostructure.

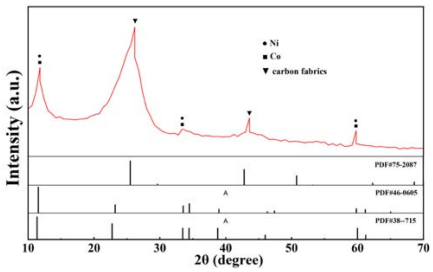

Figure 6.7 X-ray diffraction (XRD) image of $Ni_{20}Co_{40}$ LDH@CNT_2SBS_1@F.

The electrochemical performance of the prepared fabrics is systematically investigated by a standard three-electrode system in 3M KOH solution, including cyclic voltammetry (CV), galvanostatic charge-discharge (GCD), and electrochemical impedance spectroscopy (EIS). The NiCo-LDH growth fabrics, including $Ni_{20}Co_{40}$ LDH@CNT_2SBS_1@F, $Ni_{20}Co_{40}$ LDH@CNT_1SBS_1@F, $Ni_{20}Co_{40}$ LDH@CNT_3SBS_1@F, $Ni_{40}Co_{20}$ LDH@CNT_2SBS_1@F, and $Ni_{20}Co_{20}$ LDH@CNT_2SBS_1@F are named as I, II, III, IV, and V, respectively. The fabrics without NiCo-LDH growth, including pure knitted carbon fabric, CNT_3SBS_1@F,

CNT_1SBS_1@F, SBS@F, and (X) CNT_2SBS_1@F are named as VI, VII, VIII, IX, and X, respectively. The CV curves (**Figure 6.8 (a)** and **6.9**) for the as-prepared fabrics at 10 mV s^{-1} present rectangular shapes with obvious redox peaks, revealing the combination of EDLC characteristic of CNTs and pseudocapacitive nature of NiCo-LDH. Among the NiCo-LDH fabrics, sample I exhibits the highest current response and the largest enclosed CV area, indicating the best electrochemical performance owing to its well-defined, uniformly buckled and porous structure, which facilitates the optimal growth of NiCo-LDH nanowires. As the sample progresses to V, there is a noticeable reduction in both the current response and the CV area, signifying a gradual decrease in capacitance. This is due to the excessive dosage of NiCo-LDH nanosheets with uneven distribution or insufficient NiCo-LDH nanowires on the porous structure of the knitted fabric substrate. For the fabrics without NiCo-LDH growth, the current response and the CV area are greatly reduced, becoming almost identical. These samples exhibit moderate current response and CV area owing to inherent capacitive nature of pure knitted carbon fabric and CNTs. These results demonstrate that the electrochemical performance of the knitted fabrics is attributed to the appropriate CNTs and NiCo-LDH distribution.

The GCD curves at 2 mA cm^{-2} of the fabrics are presented in **Figure 6.8 (b)** and **6.10**. Sample I demonstrates the longest discharge time, reflecting its highest energy storage capacity. Meanwhile, its nearly symmetrical charge and discharge profiles suggest excellent Coulombic efficiency owing to the highly interconnected porous structure and reversible redox reactions of NiCo-LDH/CNT composite. As the sample

progresses to V, there is a gradual reduction in the discharge time. For the samples without NiCo-LDH growth, shorter discharge times are observed. In **Figure 6.8 (c)** and **6.11**, all fabrics exhibit minor interceptions on the x-axis and small semicircles in the high-frequency region, indicating low internal resistance Rs and charge transfer resistance (Rct), along with high conductivity and efficient charge transport. **Figure 6.8 (d)** and **6.12** show the CV curves of all samples at various scan rates. As the scan rate increases, the redox peaks symmetrically shift toward more positive and more negative potentials, respectively, suggesting good electrochemical reversibility. At 2 mV/s, two distinct redox peaks (Peak 1 and Peak 2) are observed, highlighting the pseudocapacitive behavior. **Figure 6.8 (e)** further analyzes the fitting relationship between the two peak currents and scan rates in a logarithmic plot of sample I. Peak 1 exhibits a slope of 0.5882 and Peak 2 shows a slope of 0.2445，indicating that diffusion-controlled process governs electrochemical behavior.

Figure 6.8 (f) and **6.13** present GCD curves of all samples at various current densities. As the discharge current increases, the discharge time decreases. Among the fabrics with NiCo-LDH growth, sample I exhibits the longest discharge time at the same discharge current, indicating its highest charge storage capability. Compared with the fabrics with NiCo-LDH, the fabrics without NiCo-LDH growth exhibit shorter discharge times. Based on the GCD files, **Figure 6.8 (g)** illustrates the specific capacitance of sample I at different discharge currents. At 2 mA cm^{-2}, sample I demonstrates a maximum specific capacitance of 4,948 mF cm^{-2}, indicating its excellent charge storage capacity. As the discharge current increases to 10 mA cm^{-2}, the

specific capacitance gradually decreases to 3,288 mF cm^{-2}, reaching a high capacitance rate of 66.45%. **Figure 6.8 (h)** compares the specific capacitance of all samples at 2 mA cm^{-2}. Sample I exhibits the highest specific capacitance (4,948 mF cm^{-2}) among the fabrics with NiCo-LDH growth, which is attributed to the optimized porous structure of the knitted fabrics and appropriate distributions of CNTs and NiCo-LDH nanowires. For the samples without NiCo-LDH, the specific capacitance values drop sharply. **Figure 6.8 (i)** further illustrates the diffusion-controlled and surface-controlled contributions at various scan rates of sample I. At lower scan rates of 2 mV s^{-1}, diffusion-controlled contributions are approximately 80.55%, indicating that ions have sufficient time to penetrate deep into the porous structure of fabric and participate in the redox reactions. An increasing scan rate enhances the dominance of surface-controlled charge storage mechanisms, which account for 69.97% at 50 mV·s^{-1}, implying that the electrochemical process is primarily governed by surface-confined reactions. These results demonstrate that the sample I exhibits both diffusion-controlled and surface-controlled charge storage behaviors depending on the scan rate.

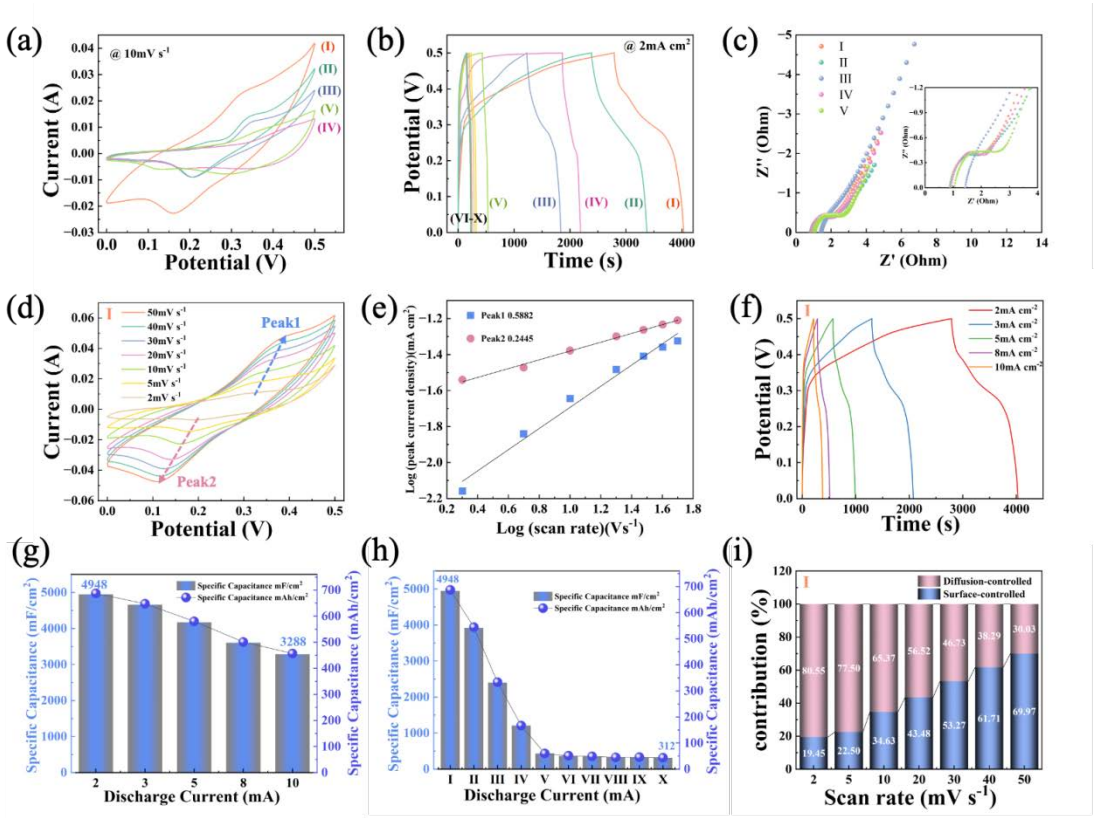

Figure 6.8 Electrochemical performance of Samples I-X. (a) CV curves of samples I-V at 10 mV s^{-1}. (b) GCD curves of samples I-X at 2 mA cm^{-2}. (c) Nyquist plots of samples I-V, the inset shows the magnified high-frequency region. (d) CV curves of Sample I at varying scan rates. (e) Log-log plot of peak current density vs. scan rate for sample I. (f) GCD curves of sample I at different current densities. (g) Specific capacitance of sample I as a function of discharge current density. (h) Specific capacitance of samples I-X at 2 mA cm^{-2}. (i) Contribution of diffusion-controlled and surface-controlled capacitance for Sample I at different scan rates.

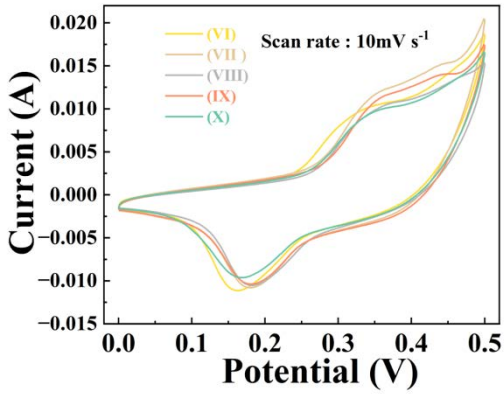

Figure 6.9 Cyclic voltammetry (CV) curves of Samples VI-X at a scan rate of 10 mV.

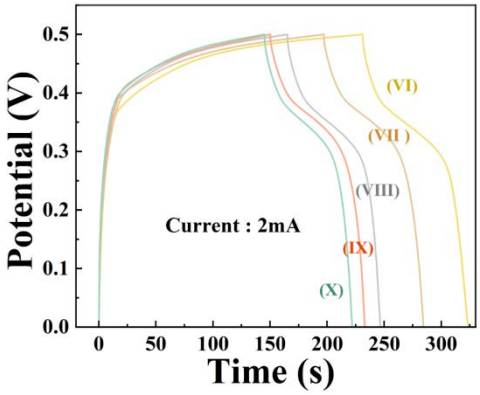

Figure 6.10 Galvanostatic charge-discharge (GCD) curves of Samples VI-X at a 2 mA cm^{-2} current density.

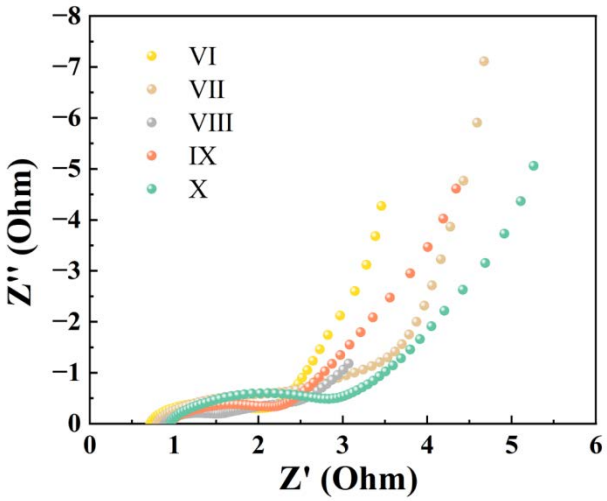

Figure 6.11 Nyquist plots of Samples VI-X obtained from electrochemical impedance spectroscopy (EIS).

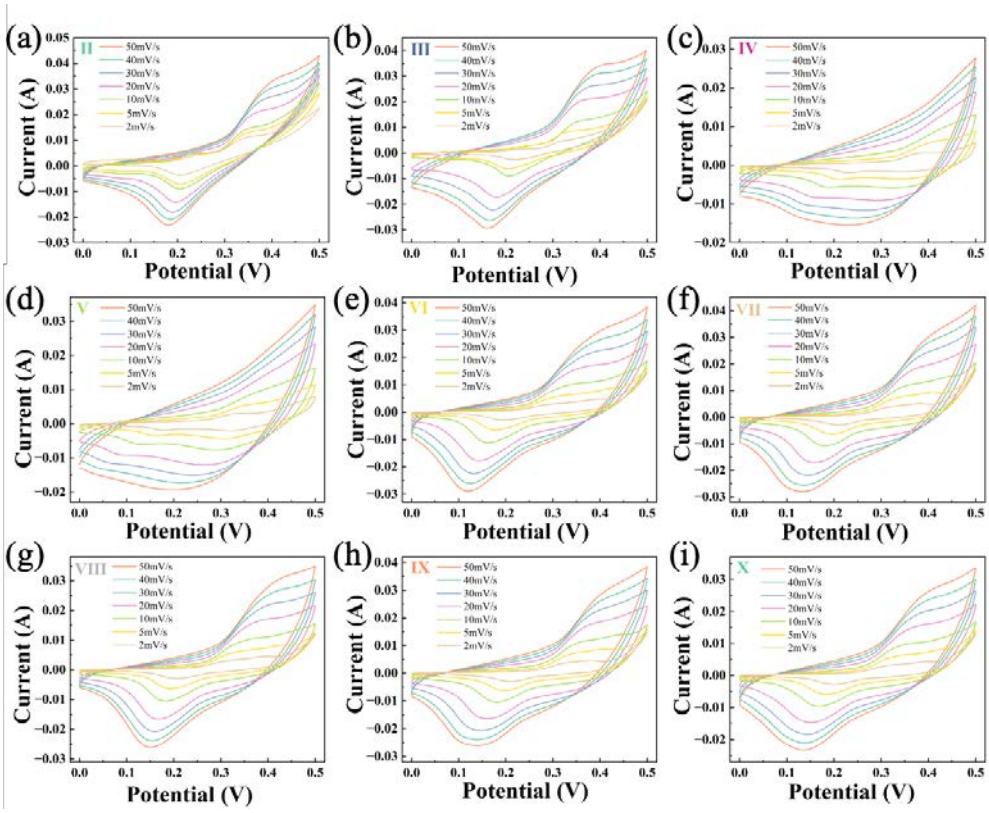

Figure 6.12 Cyclic voltammetry (CV) curves of Samples II-X at various scan rates (2 mV/s to 50 mV/s).

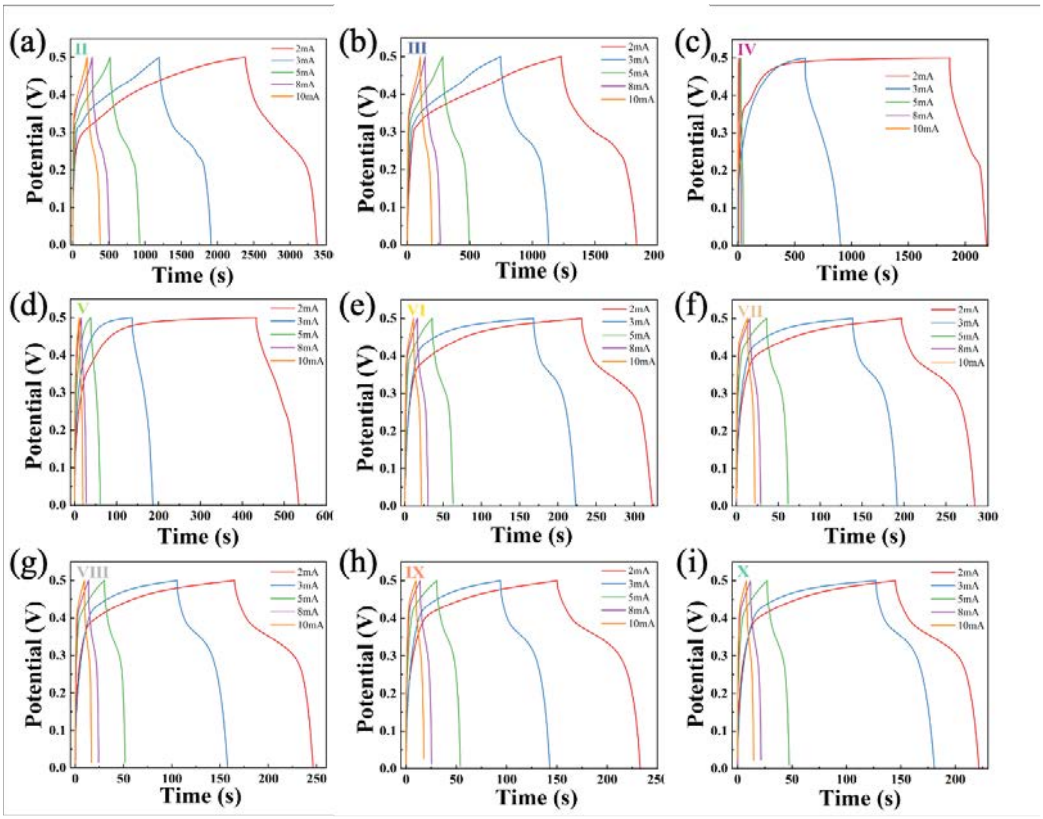

Figure 6.13 Galvanostatic charge-discharge (GCD) curves of Samples II-X at different current densities (2, 3, 5, 8, and 10 mA cm^{-2}).

A symmetric stretchable supercapacitor is further assembled to assess the practical applicability of $Ni_{20}Co_{40}$ LDH@CNT_2SBS_1@F. The assembled stretchable supercapacitor, where two $Ni_{20}Co_{40}$ LDH@CNT_2SBS_1@Fs are sandwiched with a gel electrolyte. **Figure 6.14** shows that the potential windows of the $Ni_{20}Co_{40}$ LDH@CNT_2SBS_1@F as the negative electrode (0~ 0.5 V) and the positive electrode (-0.9~ 0 V). **Figure 6.15 (a)** shows the GCD curves of the symmetric supercapacitor at different voltage windows. The nearly symmetrical and linear charge-discharge curves demonstrate excellent reversibly capacitive behavior. As the voltage increases, the discharge time extends without significant distortion in the charge–discharge curves, indicating the device's capability to store energy at higher voltage windows. **Figure 6.15 (b)** illustrates the GCD profiles at various current densities. **Figure 6.15 (c)** shows the CV curves at different voltage windows with a scan rate of 20 mV s^{-1}. The quasi-rectangular shapes of the curves indicate typical capacitive behavior, along with redox peaks corresponding to the pseudocapacitive behavior, which are associated with the NiCo-LDH/CNT composite. **Figure 6.15 (d)** shows that the redox peaks on the CV curves slightly shift at different scan rates, suggesting a stable energy storage behavior. **Figure 6.15 (e)** compares the GCD curves at 2 mA cm^{-2} of the stretchable supercapacitor before and after stretching (80%). The near-identical curves demonstrate that the charge-discharge curve of the stretchable supercapacitor remains almost unchanged before and after mechanical deformation, demonstrating excellent flexibility and structural integrity. This is attributed to the hierarchically porous

structure of knitted fabric, which enables the stretchable supercapacitor to maintain its high energy storage performance in the stretched state.

Figure 6.15 (f) presents the GCD curves of a single device, two devices in series, and two devices in parallel at 25 mA cm^{-2}. The series configuration increases the voltage, while the parallel configuration increases the current, demonstrating the device's modular capability to meet various energy and power requirements. Such flexibility in configuration is essential for scalable energy storage systems. **Figure 6.15 (g)** shows the specific capacitance as a function of discharge current density. As the current density increases from 5 to 30 mA cm^{-2}, the specific capacitance decreases from approximately 2944.71 to 555.21 mF cm^{-2}. The supercapacitor still demonstrates good rate capability, retaining a significant proportion of its capacitance even at high current densities. **Figure 6.15(h)** shows the Ragone plot, illustrating the relationship between energy density and power density. As the power density increases, the energy density decreases, a typical trade-off for supercapacitors. The device achieves competitive energy density even at higher power densities, making it suitable for applications requiring high power and reasonable energy storage. The relationship between the power density and the energy density for the NiCo-LDH device and other reported counterparts are shown in Figure 5h. The NiCo-LDH device delivered a high energy density of 801.6 μWh cm^{-2} (400.6Wh kg^{-1}) at a power density of 3.5 mW cm^{-1} (1749.5 W kg^{-1}), which was higher than its counterparts, such as LDH materials of 3D NiCo-LDH microflowers derived from ZIF-67 (53.31 Wh kg^{-1} at 749.7 W kg^{-1})[248], Al-doped NiCoP derived from NiCo-LDH precursors (51.7 Wh kg^{-1} at 500W kg^{-1})[205], GQDs pinned on NiCo-LDH hollow

micro-tunnels (46 Wh kg^{-1} at 7440W kg^{-1})[249], NiCo-LDH microspheres derived from Ni-MOF (36.1 Wh kg^{-1} at 649 W kg^{-1})[250], NiCo-LDH nanosheet array/Ag nanowire (42.9 Wh kg^{-1} at 800 W kg^{-1})[251], NiCo-LDH nanowires@nanosheets core-shell (298.6 μWh cm^{-2} at 0.80 mW cm^{-2})[252], yarn coated with Ni-Co-S (48.7 μWh cm^{-2} at 0.553mW cm^{-2})[253], $Ni(OH)_2$ nanosheet wrapped $NiCo_2O_4$ on CNTF (103.8 μWh cm^{-2} at 0.8 mW cm^{-2})[254], 3D hierarchical $NiCo_2O_4$@NiCo-LDH (49 Wh kg^{-1} at 750 W kg^{-1})[255]. **Table 6.1** shows a comprehensive comparison of NiCo-LDH with the previously reported NiCo-based supercapacitor. In contrast to typical capacitance retention values, the symmetric capacitor exhibits remarkable long-term stability in both liquid and gel electrolytes. As shown in **Figure 6.16**, the capacitor in 3M KOH solution achieves a coulombic efficiency of 95.06% after 5000 cycles and maintains 93.97% efficiency even after 20,000 cycles at 20 mA cm^{-2}. Meanwhile, the symmetric capacitor of $Ni_{20}Co_{40}$ LDH@CNT_2SBS_1@F using a gel electrolyte retains 86.37% of its initial capacity after 5000 cycles, demonstrating enhanced durability and suitability for encapsulated solid-state devices. **Figure 6.15 (i)** shows a practical application demonstration of the stretchable supercapacitor, which powers an electronic thermo-hygrometer when stretched. This demonstrates the real-world applicability of stretchable supercapacitors in wearable electronic devices.

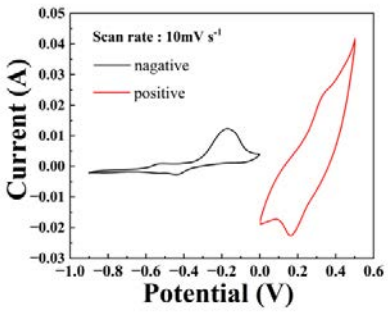

Figure 6.14 CV curves of sample I as negative and positive.

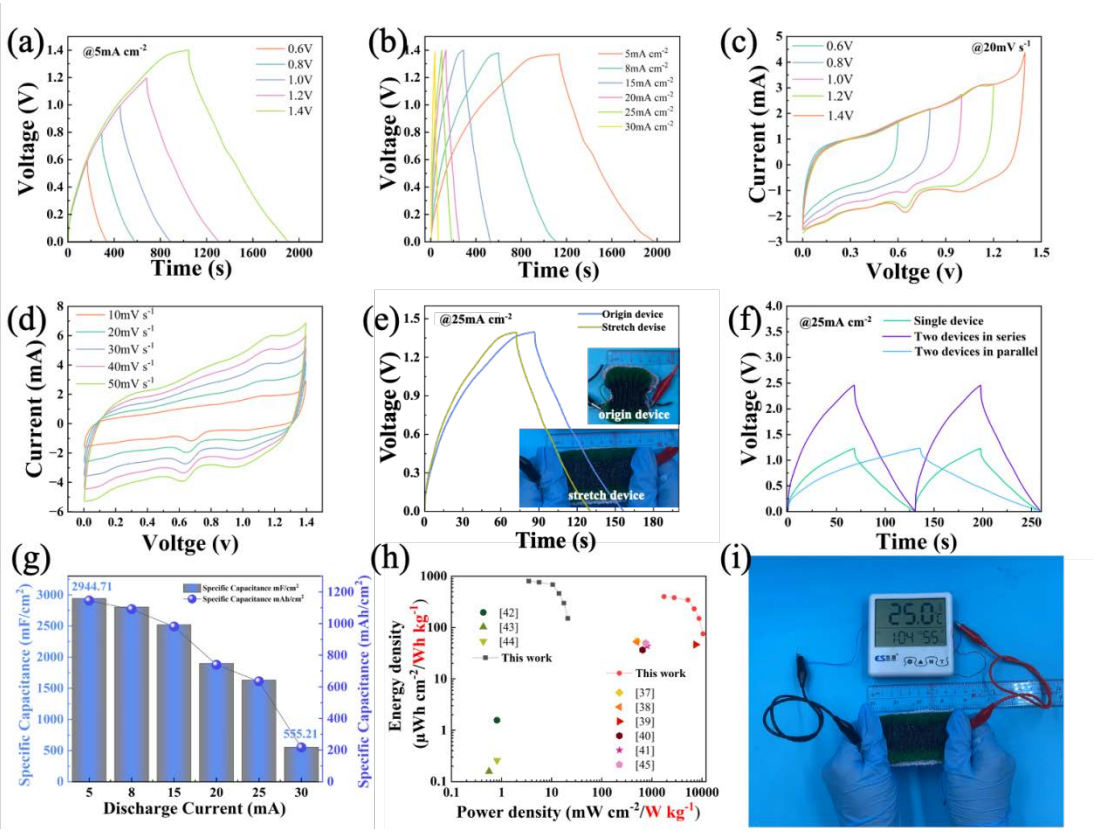

Figure 6.15 Electrochemical performance of the symmetric supercapacitor based on $Ni_{20}Co_{40}$ LDH@CNT$_2$SBS$_1$@F electrodes. (a) Galvanostatic charge-discharge (GCD) curves at different voltages with a constant current density of 5 mA cm^{-2}. (b) GCD curves at varying current densities at 1.4V. (c) CV curves at different voltages and a scan rate of 20 mV s^{-1}. (d) CV curves at different scan rates at 1.4V. (e) GCD curves at 2 mA cm^{-2}, comparing the performance of the original device and the device under stretch (80%). (f) GCD curves for a single device, two devices in series, and two devices in parallel. (g) Specific capacitance as a function of discharge current density. (h) Ragone plot showing the comparison of energy density and power density between stretchable supercapacitor of $Ni_{20}Co_{40}$ LDH@CNT2$_S$BS$_1$@F and NiCo-LDH with the previously reported NiCo-based supercapacitor. (i) Demonstration application.

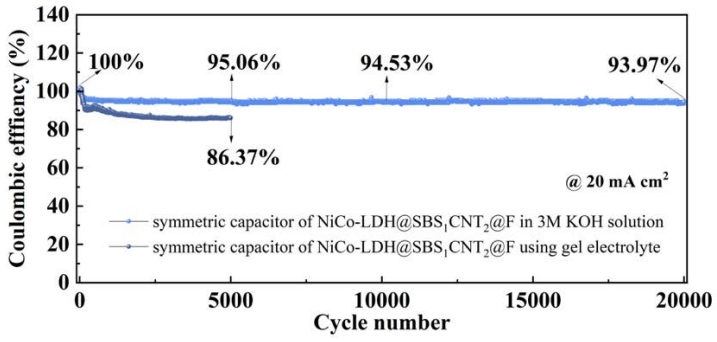

Figure 6.16 Long-term cycling performance of asymmetric capacitor of $Ni_{20}Co_{40}$ LDH@CNT_2SBS_1@F in different condision.

Table 6.1 Comparison of NiCo materials used as active materials for supercapacitors.

LDH materials	Capacitance	Stability (Cycle)	Energy Density (E)	Power Density (P)	Ref.
3D NiCo-LDH microflowers derived from ZIF-67	1765 F g^{-1} at 1 A g	84.3% retention after 6000 cycles	53.31 Wh kg^{-1}	749.7 W kg^{-1}	248
Al-doped NiCoP derived from NiCo-LDH precursors	1059 F g^{-1} at 1 A g^{-1}	99% retention after 10000 cycles	51.7 Wh kg^{-1}	500 W kg^{-1}	205
Graphene Quantum Dots (GQDs) pinned on NiCo-LDH hollow micro-tunnels	1628 F g^{-1} at 1 A g^{-1}	86.2% retention after 8000 cycles	46 Wh kg^{-1}	7440 W kg^{-1}	249
NiCo-LDH microspheres derived from Ni-MOF	1272 C g^{-1} at 2 A g^{-1}	103.9% retention after 5000 cycles	36.1 Wh kg^{-1}	649 W kg^{-1}	250
NiCo-LDH nanosheet array/Ag nanowire	2920.6 F g^{-1} at 5 A g^{-1}	89.8% retention after 2000 cycles	42.9 Wh kg^{-1}	800 W kg^{-1}	251
NiCo-LDH nanowires@nanosheets core-shell	9.67 F cm^{-2} at 5 mA cm^{-2}	75% retention after 2000 cycles	298.6 μWh cm^{-2}	0.80 mW cm^{-2}	252
Yarn coated with Ni-Co-S	127.2 mF cm^{-2} at 0.1 mA/cm	90% retention after 3000 cycles	48.7 μWh cm^{-2}	0.553mW cm^{-2}	253
$Ni(OH)_2$ nanosheet wrapped $NiCo_2O_4$ on CNTF	291.9 mF cm^{-2} at 1 mA/cm^2	95% retention after 5000 cycles	103.8 μWh cm^{-2}	0.8 mW cm^{-2}	254
3D hierarchical $NiCo_2O_4$@NiCo-LDH	6092 mF cm^{-2}	83.3% retention after 2000 cycles	49 Wh kg^{-1}	750 W kg^{-1}	255
NiCo-LDH nanowires	**4948 mF cm^{-2} at 2 mA cm^{-2}**	**93.97% retention after 20000 cycles**	**801.6μWh cm^{-2} /400.5 Wh kg^{-1}**	**3.5mW cm^{-2} /1749.5 W kg^{-1}**	**This work**

6.4 Conclusion

This study develops a stretchable supercapacitor with high flexibility and excellent energy storage performance to meet the energy needs of wearable electronic devices. The CNT/SBS composite scaffold, constructed under high humidity conditions using the BF method, forms an electrode with a hierarchical porous structure, which improves conductivity and surface area while providing support for the uniform growth of NiCo-LDH. The experimental results show that the $Ni_{20}Co_{40}$ LDH@CNT_2SBS_1@F electrode reaches a capacitance of 4,948 mF cm^{-2} at 2 mA cm^{-2}, showing excellent energy storage capability. In addition, under 80% tensile strain, the device can maintain 94% of the initial capacitance; after 20,000 charge and discharge cycles, its capacitance decay is only 8%, proving its stability in repeated mechanical deformation and long-term use. The energy density of the supercapacitor reaches 801.6 μWh cm^{-2} (400.6 Wh kg^{-1}), and it still shows excellent energy output efficiency at a power density of 3.5 mW cm^{-2} (1749.5 W kg^{-1}). These characteristics indicate that the composite material not only has broad application prospects in flexible and wearable devices, but also provides a new solution for the design of high-performance, stretchable energy storage devices in the future. This design idea lays the foundation for the development of energy storage devices with both high electric performance and high mechanical flexibility, and is expected to promote the development of next-generation wearable electronic devices and flexible energy systems.

Chapter 7 Conclusions and Recommendations for Future Work

7.1 Conclusions

This thesis systematically investigates the development, characterization, and applications of hierarchically buckled porous microstructured textiles (HBPMTs), providing a comprehensive framework for integrating advanced functionalities into flexible and wearable textiles. The research demonstrates how the unique properties of HBPMTs, such as stretchability, and hierarchical porous architectures, can be leveraged to address challenges in energy harvesting, self-powered sensing, and energy storage. By combining innovative fabrication techniques with functional material integration, this work establishes a solid foundation for the next generation of smart textiles. The main findings and conclusions of the study are described as follow:

First study introduces the novel fabrication strategy for hierarchically buckled porous microstructured fibers (HBPMFs), inspired by the surface buckling of human skin. Through the combination of material manipulation, interfacial self-assembly, and thermal annealing, the study achieves fibers with enhanced stretchability, increased surface area, and effective functional material integration. The demonstrated applications, such as TiO_2-enhanced fibers for photocatalytic degradation, highlight the transformative potential of these advanced materials.

Second study explores the development of HBPMFs tailored for triboelectric nanogenerators (TENGs). The integration of functional nanomaterials, such as Ag nanoparticles, significantly enhances the electrical performance of the HBPMFs-

TENGs, achieving up to six-fold increases in output metrics. Additionally, the study illustrates their ability to act as self-powered sensors for detecting fine human motions, such as breathing and joint movements, making them suitable for wearable healthcare applications.

Third study extends the scope of HBPS to energy storage, presenting advanced stretchable supercapacitors fabricated using HBPS modified with nickel-cobalt layered double hydroxides (NiCo-LDH). These devices exhibit excellent electrochemical performance and mechanical resilience under strain. This work emphasizes the synergy between hierarchical structures and energy storage materials for wearable electronics.

Fourth study delves into advanced energy storage systems, demonstrating the synthesis of CNT/SBS composites with hierarchically buckled porous architectures on knitted fabrics. The resulting supercapacitors achieve exceptional energy density and mechanical robustness, providing a pathway for integrating energy storage capabilities into smart textiles. The chapter highlights the practical applications of these systems in powering wearable devices under dynamic conditions.

7.2 Recommendations for future work

Building on the findings of this research, several areas of further investigation are proposed to expand the scope and impact of HBPMTs:

7.2.1 Scalability and Sustainable Fabrication

The scalability of HBPMTs fabrication is crucial for their commercial viability. Future research should focus on developing cost-effective, scalable manufacturing

processes while maintaining the uniformity and quality of the hierarchical structures. Additionally, integrating sustainable materials, such as biodegradable polymers, and adopting green fabrication methods, like water-based processes or solvent-free approaches, can minimize the environmental impact of production, aligning with the principles of eco-friendly manufacturing.

7.2.2 Integration of Dynamic Functionalities

Expanding the scope of HBPMTs through the integration of dynamic and stimuli-responsive materials, such as hydrogels or shape-memory polymers, can enhance their adaptability to changing environments. These materials could enable self-healing, thermal regulation, or environmental responsiveness, further broadening the application areas of HBPMTs in fields such as biomedical devices, adaptive clothing, and environmental monitoring systems.

7.2.3 Enhancing Durability and Long-Term Stability

While HBPMTs have demonstrated excellent mechanical and functional performance, their durability under prolonged mechanical deformation and harsh environmental conditions requires further investigation. Future work should focus on evaluating the performance of HBPMTs under real-world conditions, such as exposure to humidity, temperature fluctuations, and repeated mechanical stress, and developing strategies to mitigate wear and fatigue, such as reinforced interfacial bonding or protective coatings.

7.2.4 Advanced Functional Material Integration

Expanding the range of functional nanomaterials incorporated into HBPMTs can unlock new applications. For instance, integrating quantum dots, conductive polymers, or novel 2D materials like MXene could lead to advancements in energy storage, optical sensing, or wearable electronics. Hybrid systems combining HBPMTs with rigid electronics or microfluidics could also create multifunctional textile platforms for healthcare and beyond.

7.2.5 AI-Assisted Design and Modeling

Artificial intelligence (AI) and machine learning offer promising tools for optimizing the design and performance of HBPMTs. Future research could develop predictive models to simulate the effects of fabrication parameters on material properties, enabling rapid prototyping and customization. Additionally, machine learning algorithms could analyze large datasets to identify optimal combinations of materials, structures, and functionalities, streamlining the development process.

References

1. Salvatore GA, Münzenrieder N, Kinkeldei T, et al. Wafer-scale design of lightweight and transparent electronics that wraps around hairs. *Nat Commun*. 2014;5(1):2982.

2. Wang F, Zhu B, Shu L, Tao X. Flexible pressure sensors for smart protective clothing against impact loading. *Smart Mater Struct*. 2013;23(1):015001.

3. Someya T, Bao Z, Malliaras GG. The rise of plastic bioelectronics. *Nature*. 2016;540(7633):379-385.

4. Gao W, Emaminejad S, Nyein HYY, et al. Fully integrated wearable sensor arrays for multiplexed in situ perspiration analysis. *Nature*. 2016;529(7587):509-514.

5. Harvesting electrical energy from carbon nanotube yarn twist | Science.

6. Soin N, Shah TH, Anand SC, et al. Novel "3-D spacer" all fibre piezoelectric textiles for energy harvesting applications. *Energy Environ Sci*. 2014;7(5):1670-1679.

7. Fan JA, Yeo WH, Su Y, et al. Fractal design concepts for stretchable electronics. *Nat Commun*. 2014;5(1):3266.

8. Hussain AM, Ghaffar FA, Park SI, Rogers JA, Shamim A, Hussain MM. Metal/Polymer Based Stretchable Antenna for Constant Frequency Far-Field Communication in Wearable Electronics. *Adv Funct Mater*. 2015;25(42):6565-6575.

9. Epidermal Electronics | Science.

10. Wang S, Xu J, Wang W, et al. Skin electronics from scalable fabrication of an intrinsically stretchable transistor array. *Nature*. 2018;555(7694):83-88.

11. Oh JY, Rondeau-Gagné S, Chiu YC, et al. Intrinsically stretchable and healable semiconducting polymer for organic transistors. *Nature*. 2016;539(7629):411-415.

12. Hierarchically buckled sheath-core fibers for superelastic electronics, sensors, and muscles | Science.

13. Study of Fiber-Based Wearable Energy Systems | Accounts of Chemical Research.

14. Li Q, Zhang LN, Tao XM, Ding X. Review of Flexible Temperature Sensing Networks for Wearable Physiological Monitoring. *Advanced Healthcare Materials*. 2017;6(12):1601371.

15. Shi J, Liu S, Zhang L, et al. Smart Textile-Integrated Microelectronic Systems for Wearable Applications. *Advanced Materials*. 2020;32(5):1901958.

16. Zhang L, Lin S, Hua T, Huang B, Liu S, Tao X. Fiber-Based Thermoelectric Generators: Materials, Device Structures, Fabrication, Characterization, and Applications. *Advanced Energy Materials*. 2018;8(5):1700524.

17. Sen AK. *Coated Textiles: Principles and Applications, Second Edition*. CRC Press; 2007.

18. Wei Q. 14 - Emerging approaches to the surface modification of textiles. In: Wei Q, ed. *Surface Modification of Textiles*. Woodhead Publishing Series in Textiles. Woodhead Publishing; 2009:318-323.

19. Zhang A, Bai H, Li L. Breath Figure: A Nature-Inspired Preparation Method for Ordered Porous Films. *Chem Rev*. 2015;115(18):9801-9868.

20. Nicholls JR. Advances in Coating Design for High-Performance Gas Turbines. *MRS Bulletin*. 2003;28(9):659-670.

21. Baruwa AD, Akinlabi ET, Oladijo OP. Surface Coating Processes: From Conventional to the Advanced Methods; a Short Review. In: Emamian SS, Awang M, Yusof F, eds. *Advances in Manufacturing Engineering*. Springer; 2020:483-494.

22. Boulos MI, Fauchais PL, Heberlein JVR. Overview of Surface Modification Technologies. In: Boulos MI, Fauchais PL, Heberlein JVR, eds. *Thermal Spray*

Fundamentals: From Powder to Part. Springer International Publishing; 2021:17-55.

23. Butt MA. Thin-Film Coating Methods: A Successful Marriage of High-Quality and Cost-Effectiveness—A Brief Exploration. *Coatings*. 2022;12(8):1115.

24. Rasool A, Kossar S, Amiruddin R. Different Types of Thin Film Deposition Techniques and Application. In: Song YS, Thoutam LR, Tayal S, Rahi SB, Samuel TSA, eds. *Handbook of Emerging Materials for Semiconductor Industry*. Springer Nature Singapore; 2024:165-177.

25. Mujin S, Baorong H, Yisheng W, Ying T, Weiqiu H, Youxian D. The Surface of Carbon Fibres Continuously Treated by Cold Plasma.

26. Cho BG, Hwang SH, Park M, Park JK, Park YB, Chae HG. The effects of plasma surface treatment on the mechanical properties of polycarbonate/carbon nanotube/carbon fiber composites. *Composites Part B: Engineering*. 2019;160:436-445.

27. Lee YM, You J, Kim M, et al. Highly improved interfacial affinity in carbon fiber-reinforced polymer composites via oxygen and nitrogen plasma-assisted mechanochemistry. *Composites Part B: Engineering*. 2019;165:725-732.

28. Chen X, Ding F, Hou X, Ren X. Novel efficient flame-retardant, smoke suppression and antibacterial treatment for cotton fabrics by surface graft copolymerization. *Cellulose*. 2024;31(15):9487-9502.

29. Shavandi A, Ali MA. Graft polymerization onto wool fibre for improved functionality. *Progress in Organic Coatings*. 2019;130:182-199.

30. He T, Chen X, Wang Y, et al. Fabrication of durable superhydrophobic surfaces of polyester fabrics via fluorination-induced grafting copolymerization. *Applied Surface Science*. 2020;515:146006.

31. Tian H, Yao Y, Liu D, et al. Enhanced Interfacial Adhesion and Properties of Polypropylene/Carbon Fiber Composites by Fiber Surface Oxidation in Presence

of a Compatibilizer. *Polymer Composites*. 2019;40(S1):E654-E662.

32. Nayak SY, Shenoy Heckadka S, Seth A, Prabhu S, Sharma R, Shenoy KR. Effect of chemical treatment on the physical and mechanical properties of flax fibers: A comparative assessment. *Materials Today: Proceedings*. 2021;38:2406-2410.

33. Hybrid Micro Textures – A Multi-Scale Surface Engineering Approach For Enhancing Tribological Characteristics. *JLMN*. Published online December 2019.

34. Stratakis E, Bonse J, Heitz J, et al. Laser engineering of biomimetic surfaces. *Materials Science and Engineering: R: Reports*. 2020;141:100562.

35. He Y, Wang L, Wu T, Wu Z, Chen Y, Yin K. Facile fabrication of hierarchical textures for substrate-independent and durable superhydrophobic surfaces. *Nanoscale*. 2022;14(26):9392-9400.

36. Chung S, Kadala K, Taylor H. Enhancement of Water Repellence by Hierarchical Surface Structures Integrating Micro-dome and Micro-pillar Arrays with Nanoporous Coatings. Published online December 12, 2019.

37. Zhang S, Jiang Q, Xu Y, Guo CF, Wu Z. Facile Fabrication of Self-Similar Hierarchical Micro-Nano Structures for Multifunctional Surfaces via Solvent-Assisted UV-Lasering. *Micromachines*. 2020;11(7):682.

38. Zhang L, Uzoma PC, Xiaoyang C, Penkov OV, Hu H. Bio-Inspired Hierarchical Micro/Nanostructured Surfaces for Superhydrophobic and Anti-Ice Applications. *Front Bioeng Biotechnol*. 2022;10.

39. Mandal P, Perumal G, Arora HS, Ghosh SK, Grewal HS. Green manufacturing of nanostructured Al-Based sustainable self-cleaning metallic surfaces. *Journal of Cleaner Production*. 2021;278:123373.

40. Wang L, Zhang F, Liu Y, Leng J. Shape Memory Polymer Fibers: Materials, Structures, and Applications. *Adv Fiber Mater*. 2022;4(1):5-23.

41. Ma Y, Zou Y, Zhang Z, et al. Luminescent and hydrophobic textile coatings with

recyclability and self-healing capability against both chemical and physical damage. *Cellulose*. 2020;27(1):561-573.

42. Advanced Functional Fiber and Smart Textile | Advanced Fiber Materials.

43. Chen Z, Yang J, Zhang L, et al. Biocompatible wearable touch panel based on ionically conductive organic hydrogels with anti-freezing, anti-dehydration, self-healing, and underwater adhesion properties. Published online September 7, 2023.

44. Smart textiles: A toolkit to fashion the future | Journal of Applied Physics | AIP Publishing.

45. Kayser LV, Lipomi DJ. Stretchable Conductive Polymers and Composites Based on PEDOT and PEDOT:PSS.

46. Lee WK, Odom TW. Designing Hierarchical Nanostructures from Conformable and Deformable Thin Materials. *ACS Nano*. 2019;13(6):6170-6177.

47. Mungekar M, Ma L, Yan W, Kackar V, Shokrzadeh S, Jawed MK. Design of Bistable Soft Deployable Structures via a Kirigami-Inspired Planar Fabrication Approach. *Advanced Materials Technologies*. 2023;8(16):2300088.

48. Schedl AE, Neuber C, Fery A, Schmidt HW. Controlled Wrinkling of Gradient Metal Films. *Langmuir*. 2018;34(47):14249-14253.

49. Tokudome Y, Kuniwaki H, Suzuki K, Carboni D, Poologasundarampillai G, Takahashi M. Thermoresponsive Wrinkles on Hydrogels for Soft Actuators. *Adv Materials Inter*. 2016;3(12):1500802.

50. Three-Dimensional Hierarchical Wrinkles on Polymer Films: From Chaotic to Ordered Antimicrobial Topographies: Trends in Biotechnology.

51. Brodoceanu D, Bauer CT, Kroner E, Arzt E, Kraus T. Hierarchical bioinspired adhesive surfaces—a review. *Bioinspir Biomim*. 2016;11(5):051001.

52. Pishvar M, Harne RL. Foundations for Soft, Smart Matter by Active Mechanical Metamaterials. *Advanced Science*. 2020;7(18):2001384.

53. Ma L, He L, Ni Y. Tunable hierarchical wrinkling: From models to applications. *Journal of Applied Physics*. 2020;127(11):111101.

54. Buckling analysis in stretchable electronics | npj Flexible Electronics.

55. Meng W, Nie M, Liu Z, Zhou J. Buckled Fiber Conductors with Resistance Stability under Strain. *Adv Fiber Mater*. 2021;3(3):149-159.

56. Jiao P. Hierarchical metastructures with programmable stiffness and zero Poisson's ratio. *APL Materials*. 2020;8(5):051109.

57. Li J, Li S, Huang J, et al. Spider Silk-Inspired Artificial Fibers. *Advanced Science*. 2022;9(5):2103965.

58. Han J, Xu B, Li Z, et al. Skin-inspired hierarchically buckled fibers with stretchable porous microarchitectures and customizable functionalities. *Chemical Engineering Journal*. 2023;464:142606.

59. Wang Y, Qin W, Hu X, et al. Hierarchically buckled Ti3C2Tx MXene/carbon nanotubes strain sensor with improved linearity, sensitivity, and strain range for soft robotics and epidermal monitoring. *Sensors and Actuators B: Chemical*. 2022;368:132228.

60. Morphology modulation of artificial muscles by thermodynamic-twist coupling | National Science Review | Oxford Academic.

61. Li J, Zhang G, Cui Z, et al. High Performance and Multifunction Moisture-Driven Yin–Yang-Interface Actuators Derived from Polyacrylamide Hydrogel. *Small*. 2023;19(38):2303228.

62. Wang Y, Qin W, Yang M, et al. High Linearity, Low Hysteresis Ti3C2T MXene/AgNW/Liquid Metal Self-Healing Strain Sensor Modulated by Dynamic Disulfide and Hydrogen Bonds. *Advanced Functional Materials*. 2023;33(37):2301587.

63. Leng X, Mei G, Zhang G, Liu Z, Zhou X. Tethering of twisted-fiber artificial

muscles. *Chem Soc Rev*. 2023;52(7):2377-2390.

64. Bhanja P, Das SK, Bhunia K, et al. A New Porous Polymer for Highly Efficient Capacitive Energy Storage. *ACS Sustainable Chem Eng*. 2018;6(1):202-209.

65. Porous Conductive Textiles for Wearable Electronics | Chemical Reviews.

66. Islam GMN, Ali A, Collie S. Textile sensors for wearable applications: a comprehensive review. *Cellulose*. 2020;27(11):6103-6131.

67. Zhao Z, Xia K, Hou Y, Zhang Q, Ye Z, Lu J. Designing flexible, smart and self-sustainable supercapacitors for portable/wearable electronics: from conductive polymers. *Chem Soc Rev*. 2021;50(22):12702-12743.

68. Ju J, Hao L, Yang S, et al. Designing Robust, Breathable, and Antibacterial Multifunctional Porous Membranes by a Nanofluids Templated Strategy. *Advanced Functional Materials*. 2020;30(46):2006544.

69. Lin Y, Bariya M, Nyein HYY, et al. Porous Enzymatic Membrane for Nanotextured Glucose Sweat Sensors with High Stability toward Reliable Noninvasive Health Monitoring. *Advanced Functional Materials*. 2019;29(33):1902521.

70. Zhang Y, Xia X, Ma K, et al. Functional Textiles with Smart Properties: Their Fabrications and Sustainable Applications. *Advanced Functional Materials*. 2023;33(33):2301607.

71. Three-dimensional printed electrospun fiber-based scaffold for cartilage regeneration. *Materials & Design*. 2019;179:107886.

72. Cui M, Guo H, Zhai W, Liu C, Shen C, Dai K. Template-Assisted Electrospun Ordered Hierarchical Microhump Arrays-Based Multifunctional Triboelectric Nanogenerator for Tactile Sensing and Animal Voice-Emotion Identification. *Advanced Functional Materials*. 2023;33(46):2301589.

73. Tetik H, Wang Y, Sun X, et al. Additive Manufacturing of 3D Aerogels and Porous

Scaffolds: A Review. *Advanced Functional Materials*. 2021;31(45):2103410.

74. Zarei M, Żwir MJ, Michalkiewicz B, Gorący J, Fray ME. Template-assisted electrospinning and 3D printing of multilayered hierarchical vascular grafts. Published online October 18, 2024.

75. Dilamian M, Joghataei M, Ashrafi Z, Bohr C, Mathur S, Maleki H. From 1D electrospun nanofibers to advanced multifunctional fibrous 3D aerogels. *Applied Materials Today*. 2021;22:100964.

76. Ni J, Zhang Y, Song Z, et al. Salt-template-assisted melt-processed porous poly (vinylidene fluoride) nanocomposites for highly efficient all-day passive radiative cooling. *Composites Part A: Applied Science and Manufacturing*. 2023;164:107311.

77. Arif ZU, Khalid MY, Noroozi R, Sadeghianmaryan A, Jalalvand M, Hossain M. Recent advances in 3D-printed polylactide and polycaprolactone-based biomaterials for tissue engineering applications. *International Journal of Biological Macromolecules*. 2022;218:930-968.

78. Bai Z, Xu Y, Li J, et al. An Eco-friendly Porous Nanocomposite Fabric-Based Triboelectric Nanogenerator for Efficient Energy Harvesting and Motion Sensing. *ACS Appl Mater Interfaces*. 2020;12(38):42880-42890.

79. Wang J, He J, Ma L, et al. A humidity-resistant, stretchable and wearable textile-based triboelectric nanogenerator for mechanical energy harvesting and multifunctional self-powered haptic sensing. *Chemical Engineering Journal*. 2021;423:130200.

80. Bayramol DV, Soin N, Shah T, Siores E, Matsouka D, Vassiliadis S. Energy Harvesting Smart Textiles. In: Schneegass S, Amft O, eds. *Smart Textiles: Fundamentals, Design, and Interaction*. Springer International Publishing; 2017:199-231.

81. Khan AS, Khan FU. A survey of wearable energy harvesting systems.

International Journal of Energy Research. 2022;46(3):2277-2329.

82. Mamun MAA, Yuce MR. Recent Progress in Nanomaterial Enabled Chemical Sensors for Wearable Environmental Monitoring Applications. *Advanced Functional Materials*. 2020;30(51):2005703.

83. Smith MK, Mirica KA. Self-Organized Frameworks on Textiles (SOFT): Conductive Fabrics for Simultaneous Sensing, Capture, and Filtration of Gases. *J Am Chem Soc*. 2017;139(46):16759-16767.

84. Sharma A, Babu Eadi S, Noothalapati H, Otyepka M, Lee HD, Jayaramulu K. Porous materials as effective chemiresistive gas sensors. *Chemical Society Reviews*. 2024;53(5):2530-2577.

85. Iakovleva E, Sillanpää M. The use of low-cost adsorbents for wastewater purification in mining industries. *Environ Sci Pollut Res*. 2013;20(11):7878-7899.

86. Douguet O, Buet-Gautier K, Leyssens G, et al. Evaluation of structural parameters to predict particle filtration and air permeability performance of woven textiles. *Textile Research Journal*. Published online May 22, 2023.

87. Otrisal P, Obsel V, Buk J, Svorc L. Preparation of Filtration Sorptive Materials from Nanofibers, Bicofibers, and Textile Adsorbents without Binders Employment. *Nanomaterials*. 2018;8(8):564.

88. Gugliuzza A, Drioli E. A review on membrane engineering for innovation in wearable fabrics and protective textiles. *Journal of Membrane Science*. 2013;446:350-375.

89. Liu Y, Chen L, Li W, et al. Scalable Production of Functional Fibers with Nanoscale Features for Smart Textiles. *ACS Nano*. 2024;18(43):29394-29420.

90. Yilmaz ND. Design of Acoustic Textiles: Environmental Challenges and Opportunities for Future Direction. In: Padhye R, Nayak R, eds. *Acoustic Textiles*. Springer; 2016:185-210.

91. Stucki M, Kellenberger CR, Loepfe M, Stark WJ. Internal polymer pore functionalization through coated particle templating affords fluorine-free green functional textiles. *J Mater Chem A*. 2016;4(39):15197-15206.

92. Wu S. An Overview of Hierarchical Design of Textile-Based Sensor in Wearable Electronics. *Crystals*. 2022;12(4):555.

93. Bagherzadeh R, Abrishami S, Shirali A, Rajabzadeh AR. Wearable and flexible electrodes in nanogenerators for energy harvesting, tactile sensors, and electronic textiles: novel materials, recent advances, and future perspectives. *Materials Today Sustainability*. 2022;20:100233.

94. Wu H, Huang Y, Xu F, Duan Y, Yin Z. Energy Harvesters for Wearable and Stretchable Electronics: From Flexibility to Stretchability. *Advanced Materials*. 2016;28(45):9881-9919.

95. Zhang Y, Li Y, Li K, et al. A large-area versatile textile for radiative warming and biomechanical energy harvesting. *Nano Energy*. 2022;95:106996.

96. Li Y, Fu ZY, Su BL. Hierarchically Structured Porous Materials for Energy Conversion and Storage. *Advanced Functional Materials*. 2012;22(22):4634-4667.

97. Sun MH, Huang SZ, Chen LH, et al. Applications of hierarchically structured porous materials from energy storage and conversion, catalysis, photocatalysis, adsorption, separation, and sensing to biomedicine. *Chem Soc Rev*. 2016;45(12):3479-3563.

98. Li C, Duan Y, Wang S, et al. Hierarchical Porous Fibers for Intrinsically Thermally Insulated and Self-Sensing Integrated Smart Textile. *ACS Appl Mater Interfaces*. 2024;16(11):14124-14132.

99. Pressly A, MajidiRad A, Damircheli M. Advancements in Stretchable and Washable Energy-Storage Devices.

100. Stretchable, Porous, and Conductive Energy Textiles | Nano Letters.

101. Liu C, Li Q, Kang W, et al. Structural design and mechanism analysis of hierarchical porous carbon fibers for advanced energy and environmental applications. *Journal of Materials Chemistry A*. 2022;10(1):10-49.

102. Yang XY, Chen LH, Li Y, Rooke JC, Sanchez C, Su BL. Hierarchically porous materials: synthesis strategies and structure design. *Chem Soc Rev*. 2017;46(2):481-558.

103. Han J, Li Z, Fang C, et al. Hierarchically porous architectured stretchable fibrous materials in energy harvesting and self-powered sensing. *Nano Energy*. 2024;129:110080.

104. Cai G, Yan P, Zhang L, Zhou HC, Jiang HL. Metal–Organic Framework-Based Hierarchically Porous Materials: Synthesis and Applications. *Chem Rev*. 2021;121(20):12278-12326.

105. Li S, Zhang H, Li S, Wang J, Wang Q, Cheng Z. Advances in hierarchically porous materials: Fundamentals, preparation and applications. *Renewable and Sustainable Energy Reviews*. 2024;202:114641.

106. Duan Y, You G, Sun K, et al. Advances in wearable textile-based micro energy storage devices: structuring, application and perspective. *Nanoscale Advances*. 2021;3(22):6271-6293.

107. Yang XY. Hierarchically porous materials: synthesis strategies and structure design. *Chem Soc Rev*. Published online 2017.

108. Tat T, Chen G, Zhao X, Zhou Y, Xu J, Chen J. Smart Textiles for Healthcare and Sustainability. *ACS Nano*. 2022;16(9):13301-13313.

109. Chen G, Xiao X, Zhao X, Tat T, Bick M, Chen J. Electronic Textiles for Wearable Point-of-Care Systems. *Chem Rev*. 2022;122(3):3259-3291.

110. Tokuçoğlu F. Monitoring Physical Activity with Wearable Technologies. *Noro Psikiyatr Ars*. 2018;55(Suppl 1):S63-S65.

111. Wen J, Xu B, Gao Y, Li M, Fu H. Wearable technologies enable high-performance textile supercapacitors with flexible, breathable and wearable characteristics for future energy storage. *Energy Storage Materials*. 2021;37:94-122.

112. Ismar E, Kurşun Bahadir S, Kalaoglu F, Koncar V. Futuristic Clothes: Electronic Textiles and Wearable Technologies. *Global Challenges*. 2020;4(7):1900092.

113. Xu W, Jambhulkar S, Ravichandran D, et al. A mini-review of microstructural control during composite fiber spinning. *Polymer International*. 2022;71(5):569-577.

114. Clemons C. Nanocellulose in Spun Continuous Fibers: A Review and Future Outlook. *Journal of Renewable Materials*. 2016;4(5):327-339.

115. Pelzer M, Vad T, Becker A, Gries T, Markova S, Teplyakov V. Melt spinning and characterization of hollow fibers from poly(4-methyl-1-pentene). *Journal of Applied Polymer Science*. 2021;138(1):49630.

116. Wang F, Liu L, Xue P, Jia M, Wang S, Cai J. The influence of formation temperatures on the crystal structure and mechanical properties of ultrahigh-molecular-weight polyethylene/high-density polyethylene-blend fibers prepared by melt spinning. *Journal of Industrial Textiles*. 2020;49(8):1011-1035.

117. Koeppel A, Holland C. Progress and Trends in Artificial Silk Spinning: A Systematic Review. *ACS Biomater Sci Eng*. 2017;3(3):226-237.

118. Sun J, Chen J, Liu K, Zeng H. Mechanically Strong Proteinaceous Fibers: Engineered Fabrication by Microfluidics. *Engineering*. 2021;7(5):615-623.

119. Liu L, Xu W, Ding Y, Agarwal S, Greiner A, Duan G. A review of smart electrospun fibers toward textiles. *Composites Communications*. 2020;22:100506.

120. Han D, Steckl AJ. Coaxial Electrospinning Formation of Complex Polymer Fibers and their Applications. *ChemPlusChem*. 2019;84(10):1453-1497.

121. Zhu M, Li J, Yu J, Li Z, Ding B. Superstable and Intrinsically Self-Healing

Fibrous Membrane with Bionic Confined Protective Structure for Breathable Electronic Skin. *Angewandte Chemie*. 2022;134(22):e202200226.

122. Chen Y, Su N, Zhang K, et al. Effect of fiber surface treatment on structure, moisture absorption and mechanical properties of luffa sponge fiber bundles. *Industrial Crops and Products*. 2018;123:341-352.

123. Lu KJ, Zuo J, Chung TS. Tri-bore PVDF hollow fibers with a super-hydrophobic coating for membrane distillation. *Journal of Membrane Science*. 2016;514:165-175.

124. Gonçalves C, Ferreira da Silva A, Gomes J, Simoes R. Wearable E-Textile Technologies: A Review on Sensors, Actuators and Control Elements. *Inventions*. 2018;3(1):14.

125. Böker A, Lin Y, Chiapperini K, et al. Hierarchical nanoparticle assemblies formed by decorating breath figures. *Nature Mater*. 2004;3(5):302-306.

126. Guan X, Gong J, Xu B. Three-Dimensional Conformal Porous Microstructural Engineering of Textile Substrates with Customized Functions of Brick Materials and Inherent Advantages of Textiles. *ACS Appl Mater Interfaces*. 2020;12(15):17967-17978.

127. Huang J, Xu B, Gao Y, et al. Surface microstructural engineering of continuous fibers as one-dimensional multifunctional fiber materials for wearable electronic applications. *Chemical Engineering Journal*. 2022;446:137192.

128. Gong J, Xu B, Tao X, Li L. Binary breath figures for straightforward and controllable self-assembly of microspherical caps. *Physical Chemistry Chemical Physics*. 2016;18(19):13629-13637.

129. Park Y, Vella G, Loh KJ. Bio-Inspired Active Skins for Surface Morphing. *Sci Rep*. 2019;9(1):18609.

130. Lee Y, Park J, Choe A, Cho S, Kim J, Ko H. Mimicking Human and Biological Skins for Multifunctional Skin Electronics. *Advanced Functional Materials*.

2020;30(20):1904523.

131. Nie B, Liu S, Qu Q, Zhang Y, Zhao M, Liu J. Bio-inspired flexible electronics for smart E-skin. *Acta Biomaterialia*. 2022;139:280-295.

132. Hu X, Dou Y, Li J, Liu Z. Buckled Structures: Fabrication and Applications in Wearable Electronics. *Small*. 2019;15(32):1804805.

133. de Boer B, Stalmach U, Nijland H, Hadziioannou G. Microporous Honeycomb-Structured Films of Semiconducting Block Copolymers and Their Use as Patterned Templates. *Advanced Materials*. 2000;12(21):1581-1583.

134. Romero-Sánchez MD, Walzak MJ, Torregrosa-Maciá R, Martín-Martínez JM. Surface modifications and adhesion of SBS rubber containing calcium carbonate filler by treatment with UV radiation. *International Journal of Adhesion and Adhesives*. 2007;27(6):434-445.

135. Wang K, Amin K, An Z, et al. Advanced functional polymer materials. *Materials Chemistry Frontiers*. 2020;4(7):1803-1915.

136. Peng J, Han Y, Yang Y, Li B. The influencing factors on the macroporous formation in polymer films by water droplet templating. *Polymer*. 2004;45(2):447-452.

137. Vamvounis G, Nyström D, Antoni P, Lindgren M, Holdcroft S, Hult A. Self-Assembly of Poly(9,9‘-dihexylfluorene) to Form Highly Ordered Isoporous Films via Blending. *Langmuir*. 2006;22(9):3959-3961.

138. Ferrari E, Fabbri P, Pilati F. Solvent and Substrate Contributions to the Formation of Breath Figure Patterns in Polystyrene Films. *Langmuir*. 2011;27(5):1874-1881.

139. Bunz UHF. Breath Figures as a Dynamic Templating Method for Polymers and Nanomaterials. *Advanced Materials*. 2006;18(8):973-989.

140. Chiu YC, Kuo CC, Lin CJ, Chen WC. Highly ordered luminescent microporous films prepared from crystalline conjugated rod-coil diblock copolymers of PF- b -

PSA and their superhydrophobic characteristics. *Soft Matter*. 2011;7(19):9350-9358.

141. Wang C, Mao Y, Wang D, Qu Q, Yang G, Hu X. Fabrication of highly ordered microporous thin films by PS- b -PAA self-assembly and investigation of their tunable surface properties. *Journal of Materials Chemistry*. 2008;18(6):683-690.

142. Li Z, Ma X, Zang D, et al. Morphology and wettability control of honeycomb porous films of amphiphilic fluorinated pentablock copolymers via breath figure method. *RSC Advances*. 2014;4(91):49655-49662.

143. Zhao B, Zhang J, Wang X, Li C. Water-assisted fabrication of honeycomb structure porous film from poly(l -lactide). *Journal of Materials Chemistry*. 2006;16(5):509-513.

144. Green E, Fullwood E, Selden J, Zharov I. Functional membranes via nanoparticle self-assembly. *Chemical Communications*. 2015;51(37):7770-7780.

145. Nie Z, Petukhova A, Kumacheva E. Properties and emerging applications of self-assembled structures made from inorganic nanoparticles. *Nature Nanotech*. 2010;5(1):15-25.

146. Sun W, Ji J, Shen J. Rings of Nanoparticle-Decorated Honeycomb-Structured Polymeric Film: The Combination of Pickering Emulsions and Capillary Flow in the Breath Figures Method. *Langmuir*. 2008;24(20):11338-11341.

147. Kim D, Kim H, Chang JY. Designing Internal Hierarchical Porous Networks in Polymer Monoliths that Exhibit Rapid Removal and Photocatalytic Degradation of Aromatic Pollutants. *Small*. 2020;16(22):1907555.

148. Lee CG, Javed H, Zhang D, et al. Porous Electrospun Fibers Embedding TiO2 for Adsorption and Photocatalytic Degradation of Water Pollutants. *Environ Sci Technol*. 2018;52(7):4285-4293.

149. Kim KN, Chun J, Kim JW, et al. Highly Stretchable 2D Fabrics for Wearable Triboelectric Nanogenerator under Harsh Environments. *ACS Nano*.

2015;9(6):6394-6400.

150. He A, Xing T, Liang Z, et al. Advanced Aramid Fibrous Materials: Fundamentals, Advances, and Beyond. *Adv Fiber Mater*. 2024;6(1):3-35.

151. Chen M, Li P, Wang R, et al. Multifunctional Fiber-Enabled Intelligent Health Agents. *Advanced Materials*. 2022;34(52):2200985.

152. Ma S, Wang X, Li P, et al. Optical Micro/Nano Fibers Enabled Smart Textiles for Human–Machine Interface. *Adv Fiber Mater*. 2022;4(5):1108-1117.

153. Xiong J, Chen J, Lee PS. Functional Fibers and Fabrics for Soft Robotics, Wearables, and Human–Robot Interface. *Advanced Materials*. 2021;33(19):2002640.

154. Zhang Y, Zhou J, Zhang Y, Zhang D, Yong KT, Xiong J. Elastic Fibers/Fabrics for Wearables and Bioelectronics. *Advanced Science*. 2022;9(35):2203808.

155. Tian B, Fang Y, Liang J, et al. Fully Printed Stretchable and Multifunctional E-Textiles for Aesthetic Wearable Electronic Systems. *Small*. 2022;18(13):2107298.

156. Hou Y, Yang Y, Wang Z, et al. Whole Fabric-Assisted Thermoelectric Devices for Wearable Electronics. *Advanced Science*. 2022;9(1):2103574.

157. Zhao J, Fu Y, Xiao Y, Dong Y, Wang X, Lin L. A Naturally Integrated Smart Textile for Wearable Electronics Applications. *Advanced Materials Technologies*. 2020;5(1):1900781.

158. Yang Z, Zhai Z, Song Z, et al. Conductive and Elastic 3D Helical Fibers for Use in Washable and Wearable Electronics. *Advanced Materials*. 2020;32(10):1907495.

159. Liu M, Pu X, Jiang C, et al. Large-Area All-Textile Pressure Sensors for Monitoring Human Motion and Physiological Signals. *Advanced Materials*. 2017;29(41):1703700.

160. Liu Z, Fang S, Moura FA, et al. Hierarchically buckled sheath-core fibers for

superelastic electronics, sensors, and muscles. *Science*. 2015;349(6246):400-404.

161. Lee KY, Chun J, Lee J, et al. Hydrophobic Sponge Structure-Based Triboelectric Nanogenerator. *Advanced Materials*. 2014;26(29):5037-5042.

162. Jeong CK, Baek KM, Niu S, et al. Topographically-Designed Triboelectric Nanogenerator via Block Copolymer Self-Assembly. *Nano Lett*. 2014;14(12):7031-7038.

163. Zhang Y, Zhang T, Huang Z, Yang J. A New Class of Electronic Devices Based on Flexible Porous Substrates. *Advanced Science*. 2022;9(7):2105084.

164. Yu Y, Zheng G, Dai K, et al. Hollow-porous fibers for intrinsically thermally insulating textiles and wearable electronics with ultrahigh working sensitivity. *Materials Horizons*. 2021;8(3):1037-1046.

165. He Y, Wu D, Zhou M, et al. Wearable Strain Sensors Based on a Porous Polydimethylsiloxane Hybrid with Carbon Nanotubes and Graphene. *ACS Appl Mater Interfaces*. 2021;13(13):15572-15583.

166. Wu L, Li Y, Fu Z, Su BL. Hierarchically structured porous materials: synthesis strategies and applications in energy storage. *National Science Review*. 2020;7(11):1667-1701.

167. Zhang A, Bai H, Li L. Breath Figure: A Nature-Inspired Preparation Method for Ordered Porous Films. *Chem Rev*. 2015;115(18):9801-9868.

168. Gong J, Xu B, Tao X. Breath Figure Micromolding Approach for Regulating the Microstructures of Polymeric Films for Triboelectric Nanogenerators. *ACS Appl Mater Interfaces*. 2017;9(5):4988-4997.

169. Li X, Jiang C, Zhao F, et al. Fully stretchable triboelectric nanogenerator for energy harvesting and self-powered sensing. *Nano Energy*. 2019;61:78-85.

170. F. Dumée L, He L, Lin B, et al. The fabrication and surface functionalization of porous metal frameworks – a review. *Journal of Materials Chemistry A*.

2013;1(48):15185-15206.

171. Zou Y, Xu J, Chen K, Chen J. Advances in Nanostructures for High-Performance Triboelectric Nanogenerators. *Advanced Materials Technologies*. 2021;6(3):2000916.

172. Cho H, Lee B, Jang D, Yoon J, Chung S, Hong Y. Recent progress in strain-engineered elastic platforms for stretchable thin-film devices. *Materials Horizons*. 2022;9(8):2053-2075.

173. Luo T, Bai H, Li L. Breath Figure in Reactive Vapor: A New Route to Nanopore Array. *Langmuir*. 2017;33(1):347-352.

174. Huang J, Zhu J, Sun W, Ji J. Versatile and Functional Surface Patterning of in Situ Breath Figure Pore Formation via Solvent Treatment. *ACS Appl Mater Interfaces*. 2020;12(41):47048-47058.

175. Preuksarattanawut C, Kosolwattana S, Siralertmukul K, et al. Tunable honeycomb-hierarchical multiscale structures of 2D/3D porous PLA/CCN composite films fabricated by the breath figure method. *Advanced Industrial and Engineering Polymer Research*. 2024;7(2):234-244.

176. Qin Z, Yin Y, Zhang W, Li C, Pan K. Wearable and Stretchable Triboelectric Nanogenerator Based on Crumpled Nanofibrous Membranes. *ACS Appl Mater Interfaces*. 2019;11(13):12452-12459.

177. Mi HY, Jing X, Zheng Q, et al. High-performance flexible triboelectric nanogenerator based on porous aerogels and electrospun nanofibers for energy harvesting and sensitive self-powered sensing. *Nano Energy*. 2018;48:327-336.

178. Haleem A, Haider Z, Ahmad R u S, et al. Highly porous and thermally stable tribopositive hybrid bimetallic cryogel to boost up the performance of triboelectric nanogenerators. *International Journal of Energy Research*. 2020;44(11):8442-8454.

179. Zhang P, Li PF, Zhang HH, Deng L. Effect of Ag nanoparticle size on triboelectric

nanogenerator for mechanical energy harvesting. *Nanotechnology*. 2022;33(47):475402.

180. Wang S, Lin L, Wang ZL. Nanoscale Triboelectric-Effect-Enabled Energy Conversion for Sustainably Powering Portable Electronics. *Nano Lett*. 2012;12(12):6339-6346.

181. Dong K, Deng J, Zi Y, et al. 3D Orthogonal Woven Triboelectric Nanogenerator for Effective Biomechanical Energy Harvesting and as Self-Powered Active Motion Sensors. *Advanced Materials*. 2017;29(38):1702648.

182. Shen J, Li Z, Yu J, Ding B. Humidity-resisting triboelectric nanogenerator for high performance biomechanical energy harvesting. *Nano Energy*. 2017;40:282-288.

183. Wen Z, Yang Y, Sun N, et al. A Wrinkled PEDOT:PSS Film Based Stretchable and Transparent Triboelectric Nanogenerator for Wearable Energy Harvesters and Active Motion Sensors. *Advanced Functional Materials*. 2018;28(37):1803684.

184. Xiao Y, Xu Y, Qu C, et al. Micro-Crack Assisted Wrinkled PEDOT: PSS to Detect and Distinguish Tensile Strain and Pressure Based on a Triboelectric Nanogenerator. *Advanced Materials Technologies*. 2022;7(1):2100423.

185. Ha M, Lim S, Ko H. Wearable and flexible sensors for user-interactive health-monitoring devices. *J Mater Chem B*. 2018;6(24):4043-4064.

186. Wearable Electronics and Smart Textiles: A Critical Review.

187. A comparison of wearable fitness devices | BMC Public Health.

188. Cheng H, Li Q, Zhu L, Chen S. Graphene Fiber-Based Wearable Supercapacitors: Recent Advances in Design, Construction, and Application. *Small Methods*. 2021;5(9):2100502.

189. Tawiah B, Seidu RK, Asinyo BK, Fei B. A review of fiber-based supercapacitors and sensors for energy-autonomous systems. *Journal of Power Sources*. 2024;595:234069.

190. Rashid Khan H, Latif Ahmad A. Supercapacitors: Overcoming current limitations and charting the course for next-generation energy storage. *Journal of Industrial and Engineering Chemistry*. 2025;141:46-66.

191. Qin S, Seyedin S, Zhang J, et al. Elastic Fiber Supercapacitors for Wearable Energy Storage. *Macromolecular Rapid Communications*. 2018;39(13):1800103.

192. Wang J, Li X, Zi Y, et al. A Flexible Fiber-Based Supercapacitor–Triboelectric-Nanogenerator Power System for Wearable Electronics. *Advanced Materials*. 2015;27(33):4830-4836.

193. Joseph KM, Kasparian HJ, Shanov V. Carbon Nanotube Fiber-Based Wearable Supercapacitors—A Review on Recent Advances. *Energies*. 2022;15(18):6506.

194. Zhai S, Chen Y. Graphene-Based Fiber Supercapacitors. *Acc Mater Res*. 2022;3(9):922-934.

195. Lu Z, Raad R, Safaei F, Xi J, Liu Z, Foroughi J. Carbon Nanotube Based Fiber Supercapacitor as Wearable Energy Storage. *Front Mater*. 2019;6.

196. Anna Thomas S, Cherusseri J, N. Rajendran D. Recent advancements in carbon fiber-based sustainable electrodes for flexible and wearable supercapacitors. *RSC Sustainability*. 2024;2(9):2403-2443.

197. Pullanchiyodan A, Joy R, Sreeram P, et al. Recent advances in electrospun fibers based on transition metal oxides for supercapacitor applications: a review. *Energy Advances*. 2023;2(7):922-947.

198. Zhao N, Feng Y, Fan H, Fu P, Tian S, Zhao Y. Recent advancement in metal oxides based fiber-shaped supercapacitors: Materials, fabrication, device assembly, and challenges. *Journal of Alloys and Compounds*. 2024;976:173319.

199. Qi K, Hou R, Zaman S, Qiu Y, Xia BY, Duan H. Construction of Metal–Organic Framework/Conductive Polymer Hybrid for All-Solid-State Fabric Supercapacitor. *ACS Appl Mater Interfaces*. 2018;10(21):18021-18028.

200. Zhou Z, Zhang Q, Sun J, et al. Metal–Organic Framework Derived Spindle-like Carbon Incorporated α-Fe2O3 Grown on Carbon Nanotube Fiber as Anodes for High-Performance Wearable Asymmetric Supercapacitors. *ACS Nano*. 2018;12(9):9333-9341.

201. Liang H, Lin J, Jia H, et al. Hierarchical NiCo-LDH/NiCoP@NiMn-LDH hybrid electrodes on carbon cloth for excellent supercapacitors. *J Mater Chem A*. 2018;6(31):15040-15046.

202. Zhang X, Lu W, Tian Y, et al. Nanosheet-assembled NiCo-LDH hollow spheres as high-performance electrodes for supercapacitors. *Journal of Colloid and Interface Science*. 2022;606:1120-1127.

203. Liu Y, Wang Y, Shi C, et al. Co-ZIF derived porous NiCo-LDH nanosheets/N doped carbon foam for high-performance supercapacitor. *Carbon*. 2020;165:129-138.

204. Zhang X, Lu Q, Guo E, Feng J, Wei M, Ma J. NiCo layer double hydroxide/biomass-derived interconnected porous carbon for hybrid supercapacitors. *Journal of Energy Storage*. 2021;38:102514.

205. Liu R, Chen L, Mo F, et al. Porous Cobalt-nickel phosphides prepared from Al-doped NiCo-LDH precursors for supercapacitor and electrocatalysis applications. *Chemical Engineering Journal*. 2023;455:140545.

206. Barakzehi M, Montazer M, Sharif F, Norby T, Chatzitakis A. A textile-based wearable supercapacitor using reduced graphene oxide/polypyrrole composite. *Electrochimica Acta*. 2019;305:187-196.

207. Kou L, Huang T, Zheng B, et al. Coaxial wet-spun yarn supercapacitors for high-energy density and safe wearable electronics. *Nat Commun*. 2014;5(1):3754.

208. Yang SY, Wang YF, Yue Y, Bian SW. Flexible polyester yarn/Au/conductive metal-organic framework composites for yarn-shaped supercapacitors. *Journal of Electroanalytical Chemistry*. 2019;847:113218.

209. Qu G, Cheng J, Li X, et al. A Fiber Supercapacitor with High Energy Density Based on Hollow Graphene/Conducting Polymer Fiber Electrode. *Advanced Materials*. 2016;28(19):3646-3652.

210. Xiao G, Ju J, Li M, et al. Weavable yarn-shaped supercapacitor in sweat-activated self-charging power textile for wireless sweat biosensing. *Biosensors and Bioelectronics*. 2023;235:115389.

211. Cheng T, Wang F, Zhang YZ, et al. 3D printable conductive polymer hydrogels with ultra-high conductivity and superior stretchability for free-standing elastic all-gel supercapacitors. *Chemical Engineering Journal*. 2022;450:138311.

212. Zhang C (John), McKeon L, Kremer MP, et al. Additive-Free MXene Inks and Direct Printing of Micro-Supercapacitors. In: *MXenes*. Jenny Stanford Publishing; 2023.

213. Singh SB, Kshetri T, Singh TI, Kim NH, Lee JH. Embedded PEDOT:PSS/AgNFs network flexible transparent electrode for solid-state supercapacitor. *Chemical Engineering Journal*. 2019;359:197-207.

214. Muralee Gopi CVV, Vinodh R, Sambasivam S, Obaidat IM, Kim HJ. Recent progress of advanced energy storage materials for flexible and wearable supercapacitor: From design and development to applications. *Journal of Energy Storage*. 2020;27:101035.

215. Islam MR, Afroj S, Novoselov KS, Karim N. Smart Electronic Textile-Based Wearable Supercapacitors. *Advanced Science*. 2022;9(31):2203856.

216. Fang C, Xu B, Han J, Liu X, Gao Y, Huang J. Pre-Intercalation of Zn Ions to Enlarge and Stabilize Hierarchical Structure of $Zn_x Mn_{1-x}$ Se Cathode for Flexible Zn-Ion Capacitor. *Adv Funct Materials*. 2024;34(26):2310909.

217. Swain N, Tripathy A, Thirumurugan A, Saravanakumar B, Schmidt-Mende L, Ramadoss A. A brief review on stretchable, compressible, and deformable supercapacitor for smart devices. *Chemical Engineering Journal*.

2022;446:136876.

218. Fang C, Han J, Yang Q, et al. Boosting Zn-Ion Storage Behavior of Pre-Intercalated MXene with Black Phosphorus toward Self-Powered Systems. *Advanced Science*. 2024;11(40):2408549.

219. Keum K, Kim JW, Hong SY, Son JG, Lee S, Ha JS. Flexible/Stretchable Supercapacitors with Novel Functionality for Wearable Electronics. *Advanced Materials*. 2020;32(51):2002180.

220. Borenstein A, Hanna O, Attias R, Luski S, Brousse T, Aurbach D. Carbon-based composite materials for supercapacitor electrodes: a review. *J Mater Chem A*. 2017;5(25):12653-12672.

221. Yang K, Luo M, Zhang D, et al. Ti3C2T*x*/carbon nanotube/porous carbon film for flexible supercapacitor. *Chemical Engineering Journal*. 2022;427:132002.

222. Wang K, Wang Z, Wang C, Zhang X, Wu L. Carbon fiber electrodes for composite structural supercapacitor: Preparation and modification methods. *Journal of Energy Storage*. 2024;98:113129.

223. Xia GT, Li C, Wang K, Li LW. Structural Design and Electrochemical Performance of PANI/CNTs and MnO2/CNTs Supercapacitor. *Science of Advanced Materials*. 2019;11(8):1079-1086.

224. Kumar S, Saeed G, Zhu L, Hui KN, Kim NH, Lee JH. 0D to 3D carbon-based networks combined with pseudocapacitive electrode material for high energy density supercapacitor: A review. *Chemical Engineering Journal*. 2021;403:126352.

225. Sekitani T, Noguchi Y, Hata K, Fukushima T, Aida T, Someya T. A Rubberlike Stretchable Active Matrix Using Elastic Conductors. *Science*. 2008;321(5895):1468-1472.

226. Lu Z, Chao Y, Ge Y, et al. High-performance hybrid carbon nanotube fibers for wearable energy storage. *Nanoscale*. 2017;9(16):5063-5071.

227. Jang Y, Kim SM, Spinks GM, Kim SJ. Carbon Nanotube Yarn for Fiber-Shaped Electrical Sensors, Actuators, and Energy Storage for Smart Systems. *Advanced Materials*. 2020;32(5):1902670.

228. Tomboc GM, Kim J, Wang Y, et al. Hybrid layered double hydroxides as multifunctional nanomaterials for overall water splitting and supercapacitor applications. *J Mater Chem A*. 2021;9(8):4528-4557.

229. Mallakpour S, Radfar Z, Hussain CM. Current advances on polymer-layered double hydroxides/metal oxides nanocomposites and bionanocomposites: Fabrications and applications in the textile industry and nanofibers. *Applied Clay Science*. 2021;206:106054.

230. Zhao M, Zhao Q, Li B, Xue H, Pang H, Chen C. Recent progress in layered double hydroxide based materials for electrochemical capacitors: design, synthesis and performance. *Nanoscale*. 2017;9(40):15206-15225.

231. Choi C, Kim SH, Sim HJ, et al. Stretchable, Weavable Coiled Carbon Nanotube/MnO2/Polymer Fiber Solid-State Supercapacitors. *Sci Rep*. 2015;5(1):9387.

232. Zhang C, Guo R, Wang H, Xie X, Du C. Composite electrodes with NiCoAl-LDH coated Ti3C2Tx MXene and incorporated Ag nanowires for screen-printable in-plane hybrid supercapacitors on textiles. *Applied Surface Science*. 2022;598:153796.

233. Zhong Y, Liao R, He G, Liu S, Zhang J, Chen C. An electrochemical sensor based on porous heterojunction hollow NiCo-LDH/Ti3C2Tx MXenes composites for the detection of quercetin in natural plants. *Microchim Acta*. 2024;191(10):572.

234. Huang J. A hierarchical layered double hydroxide electrode with surface porous microstructured fibers for flexible and wearable energy storage. *J Mater Chem A*. Published online 2024.

235. Liu T, Zhang F, Song Y, Li Y. Revitalizing carbon supercapacitor electrodes with

hierarchical porous structures. *J Mater Chem A*. 2017;5(34):17705-17733.

236. Xu H, Zhang Y, Wang L, Chen Y, Gao S. Hierarchical porous biomass-derived carbon framework with ultrahigh surface area for outstanding capacitance supercapacitor. *Renewable Energy*. 2021;179:1826-1835.

237. Benzigar MR, Dasireddy VDBC, Guan X, Wu T, Liu G. Advances on Emerging Materials for Flexible Supercapacitors: Current Trends and Beyond. *Advanced Functional Materials*. 2020;30(40):2002993.

238. Jafari A. Stretchable electronics: Advances in elastic conductive fibers for multifunctional applications. *Organic Electronics*. 2024;135:107145.

239. Han J, Xu B, Li Z, et al. Skin-inspired hierarchically buckled fibers with stretchable porous microarchitectures and customizable functionalities. *Chemical Engineering Journal*. 2023;464:142606.

240. Xiang D, Zhang X, Liu Z, et al. Preparation and performance of biaxially stretched CNT-SBS/POE flexible strain sensor with a double percolation structure. *Sensors and Actuators A: Physical*. 2024;371:115340.

241. Xiang D, Liu L, Xu F, et al. Highly Sensitive Flexible Strain Sensor Based on a Double-percolation Structured Elastic Fiber of Carbon Nanotube (CNT)/Styrene Butadiene Styrene (SBS) @ Thermoplastic Polyurethane (TPU) for Human Motion and Tactile Recognition. *Appl Compos Mater*. 2023;30(1):307-322.

242. Feng Q, Zhang H, Guo Z, et al. Three-Dimensional Porous Flower-like NiCo-MOF@Ni-LDH Composite Electrode for High-Performance Supercapacitors. *ACS Appl Energy Mater*. 2024;7(15):6267-6277.

243. Zhu F, Liu W, Liu Y, Shi W. Construction of porous interface on CNTs@NiCo-LDH core-shell nanotube arrays for supercapacitor applications. *Chemical Engineering Journal*. 2020;383:123150.

244. Gao X, Zhao Y, Dai K, Wang J, Zhang B, Shen X. NiCoP nanowire@NiCo-layered double hydroxides nanosheet heterostructure for flexible asymmetric

supercapacitors. *Chemical Engineering Journal*. 2020;384:123373.

245. Shan X, Guo Z, Zhang C, Wang W, Zhao L. Nickel aerogel @ ultra-thin NiCo-LDH nanosheets integrated freestanding film as a collaborative adsorption and accelerated conversion cathode to improve the rate performance of lithium sulfur batteries. *Chemical Engineering Journal*. 2024;488:151105.

246. Wang J, Zang N, Xuan C, Jia B, Jin W, Ma T. Self-Supporting Electrodes for Gas-Involved Key Energy Reactions. *Advanced Functional Materials*. 2021;31(43):2104620.

247. Elemike EE, Osafile OE, Omugbe E. New perspectives 2Ds to 3Ds MXenes and graphene functionalized systems as high performance energy storage materials. *Journal of Energy Storage*. 2021;42:102993.

248. Tahir MU, Arshad H, Xie W, et al. Synthesis of morphology controlled NiCo-LDH microflowers derived from ZIF-67 using binary additives and their excellent asymmetric supercapacitor properties. *Applied Surface Science*. 2020;529:147073.

249. Zhao T, Liu C, Meng T, et al. Graphene Quantum Dots Pinned on Nanosheets-Assembled NiCo-LDH Hollow Micro-Tunnels: Toward High-Performance Pouch-Type Supercapacitor via the Regulated Electron Localization. *Small*. 2022;18(20):2201286.

250. Ramachandran R, Lan Y, Xu ZX, Wang F. Construction of NiCo-Layered Double Hydroxide Microspheres from Ni-MOFs for High-Performance Asymmetric Supercapacitors. *ACS Appl Energy Mater*. 2020;3(7):6633-6643.

251. Guan T, Fang L, Liu L, et al. Self-supported ultrathin NiCo-LDH nanosheet array/Ag nanowire binder-free composite electrode for high-performance supercapacitor. *Journal of Alloys and Compounds*. 2019;799:521-528.

252. Su W, Wu F, Fang L, et al. NiCo-LDH nanowires@nanosheets core-shell structure grown on carbon fiber cloth for high performance flexible supercapacitor electrode. *Journal of Alloys and Compounds*. 2019;799:15-25.

253. Chen Y, Xu B, Wen J, et al. Design of Novel Wearable, Stretchable, and Waterproof Cable-Type Supercapacitors Based on High-Performance Nickel Cobalt Sulfide-Coated Etching-Annealed Yarn Electrodes. *Small*. 2018;14(21):1704373.

254. Wang X, Sun J, Zhao J, et al. All-Solid-State Fiber-Shaped Asymmetric Supercapacitors with Ultrahigh Energy Density Based on Porous Vanadium Nitride Nanowires and Ultrathin $Ni(OH)_2$ Nanosheet Wrapped $NiCo_2$ O_4 Nanowires Arrays Electrode. *J Phys Chem C*. 2019;123(2):985-993.

255. Li S, Luo Y, Wang C, et al. A novel hierarchical core-shell structure of NiCo2O4@NiCo-LDH nanoarrays for higher-performance flexible all-solid-state supercapacitor electrode materials. *Journal of Alloys and Compounds*. 2022;920:165986.